GEOCIÊNCIAS
USP
INSTITUTO DE GEOCIÊNCIAS

TESE DE DOUTORADO
N° 572

EVOLUÇÃO METALOGENÉTICA DO DEPÓSITO DE Cu-(Ni-Zn) JATOBÁ, PROVÍNCIA MINERAL DE CARAJÁS

Ângela Suélem Rocha Veloso

Profa. Dra. Lena Virgínia Soares Monteiro
Orientadora

Pós Graduação em Geociências
Programa de Recursos Minerais e Hidrogeologia

USP
Universidade de São Paulo

UNIVERSIDADE DE SÃO PAULO
INSTITUTO DE GEOCIÊNCIAS

EVOLUÇÃO METALOGENÉTICA DO DEPÓSITO DE Cu-(Ni-Zn) JATOBÁ, PROVÍNCIA MINERAL DE CARAJÁS

ÂNGELA SUÉLEM ROCHA VELOSO

Orientadora: Profª. Drª. Lena Virgínia Soares Monteiro

Tese de Doutorado

Nº 572

COMISSÃO JULGADORA

Dra. Lena Virgínia Soares Monteiro

Dra. Carolina Penteado Natividade Moreto

Dra. Rosaline Cristina Figueiredo e Silva

Dr. Claudinei Gouveia de Oliveira

Dr. Rafael Rodrigues de Assis

SÃO PAULO
2017

ÂNGELA SUÉLEM ROCHA VELOSO

EVOLUÇÃO METALOGENÉTICA DO DEPÓSITO DE Cu-(Ni-Zn) JATOBÁ, PROVÍNCIA MINERAL DE CARAJÁS

Versão corrigida

Tese de Doutorado apresentada ao Programa de Pós-graduação em Recursos Minerais e Hidrogeologia, da Faculdade de Geociências da Universidade de São Paulo, como parte dos requisitos necessários à obtenção do título de Doutora em Geociências.

Área de concentração: Recursos Minerais

Orientadora: Prof[a] Dr[a] Lena Virgínia Soares Monteiro

São Paulo

2017

Ficha catalográfica preparada pelo Serviço de Biblioteca e Documentação do Instituto de Geociências da Universidade de São Paulo

Veloso, Ângela Suélem Rocha
Evolução metalogenética do Depósito Cu-(Ni-Zn) Jatobá, Província Mineral de Carajás. - São Paulo, 2017.
213 p. : il

Tese (Doutorado) : IGc/USP
Orient.: Monteiro, Lena Virgínia Soares

1. Província Carajás 2.Depósito Jatobá 3. Metalogênese I. Título

A Eles.

AGRADECIMENTOS

Eis que chega o momento tão esperado, pois é sinal de que os esforços na tentativa da concretização de mais um ciclo acadêmico passam a tomar "corpo".

Gente!, tão importante quanto agradecer às pessoas que estiveram presentes ao longo dos vários anos de minha estada em São Paulo, que representam o tempo de dedicação a essa jornada, são as instituições de ensino, de fomento e empresa privada. Dessa maneira, mesmo sabendo que tais agradecimentos, para muitos, não passam de mera hierárquica formalidade, aqui serão inestimadamente reconhecidos e prazerosamente agradecidos. Pois é sabido que em muitos países, formar um protótipo de profissional de "alta patente" é possibilitada apenas aos estudantes em condições econômicas favoráveis. O que não seria o caso de me incluir.

Dessa maneira torno público meus sinceros agradecimentos aos órgãos do Ministério da Educação destinados a incentivar a pesquisa no Brasil, sendo eles: Coordenação de Aperfeiçoamento de Pessoal de Nível Superior (CAPES), pela concessão da bolsa, pois sem essa seria impossível atingir tal etapa de estudo, e do Ministério de Ciência e Tecnologia, como o Conselho Nacional de Desenvolvimento Científico e Tecnológico (CNPq) e o Instituto Nacional de Ciência e Tecnologia de Geociências da Amazônia (INCT Geociam), pelo valioso auspício financeiro, a partir de projetos de pesquisa, que permitiram a obtenção do conjunto de dados analíticos laboratoriais, aqui apresentados. À Universidade de São Paulo por me possibilitar conviver e aprender com os melhores professores da área de estudo que escolhi para traçar futuramente a carreira de professora universitária. E, finalmente, à empresa VALE e seus geólogos Fernando Matos, Sergio Bacelar Hunh, Benevides Aires e Fabrício Franco, aos quais devoto meus mais sinceros agradecimentos, pois sem o seu apoio, de fato, o estudo não teria sido realizado. Sua participação e contribuição foi de suma e imprescindível importância, por possibilitar acesso a testemunhos de sondagens e informações geológicas de inestimável valor para essa pesquisa.

Contudo, é difícil lembrar de todas as pessoas a quem devemos agradecer quando chega o momento, dessa maneira, torno "genérico" meus agradecimentos, para que ninguém "brigue" achando que lembrei de um em detrimento de outro. Assim, agradeço aos familiares, professores, amigos, técnicos, secretárias e porteiros. Mas saibam, vocês foram muito importantes!

No entanto, uma pessoa não deveria e não deverá ser meramente sujeito de um simples e formal agradecimento. Professora Lena Virgínia Soares Monteiro, sem dúvida nenhuma, é a pessoa a quem devo maior *cândido, sério, lhano, sincero, natural, honrado, genuíno, verídico, franco, claro, autêntico, honesto, verdadeiro e fiel* agradecimento (todos os prováveis adjetivos). Agradeço ainda por acreditar em mim e por orientar e me ensinar a como me portar cientificamente. E um dos maiores agradecimentos por ter confiado nas escolhas que fiz para o bom andamento deste trabalho. Ademais, outros agradecimentos que somente nós sabemos, dos quais já tive a oportunidade de agradecer imensamente, devem ser ressaltados. E por todos os valiosos conselhos, os quais se refletiram na minha vida pessoal.

Reintero e termino meus sinceros agradecimentos a essa Profissional do Ensino. Porque não basta passar em um concurso público para daí se tornar professor, tem que ter o Dom e essa Mulher nasceu com ele (Palmas!). Pois além de um ser humano primoroso, sua ética profissional é irrefutável.

"Agradeço por todas as dificuldades que enfrentei, não fosse por elas eu não teria saído do lugar..."

Chico Xavier

RESUMO

Veloso, A.S.R. **Evolução metalogenética do depósito de Cu-(Ni-Zn) Jatobá, Província Mineral de Carajás.** 2017. 213p. Tese (Doutorado), Instituto de Geociências, Universidade de São Paulo, São Paulo, 2017.

A Província de Carajás, localizada no Cráton Amazônico, possui vários depósitos cupro-auríferos que merecem atenção devido ao seu conteúdo elevado de magnetita hidrotermal e altos teores de ETR, P, Ni, Co, Pd e U, semelhantes aos dos depósitos de óxido de ferro-cobre-ouro (IOCG).

O depósito Jatobá é parte de um conjunto de depósitos IOCG reconhecidos no Cinturão Sul do Cobre em Carajás. Estes depósitos, que incluem Sossego, Cristalino, Alvo 118, Bacaba, Castanha, Bacurim, Visconde e outros, estão localizados em estruturas subsidiárias na Zona de Cisalhamento Canaã de direção E-W e WNW-ESE. As rochas hospedeiras do depósito Jatobá compreendem metadiabásio, metabasalto amigdaloidal, brechas metavolcaniclásticas félsicas, metalapilli tufos máficos e metariodacito porfirítico (LA-ICP-MS U-Pb em zircão, 2.700 ± 16 Ma, MSWD = 22), do Grupo Grão Pará, atribuídos ao Supergrupo Itacaiúnas.

As rochas hospedeiras menos alteradas derivadas de protólitos máficos registram paragênese de fácies xisto verde inferior (albita-actinolita I). Em todos os litotipos, a intensa e pervasiva alteração hidrotermal foi prévia, sin-tectônica e tardia em relação ao desenvolvimento da zona de cisalhamento Canaã. A alteração hidrotermal precoce abrange silicificação, alteração sódica (albita I, scapolita I), sódica-cálcica (ferro-pargasita) e potássica (biotita I, turmalina, Cl-apatita I, Ce-allanita I). Os porfiroclastos de albita (I) e escapolita (I) são amendoados e apresentam sombra de pressão nas rochas miloníticas, indicando a sua blastese anterior ao desenvolvimento da zona de cisalhamento.

Os principais estágios de alteração hidrotermal sin-tectônica compreendem alteração sódico-cálcica (escapolita II), cálcico (actinolita II, Cl-apatita II, Ce-allanita II, quartzo) e potássica (Cl-K-hastingsita I, biotita II, quartz, Co-magnetita IV, Cl-apatita III, Ce-allanita III) controlada pela foliação milonítica. Veios com magnetita (III) e corpos de magnetita maciça (IV) representam envelopes proximais de zonas mineralizadas. Os magnetititos são cortados por actinolita fibrosa (II), magnetita (V) e Cl-apatita, que também promovem a sua brechação. A alteração hidrotermal tardi tectônica é representada por cloritização e por veios de escapolita (III), que por sua vez são cortadas por vênulas com escapolita (IV), Cl-K-hastingsita (II) e biotita (III).

As zonas mineralizadas em cobre-ouro-(níquel) no depósito de Jatobá compreendem corpos de minério verticais a subverticais espacialmente relacionados a diques de metadiabásio e zonas de contato entre metariodacitos e metabasaltos. As zonas mineralizadas foram formadas em quatro estágios. O estágio de mineralização (I) é espacialmente relacionado a corpos de magnetita maciça e à alteração cálcica sin-tectônica (actinolita II-magnetita IV). Caracteriza-se pela associação de Ni-pirrotita, Ni-pirita e Cl-apatita (II), e subordinadamente, Co-calcopirita, Ce-allanita II, Co-pentlandita, quartzo e Ce-monazita. A transição para o estágio de mineralização (II) foi acompanhada por diminuição dos teores de Ni e Co e da quantidade de pirrotita e actinolita. O estilo de mineralização evoluiu de frentes de substituição controladas pela foliação milonítica a zonas de brechas hidráulicas. O estágio de mineralização (II) foi relacionado ao desenvolvimento da alteração potássica sin-tectônica (II) e representado por um sistema de corpos fortemente orientados e interligados com biotita (II), Cl-apatita (III), Co-magnetita (IV), Ilmenita (I), Ce-allanita (III) e quartzo, além de porções discretas contendo Ni-pirita e Co-calcopirita. Brechas com matriz constituída de biotita (II) e Co-calcopirita (± Ni-pirita ± Ni-pirrotita) e fragmentos de magnetita maciça representam os corpos mais ricos em cobre formados nesse estágio.

O terceiro estágio de mineralização do depósito de Jatobá se distingue dos outros por seu controle estrutural exercido por estruturas dúcteis-rúpteis. Esse estágio foi sincrônico à alteração hidrotermal com biotita mais clara ou verde (III), escapolita (IV), F-Cl-apatita (IV), Cl-K hastingsita (II), Co-calcopirita e siegenita I (± Co-pirita, ± Co-magnetita ± cassiterita).

O estágio de mineralização tardia (IV), o mais expressivo no depósito Jatobá, foi concomitante à formação de clorita (II), quartzo, epidoto e calcita. Ocorre em uma variedade de veios ramificados e brechas com Co-calcopirita, Co-pirita, esfalerita, molibdenita, uraninita e monazita. Outros tipos de veios tardios compreendem aqueles com quartzo-calcopirita-feldspato potássico (± molibdenita, Co-pentlandita e siegenita II) e vênulas finas com clorita-calcopirita, hematita, carbonatos de terras raras (bastnäsita, coskrenita e sahamalita), pirita, esfalerita, ilmenita, marcassita, leucoxênio e adulária.

Os dados litoquímicos para amostras de minério mostram que o estágio inicial de mineralização (I) se caracteriza pelo maior conteúdo de Fe_2O_3 (71,49 a 63,91%), Ni (3930 a 1270 ppm), Co (2320 a 670 ppm), V (740 a 590 ppm), Pd (81 a 372 ppb) e Pt (2 a 17 ppb). Os conteúdos mais alto de ΣETR (até 6773,92 ppm), U (até 48,50 ppm), Th (até 23,30 ppm), P_2O_5 (até 7,97%), Sn (até 24 ppm), Nb (até 7,50 ppm), W (até 322,50 ppm), Zn (até 482 ppm) e ouro (até 1310,80 ppm) foram caracterizados em amostras de minério formadas durante o estágio de mineralização (IV).

A concentração elevada de Ti, V, Ni e Cr em magnetita do depósito Jatobá aponta para condições de alta temperatura (> 500 °C) durante a sua formação, semelhante à dos sistemas magmático-hidrotermais (por exemplo, IOCG, óxido de ferro-apatita (IOA) do tipo Kiruna e depósitos de cobre do tipo pórfiro), especialmente durante o evento inicial de mineralização. Os dados de isótopos de oxigênio apontam para a diminuição da temperatura do estágio de metassomatismo de ferro pré-mineralização (558 °C) aos estágios de mineralização (II = 507 °C; III = 422 °C; IV = 327 °C). No entanto, uma variação relativamente pequena dos valores calculados de $\delta^{18}O_{H2O}$ (9,53 ‰ a 5,41 ‰) foi registrada durante a evolução paragenetica do depósito Jatobá. Os valores de $\delta^{18}O_{H2O}$ e δD_{H2O} (-44,88 ‰ a -30,25 ‰) se sobrepõem ao das águas magmáticas primárias e água magmática félsica.

O aumento gradual do conteúdo de Cl na estrutura da escapolita (I) a (III) também indica uma evolução progressiva a partir de fluidos hipersalinos de alta temperatura e tamponamento das atividades de cloro no sistema. A composição química da escapolita, juntamente aos dados de isótopos estáveis, pode apontar para limitada mistura de fluidos envolvendo fluidos externamente derivados.

Os valores de $\delta^{34}S$ de sulfetos (0,27 ‰ a 1,80 ‰) indicam fontes magmáticas de enxofre. O aumento dos valores de $\delta^{34}S_{sulfetos}$ durante a evolução paragenética foi acompanhado da diminuição dos teores de Ni + Co e V e aumento do teor de Sn + W + Nb em amostras de minério, sugerindo que parte do enxofre e metais podem ter sido lixiviados de rochas máficas-(ultramáficas) adjacentes ao depósito.

A composição altamente radiogênica dos isótopos de Pb em calcopirita ($^{206}Pb/^{204}Pb$ = 99,35 a 245,73; $^{207}Pb/^{204}Pb$ = 32,53 a 62,24; $^{208}Pb/^{204}Pb$ = 55,58 a 172,6) sugere idade arqueana para o último estágio de mineralização (IV). Tais assinaturas podem ter resultado de perturbações no sistema devido ao alto conteúdo de U nos fluidos hidrotermais e à incorporação de Pb (ou U) radiogênico nos sulfetos a partir de uma fonte externa após a sua formação.

O conjunto de dados indica que o depósito de Jatobá teria se formado nas raízes de um sistema mineral IOCG arqueano a partir de fluxo canalizado de fluidos magmáticos. A assinatura do minério de Jatobá pode refletir evolução estreitamente relacionada com o extensivo magmatismo reconhecido na Província Carajás em ca. 2,74 Ga, com herança de granitos tipo A e gabros, a partir de intensos processos de interação fluido-rocha com envolvimento de fluidos alcalinos residuais.

Palavras-chave: depósito Jatobá, depósito de óxido de ferro-cobre-ouro, Província Carajás, alteração hidrotermal, química mineral, isótopos estáveis.

ABSTRACT

Veloso, A.S.R. **Metallogenetic evolution of the Cu-(Ni-Zn) Jatobá deposit, Carajás Mineral Province.** 2017. 213p. (Doctoral) Thesis, Institute of Geosciences, University of São Paulo, São Paulo, 2017.

The Carajás Province, located in the Amazon Craton, hosts several Cu-Au deposits that deserve attention due to their high volume of hydrothermal magnetite and elevated contents of REE, P, Ni, Co, Pd, and U, similar to those of iron oxide-copper-gold (IOCG) deposits.

The Jatobá deposit is part of a cluster of iron oxide–copper–gold (IOCG) deposits recognized in the Southern Copper Belt, in the Carajás Province. These deposits (e.g. Sossego, Cristalino, Alvo 118, Bacaba, Visconde, and others) are located in subsidiary structures within the E-W and WNW–ESE-trending Canaã shear zone. The host rocks at Jatobá comprise metadiabase, amygdaloidal metabasalt, metavolcaniclastic breccias and mafic metalapilli and metacrystal metatuffs and porphyritic metarhyodacite (LA–ICP–MS U–Pb zircon; 2,700 ±16 Ma; MSWD = 22), which are attributed to the Itacaiúnas Supergroup.

The least-altered host rocks derived from mafic protoliths record lower greenschist facies (albite- actinolite I) paragenesis. All lithotypes underwent pre-, syn- and late tectonic hydrothermal alteration associated with the Canaã shear zone development. Early hydrothermal alteration encompasses silicification, sodic (albite I, scapolite I), sodic-calcic (ferro-pargasite), and potassic (biotite I, tourmaline, Cl-apatite I, Ce-allanite I) alteration. Almond-shaped albite (I) or scapolite (I) porphyroclasts involved by pressure in mylonitic rocks indicate their blastesis previously to the shear zone development.

The main syn-tectonic hydrothermal alteration stages comprise sodic-calcic (scapolite II), calcic (actinolite II, Cl-apatite II, Ce-allanite II, quartz) and potassic (Cl-K-hastingsite I, biotite II, quartz-Co-magnetite IV, Cl-apatite III, Ce-allanite III) alteration controlled by the mylonitic foliation. Early veins with magnetite (III) and massive magnetite bodies (IV), represent proximal envelopes of mineralized zones. The magnetitites are cut by fibrous actinolite (II), magnetite (V) and Cl-apatite, which also promote their brecciation. Late tectonic hydrothermal alteration is represented by chlorite alteration and scapolite (III) veins, which in turn are cut by scapolite (IV), Cl-K-hastingsite (II) and biotite (III) veinlets.

The copper-(nickel) mineralized zones in the Jatobá deposit occur as swarms of vertical to subvertical orebodies spatially related to metadiabase dikes and contact zones between metarhyodacites and metabasalts. The mineralized zones were formed in four stages, coeval to ductile and ductile-brittle deformational events. The mineralization stage (I) is spatially related to massive magnetite bodies and to syn-tectonic calcic alteration (actinolite II-magnetite V). It is characterized by Ni-pyrrhotite, Ni-pyrite and Cl-apatite (II), and subordinately, Co-chalcopyrite, Ce-allanite II, Co-pentlandite, quartz and Ce-monazite. The transition to the mineralization stage (II) was accompanied by decreasing contents of Ni and Co and pyrrhotite and actinolite concentration. Mineralization style evolved from replacement fronts controlled by mylonitic foliation to hydraulic breccia zones. The mineralization stage (II) was related to the development of the syn-tectonic potassic alteration (II) and represented by a system of strongly oriented and interconnected bodies with biotite (II), Cl-apatite (III), Co-magnetite (IV), ilmenite (I), Ce-allanite (III) and quartz, besides discrete portions containing Ni-pyrite and Co-chalcopyrite. Breccia zones with matrix made of biotite (II) and Co-chalcopyrite (± Ni-pyrite ± Ni-pyrrhotite) and fragments of massive magnetite represent Cu-richer bodies.

The third mineralizing stage recognized in the Jatobá deposit is distinguished from the others due to the control by ductile-brittle and brittle structures, which enabled the formation of veins with typical open-space filling textures. It was coeval to the late tectonic alteration thet comprises paler brown or green biotite (III), scapolite (IV), F-Cl-apatite (IV), and Cl-K hastingsite (II), Co-chalcopyrite and siegenite I (± Co-pyrite, ±Co-magnetite, ± cassiterite).

The late mineralization stage (IV) was the most expressive at Jatobá. It was coeval to widespread chlorite (II), quartz, epidote and calcite development. It occurs in a variety of branching

veinlets and breccias with Co-chalcopyrite, Co-pyrite, sphalerite, molybdenite, uraninite and monazite. Other late vein types comprise those with quartz-chalcopyrite-K (±molybdenite, Co-pentlandite, and siegenite II) and fine veinlets with chlorite-chalcopyrite, W-bearing hematite, rare earth carbonates (bastnäsite, coskrenite and sahamalite), Co- and Ni-pyrite, sphalerite, ilmenite, marcasite, leucoxene and adularia.

Lithochemical data for ore samples show that the early mineralization stage (I) is characterized by the highest contents of Fe_2O_3 (71.49 to 63.91 wt. %), Ni (3930 to 1270 ppm), Co (2320 to 670 ppm), V (740 to 590 ppm), Pd (81 to 372 ppb) and Pt (2 to 17 ppb) contents. However, highest contents of ΣREE (up to 6773.92 ppm), U (up to 48.50 ppm), Th (up to 23.30 ppm), P_2O_5 (up to 7.97 wt. %), Sn (up to 24 ppm), Nb (up to 7.50 ppm), W (up to 322.50), Zn (up to 482 ppm), gold (up to 1310.80 ppm) were characterized in ore samples formed during the mineralization stage (IV).

The high Ti, V, Ni and Cr concentration in Jatobá magnetite point to high-temperature conditions (ca. > 500 °C), similar to that of high-temperature magmatic-hydrothermal systems (e.g. IOCG, iron oxide-apatite ore and porphyry copper), especially during the early nickel-enriched mineralization event. Oxygen isotope data point to temperature decrease from the pre-mineralization iron metasomatism (558 °C) to mineralization stages (II = 507 °C; III = 422 °C; IV = 327 °C). However, a relatively narrow variation of calculated $\delta^{18}O_{H2O}$ values (9.53‰ to 5.41‰) was recorded during the paragenetic evolution at Jatobá. The $\delta^{18}O_{H2O}$ and δD_{H2O} (–44.88‰ to –30.25‰) values overlap with those of primary magmatic waters and felsic magmatic water.

The gradual increase in Cl contents of scapolite (I) to (III) also indicated a progressive evolution from high-temperature hipersaline fluids and buffering of chlorine activities. Coupled scapolite mineral chemistry and stable isotope data could imply that fluid mixing involving externally-derived fluids was limited at Jatobá.

The $\delta^{34}S_{sulfide}$ values of Jatobá sulfides (0.27‰ to 1.80‰) indicate magmatic sulfur sources. Increasing of $\delta^{34}S_{sulfide}$ values during the paragenetic evolution was accompanied by decrease of Ni + Co and V contents and increase of Sn + W + Nb content in ore samples, suggesting that part of the sulfur and metals may have been leached from mafic-(ultramafic) rocks.

The highly radiogenic Pb isotope composition of Jatobá chalcopyrite ($^{206}Pb/^{204}Pb$ = 99.35 to 245.73; $^{207}Pb/^{204}Pb$ = 32.53 to 62.24; $^{208}Pb/^{204}Pb$ = 55.58 to 172. 76) points to imprecise Archean ages for the last mineralization stage (IV). Highly radiogenic lead signatures may have resulted from striking disturbance due to high U contents in the hydrothermal fluids and to incorporation of radiogenic Pb (or U) into the sulfide from an external source after its formation.

The Jatobá deposit was formed in the roots of a wider Archean IOCG mineral system from focused magmatic-derived fluids. The Jatobá ore signature may reflect evolution closely related to the ca. 2.74 Ga widespread alkaline magmatism, with inheritance of both A-type granites and gabbros, due to intense fluid-rock interaction involving residual alkaline-rich fluids.

Keywords: Jatobá deposit, Iron-oxide-copper-gold deposit, Carajás Mineral Province, Hydrothermal alteration, Mineral chemistry, Stable isotopes.

SUMÁRIO

ÍNDICE DE FIGURAS

Abbreviations: Qtz = quartz; Act = actinolite; Cl-K-hast-I = hastingsite; Scp = escapolite; Bt = biotite; Ab = albite; Ms = muscovite; Mag = magnetite. 38

Figure 5. Distribution of pre-, syn-, and post-shearing types of hydrothermal alteration in the Jatobá deposit. A to F: features in isotropic rocks; A) metabasalt with amygdales infilled by quartz and partially replaced by biotite (I); B) amygdales with quartz and magnetite (II) that replace original infilling in metabasalt; C) Albite (II) alteration fronts in metarhyodacite; D) scapolite (I) and biotite (I) in metadiabase; E) K-feldspar replaces previous sacpolite (I) in metadiabase; F) quartz-magnetite vein in the metadiabase; G to L: hydrothermal alteration controlled by mylonitic foliation; G) metabasalt replaced by biotite (II) and scapolite; H) foliated amygdaloidal metabasalt with hastingsite (I) developed along the mylonitic foliation; I) metadiabase replaced by magnetite and hastingsite; J) metarhyodacite strongly replaced by actinolite (II); K) silicification associated with actinolite (II) in the metarhyodacite; L) metadiabase with potassic alteration with K-feldspar; M to R: fissural-controlled alteration; M) Vein infilled by fibrous scapolite (III) partilaly replaced by albite, epidote and sericite in the metadiabase; N) quartz vein with coarse biotite in the metadiabase (III); O) Metarhyodacite replaced by actinolite (II) and thereafter by coarse green biotite (III); P) chlorite (II) veinlets cut previous potassic alteration zone in the metarhyodacite; Q) potassic alteration with K-feldspar with intense red colour due to tiny hematite inclusions crosscut by calcite; R) breccia with fragments of potassic-altered rock involved by calcite. Abbreviation: Qtz = quartz; Act = actinolite; Cl-K-hast-I = hastingsite; Scp = scapolite; Bt = biotite; Ab = albite; Mag = magnetite. 40

Figure 6. Main early pre-tectonic hydrothermal alteration in the Jatobá deposit. A to D) amydaloidal metabasalt with: A) amygdale infilled by quartz (I) and magnetite (I); B) pervasive potassic alteration with biotite (I) and amygdale with quartz and biotite (I); C) magnetite with pressure shadow in amygdale (TL-PP); D) actinolite (II) in amygdale (TL-PP); E) metadiabase with pervasive potassic alteration with biotite (I) and fissural albite (I) and K-feldspar (I) alteration; F and G) albite (I) in metadiabase partially replaced by scapolite (I) (TL-PP and TL-CP); H) Ferro-pargasite associated with scapolite (I) replacing actinolite (I) in metadiabase (TL-PP); I) previous albite (I) porphyroblasts replaced by scapolite (I) and K-feldspar (I) (TL-CP); J and K) porphyritic metarhyodacite with plagioclase and quartzo phenocrysts in matrix composed of fine biotite (I) (TL-PP); plagioclase was partially replaced by albite (I), scapolite (I) and biotite; L) metarhyodacite with scapolite (I) replaced by K-feldspar in its core and by chlorite in the rims (TL-PP); M) metarhyodacite with tourmaline associated with biotite (I) (TL-PP). Abbreviations: Qtz = quartz; Act = Actinolite; Cl-K-Hast-I = Cl-K-hastingsite; Scp = scapolite; Bt = Biotite; Ab = Albite; Mag = Magnetite. 41

Figure 7. Distinct magnetite generations identified in the Jatobá deposit. A and B) magnetite in metadiabase; A) metadiabase with fine-grained magnetite (I); B) Igneous magnetite (I) partically altered in metadiabase; C and D) magnetite in metabasalt; C) Metabasalts with amygdale infilled by magnetite (II) and quartz; D) Metabasalts with amygdale infilled by magnetite (II) with pressure shadow composed of quartz (TL;CP); E and F) magnetite in metarhyodacite; E) Vein with coarse-grained euhedral to subhedral magnetite (III) and quartz; F) SEM image showing Co-rich magnetite (V) crystals with thin ilmenite lamellae cut by quartz and ilmenite, which is turn partilally replaced by titanite-hematite; G and H) magnetite in metarhyodacite; G) pervasive magnetite (IV) replacement front involved by actinolite (II); H) SEM image showing actinolite (II), apatite (II) and magnetite (IV); I and J) magnetite in metarhyodacite; I) syn-tectonic magnetite (V) associated with chalcopyrite and pyrite in metarhyodacite; J) syn-tectonic magnetite (V) and biotite (II). Abbreviations: Abbreviation: Qtz =quartz; Act = actinolite; Hs = hastingsite; Scp = scapolite; Bt = biotite; Mag = magnetite; Ilm = ilmenite; Ccp = chalcopyrite; Ttn = titanite; Hem = hematite. ..... 44.

Figure 8. Main features of syn-tectonic hydrothermal alteration in the Jatobá deposit. A to C: metadiabase with sodic-calcic and potassic alteration; A) replacement of foliated metadiabase by biotite (II), hastingsite and scapolite (I); B) deformed scapolite (I) porphyroblast with scapolite (II) in its rim and pressure shadow with hastingstite (I) and quartz (TL-PP); C) clear scapolite (II) on the border of a stretched scapolite (I) crystal; scapolite (I) was replaced by K-feldspar and chlorite (TL-PP); D to E: metabasalt with sodic-calcic and potassic alteration; D) foliated metabasalt with stretched amygdales infilled by biotite (I) and quartz and mylonitic foliation defined by biotite (II) and Cl-K-hastingsite (I); E) Cl-K-hastingsite (I) involves and replaces previous actinolite (I) (TL-PP); F) scapolite (I) porphyroblasts with pressure shadow and foliation defined by Cl-K-hastingsite (I) and biotite (II) (TL-PP); G to K: porphyritic metarhyodacite; G) magnetite-rich rock replaced by actinolite (II) and apatite (II); H) Biotite (II) along the mylonitic foliation and relicts of actinolite (II) in the porphyritic metarhyodacite with deformed quartz blastophenocryst (TL-PP); I) deformed scapolite (I) porphyroblasts partially or totally replaced by euhedral hornblende and Cl-K-hastingsite (TL-PP); J to K: intense potassic alteration; J) metabasalt with amygdales infilled by actinolite (II) and mylonitic foliation defined by biotite (II), magnetite (IV), apatite (III) e ± quartz; K) boudin neck in scapolite (I) infilled by biotite (II) and

ÍNDICE DE TABELAS

CAPÍTULO I - APRESENTAÇÃO

1.1 INTRODUÇÃO

A Província Carajás, localizada no Cráton Amazônico (Santos *et al.* 2000, Santos 2003), representa uma das áreas metalogenéticas mais importantes do planeta. A província é mundialmente reconhecida por abrigar uma ampla variedade de depósitos minerais, incluindo expressivas reservas de Fe (Mina de N4 a N5; Serra Norte e SL1 a SL3; Serra Sul; Lobato *et al.* 2005), Au-Pd-Pt (Serra Pelada; Meireles & Silva 1988, Tallarico *et al.* 2000, Moroni *et al.* 2001, Cabral *et al.* 2002a, 2002b), Au-laterítico (Mina de Igarapé Bahia; Zang & Fyfe 1995, Angélica 1996, Porto *et al.* 2010), bauxita (Platô N5; Amazônia Mineração, 1974 (Kotschoubey & Lemos (1985), Mn (Mina do Azul; Dardenne & Schobbenhaus 2001), Ni (Mina do Vermelho; (Klein & Carvalho 2008), Cr-Ni-EGP (Complexo máfico-ultramáfico diferenciado Luanga; Macambira & Vale 1997) e de Cu-Au (Villas & Santos, 2001; Xavier *et al.*, 2012; Monteiro et al., 2014).

Parte dos depósitos cupro-auríferos conhecidos em Carajás apresentam elevados conteúdos de magnetita e/ou hematita hidrotermal, além de importantes conteúdos de ETRL, P, Ni, Co, Pd e U. Tais características são semelhantes às da classe de depósitos de óxidos de ferro-cobre-ouro (*iron oxide-copper-gold deposits* ou IOCG), formados em uma faixa de profundidade característica de zonas de substituição com forte controle estrutural, como proposto por Hitzman *et al.* (1992).

A Província Carajás, dessa forma, é conhecida por abrigar, além de depósitos IOCG formados no Paleoproterozoico, os únicos depósitos dessa classe mundial de idade arqueana (Réquia *et al.* 2003, Tallarico *et al.* 2005, Groves *et al.* 2010, Xavier *et al.* 2010, Moreto *et al.* 2015a,b), que refletem particular evolução em relação aos demais depósitos IOCG no mundo.

Apesar do avanço no conhecimento sobre os depósitos IOCG na Província Carajás, com respeito à evolução geológica, geoquímica, geocronológica e metalogenética nos últimos anos, estudos geológicos mais detalhados sobre a maioria deles ainda são escassos. Nesse sentido, o estudo do depósito Jatobá se fez necessário. Esse depósito apresenta forte associação espacial com a Mina de Sossego, que representa um depósito IOCG arqueano de classe mundial. O depósito Jatobá se localiza a apenas 3 km a norte da Mina de Sossego e faz parte de um *cluster* de alvos e depósitos

cupro-auríferos localizados em seu entorno (Fig. 2.2). O estudo desse depósito pode contribuir para a compreensão de processos genéticos que atuaram em amplos sistemas minerais, resultando em depósitos com atributos geológicos bastante variados. Os estudos incluíram estudos petrográficos refinados, de química mineral, litoquímicos, geocronológicos, e de geoquímica de isótopos estáveis e radiogênicos.

Os resultados obtidos permitiram reconstituir a história evolutiva do sistema metalogenético responsável pela formação do depósito IOCG Jatobá e, portanto, sua comparação direta com a de outros depósitos IOCG na província. Essa comparação se faz necessária, pois o depósito Jatobá mostra evolução contrastante com a de outros depósitos IOCG na província, em especial, com a Mina de Sossego, principalmente no que diz respeito aos eventos mineralizantes.

1.2 ESTRUTURA DA TESE

Esta tese foi elaborada no âmbito do Programa de Pós-Graduação em Geociências (Recursos Minerais e Hidrogeologia) do Instituto de Geociências da Universidade de São Paulo (USP), sob a orientação da Profa. Dra. Lena Virgínia Soares Monteiro, e segue a seguinte organização:

CAPÍTULO I – INTRODUÇÃO: apresenta o tema deste trabalho, sua localização, objetivos, bem como os materiais e métodos usados para alcançar tais objetivos.

CAPÍTULO II – FUNDAMENTAÇÃO TEÓRICA: constitui abordagem de cunho bibliográfico, com apresentação do contexto geológico regional da Província Carajás, incluindo os Domínios Rio Maria e Carajás, além dos aspectos da evolução tectônica da Província Carajás.

Anexo I - Inclui manuscrito a ser submetido a periódico internacional, compreendendo a apresentação do depósito Jatobá e sua caracterização geológica, incluindo a natureza das rochas hospedeiras, assim como dos tipos, estilos e estágios de alteração hidrotermal e o reconhecimento das diversas zonas mineralizadas no depósito. Os estudos paragenéticos foram integrados a estudos de química mineral, visando à identificação de variações químicas das fases hidrotermais e parâmetros físico-químicos do sistema hidrotermal.

Anexo II - Inclui o segundo manuscrito a ser submetido a periódico internacional, que abrange os estudos isotópicos e litoquímicos com ênfase na caracterização da origem dos fluidos, do enxofre e dos metais, assim como o modelamento metalogenético proposto para o depósito Jatobá.

CAPÍTULO III – CONCLUSÃO. Este capítulo apresenta de modo integrado as conclusões alcançadas no desenvolvimento da Tese, além de proposições de estudos futuros para a área do depósito Jatobá.

1.3 LOCALIZAÇÃO DA ÁREA DE ESTUDO

A área de estudo se localiza na região sudeste do Estado do Pará, no município de Canaã dos Carajás e se insere no contexto do Cráton Amazônico (Fig 1.1). Partindo de Belém (capital do Estado do Pará), o acesso à área pode ser feito por vias terrestres ou aérea até a cidade de Marabá, daí sendo necessária locomoção utilizando as rodovias estaduais PA-150 e PA-275 até a cidade de Canaã dos Carajás e finalmente por estradas vicinais até a Mina de Sossego.

1.4 OBJETIVOS

Objetivando contribuir para o avanço do conhecimento a respeito dos processos hidrotermais que deram origem aos depósitos de óxido de ferro-cobre-ouro (IOCG) da Província Mineral de Carajás, o presente Projeto de Doutoramento visa o entendimento da origem da mineralização cuprífera do depósito Jatobá, a partir da reconstituição da sua história evolutiva e de suas relações com eventos magmáticos e tectônicos, fornecendo subsídios para a elaboração de um modelo genético integrado para os depósitos cupro-auríferos de Carajás.

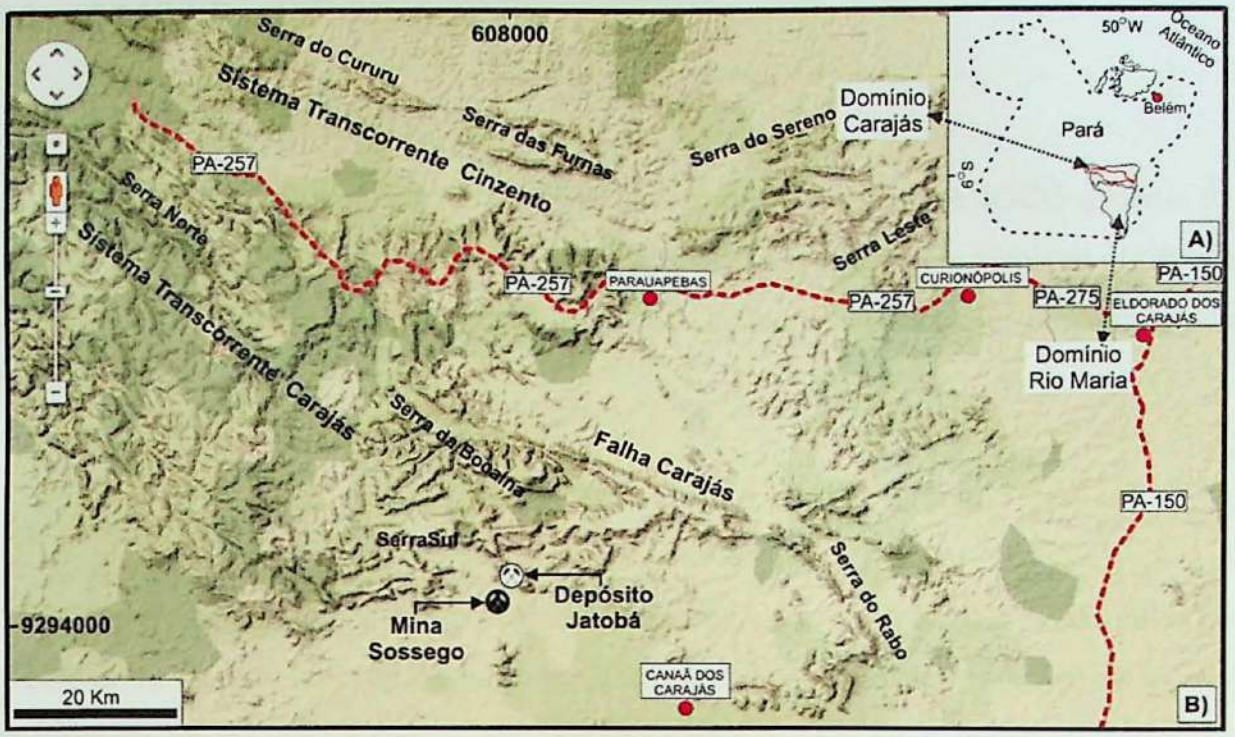

Figura 1.1. A) Mapa de localização esquemático da Província Mineral de Carajás, composta pelos domínios Carajás e Rio Maria, no contexto do Estado do Pará, Brasil (Vasquez et al. 2008). No Domínio Carajás a Bacia Carajás está representada em vermelho. B) compreende imagem de relevo ampliada do Domínio Carajás, extraída do Google Earth, mostrando as principais feições geomorfológicas, acessos e localidades, além da localização aproximada do depósito Jatobá e da Mina de Sossego.

Para alcançar esses objetivos, as metas incluíram:

- Caracterização da natureza das rochas hospedeiras e do minério, a partir de estudos petrográficos e mineralógicos;
- Identificação de relações entre paragênese de alteração hidrotermal e mineralização, bem como caracterização de evidências de múltiplos pulsos de circulação de fluidos e sobreposições de eventos associados à mineralização ou não;
- Determinação das idades de cristalização (U-Pb em zircão) das rochas hospedeiras do depósito;
- Caracterizar as variações nas composições químicas das principais fases minerais da alteração hidrotermal, visando à determinação de parâmetros físico-químicos nos diferentes estágios evolutivos do depósito;
- Caracterização da assinatura isotópica das fontes de metais, enxofre e fluidos, a partir das assinaturas isotópicas Pb-Pb, O, H e S dos principais minerais hidrotermais;
- Identificação da assinatura química do minério a partir de análises litoquímicas.

1.5 MATERIAS E MÉTODOS

1.5.1 Revisão Bibliográfica

A revisão bibliográfica teve ênfase no estudo dos depósitos IOCG a partir de análises de publicações científicas em nível global e das diferentes técnicas analíticas voltadas a estudos metalogenéticos, incluindo conceitos básicos e procedimentos analíticos.

1.5.2 Trabalho de Campo

Duas campanhas de campo foram realizadas entre os dias 19 e 30 de julho de 2014 e entre os dias 25 e 29 de julho de 2016. Essas campanhas foram realizadas nas litotecas das minas de Sossego e N5, pertencentes à VALE/SA e incluiram descrição macroscópica detalhada de testemunhos de sondagens do depósito Jatobá, registros fotográficos e amostragem sistemática.

A primeira etapa permitiu descrição e amostragem de testemunhos das sondagens JATD-15, JATFD-21 e JATFD-28, que foram integradas aos estudos já realizados em amostragens provenientes de outras três sondagens, previamente descritas pela orientadora (JATD-01, JATD-02 e JATD-03).

Na última etapa de campo, as sondagens JATD-32 e JATD-33 foram também descritas e amostradas, totalizando 8 furos de sondagem e aproximadamente 2.270 metros de sondagens descritas nesta tese. A nomenclatura das amostras segue o padrão adotado pela empresa, onde o código de identificação das amostras é formado pelo nome abreviado do depósito, seguido do tipo de furo, número do furo e da profundidade em que as amostras foram coletadas, JATD-15 211,30, assim, exemplificando-se tem: depósito Jatobá, em furo diamantado, de número 15, na profundidade de 211,30m.

1.5.3 Etapas analíticas

Petrografia

Petrografia, que utiliza como base as propriedades óticas dos minerais, foi exaustivamente empregada neste estudo, consistindo o primeiro passo antes da utilização dos demais métodos empregados. Para esse estudo foram confeccionadas 150

lâminas, das quais 90 delgadas, 56 delgadas-polidas e 3 bipolidas. Registros fotográficos das principais feições presentes nas lâminas foram obtidos por sistema de captura de imagens, com câmera acoplada a um microscópio Leica, modelo QWIN 550. Os equipamentos são pertencentes ao Laboratório de Petrografia Sedimentar, do Departamento de Geologia Sedimentar e Ambiental do Instituto de Geociências da Universidade de São Paulo (IGc-USP).

Microscopia Eletrônica de Varredura

Objetivando identificar fases minerais metálicas e não metálicas, finas ou pouco abundantes tanto no minério como nas rochas hospedeiras, foram realizados estudos petrográficos com uso de microscópio eletrônico de varredura (MEV), modelo LEO 440I, acoplado a Espectrômetro de Energia Dispersiva de raio-X (EDS; *Energy Dispersive X-Ray Spectrometry*) Oxford. Os equipamentos são pertencentes ao Laboratório de Microscopia Eletrônica, do Instituto de Geociências da Universidade de São Paulo (IGc-USP).

Química mineral

As análises químicas quantitativas foram realizadas em microssonda eletrônica modelo JEOL JXA-8530F (*Field Emission Electron Probe Microanalyser*) com cinco espectrômetros WDS e um espectrômetro EDS, pertencentes ao laboratório de Microssonda Eletrônica, do Instituto de Geociências da USP (IGc-USP). Essas análises, conduzidas em 9 lâminas delgadas-polidas, visaram a quantificação da composição química das principais fases minerais metamórficas e hidrotermais presentes no depósito Jatobá.

As condições analíticas empregadas consistiram de aceleração de voltagem de 15 kV, corrente de 20 nA e feixe de elétrons com 5 μm de diâmetro, excetuando-se para análises de feldspato, para as quais foi usado diâmetro do feixe de 10 μm. O tempo de contagem foi de 10 s, com exceção de análises do Al (15 s); Ca e Cr (20 s); Zn, Ba e Cu (30 s); Mn e Sr (40 s), Ni (50 s) e V (260 s). Fases voláteis foram incluídas, especialmente o Cl. A qualidade do procedimento analítico foi verificada em relação aos padrões sintéticos Smithsonian e Geller, sob o método de correção PRZ Armstrong method (Armstrong, 1991).

Os resultados obtidos foram tratados com uso de planilhas da *The Open University* (2010) ou em planilhas Excel para escapolita, biotita, magnetita e feldspato

potássico. O cálculo de fórmula estrutural da clorita foi feito com uso do *software* WinCcac (Yavuz *et. al.*, 2015). Para os anfibólios utilizou-se a planilha Excel apresentada em Locock (2014), enquanto que a subsequente classificação desses anfibólios foi feita de acordo com Hawthorne *et al.* (2012). A apresentação gráfica das variações composicionais desses minerais foi feita com utilização dos *softwares* Grapher 12 e Excel.

Preparação e separação de minerais para análises isotópicas

A preparação das amostras para análises de isótopos radiogênicos (U-Pb e Pb-Pb) e estáveis (S, O, D) foi realizada no laboratório de Separação do Centro de Pesquisas Geocronológicas do Instituto de Geociências da Universidade de São Paulo (CPGeo da USP). Os procedimentos de preparação adotados por este laboratório estão descritos em Loios (2009).

De forma simplificada, os procedimentos adotados neste estudo obedeceram às seguintes etapas: redução granulométrica do material escolhido em britador de mandíbulas, seguido de moinho de disco vibratório e peneiramento (<250 mesh). Para o método U-Pb, essa fração foi lavada em mesa de separação ou Mesa de Wiffley, com secagem para eliminação de resíduos como pó, deixando os minerais prontos para a etapa de purificação. Nessa etapa foi feita a eliminação de minerais magnéticos com uso de imã de mão. Outras técnicas auxiliaram na purificação, como o uso de separador eletromagnético (Frantz) e os líquidos densos. As etapas subsequentes incluíram peneiramento, separação manual dos grãos com uso em lupa binocular para produção dos concentrados minerais.

Para as análises de isótopos estáveis, a separação mineral foi feita com auxílio de microrretífica, catação com uso de lupa binocular e moagem em almofariz. No entanto, para a concentração de minerais com granulação entre 60 – 100 mesh foi utilizada Placa de Petri recoberta com álcool comum e a catação foi feita com o auxílio de uma agulha de seringa de 1 mm e lupa binocular. Para o recolhimento dos minerais foi utilizada pepita com ponteira de 1 mm. As amostras foram dispostas em papel de filtro, secas com auxílio de lâmpada infravermelho e pesadas em balança de precisão. A separação resultou em concentrados com grau de pureza superior a 95%. Alíquotas de 0,5 miligramas foram obtidas para sulfetos. Para os silicatos, uma alíquota superior a 0,15 miligramas foi obtida para posterior cominuição em pilão de ágata.

Litoquímica

Com base nos estudos petrográficos realizados nas amostras representativas dos diferentes estilos morfogenéticos das diferentes zonas mineralizadas, 10 amostras foram cominuídas em prensa hidráulica a menos de 0,5 cm de diâmetro e moídas em moinho de carbeto de tungstênio durante 3 a 4 minutos e peneiradas com uso de peneira de 0,075 (250 mesh) e quarteadas, com separação de uma alíquota para arquivo e outra para análises litoquímicas.

As amostras foram analisadas em dois laboratórios distintos, a saber: (1) ACME (*Analytical Laboratories* Ltd); (2) Laboratório ALS (*Australian Laboratory Services Pty Ltd*). Elementos maiores (SiO_2, Al_2O_3, Fe_2O_3, CaO, Na_2O, K_2O, MgO) foram analisados por ICP-AES (*Inductively Coupled Plasma-Atomic Emission Spectroscopy*), enquanto os elementos menores (MnO, TiO_2, P_2O_5, Cr_2O_3), ETR (La, Ce, Pr, Nd, Pm, Sm, Eu, Gd, Tb, Dy, Ho, Er, Tm, Yb, Lu), traços (Ba, Be, Co, Ga, Nbd, Ni, Rb, Sc, Sn, Sr, V, W, Y, Zr, Ag, As, Au, Bi, Cd, Cu, Hg, Mo, Ni, Pb, Sb, Se, Tl, Zn) e ultra-traços (Cs, Hf, Ta, Th, U), foram determinados por ICP-MS (*Inductively Coupled Plasma Mass Spectrometry*). Os resultados foram tratados com uso de planilhas Excel e do *software* GCDKit (Janoušek *et al.* 2006) e apresentados em formato gráfico.

Isótopos Estáveis

A fim de se desvendar a origem da(s) fonte(s) dos fluidos e do enxofre, e determinar parâmetros físico-químicos relativos à evolução do sistema hidrotermal, foram realizados estudos de isótopos estáveis de oxigênio, deutério e enxofre.

- Oxigênio e Deutério

Para o estudo de isótopos de oxigênio e hidrogênio, quatro pares de minerais cogenéticos representativos de diferentes estágios de alteração hidrotermal relacionadas às principais fases mineralizantes foram selecionados. Desses, 2 pares de biotita-quartzo das sondagens JATD-21 e JATD-28 e 1 par de clorita-quartzo da sondagem JATD-28 foram separados, os quais compreendem três das quatro zonas mineralizadas. Adicionalmente, 1 par de magnetita-quartzo (não mineralizado) da sondagem JATD-32 foi também selecionado. As análises de isótopos de oxigênio e hidrogênio foram realizadas no laboratório de Serviços de Análises de Isótopos Estáveis da Universidade de Salamanca, Espanha, sob supervisão do Prof. Dr. Clemente Récio Hernández.

As medidas de espectrometria de massa para as razões isotópicas de $^{18}O/^{16}O$ foram realizadas com base em Sharp (1990), a partir das técnicas originais de Clayton & Mayeda (1963) usando espectrômetro de massa SIRA-II. O método consistiu na libertação de O_2 por ablação a laser (laser de CO_2 SYNRAD 25W) em atmosfera de ClF_3. A liberação de água e redução para H_2 e determinação das relações D/H foi realizada de acordo com Godfrey (1962) em espectrômetro de massa de fonte gasosa em modo "Dual Inlet" (2 espectrômetros SIRA-II + 1 espectrômetro SIRA-10). Os resultados dos isótopos de oxigênio e hidrogênio são expressos na notação delta (δ) convencional, per mil (‰), e são relatados em relação aos padrões *Vienna Standard Mean Ocean Water* (VSMOW). A reprodutibilidade das análises foi de ± 0,2 ‰ para $\delta^{18}O$ e ± 5 ‰ para δD.

➢ Enxofre

O estudo isotópico de enxofre incluiu 11 análises em sulfetos, sendo 8 em calcopirita distribuídas entre as sondagens JATD-15, JATD-21 e JATD-28, e 3 de pirrotita da sondagem JATD-32. As análises isotópicas das diferentes gerações e tipos de sulfeto foram realizadas no Laboratório de Isótopos Estáveis (LAIS) do Instituto de Geociências da Universidade de Brasília, utilizando-se a técnica IRMS-*Espectrometria de Massa por Razão Isotópica* (*Isotopic Ratio Mass Spectrometry).*

Para a obtenção dos valores de $\delta^{34}S$, a amostra de sulfeto (200μg a 2000μg) foi convertida em gás por combustão dinâmica com injeção automática de oxigênio em um forno especial a 1020 °C. Os produtos gasosos da combustão foram carreados por um fluxo de gás hélio através do trióxido de tungstênio (catalisador de combustão) e em seguida reduzidos por fios de cobre de alta pureza. O gás SO_2 foi separado por uma coluna cromatográfica empacotada a uma temperatura isotérmica. O gás SO_2 resultante foi então canalizado para a fonte de íons do Thermo Scientific MAT253 IRMS, onde foi ionizado e acelerado. As espécies gasosas de massas diferentes foram separadas em um campo magnético e em seguida foram medidas por um arranjo de coletores representados por copos de *Faraday*. Para o SO_2, as massas 64, 65 e 66 foram monitoradas. O processamento dos dados, assim como o controle do espectrômetro de massa e seus periféricos foram realizados pelo *software* Isodat 3.0 (Sharp, 2007). Os dados foram reportados como $\delta^{34}S$ em permil em relação ao padrão CDT (*Canion Diablo Troillite*) e apresentaram acurácia de 0.01 ‰ com erro associado de $\delta^{34}S$ = 0,2‰.

Isótopos Radiogênicos:

Método U-Th-Pb

Visando a delimitação do intervalo de idades das rochas hospedeiras do depósito Jatobá, e suas relações com a evolução tectono-magmática do Domínio Carajás, foi empregado o método U-Pb em zircão, em quatro das cinco diferentes rochas hospedeiras do depósito, compreendendo rochas metavulcânicas máficas, félsicas, metadiabásio, brechas vulcânicas e metatufos máficos. A determinação das idades foi realizada nas rochas metariodacíticas. Foi utilizado espectrômetro de massa com ablação a laser com plasma indutivamente acoplado (*Laser ablation Inductively coupled plasma mass spectrometry*; LA-ICP-MS), associado a um multi-coletor do tipo Neptune (Thermo) e Laser 193 nm Excimer (Photon Machines). Os equipamentos são pertencentes ao Centro de Pesquisas Geocronológicas, do Instituto de Geociências da Universidade de São Paulo (CPGeo-USP).

Pb-Pb

Análises isotópicas com uso da sistemática Pb-Pb em concentrado mineral, foram feitas objetivando determinar a fonte dos metais. Os procedimentos analíticos adotados nesse trabalho estão de acordo com o recomendado em Magdaleno & Ruiz (2009). Consistem em uso de laboratório limpo Classe 10.000 (ISO n°7), providos de capelas de fluxo laminar Classe 100 (ISSO N°5), seguindo a norma de referência ABNT NBR ISSO 14644-1, uma vez que a técnica requer cuidados quanto a purificação de reagentes e manuseios de materiais, a fim de que se evite prováveis contaminações por Pb. A técnica utilizou-se da dissolução total da amostra por digestão ácida em um béquer de teflon (SAVILLEX) utilizando, em etapas distintas, HCl + HNO_3, a temperatura de 100 °C. As razões isotópicas de Pb foram obtidas por espectrometria de massa por ionização térmica (TIMS), utilizando-se o espectrômetro FINNIGAN MAT 262, no Centro de Pesquisas Geocronológicas do Instituto de Geociências da Universidade de São Paulo (CPGeo-USP).

CAPÍTULO II: FUNDAMENTAÇÃO TEÓRICA

2. CONTEXTO GEOLÓGICO DA PROVÍNCIA CARAJÁS

A região de Carajás (Fig. 2.1) compreende porção crustal majoritariamente arqueana, supostamente não afetada pelas orogêneses do Ciclo Transamazônico (Teixeira *et al.*, 1989) e representa o núcleo crustal mais antigo do Cráton Amazônico (Teixeira *et al.*, 1989; Brito Neves & Cordani, 1991; Tassinari, 1996; Tassinari & Macambira, 1999, 2004).

A região de Carajás foi considerada parte da Província Amazônia Central na proposta de compartimentação tectônica do Cráton Amazônico de Tassinari e Macambira (1999, 2004). Posteriormente, Santos *et al.* (2006) e Vasquez *et al.* (2008a), individualizaram a Província Carajás.

Segundo Vasquez *et al.* (2008a), a Província Carajás é limitada ao norte e ao sul pela Província Transamazonas (2,26 – 1,90 Ga), respectivamente pelos domínios Bacajá e Santana do Araguaia, que apresentam rochas juvenis paleoproterozoicas e segmentos arqueanos retrabalhados durante o Paleoproterozoico. Ao leste a Província Carajás é limitada pelo Cinturão Araguaia de idade neoproterozoica formado durante a Orogênese Brasiliana (Pan-Africana). Ao oeste, por fim, a província é recoberta pelas rochas vulcano-plutônicas e sedimentares paleoproterozoicas do Domínio Iriri-Xingu da Província Amazônia Central.

Com base nas idades dos eventos magmáticos e deformacionais da Província Carajás, bem como na natureza e idade das unidades supracrustais e seus ambientes tectônicos, reportadas nos estudos de Huhn *et al.*, 1988; DOCEGEO, 1988; Souza *et al.* (1996); Althoff *et al.* (2000); Dall'Agnol *et al.* (2006); Vasquez *et al.* (2008a), a província foi dividida em dois domínios tectônicos, Carajás, ao norte, e Rio Maria, ao sul (Fig. 2.1), que são limitados por uma descontinuidade regional de direção aproximada E-W (Vasquez *et al.* (2008a).

2.1 DOMÍNIO RIO MARIA

O Domínio Rio Maria (Fig. 2.1) foi, inicialmente, denominado de Terreno Granito-*Greenstone* Rio Maria (TGGRM) por Costa *et al.* (1995). Esse domínio teria evolução restrita ao Mesoarqueano e, segundo Avelar *et al.* (1999), resultou de

amalgamações em margem ativa de arcos intra-oceânicos, com evolução em dois estágios (3,05 Ga a 2,90 Ga e 2,88 Ga a 2,82 Ga; Leite, 2001; Souza *et al.*, 2001; Santos, 2003; Tassinari *et al.*, 2005; Vasquez *et al.*, 2008; Almeida *et al.*, 2011). O processo de amalgação seria relacionado a movimentos compressivos e de encurtamento na direção N-S, com duração até 2,86-2,85 Ga, que é a idade atribuída ao último evento metamórfico de alto grau registrado nas rochas do Complexo Pium.

Os estágios evolutivos registrados no Domínio Rio Maria (Tabela 2.1) incluem:

(1) (3,05 Ga - 2,90 Ga) formação de faixas de *greenstone belts strictu sensu* (grupos Gradaús, Serra do Inajá, Babaçu, Lagoa Seca, Tucumã e Sapucaia), com lavas almofadadas komatiíticas e tholeiíticas; intrusões de complexos máfico-ultramáficos (grupos Serra Azul e Guará Pará; Pimentel & Machado, 1994; Macambira & Lancelot, 1996; Souza *et al.*, 2001; Tassinari *et al.*, 2005) e colocação de granitoides da série TTG (Tonalito Arco Verde, Tonalito Caracol, Trondhjemito Mogno, Trondhjemito Água Fria e Tonalito Parazônia; Rolando & Macambira, 2003; Almeida *et al.*, 2010, 2011, 2013) e leucogranodioritos;

(2) (2,88 Ga - 2,82 Ga), formação de complexos TTG mais jovens, com magmatismo trondhjemítico e colocação de sanukitoides (Oliveira *et al.*, 2009, 2010), seguidos de leucogranitos. Esses últimos vinculam-se a magmatismo cálcio-alcalino sin-colisional, que marca o fim do ciclo orogênico no Domínio Rio Maria (Lafon *et al.*, 1994; Rolando & Macambira 2003; Leite *et al.*, 2004; Almeida *et al.*, 2011)

Coberturas sedimentares paleoproterozoicas no Domínio Rio Maria são representadas pelas unidades sedimentares dos grupos Rio Fresco e Gemaque (Vasquez *et al.* 2008a). Magmatismo granítico do tipo A_2 de ca. 1,88 Ga é amplamente reconhecido nesse domínio, sendo representado pela Suíte Intrusiva Granítica, que inclui os granitios Jamon, Bannach, Cachoeirinha, Gradaús, Manda Saia, Marajoara, Musa, São João, São José, Velho Guilherme, Redenção e Seringa; Dall'Agnol *et al.* 1999, 2005, Dall'Agnol & Oliveira 2007), além de diques de rochas vulcânicas intermediárias a félsicas relacionadas ao magmatismo anorogênico do Orosiriano (Vasquez *et al.*, 2008b; Tabela 2.1).

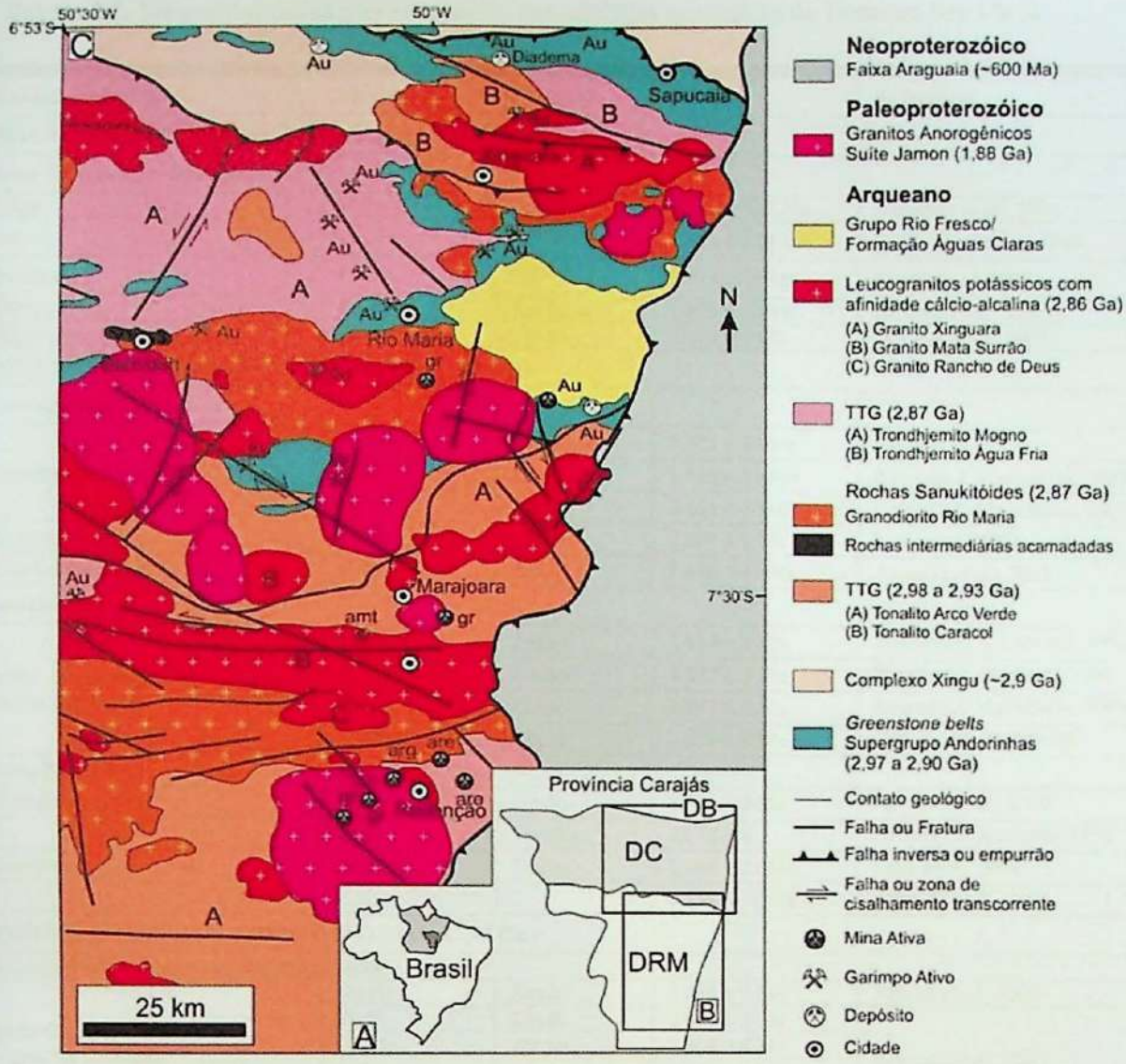

Figura 2.1. A) Localização da Província Carajás no contexto do Cráton Amazônico; B) Subdivisão da província em dois domínios tectônicos distintos, Carajás (DC), ao norte, e Rio Maria (DRM), ao sul, além do limite da província com Domínio Bacajá (DB), pertencente à Província Tansamazonas no extremo norte do mapa; C) Mapa Geológico do Domínio Rio Maria (compilado de Vasquez *et al.*, 2008; Oliveira *et al.*, 2009; Almeida *et al.*, 2011).

No Domínio Rio Maria são reconhecidos depósitos auríferos orogênicos (Diadema, Lagoa Seca, Babaçu, Mamão, Tucumã, Inajá, Cuca) e garimpos de ouro (Serqueiro, Peladinha, Serrinha e Tatu Frango) associados a filões de quartzo estruturalmente controlados, que ocorrem em zonas de cisalhamento regionais que interceptam as sequências de *greenstone belts* (Oliveira & Leonardos 1990, Leonardos *et al.* 1991, Huhn 1992, Santos *et al.* 1998, Villas & Santos 2001, Oliveira & Santos 2003).

Tabela 2.1. Síntese dos dados geocronológico das unidades geológicas do Domínio Rio Maria.

Unidade Estratigráfica	Método	Material	Idade	Referência
MAGMATISMO ANOROGÊNICO TIPO A_2 (1,88 Ga)				
Suíte Granítica intrusiva Jamon				
Musa	U-Pb	Zircão	1.883 ± 5/-2 Ma	Machado *et al.*, 1991
Jamon	Pb-Pb	Zircão	1.885 ± 32 Ma	Dall' Agnol *et al.*, 1999
Seringa	Pb-Pb	Zircão	1.893 ± 15 Ma	Avelar *et al.* 1999
Redenção	Pb-Pb	Rocha total	1.870 ± 68 Ma	Barbosa *et al.*, 1995
Diques félsicos	Pb-Pb	Zircão	1.885 ± 4 Ma	Oliveira *et al.*, 2002
SEGUNDO ESTÁGIO EVOLUTIVO (2,88 Ga a 2,82 Ga)				
Leucogranitos Potássicos				
Granito Mata Surrão	Pb-Pb	Rocha Total	2.872 ± 10 Ma	Lafon *et al.*, 1994
	Pb-Pb	Zircão	2.875 ± 11 Ma	Rolando & Macambira, 2003
	Pb-Pb	Zircão	2.881 ± 2 Ma	Rolando & Macambira, 2003
Granito Xinguara	Pb-Pb	Zircão	2.865 ± 1 Ma	Leite *et al.*, 2004
Granito Rancho de Deus	U-Pb	Zircão	2.888 ± 27 Ma	Almeida *et al.*, 2011
Sanukitóides				
Suíte Sanukitoide Rio Maria e rochas associadas	U-Pb	Zircão	2.874 ± 9 Ma	Macambira & Lancelot, 1991
	U-Pb	Zircão	2.872 ± 5 Ma	Pimentel & Machado, 1994
	Pb-Pb	Zircão	2.877 ± 6 Ma	Rolando & Macambira, 2003
	Pb-Pb	Zircão	2.878 ± 4 Ma	Dall' Agnol *et al.*, 1999
Série TTG jovem				
Tonalito Parazônia	Pb-Pb	Zircão	2.876 ± 2 Ma	Almeida *et al.*, 2010
	U-Pb	Titanita	2.858 Ma	Pimentel & Machado, 1994
Trondhjemito Água Fria	Pb-Pb	Zircão	2.864 ± 21 Ma	Leite *et al.*, 2004
			2.854 ± 17 Ma	Almeida *et al.*, 2011
PRIMEIRO ESTÁGIO EVOLUTIVO (3,05 Ga a2,90 Ga)				
Leucogranodioritos e Leucomonzogranitos				
Suíte Guarantã e granitos similares	Pb-Pb	Zircão	2.868 ± 5 Ma	Althoff *et al.*, 2000
	Pb-Pb	Zircão	2.870 ± 5 Ma	Almeida *et al.*, 2011
	Pb-Pb	Zircão	2.864 ± 8 Ma	
	U-Pb	Zircão	2.875 ± 8 Ma	
	U-Pb	Zircão	2.872 ± 7 Ma	
Série TTG antiga				
Tonalito Mariazinha	U-Pb	Zircão	2.925 ± 3 Ma	Almeida *et al.*, 2011
	U-Pb	Zircão	2.918 ± 13 Ma	
Complexo Tonalítico Caracol	Pb-Pb	Zircão	2.948 ± 5 Ma	Leite *et al.*, 2004
	Pb-Pb	Zircão	2.936 ± 3 Ma	
Trondhjemito Mogno	Pb-Pb	Zircão	2.857 ± 13 Ma	Macambira *et al.*, 2000
	Pb-Pb	Zircão	2.900 ± 21 Ma	
	Pb-Pb	Zircão	2.962 ± 8 Ma	Almeida *et al.*, 2011
	U-Pb	Zircão	2.965 ± 7 Ma	
	Pb-Pb	Zircão	2.968 ± 2 Ma	
	U-Pb	Zircão	2.968 ± 3 Ma	
	Pb-Pb	Zircão	2.959 ± 5 Ma	
	Pb-Pb	Zircão	2.959 ± 2 Ma	
Tonalito Arco Verde	U-Pb	Zircão	2.964 ± 4 Ma	Vasquez *et al.*, 2008b
	Pb-Pb	Zircão	2.948 ± 7 Ma	Rolando & Macambira, 2003
	Pb-Pb	Zircão	2.952 ± 2 Ma	Almeida *et al.*, 2011
	Pb-Pb	Zircão	2.926 ± 2 Ma	
	U-Pb	Zircão	2.935 ± 5 Ma	
	Pb-Pb	Zircão	2.937 ± 3 Ma	
	U-Pb	Zircão	2.973 ± 11 Ma	
Complexo Máfico-Ultramáfico				
Serra Azul	U-Pb	Zircão	2.970 ± 7 Ma	Pimentel & Machado, 1994
Greenstone Belts				
Grupo Lagoa Seca	U-Pb	Zircão	2.904+29/-22 Ma	Macambira & Lancelot, 1996
	U-Pb	Zircão	2.971 ± 18 Ma	
	U-Pb	Zircão	2.972 ± 5 Ma	Pimentel & Machado, 1994
Grupo Gradaús	U-Pb	Zircão	3.002 ± 3 Ma	Tassinari *et al.*, 2005

Esse domínio também hospeda o principal depósito de tungstênio conhecido na Amazônia (Pedra Preta), vinculado à *greisens* na cúpola do granito paleoproterozoico do tipo A_2 Musa (Cordeiro *et al.* 1984, Rios *et al.* 1998).

2.2. DOMÍNIO CARAJÁS (DC)

O Domínio Carajás (Vasquez *et al.*, 2008a; Fig. 2.2), anteriormente denominado Cinturão de Cisalhamento Itacaiúnas (Araújo *et al.* 1988; Costa *et al.* 1995), difere do Domínio Rio Maria por registrar particular evolução tectônica e magmática neoarqueana (ca. 2.76 – 2.70 Ga; Tabela 2.2) e por seu notável potencial metalogenético, com expressivos depósitos de ferro, manganês, níquel-EGP, ouro, ouro-EGP e cobre-ouro.

As rochas do embasamento mesoarqueano desse domínio foram inicialmente atribuídas ao complexo gnáissico migmatítico Xingu (Silva *et al.*, 1974; Machado *et al.*, 1991) e aos ortogranulitos do Complexo Pium, com idades de cristalização de protólitos em 3,0 Ga (Pidgeon *et al.*, 2000). Estudos recentes, no entanto, permitiram a individualização de granitoides com idades de cristalização em ca. 3,0 Ga; ca. 2,96 a 2,93 Ga, ca. 2,88 a 2,87 Ga e ca. 2,87 a 2,83 Ga na área antes atribuída ao Complexo Xingu, o que restringe a ocorrência desse complexo no Domínio Carajás.

Esses granitoides incluem:

(i) ca. 3,0 Ga (e.g. Tonalito Bacaba; Moreto *et al.* 2011; Granito Sequeirinho; Moreto *et al.*, 2015b);

(ii) ca. 2,96-2,93 Ga (e.g. Granito Canaã dos Carajás; Feio *et al.*, 2013);

(iii) ca. 2,88 – 2,87 Ga (e.g. granodioritos Água Azul; Sousa *et al.*, 2010; Água Limpa; Gabriel *et al.*, 2010; Tonalito Campina Verde (Feio *et al.*, 2012) e Granito Bom Jesus (Feio *et al.*, 2013).

(iv) ca. 2,87 a 2,83 Ga (e.g. granitos Cruzadão e Serra Dourada e Trondhjemito Rio Verde; Moreto *et al.*, 2011, Feio *et al.*, 2012),

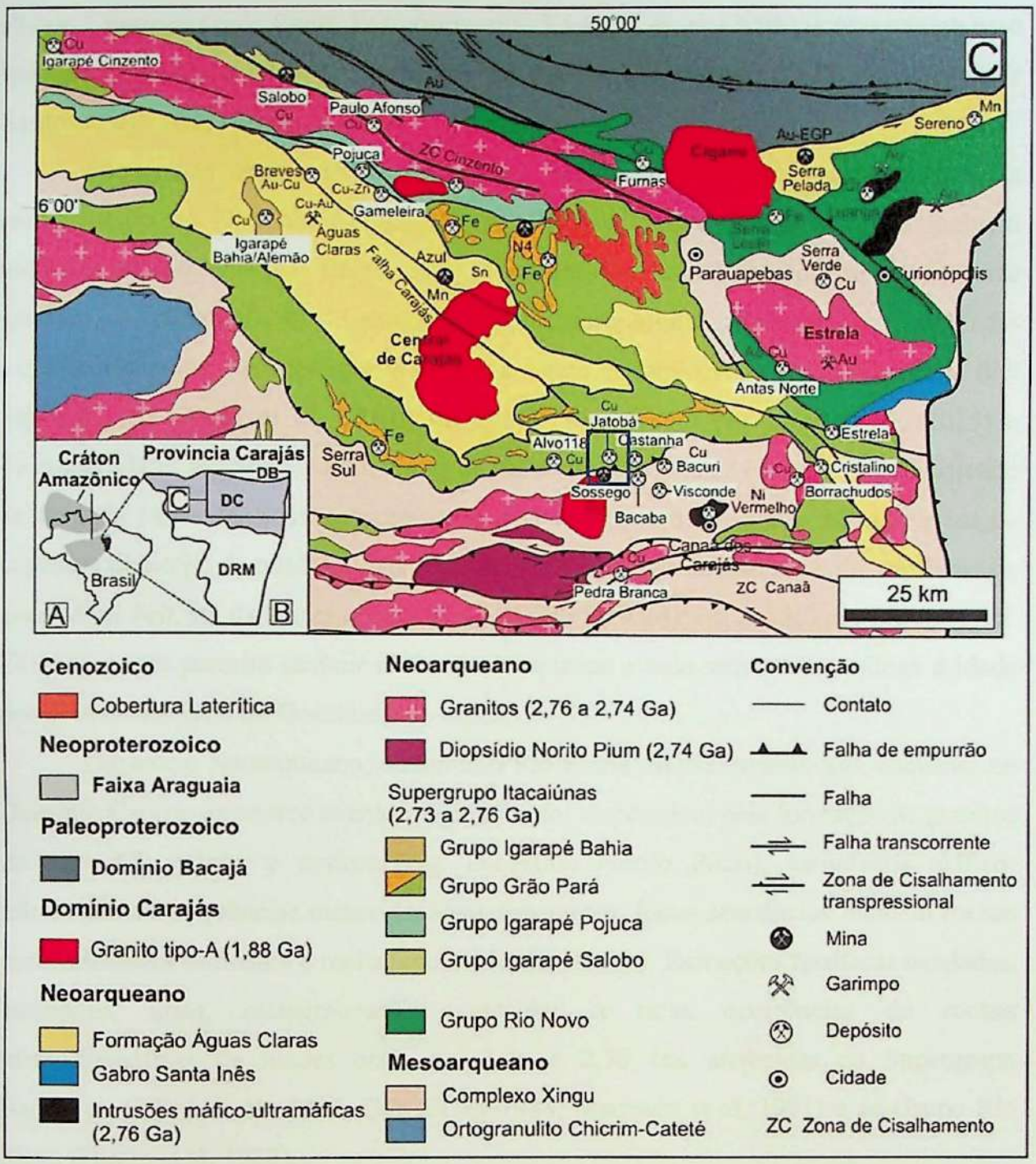

Figura 2.2. (A) Localização da Província Carajás no Cráton Amazônico; (B) Divisão da Província Carajás nos domínios Rio Maria (DRM) e Carajás (DC), limitado a norte pelo Domínio Bacajá (DB); (C) Mapa geológico do Domínio Carajás da Província Carajás e áreas adjacentes (modificado de Vasquez et al., 2008) com a localização dos principais depósitos minerais. O retângulo azul apresenta a área do depósito Jatobá.

Em relação aos ortogranulitos do Complexo Pium, o reconhecimento de uma expressiva unidade de rochas noríticas e gabroicas com texturas ígneas preservadas na área do rio Pium, antes atribuída a esse complexo, resultou na proposição de abandono desse termo (Ricci & Carvalho, 2006). Esses autores propuseram o agrupamento das rochas ortogranulíticas máficas e félsicas em uma nova unidade, denominada de Ortogranulito Chicrim-Cateté e as rochas noríticas foram agrupadas sob a designação de

Plúton Charnockitoide Pium. Posteriormente, Vasquez *et al.* (2008) denominaram essa unidade de Diopsídio Norito Pium, que foi datada pelo método Pb-Pb em zircão por Santos *et al.* (2013) em ca. 2,74 Ga.

Sequências de *greenstone belt stricto sensu* também foram reconhecidas mais recentemente no Domínio Carajás ao sul da Serra Sul de Carajás. Essas incluem unidades metaultramáficas (talco-xisto, serpentinitos e komatiitos com típicas texturas spinifex), metamáficas (actinolita-clorita-quartz-albita xistos) e unidades metassedimentares (quartzo-clorita xistos) e foram denominadas como *Greenstone Belt* Selva por Siepierski *et al.* (2016) ou Grupo Sequeirinho por Justo *et al.* (2015) e Tavares (2015). Metadacito com lentes de tremolita-talco xistos também foi identificado na área da Mina de Sossego como uma das unidades hospedeiras da mineralização cuprífera do corpo de minério Pista. Esse metadacito, considerado parte da sequência de *greenstone belt*, foi datado em ca. 2,97 Ga (U-Pb SHRIMP em zircão) por Moreto *et al.* (2015a), o que permite atribuir idade mesoarqueana a essa sequência, análoga à idade dos *greenstone belts* do Domínio Rio Maria.

Durante o Neoarqueano, o Domínio Rio Maria estaria estabilizado, enquanto no Domínio Carajás extensivo evento magmático foi responsável pela formação de granitos do tipo A2, gabros e noritos (e.g. Diopsídio Norito Pium), complexos máfico-ultramáficos e sequências metavulcanossedimentares. Essas sequências incluem rochas metavulcânicas bimodais e rochas metavulcanoclásticas, formações ferríferas bandadas, anfibolito, xisto, metagrauvaca, associadas a raras ocorrências de rochas metaultramáficas de idades entre ca. 2,76 e 2,70 Ga, atribuídas ao Supergrupo Itacaiúnas (Wirth et al., 1986, DOCEGEO1988, Machado et al. 1991) e ao Grupo Rio Novo (Hirata et al. 1982).

Os complexos máfico-ultramáficos de idade entre ca. 2,77 e 2,70 Ga são representados pelo Complexo Luanga (Jorge João *et al.*, 1982; Machado *et al.*, 1991), Complexo Ézio (Silva, 2016), além da Suíte Intrusiva Cateté (Lafon *et al.*, 2000; Macambira & Vale, 1997). Suíte máfica-ultramáfica foliada tardi-arqueana do tipo Santa Inês (Araújo & Maia, 1991) também ocorre.

Expressiva granitogênese (ca. 2,75 e 2,70 Ga) sin-tectônica em relação ao desenvolvimento de zonas de transcorrências é representada por corpos de granitos alcalinos e metaluminosos, tais como Planalto (Huhn *et al.*, 1999a; Feio *et al.*, 2012), Plaquê (Avelar, 1996), Estrela (Barros et. al. 2004), Serra do Rabo (Sardinha *et al.*, 2001), Granito Igarapé Gelado (Barbosa, 2004), Pedra Branca (Huhn *et al.*, 1999b; Feio

et al. al., 2012), Granito Granofírico Sossego (Moreto *et al.*, 2015a), Pórfiro Castanha (Moreto *et al.*, 2015b). Corpos máficos com idade semelhante (ca. 2,74 Ga) incluem o Diopsídio Norito Pium e o Diorito Cristalino (Huhn *et al.*, 1999b).

Esses eventos magmáticos foram associados ao desenvolvimento de pronunciadas zonas de cisalhamento e extensivos eventos de retrabalhamento crustal (Tassinari & Macambira, 1999; Dall'Agnol *et al.* 2006; Tavares, 2015). A colocação de granitos em ca. 2,57 Ga representados pelos granitos Old Salobo Machado *et al.* (1991) e Itacaiúnas (Machado *et al.*, 1991; Souza *et al.*, 1996) foi restrita ao setor norte desse domínio.

Coberturas sedimentares incluem a Formação Águas Claras (Nogueira *et al.* 1995), com idade máxima de sedimentação de ca. 2.7 Ga obtidas em zircões detríticos em arenito (Trendall *et al.* 1998) e por idade atribuída a *sill* de metagabro intrusivo de ca. 2,6-2,7 Ga (Dias *et al.* 1996; Mougeot *et al.* 1996). Entretanto, idades Pb-Pb de ca. 2,06 Ga em sulfetos diagenéticos em arenitos (Mougeot *et al.* 1996; Fabre *et al.* (2011) sugerem idade paleoproterozoica para a Formação Águas Claras.

Magmatismo granítico anorogênico, alcalino a subalcalino, de idade de ca. 1,88 Ga, é representado pela Suíte Intrusiva Serra dos Carajás (granitos Young Salobo, Pojuca, Breves, Central de Carajás, Cigano e Rio Branco; Machado *et al.* 1991, Dall'Agnoll *et al.* 1994, Tallarico 2003, Santos *et al.*, 2013).

2.3. EVOLUÇÃO TECTÔNICA DA PROVÍNCIA CARAJÁS

O Domínio Carajás apresenta complexa estruturação regional sigmoidal com *trends* leste-oeste e noroeste-sudeste marcadamente impressos na Bacia Carajás. Beisiegel *et al.* (1973), consideraram, inicialmente, a região do sigmoide como um sinclinório representado por uma dobra de grande dimensão composta por várias outras dobras menores com eixo na direção WNW-ESSE.

Tabela 2.2. Síntese dos dados geocronológicos das unidades do Domínio Carajás da Província Carajás.

Unidade Estratigráfica	Método	Material Analisado	Idade	Referência
Proterozoico				
Granitos				
Granito Formiga	U-Pb	Zircão	ca. 600 Ma (*)	Grainger *et al.*, 2008
Sienogranito Gameleira	U-Pb	Zircão	1.583+8.5/-6.8Ma	Pimentel *et al.*, 2003
Central de Carajás	U-Pb	Zircão	1.820 ± 49 Ma	Wirth *et al.*, 1986
Granito Seringa	Pb-Pb	Zircão	1.874 ± 30 Ma	Lafon *et al.*, 1995
Pojuca	Pb-Pb	Zircão	1.874 ± 2 Ma	Machado *et al.*, 1991
Breves	SHRIMP	Zircão	1.879 ± 6 Ma	Tallarico *et al.*, 2005
	U-Pb	Zircão	1.880 ± 2 Ma	Machado *et al.*, 1991
Salobo Joven	Rb-Sr	Rocha total	1.880 ± 80 Ma	Cordani, 1981
Cigano	U-Pb	Zircão	1.883 ± 2 Ma	Machado *et al.*, 1991
Granito Rio Branco	Pb-Pb	Zircão	1.894 ± 16 Ma	Santos *et al.*, 2013
			1.909 ± 7 Ma	
Neoarqueano				
Cobertura Sedimentar Plataformal				
Formação Águas Claras	SHRIMP	Zircão	2.681 ± 5 Ma	Trendall *et al.*, 1998
	U-Pb	Zircão	2.645 ± 12 Ma	Dias *et al.*, 1996
	U-Pb	Zircão	2.778 a 3020Ma	Mougeot *et al.*, 1996a
Greenstone Belts				
Grupo Rio Novo	Pb-Pb	Rocha total	2.658 ± 213 Ma	Reis *et al.*, 2001a
Unidades Graníticas				
Granito Old Salobo	U-Pb	Zircão	2.573 ± 2 Ma	Machado *et al.*, 1991
Suíte Plaquê	Pb-Pb	Zircão	2.736 ± 24 Ma	Avelar *et al.*, 1999
Suíte Plaquê	Pb-Pb	Zircão	2.736 ± 24 Ma	Avelar *et al.*, 1999
Suíte Planalto	Pb-Pb	Zircão	2.747 ± 2 Ma	Huhn *et al.*, 1999b
	Pb-Pb	Zircão	2.733 ± 2 Ma	Feio *et al.*, 2013b
	U-Pb	Zircão	2.729 ± 17 Ma	Feio *et al.*, 2013b
Granito Igarapé Gelado	Pb-Pb	Zircão	2.731 ± 26 Ma	Barbosa, 2004
Granito Serra do Rabo	U-Pb	Zircão	2.743 ± 1,6 Ma	Sardinha *et. al.*, 2006
Granito Estrela	Pb-Pb	Zircão	2.763 ± 7 Ma	Barros *et al.*, 2004
Granito Granofírico Sossego	U-Pb	Zircão	2.740 ± 26 Ma	Moreto et al. 2015a
Granito Serra do Rabo	U-Pb	Zircão	2.743 ± 1.6 Ma	Sardinha *et al.*, 2006
Porfiro Castanha	U-Pb	Zircão	2.744 ± 4	Moreto et al. 2015b
Porfiro Quartzo-Feldspato	U-Pb	Zircão	2.740 ± 4.7	Moreto et al. 2015b
Tonalito Alvo 118	U-Pb	Zircão	2.743 ± 3	Tallarico, 2003
Suíte Pedra Branca	U-Pb	Zircão	2.762 ± 13 Ma	Feio *et al.*, 2013b
			2.750 ± 5 Ma	Feio *et al.*, 2012b
Rochas Máficas Intrusivas				
Diorito Cristalino	Pb-Pb	Zircão	2.738 ± 6 Ma	Huhn *et al.*, 1999b
Gabro Norito Sossego	SHRIMP	Zircão	2.739 ± 5.9 Ma	Moreto *et al.*, 2015a
Gabro Curral	SHRIMP	Zircão	2.739 ± 4.2Ma	
Associação Charnoquítica ou Diopsídio Norito Pium	Pb-Pb	Zircão	2.754 ± 1 Ma	Oliveira *et al.*, 2010,
	U-Pb	Zircão	2.735 ± 5 Ma	Feio *et al.*, 2013b
	Pb-Pb	Zircão	2.747 ± 1 Ma	Galarza *et al.*, 2012
	Pb-Pb	Zircão	2.732 ± 1 Ma	Galarza *et al.*, 2012
	U-Pb	Zircão	2.831 ± 6 Ma	Feio *et al.*, 2013
Supergrupo Itacaiúnas				
Grupo Igarapé Pojuca	Sm-Nd	Rocha total	2.719 ± 80 Ma	Pimentel *et al.*, 2003
	Pb-Pb	Zircão	2.705 ± 2 Ma	Galarza & Macambira, 2002b
	U-Pb	Zircão	2.732 ± 5 Ma	Machado *et al.*, 1991
Grupo Grão-Pará	Pb-Pb	Zircão	2.759 ± 2 Ma	
	Pb-Pb	Zircão	2.751 ± 4 Ma	Krymsky *et al.*, 2002
	SHRIMP	Zircão	2.760 ± 11 Ma	Trendall *et al.*, 1998
	Pb-Pb	Zircão	2.751 ± 4 Ma	Krymsky *et al.*, 2002
	SHRIMP	Zircão	2.760 ± 11 Ma	Trendall *et al.*, 1998
Metariodacito Jatobá	U-Pb	Zircão	2.70 ± 16 Ma	(Neste estudo)
Grupo Salobo	U-Pb	Zircão	2.761 ± 3 Ma	Machado *et al.*, 1991
	U-Pb	Titanita	2.497 ± 5 Ma	
	U-Pb	Zircão	2.555 ± 4 Ma	Machado *et al.*, 1991
	Sm-Nd	Rocha total	2.812 ± 98 Ma	Pimentel *et al.*, 2003
Grupo Igarapé Bahia	SHRIMP	Zircão	2.748 ± 34 Ma	Tallarico *et al.*, 2005
	U-Pb	Zircão	2.745 ±1 Ma	Galarza & Macambira, 2002a
	U-Pb	Zircão	2.776 ± 12 Ma	Galarza *et al.*, 2003

(Continuação)

Unidade Estratigráfica	Método	Material Analisado	Idade	Referência
Complexo Máfico-Ultramáficos				
Complexo Luanga	U-Pb	Zircão	2.763 ± 6 Ma	Machado *et al.*, 1991
Complexo Ézio	Sm-Nd	Rocha total	2.77 ± 0.17 Ma	Silva, 2016
Meoarqueano				
Granitos Sub-Alcalinos Mesoarqueanos				
Granito Bom Jesus	SHRIMP	Zircão	2.833 ± 6 Ma	Feio *et al.*, 2013
Granito Serra Dourada	U-Pb	Zircão	2.831 ± 6 Ma	Feio *et al.*, 2013
	U-Pb	Zircão	2.860 ± 22 Ma	Moreto *et al.* 2011
	U-Pb	Zircão	2.848 ± 5.5 Ma	Moreto *et al.* 2015b
Granito Canaã dos Carajás	U-Pb	Zircão	2.959 ± 6 Ma	Feio *et al.*, 2012
Granito Cruzadão	U-Pb	Zircão	2.845 ± 15 Ma	Feio *et al.*, 2013
	U-Pb	Zircão	2.857 ± 8 Ma	
	U-Pb	Zircão	2.875 ± 12 Ma	
	U-Pb	Zircão	3.053 ± 8 Ma	
Granodioritos de alto Mg				
Granodiorito Água Azul	Pb-Pb	Zircão	2.884 ± 1.7 Ma	Sousa *et al.*, 2010
Granodiorito Água Limpa	Pb-Pb	Zircão	2.879 ± 1.3 Ma	Gabriel *et al.*, 2010
Tonalitos e Granodioritos				
Tonalito Campina Verde	U-Pb	Zircão	2.850 ± 7 Ma	Feio *et al.*, 2012
	Pb-Pb	Zircão	2.872 ± 1 Ma	
Trondhjemito Rio Verde	U-Pb	Zircão	2.923 ± 15 Ma	Feio *et al.*, 2012
Tonalito Bacaba	U-Pb	Zircão	3.00 ± 3.6 Ma	Moreto *et al.*, 2011
	U-Pb	Zircão	3.00 ± 5.9 Ma	
Granito Sequeirinho	U-Pb	Zircão	3.014 ± 22 Ma	Moreto *et al.*, 2015a
	U-Pb	Zircão	3.010 ± 21 Ma	
	SHRIMP	Zircão	2.989 ± 5.2 Ma	
Gabro Norito	SHRIMP	Zircão	2.739 ± 5.9 Ma	Moreto *et al.*, 2015a
Complexo Xingu	U-Pb	Zircão	2.859 ± 2 Ma	Machado *et al.*, 1991
	U-Pb	Zircão	2.974 ± 15 Ma	
	SHRIMP	Zircão	2.859 ± 9 Ma	
Metadacito Pista (*greenstone belt*)	U-Pb	Zircão	2.968 ± 15 Ma	Moreto *et al.*, 2015a
	U-Pb	Zircão	2.979 ± 5.3 Ma	
Complexo Pium (Ortogranulito Chicrim-Cateté)	SHRIMP	Zircão	2.859 ± 9 Ma	Pidgeon *et al.*, 2000
	SHRIMP	Zircão	3.002 ± 14 Ma	Pidgeon *et al.*,2000

Araújo et al. (1988), entretanto, reinterpretaram à megaestruturação sigmoidal como resultante de sistemas de cavalgamentos e transcorrências, desenvolvidos em regime compressivo oblíquo, com encurtamento na direção NW-SE, que teria ocorrido entre o Neoarqueano e o Paleoproterozoico, e o denominaram de Cinturão de Cisalhamento Itacaiúnas. Em linhas gerais, o modelo sugere que a estrutura sigmoidal de Carajás formou-se durante transtensão dextral das rochas do embasamento. Isso teria levado à formação de uma bacia do tipo *pull-apart*, controladas pela geometria anastomosada dos lineamentos principais, resultando no desenvolvimento dos sistemas de falha Carajás e Cinzento.

Os autores ainda advogam que após o término da deposição das unidades vulcanossedimentares, um evento transpressivo sinistral teria causado a inversão tectônica da bacia com geração de uma estruturação regional em flor positiva.

Pinheiro e Holdsworth (1997), entretanto, consideram o modelo de reativação tectônica de antigas zonas de cisalhamento dúcteis mesoarqueanas, como responsável pela complexa estruturação do Cinturão de Cisalhamento Itacaiúnas. Nesse modelo, o

longo período de evolução tectônica teria ocorrido em estágios subsequentes. Entre 2,85 e 2,76 Ga, as rochas do embasamento tornaram-se intensamente deformadas, como evidenciado pela foliação milonítica subvertical de direção E-W impressa nessas rochas. Posteriormente, uma bacia intracratônica desenvolveu-se sob condições de regime de transpressão sinistral regional de alta temperatura. Transtensão dextral, por volta de ca. 2,76 Ga levariam à deposição do Supergrupo Itacaiúnas e da Formação Águas Claras em uma ampla bacia intracratônica, seguida do estabelecimento das zonas de cisalhamento transcorrentes Cinzento e Carajás, marcadas por ângulos de mergulhos altos, geometria curva, anastomosada, típica de zonas de falhas transcorrentes.

A inversão tectônica da bacia, sob o regime de transpressão sinistral, teria ocorrido em ca. 2,7 Ga e perdurando até ca. 2.6 Ga (Domingos, 2009). Os sistemas transcorrentes Carajás e Cinzento, após sua formação em regime dextral, estiveram sujeitos ainda a eventos tardios de reativações tectônica, com eixos de extensão dispostos entre NE-SW a E-W, favorecendo a intrusão de diques e plútons anorogênicos da Suite Intrusiva Serra dos Carajás por volta de 1,9-1,8 Ga (Domingos, 2009).

Alternativamente, Meirelles (1986), Dardenne *et al.* (1988), Meirelles & Dardenne (1991), Teixeira & Eggler (1994), Teixeira, (1994), Silva *et al.*, (2005), Lindenmayer *et al.*, (2005), Lobato *et al.* (2005) e Teixeira *et al.* (2010) consideraram que o Domínio Carajás teria registro de ambiente de subducção, o que seria evidenciado pela afinidade cálcio-alcalina de alto potássio dos basaltos do Supergrupo Itacaiúnas. Dessa forma, esse modelo propõe a formação de uma bacia vulcano-sedimentar em ambiente de margem ativa, cuja evolução estaria relacionada à subducção de placa oceânica, seguida por colisão continente-continente. Nesse modelo de evolução geotectônica, a colisão continente-continente teria ocorrido em torno de 2,74 Ga e teria sido responsável pela justaposição dos domínios Rio Maria e Carajás (Teixeira *et al.*, 2010). No entanto, Zucchetti (2007) considera que tais características poderiam refletir vulcanismo extravasado sobre crosta continental em ambiente de *back arc* desenvolvido em ca. 2,76 Ga.

Gibbs *et al.* (1986), Wirth *et al.* (1986), DOCEGEO (1988), Olszewski *et al.* (1989) e Tallarico *et al.* (2005) atribuíram a formação da Bacia Carajás à abertura de um rifte continental marcado pela ascensão de manto astenosférico vinculada a plumas mantélicas (Condie, 1998; Isley and Abbott, 2002) em um ambiente extensional. Tallarico (2003), atribui ao evento termal de ca 2,7 Ga *underplating* de magma máfico na base da crosta inferior levando à sua fusão e geração de diferentes câmaras

magmáticas, incluindo aquelas que teriam originado o Complexo Máfico-Ultramáfico Luanga e outras intrusões, em torno de 2,76 Ga, assim como as rochas supracrustais do Supergrupo Itacaiúnas, representadas pelo vulcanismo bimodal do Grupo Grão Pará (Ferreira Filho *et al.* 2007).

Tavares (2015) propôs um novo modelo evolutivo para o Domínio Carajás, que inclui quatro eventos deformacionais cíclicos principais, sendo dois compressivos e dois extensionais. Inicialmente, a origem da estruturação do domínio estaria relacionada ao Mesoarqueano, com a instalação de uma margem continental ativa em torno de 2.87 – 2.83 Ga, que compreenderia núcleos de idade paleoarqueana. Este evento representaria a colagem entre os Domínios Rio Maria e Carajás, levando a geração de processos metamórficos de alto grau e forte migmatização (D1). Tal processo seria responsável por significativo espessamento crustal e geração de intrusões ígneas por fusão anatética.

O segundo evento estaria relacionado a um processo de rifteamento entre 2.76 e 2.70 Ga, resultando em magmatismo bimodal (Supergrupo Itacaiúnas), associado a grandes volumes de magmas sob condições de *underplating*, com subsequente sedimentação marinha de natureza clasto-química em ambiente plataformal, como já defendido por Gibbs *et al.* (1986), Wirth *et al.* (1986), DOCEGEO (1988), Olszewski *et al.* (1989) e Tallarico *et al.* (2005). Adicionalmente, Tavares (2015) contesta a relação entre o carácter sin-tectônico e espacialmente estruturado na direção E-W dos granitoides do tipo A neoarqueanos e um evento transpressivo regional, como proposto nos trabalhos de Barros *et al.*, (2001, 2004, 2009). Tavares (2015) atribui a colocação desses granitoides às falhas desenvolvidas durante colagem do embasamento mesoarqueano, que teriam sido reativadas durante o rifteamento neoarqueano, resultando em perfeitos condutos naturais à migração desses magmas. O autor também atribuiu a fortuita contemporaneidade das mineralizações IOCG de 2,70 a 2,68 Ga (Moreto *et al.*, 2015a) associadas a esse evento magmático.

O terceiro evento inclui processos compressivos na direção N-S, com vergência de topo para norte, entre ca. 2,70 Ga e 2,6 Ga. Este evento tem como principal evidência a inversão tectônica da Bacia Carajá, como considerado nos trabalhos de Pinheiro e Holdsworth (1997) e Domingos (2009), além da geração de espessamento crustal e metamorfismo de baixo grau. Tavares (2015) sugere, com isso, uma segunda colisão entre os Domínios Rio Maria e Carajás, porém de baixa magnitude e apenas de carácter intracontinental.

O quarto evento, entretanto, estaria novamente relacionado a um evento de rifteamento, entre ca. 2.61 e 2.54 Ga, no qual eventos hidrotermais mineralizantes, principalmente centrados no extremo norte da Província Carajás e ao longo do Cinturão Norte do Cobre (Moreto *et al.*, 2015a), seriam responsáveis pela formação do depósito Salobo (Réquia, *et al.*, 2003). Esse evento estaria associado à fragmentação do paleocontinente Carajás.

No norte da Província Carajás, o Orógeno Transamazônico, de idade paleoproterozoica, resultou em um sistema compressivo associado a metamorfismo regional de médio a alto grau (Macambira *et al.* 2009; Tavares, 2015), clivagem de transposição nas rochas do Domínio Carajás e xistosidade e bandamento gnáissico nos ortognaisses migmatíticos e granulitos máficos do Domínio Bacajá. Tal evento foi relativo a um sistema colisional paleoproterozoico (2,09 a 2,07 Ga), nomeado como Colisão Carajás-Bacajá, que encerra o processo de aglutinação do Riaciano (Tavares *et al.* 2013; Tavares, 2015).

Evento deformacional subsequente, no Orosiriano, se restringiu à borda oriental do Domínio Carajás. (Tavares, 2015). Compreende movimento de topo para norte-noroeste a oeste-noroeste em um sistema compressivo dominado por cisalhamento simples, com feixes de empurrões associados ao forte componente de estiramento e um sistema de imbricação tectônica com desenvolvimento de falhas transcorrentes sinistrais. É interpretado como relativo ao Evento Tectono-termal Sereno, desenvolvido em ca. 2,0 Ga (Tavares *et al.* 2013; Tavares, 2015).

Tavares (2015) conclui que estruturação de caráter rúptil a rúptil-dúctil advindos de processos extensionais a transtensionais, nas direções ENE-WSW e WNW-ESSE, foi posterior ao colapso dos orógenos paleoproterozoicos. Tal estruturação gerou feixes de falhas subverticais, frequentemente associadas a brechas tectônicas e a veios mineralizados contendo minerais de baixa temperatura tais como epidoto, clorita, quartzo, hematita, além de sulfetos. É tido como um evento rúptil dominantemente transtensivo, associado à colocação dos corpos graníticos anorogênicos de ca. 1,88 Ga e à formação de depósitos tipo IOCG em ca. 1,88 Ga (Tallarico, 2003; Moreto *et al.* 2015b).

Tavares (2015) ainda menciona fraturamento associado a sistemas de falhas normais, atribuídos ao desenvolvimento de magmatismo máfico intracontinental, e atribui provável correspondência à sutura entre os blocos Carajás-Transamazonas e Parnaíba/Oeste Africano, que teria ocorrido por volta de 750 Ma (Paixão et al. 2008). A

idade mínima de cerca de 500 Ma (Gomes et al., 1975) reconhecida na região de Carajás provavelmente reflete os estágios finais do Ciclo Brasiliano.

Por fim, Tavares (2015), pontua que os efeitos que culminaram na abertura do oceano Atlântico equatorial e na ruptura final entre a América do Sul e a África, (Soares Júnior *et al.* 2008), promoveram reflexos no interior do Cráton Amazônico como o rifteamento na região da bacia do Amazonas-Solimões e magmatismo máfico intracontinental cronocorrelato. Na região de Carajás, esse magmatismo é representado pela instalação de corpos de diques do Diabásio Rio Pajeú, com idade cerca de 220 Ma (Meireles *et al.* 1982).

ANEXO I

The iron oxide-copper-gold (IOCG) Jatobá deposit, Carajás Mineral Province, Brazil: Geology, hydrothermal alteration, mineralization and mineral chemistry

Angela Suélem Rocha Veloso, Lena Virgínia Soares Monteiro, Caetano Juliani

Instituto de Geociências, Universidade de São Paulo (São Paulo), SP 05508-080, Brazil

Abstract

The Carajás Province, located in the Amazon Craton, hosts several Cu-Au deposits that deserve attention due to their high volume of hydrothermal magnetite and elevated contents of REE, P, Ni, Co, Pd, and U, similar to those of iron oxide-copper-gold (IOCG) deposits. World-class IOCG deposits at Carajás (e.g. Sossego, Cristalino, Alvo 118) may be connected by similar genetic processes with a large mineral system. The Jatobá deposit, under evaluation, may represent a specific portion of this IOCG system.

The Jatobá deposit is hosted by metarhyodacite, amygdaloidal metabasalt, felsic metavolcaniclastic breccias and mafic metalapilli and metacrystal metatuffs, and metadiabase dikes attributed to the Itacaiúnas Supergroup. The least-altered host rocks derived from mafic protoliths record lower greenschist facies (albite- actinolite I) paragenesis.

Pre-, syn- and late tectonic hydrothermal alteration associated with the Canaã shear zone development was pervasive and intense. Early hydrothermal alteration encompasses silicification, sodic (albite I, scapolite I), sodic-calcic (ferro-pargasite), and potassic (biotite I, tourmaline, Cl-apatite I, Ce-allanite I) alteration. Almond-shaped albite (I) or scapolite (I) porphyroclasts involved by pressure shadows in mylonitic rocks indicate their blastesis previously to the shear zone development.

The main syn-tectonic hydrothermal alteration stages comprise sodic-calcic (scapolite II), calcic (actinolite II, Cl-apatite II, Ce-allanite II, quartz) and potassic (Cl-K-hastingsite I, biotite II, quartz-Co-magnetite IV, Cl-apatite III, Ce-allanite III) alteration controlled by the mylonitic foliation. Early veins with magnetite (III) and massive magnetite bodies (IV), represent proximal envelopes of mineralized zones. The magnetitite is cut by fibrous actinolite (II), magnetite (V) and Cl-apatite, which also occur as infill in breccias with magnetite fragments. Late tectonic hydrothermal alteration is represented by chlorite alteration and scapolite (III) veins, which in turn are cut by scapolite (IV), Cl-K-hastingsite (II) and biotite (III) veinlets.

The copper-(nickel) mineralized zones in the Jatobá deposit comprise swarms of vertical to subvertical orebodies spatially related to metadiabase dikes and contact zones between metarhyodacites and metabasalts. The mineralized zones were formed in four stages, coeval to ductile and ductile-brittle deformational events. The mineralization stage (I) is spatially related to massive magnetite bodies and to syn-tectonic calcic alteration (actinolite II-magnetite V). It is characterized by Ni-pyrrhotite, Ni-pyrite and Cl-apatite (II), and subordinately, Co-chalcopyrite, Ce-allanite II, Co-pentlandite, quartz and Ce-monazite. The transition to the mineralization stage (II) was accompanied by decreasing contents of Ni and Co and pyrrhotite and actinolite concentration. Mineralization style evolved from replacement fronts controlled by mylonitic foliation to hydraulic breccia zones. The mineralization stage (II) was related to the development of the syn-tectonic potassic alteration (II) and represented by a system of strongly oriented and interconnected bodies with biotite (II), Cl-apatite (III), Co-magnetite (IV), ilmenite (I), Ce-allanite (III) and quartz, besides discrete portions containing Ni-

pyrite and Co-chalcopyrite. Breccia zones with matrix made of biotite (II) and Co-chalcopyrite (± Ni-pyrite ± Ni-pyrrhotite) and fragments of massive magnetite represent Cu-richer bodies.

The third mineralizing stage recognized in the Jatobá deposit is distinguished from the others due to its control by ductile-brittle and brittle structures, which enabled the formation of veins with typical open-space filling textures. It was coeval to the late tectonic alteration that comprises paler brown or green biotite (III), scapolite (IV), F-Cl-apatite (IV), and Cl-K hastingsite (II), Co-chalcopyrite and siegenite I (± Co-pyrite, ±Co-magnetite, ± cassiterite).
The late mineralization stage (IV) was the most expressive at Jatobá. It was coeval to widespread chlorite (II), quartz, epidote and calcite development. It occurs in a variety of branching veinlets and breccias with Co-chalcopyrite, Co-pyrite, sphalerite, molybdenite, uraninite and monazite. Other late vein types comprise those with quartz-chalcopyrite-K (±molybdenite, Co-pentlandite, and siegenite II) and fine veinlets with chlorite-chalcopyrite, W-bearing hematite, rare earth carbonates (bastnäsite, coskrenite and sahamalite), Co- and Ni-pyrite, sphalerite, ilmenite, marcasite, leucoxene and adularia.

The high Ti , V, Ni and Cr contents in Jatobá magnetite point to high-temperature conditions (ca. 500-700°C), similar to that of high-temperature magmatic-hydrothermal systems (e.g. IOCG, iron oxide-apatite ore and porphyry copper), especially during the early nickel-enriched mineralization event. The gradual increase in Cl contents of scapolite (I) to (III) indicated a progressive evolution from high-temperature hipersaline fluids. However, the late scapolite (IV) points to changes in fluid composition accompanied by decreasing temperature conditions (370 °C).

The Jatobá deposit has attributes comparable to those of relatively deep portions of IOCG mineral systems with evidences of limited input of externally-derived diluted fluids. However, lower temperature conditions in the late stages, coupled with ductile-brittle structures, reveal that the main mineralizing event at Jatobá was developed after significant system exhumation.

Keywords: Jatobá deposit, Iron-oxide-copper-gold deposit, Carajás Mineral Province, Hydrothermal alteration, Mineral chemistry

Introduction

The Carajás Province, located in the Amazon Craton (Santos *et al.* 2000, Santos 2003), represents an important metallogenetic province with outstanding iron deposits (N4 and N5 mines in the Serra Norte, SL1 to SL3 deposits in the Serra Leste and S11D mine at Serra Sul; Lobato *et al.* 2005), Au-Pd-Pt (Serra Pelada; Meireles & Silva 1988, Tallarico *et al.* 2000, Moroni *et al.* 2001, Cabral *et al.* 2002a, 2002b), lateritic gold (Igarapé Bahia; Zang & Fyfe 1995, Angélica 1996, Porto *et al.* 2010), bauxite (N5; Kotschoubey & Lemos (1985), manganese (Azul; Dardenne & Schobbenhaus 2001), nickel (Vermelho; Klein & Carvalho 2008), Cr-Ni-EGP (Luanga mafic-ultramafic complex; Macambira & Vale 1997), and copper-gold deposits.

Among the copper-gold deposits, several examples deserve attention due to their high volume of hydrothermal magnetite and/or hematite and elevated contents of REE, P, Ni, Co, Pd and U, similar to those of iron oxide-copper-gold (IOCG) deposits (Hitzman et al., 1992; Hitzman et al., 2000). Part of these deposits also represents the only known Archean examples attributed to this deposit class, revealing a particular evolution of the Carajás Province (Réquia *et al.* 2003, Tallarico *et al.* 2005, Groves *et al.* 2010, Xavier *et al.* 2010, Moreto *et al.* 2015b).

At Carajás, the IOCG deposits are distributed in the Northern and Southern Copper belts within E-W e WNW-ESSE shear zones (Moreto, 2015a, b). Particularly in the Southern Copper Belt, the attributes of the IOCG deposits reflect the variable nature of host rocks, which include Neoarchean metavolcanic-sedimentary units, granite and gabbros, and Mesoarchean greenstone belts, TTG units and other granitoids (Moreto et al., 2015a, b). However, several deposits, such as Sossego, Cristalino, Alvo 118, Jatobá, Castanha, Bacaba, Bacuri, Visconde, Borrachudos (Augusto, et al. 2008; Monteiro et al., 2008a; 2008b, Pestilho, 2011, Silva et al., 2015; Melo et al., 2014; Moreto et al., 2015a; 2015b) may represent distinct portions of a large mineral system connected by similar genetic processes. The identification of paragenesis, hydrothermal alteration patterns, mechanisms of fluid-rock interaction and sources of metals, fluids and ligands in each deposit, however, is necessary to link them and unravel their evolution.

The Cu-Au Jatobá deposit, located at 3 km north of the Sossego Mine (15% de 355 Mt @ 1,5 % Cu e 0,28 g/t Au; Lancaster et al., 2000; Villas et al. 2005; Carvalho et al. 2005; Monteiro et al., 2008a,b), is still under evaluation. It is spatially related to expressive scapolite alteration zones, has notable magnetite-(apatite) contents and a

particular ore signature with Ni-(Zn) enrichment. It is spatially related to the Sossego Mine, which records multiple hydrothermal events responsible for formation of ore at ca. 2.70 Ga-2.68 Ga (e.g. Sequeirinho and Pista orebodies) and ca. 1.88 Ga (e.g. Sossego orebody). Thus, the Jatobá deposit may be formed in a specific part of a long-lived large mineral system.

This contribution aims to decipher the hydrothermal history recorded in the Jatobá deposit by means of detailed paragenetic characterization of hydrothermal alteration and Cu-Au-(Ni-Zn) ore, accompanied with the identification of variations in the mineral chemistry during the relative temporal evolution of the system. This study may provide important subsides for an integrated model for the IOCG deposits of the Carajás Mineral Province.

1. Geological setting of the Carajás Province

The Carajás Province (Santos *et al.* 2000; Santos 2003; (Fig. 1) represents a predominantly Archean nucleus, located in the Amazonian Craton (Teixeira *et al.*, 1989; Brito Neves & Cordani, 1991; Tassinari, 1996; Tassinari & Macambira, 1999, 2004). The province was divided into two tectonic domains (Santos, 2003, Vasquez *et al.*, 2008a; Fig. 1): Rio Maria, in the south, and the Carajás Domain, in thr north, limited by a regional E-W discontinuity. These domains could have shared a similar evolution during the Mesoarchean (Dall´Agnol et al., 2006). However, the Rio Maria Domain evolved and was stabilized during the Mesoarchean, whereas the Carajás Domain records expressive tectono-magmatic event(s) in the Neoarchean. The latter was responsible for emplacement of coeval mafic-ultramafic intrusions, charnockites and A_2-type granites and deposition of extensive volcano-sedimentary sequences (Huhn et al., 1988, DOCEGEO, 1988, Souza et al. 1996, Althoff et al. 2000, Dall'Agnol et al. 2006, Vasquez et al. 2008a). The majority of known IOCG deposits are concentrated in the Carajás Domain, close to its limits.

Rio Maria Domain

The Rio Maria Domain (Fig. 1B) resulted from amalgamation of intra-oceanic arcs in two stages (3,05 Ga to 2,90 Ga; 2,88 Ga to 2,82 Ga; Leite, 2001; Souza *et al.*, 2001; Santos, 2003; Tassinari *et al.*, 2005; Vasquez *et al.*, 2008; Almeida *et al.*, 2011),

accompanied by compressive regime and crustal shortening in the N-S direction until ca. 2.85 Ga.

During the first stage (Table 1), *strictu sensu* greenstone belts (DOCEGEO 1988, Araújo and Maia, 1991), mafic-ultramafic complexes (ca. 2.97 Ga; DOCEGEO 1988, Pimentel and Machado 1994) and older tonalite–trondhjemite–granodiorite (TTG) rocks were formed (Rolando & Macambira, 2003; Almeida *et al.*, 2010, 2011, 2013). The second stage (Table 1) comprises the emplacement of younger rocks of the TTG series (DOCEGEO 1988, Almeida *et al.*, 2011) and sanukitoids (DOCEGEO 1988, De Oliveira *et al.*, 2011). Potassic leucogranites (Almeida *et al.*, 2010) are considered as an evidence of the last tectono-thermal event related to the cratonization of Rio Maria Domain (Vasquez *et al.* 2008a).

The Mesoarchean units are covered by the Paleoproterozoic metasedimentary Rio Fresco and Gemaque groups (Vasquez *et al.* 2008a). Orosirian magmatism is mainly represented by widespread ca. 1.88 Ga type-A_2 granitegenesis (e.g. Jamon, Bannach, Cachoeirinha, Gradaús, Manda Saia, Marajoara, Musa, Redenção, São João, São José, Velho Guilherme, Redenção e Seringa; Dall'Agnol et al. 1999, 2005, Dall'Agnol & Oliveira 2007).

In the Rio Maria Domain, orogenic gold deposits (e.g. Diadema, Lagoa Seca, Babaçu, Mamão, Tucumã, Inajá, Cuca) and "garimpos" (e.g. Serqueiro, Peladinha, Serrinha e Tatu Frango) comprise structurally-controlled auriferous quartz veins within shear zones that intercept mainly greenstone belt sequences (Oliveira & Leonardos 1990, Leonardos *et al.* 1991, Huhn 1992, Santos *et al.* 1998, Villas & Santos 2001, Oliveira & Santos 2003). Additionally, the Pedra Preta W deposit is also hosted by metavolcano-sedimentary units close to the cupola of the ca. 1.88 Ga Musa granite (Cordeiro *et al.* 1984, Rios *et al.* 1998).

Carajás Domain

The Carajás Domain (Fig. 1C) is notable by its metallogenetic diversity, closely related to its Neoarchean and Paleoproterozoic evolution.

The Mesoarchean rocks comprise gneisses and migmatites of the Xingu Complex and granulites of the Chicrim Cateté Ortogranulite. The latter may have crystallization ages of ca. 3.0 Ga, similar to that of enderbite gneiss dated by Pidgeon *et al.* (2000) in the Pium river. Additionally, ca. 3.0 Ga granitoids (e.g. Sequeirinho and Bacaba tonalites; Moreto *et al.* 2011; 2015a), ca. 2.96-2.93 Ga Canaã dos Carajás

Granite (Feio *et al.*, 2013), ca. 2.88 – 2.87 Ga Água Azul (Sousa *et al.*, 2010) and Água Limpa (Gabriel *et al.*, 2010) granodiorites, and ca. 2.87 Ga to 2.83 Ga granites and trondjemites (e.g. Serra Dourada, Cruzadão, Rio Verde, Campina Verde and Bom Jesus (Moreto *et al.*, 2011, Feio *et al.*, 2012, 2013) were characterized.

Greenstone belts encompass metaultramafic (talc schist, serpentinite and spinifex-textured komatiite), mafic (actinolite-chlorite-quartz-albite schist), and metasedimentary units (quartz-chlorite schists), recognized to the south of the Carajás ridge (e.g. Selva greenstone belt; Sequeirinho Group; Siepierski et al., 2016; Justo et al., 2015). The Pista metadacite (ca. 2.97 Ga; U-Pb SHRIMP zircon; Moreto *et al.* 2015a) that is a host to IOCG ore at Sossego Mine, is interpreted as part of this Mesoarchean greenstone belt sequence.

The Neoarchean metavolcano-sedimentary units of the Itacaiúnas Supergroup (Wirth *et al.*, 1986, DOCEGEO1988, Machado *et al.* 1991) and Rio Novo Group (Hirata *et al.* 1982) encompass mafic and felsic metavolcanic and metavolcaniclastic rocks, banded iron formation, metagraywackes, which underwent greenschist to amphibolite facies metamorphism. The Itacaiúnas Supergroup (ca. 2.76 – 2.73 Ga; Machado et al., 1991) was divided into Igarapé Salobo, Igarapé Pojuca, Grão Pará and Igarapé Bahia groups.

The widespread Neoarchean magmatism is also revealed by ca. 2.77 Ga to 2.70 Ga mafic-ultramafic intrusions (e.g. Luanga Complex; Jorge João *et al.*, 1982; Machado *et al.*, 1991; Ézio Complex; Silva, 2016; Cateté Intrusive Suite; Lafon *et al.*, 2000; Macambira & Vale, 1997) and coeval emplacement of gabbro, norite and diorite (e.g. Diopside Norite Pium; Cristalino Diorite; Huhn *et al.*, 1999b) and granite.

The ca. 2.75 to 2.70 Ga granites are foliated and alkaline to metaluminous (e.g. Planalto; Huhn *et al.*, 1999a; Feio *et al.*, 2012, Plaquê; Avelar, 1996, Estrela; Barros et al. 2001, Serra do Rabo; Sardinha *et al.*, 2001, Igarapé Gelado; Barbosa, 2004, Pedra Branca, Huhn *et al.*, 1999b; Feio *et al.* al., 2012; Sossego Granophyric Granite; Moreto *et al.*, 2015a, Castanha; Moreto *et al.*, 2015a). The Old Salobo and Itaciaúnas granites (ca. 2.57 Ga; Machado *et al.*, 1991; Souza *et al.*, 1996) were identified locally within the Cinzento Shear Zone.

The Águas Claras Formation represents a metasedimentary sequence (Nogueira *et al.* 1995) formed in marine to fluvial environment. This formation is crosscut by a ca. 2.6 Ga gabbroic sill (Dias *et al.* 1996; Mougeot *et al.* 1996), but has diagenetic sulfides in metarenites with Pb-Pb ages of ca. 2.06 Ga (Mougeot *et al.* 1996).

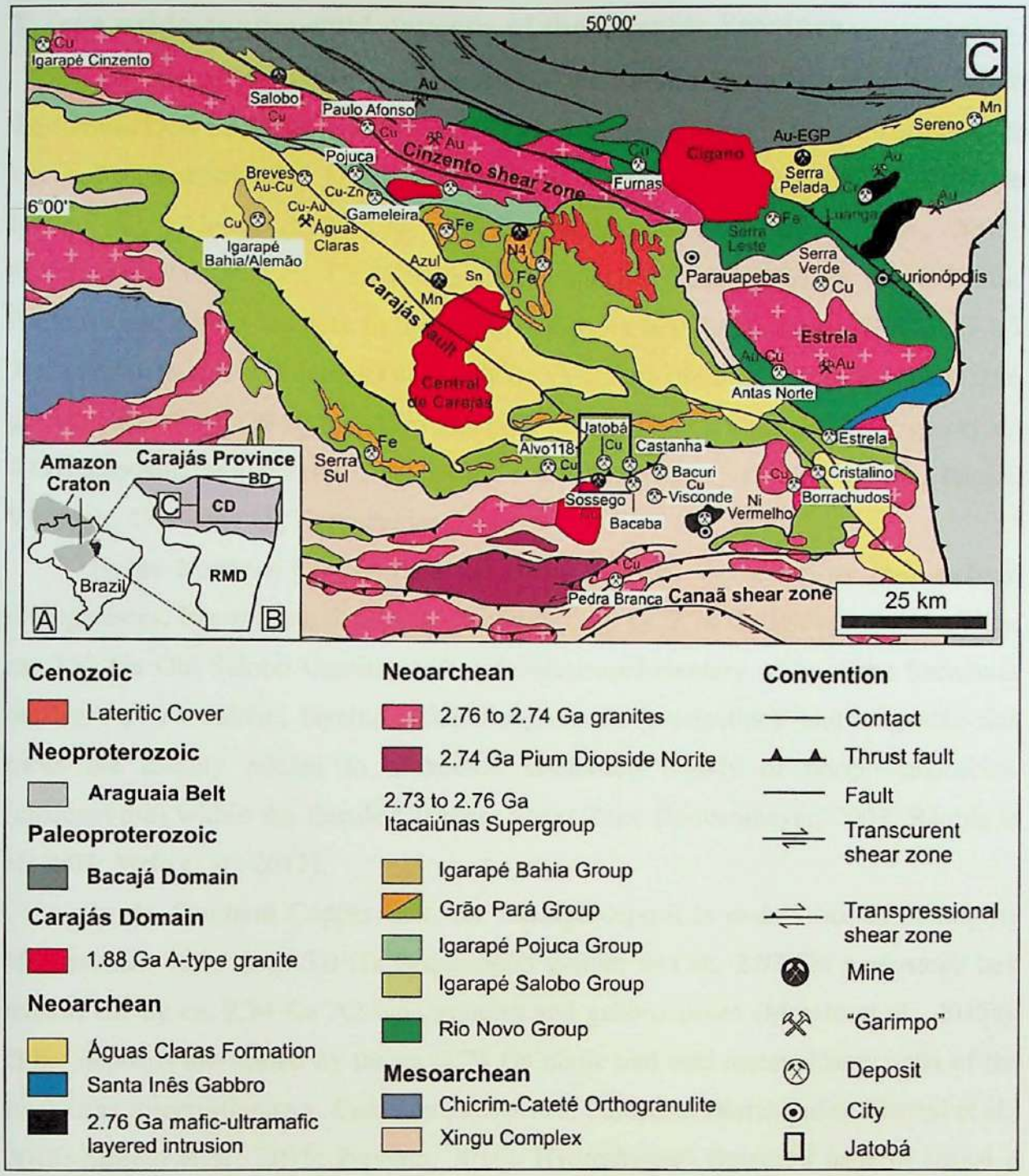

Figure 1. A. Location of the Carajás Province in the Amazon Craton. B. Division of the Carajás Province into the Rio Maria (RMD) and Carajás (CD) domains, and its north limit with the Paleoproterozoic Bacajá Domain (DB). C. Geological map of the Carajás Domain (Vazquez *et al.*, 2008b), showing the location of main mines and mineral deposits, including the Jatobá deposit (blue rectangle).

In the Carajás Domain (Fig. 1C), Paleoproterozoic (ca. 1.88 Ga) granites comprise the alkaline and subalkaline A_2-type Serra dos Carajás, Young Salobo, Pojuca, Breves, Central de Carajás, Cigano and Rio Branco suítes (Machado *et al.* 1991, Dall'Agnoll *et al.* 1994, Tallarico 2003).

2. Iron oxide-copper-gold deposits of the Carajás Province

The iron oxide-copper-gold deposits of the Carajás Province are recognized in the Carajás Domain, in the Northern and Southern Copper belts. In the northern belt are known the giant Salobo (1.112 Bt @ 0,69% wt% Cu and 0,43 g/t Au; VALE, 2012) and Igarapé Bahia/Alemão (219 Mt @ 1,4% Cu and 0,86 g/t Au (Tallarico et al., 2005), Furnas (500 Mt @ 0,7% Cu; VALE, 2010), Igarapé Cinzento/GT46, Grota Funda, Paulo Afonso e Polo deposits. In the Southern Copper Belt, the Sossego, (355 Mt @ 1,5 % Cu and 0,28 g/t Au; Lancaster et al., 2000), Cristalino (482 Mt @ 0,65% Cu and 0,06 g/t Au; NCL Brasil, 2005) and Alvo 118 (170 Mt @ 1,0% Cu e 0,3 g/t Au; Rigon et al., 2000) deposits, and several other under evaluation (e.g. Castanha, Bacaba, Bacuri, Visconde, Cristalino 88, Borrachudos, Jatobá).

In the Northern Copper Belt, the IOCG deposits are hosted by Mesoarchean orthogneisses, Neoarchean deformed granitoids (e.g. ca. 2,74 Ga Igarapé Gelado Suite; ca. 2,57 Ga Old Salobo Granite) and metavolcanosedimentary units of the Itacaiúnas Supergroup. At Salobo, fayalite-almandine-grunerite-(tourmaline)- and magnetite-rich rocks are closely related to orebodies, composed mainly of bornite-chalcocite-(chalcopyrite) within the ductile Cinzento Shear Zone (Lindenmayer, 2003; Réquia et al. 2003; Melo et al., 2017).

In the Southern Copper Belt, the Sossego deposit is mainly hosted mainly by Mesoarchean units (e.g. 3.0 Ga Sequeirinho granite and ca. 2.97 Ga greenstone belt lenses) cut by ca. 2.74 Ga A2-type granites and gabbronorites (Moreto et al., 2015a). Other deposits are hosted by the ca. 2.74 Ga mafic and acid metavolcanic units of the Itacaiúnas Supergroup (e.g. Cristalino, Alvo 118, Castanha, Borrachudos; Torresi et al., 2012; Moreto et al., 2015; Previato, 2016). Hydrothermal alteration patterns reveal a general evolution from sodic (albite-scapolite), sodic-calcic (albite-actinolite), potassic (K-Cl hastingsite-biotite-tourmaline) alteration followed by chlorite, carbonate and late calcic or hydrolytic alteration. Scapolite alteration is especially well developed in mafic metavolcanic rocks, although scapolite veins are also regionally recognized in granites and gabbros. Magnetite-(apatite)-rich rocks are spatially related to sodic-calcic alteration controlled by ductile or ductile-brittle structures. Chalcopyrite-bearing ore zones comprise hydraulic breccias, veins and stockworks enveloped by chlorite alteration zones (Réquia et al., 2003; Lindenmayer, 2003; Villas et al., 2006; Augusto et al., 2008; Monteiro et al., 2008a; 2008b; Xavier et al., 2008; 2009; Pestilho, 2011;

Xavier et al., 2010, 2012; Torresi et al., 2012; Melo et al., 2014; Silva et al., 2015; Moreto et a., 2015a, 2015b).

Multiple IOCG events have been recognized in the Carajás Province, even in a single deposit. The oldest IOCG event (ca. 2.74 Ga – 2.70 Ga) was identified in the Igarapé Bahia (Pb-Pb ages; Galarza *et al.,* 2003) and Salobo (Pb-Pb ages; Tassinari et al., 2003) deposits, in the Northern Copper Belt, and at Sossego (e.g. Sequeirinho and Pista orebodies; LA-ICP-MS U-Pb monazite and Re-Os molybdenite; Moreto et al., 2015a). These Neoarchean ages are synchronous or late in relation to that of the more expressive magmatic event of the Carajás Domain, which was responsible by metavolcanosedimentary units, mafic-ultramafic complexes, A_2-type granites and gabbronorites.

Precise geochronological data for the Igarapé Bahia and Salobo deposits also point out to a ca. 2.57 Ga age, coeval to that of the Old Salobo granite emplacement (e.g. U-Pb SHRIMP monazite; Re-Os molybdenite; Réquia *et al.,* 2003, Tallarico *et al.*, 2005). In addition, the ca. 1.88 Ga age, similar to that of the Orosirian A_2-type magmatism, was identified in the Alvo 118 and Sossego (e.g. Sossego and Curral orebody) deposits (Tallarico, 2003; Moreto *et al.*, 2015a). Thus, the Carajás IOCG deposits share a complex evolution, in which overprinting and remobilization may be present.

Intense fluid-rock interaction and inheritance of the host rocks may in part explain the diversity of geological attributes on the deposit scale. Fluid inclusion, stable isotopes (O, H, S, C, B and Cl) and Cl/Br ratios indicate that ore genesis was linked to hybrid hydrothermal systems, with magmatic and externally-derived (e.g. meteoric, formational, seawater) compounds (Rosa, 2006; Chiaradia *et al.,* 2006; Dreher *et al.,* 2008, Monteiro *et al.,* 2008a; Xavier *et al.,* 2008, 2009; Pestilho, 2011; Xavier *et al.,* 2010, 2012; Torresi *et al.,* 2012; Silva *et al.,* 2015; Monteiro *et al.*, 2014). However, the relative contribution of magmatic and externally-derived sources in each metallogenetic event (ca. 2.7 Ga; ca. 2.57 Ga; ca. 1.88 Ga) recorded at Carajás is still to be unraveled. In addition, the magmatic and tectonic controls that allowed episodic reestablishment of extensive hydrothermal systems still need to be understood.

3. Methods

Identification of the paragenetic evolution of the Jatobá deposit was based on detailed descriptions of cores from eight drill holes (JATD-01, JATD-02, JATD-03,

JATD-15, JATFD-21, JATFD-28, JATD-32 e JATD-33) integrated to petrographic studies under transmitted and reflect light. Analyses using a scanning electronic microscope (SEM), LEO 440I model, coupled to an Oxford Energy Dispersive X-Ray Spectrometry (EDS) were carried out in the Eletronic Microscope Laboratory of the Geoscience Institute, University of São Paulo (USP).

The mineral chemistry analysis were made in representative phases from the different stages of hydrothermal alteration using a JEOL JXA-8530F electronic microprobe equipped with five WDS and one EDS spectrometers of the Geoscience Institute, University of São Paulo (USP).

The analytical conditions consisted of voltage acceleration of 15 kV, current of 20 nA and electron beam of 5 μm of diameter, except for feldspar analysis, for which a beam with 10 μm diameter was used. The counting time was 10 s, with the exception of Al (15 s); Ca and Cr (20 s); Zn, Ba and Cu (30 s); Mn and Sr (40 s), Ni (50 s) and V (260 s). Volatile phases were included, especially Cl. The quality of the analytical procedure was verified in relation to the Smithsonian and Geller synthetic standards, under the PRZ Armstrong method (1991).

The results were treated using Excel spreadsheets of the Open University (2010), followed by adjustments for scapolite, biotite, magnetite and potassium feldspar. The WinCcac software (Yavuz et al., 2015) was used to calculate the chlorite structural formula. For amphiboles, the Excel spreadsheet presented in Locock (2014) was used, while the subsequent classification of amphiboles was done according to Hawthorne et al. (2012). For the graphical presentation of the compositional variations of these minerals, we used the Grapher 12 and Excel softwares.

4. The Jatobá iron-oxide-copper-gold (IOCG) deposit

Geological setting of the Jatobá deposit

The Jatobá deposit is located in the Southern Copper Belt, 3 km north from the Sossego Mine (Fig. 1C). It occurs within the WNW-ESSE-trending Canaã dos Carajás Shear Zone, which defines the contact between the Mesoarchean TTG orthogneisses, granitoids and greenstone belt, at south, and the Neoarchean metavolcanosedimentary units of the Itacaiúnas Supergroup.

The Jatobá deposit is mainly hosted by metarhyodacites in the footwall zone and felsic volcaniclastic-breccias, aside from amygdaloidal metabasalts associated with mafic metatuffs in the hanging wall zone. Metadiabase and gabbros crosscut all metavolcanic units (Fig. 2B). In the vicinity of the deposit, metaultramafic rocks occur close to the south contact between felsic metavolcanic rocks and the Mesoarchean orthogneisses. In addition, the metavolcanic rocks are intercepted by a Paleoproterozoic granite (Vale, 2014; Fig. 2A).

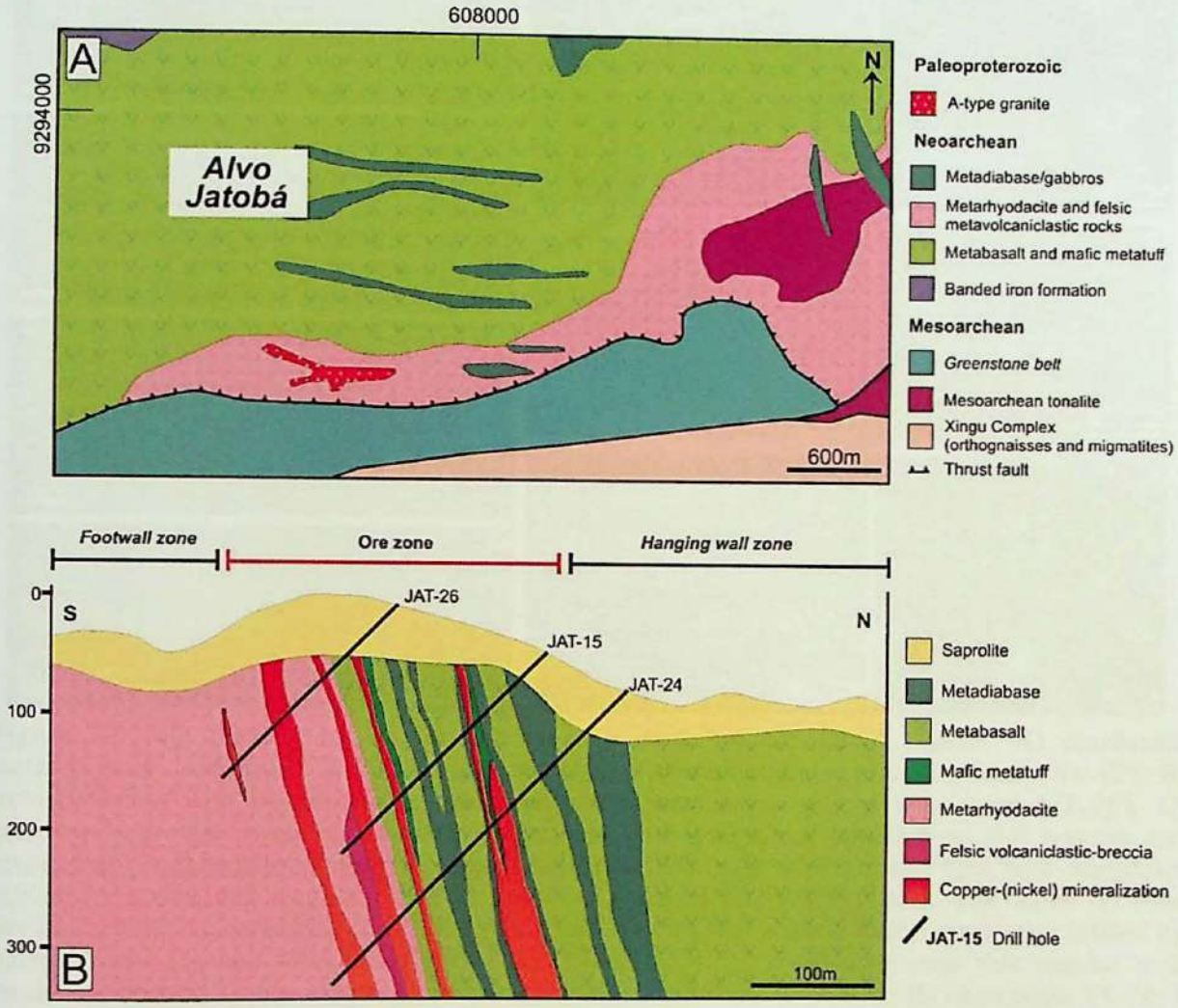

Figure 2. A) Simplified geological map showing the location of the Jatobá deposit (VALE, 2104); B) Geological cross-section of the Jatobá deposit, depicting the host rocks and copper mineralized zones (modified from VALE, 2014).

Host rocks

The least-altered metarhyodacite is light gray, fine-grained, massive and porphyritic (Fig. 3 A). Bipyramidal quartz phenocrists exhibit blue coloration, locally rounded contours, quartz overgrown over its (Fig. 3 B), and gullies and corrosion in gulf textures (Fig. 3 C). Albite-I phenocrists are also present, although they were strongly

replaced by hydrothermal minerals (e.g. biotite I; Fig. 3 C). The matrix is fine-grained, equigranular to unequigranular, and consists of quartz, albite (II), biotite (I), epidoto (I), chlorite (I) and apatite (I).

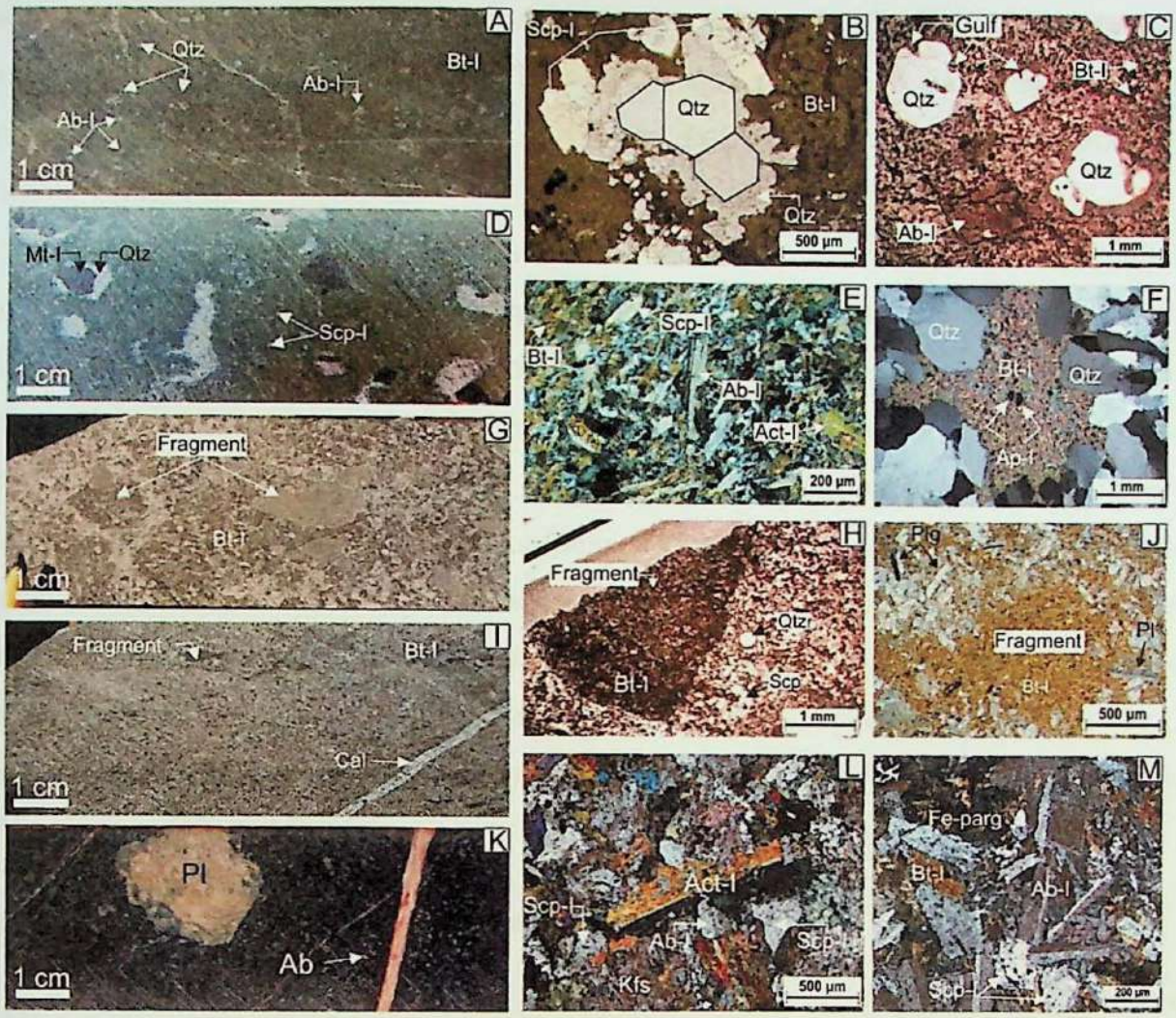

Figure 3. Main features of the least-altered host rocks of the Jatobá deposit. **A)** porphyritic metarhyodacite with quartz and albite (I) phenocrysts (transmitted light; paralell polars – TL-PP); **B)** metarhyodacite with bypiramidal quartz phenocrysts surrounded by late quartz rim (TL-PP); **C)** metarhyodacite with bypiramidal quartz phenocrysts with gullies and corrosion in gulf textures and plagioclase (I) phenocrysts strongly replaced by biotite; **D)** mafic metavolcanic rock with amygdales infilled by quartz and magnetite (I); **E)** mafic amygaloidal metavolcanic rock with albite (I) laths (transmitted light; crossed polars – TL-CP); **F)** detail of amygdale in mafic metavolcanic rock infilled by quartz, biotite (I), and subordinate apatite (I) (TL-CP); **G)** volcaniclastic-breccia with angular rock fragments replaced by fine biotite (I) in matrix composed of biotite and quartz; **H)** Idem under TL-PP; **I and J)** metatuff with fine lithic fragments replaced by biotite (I), **K)** porphyritic metadiabase with plagioclase megacrysts replaced by sericite and carbonate and cut by late albite (IV) veinlets; **L and M)** Blastosubphitic texture in metadiabase with plagioclase (albite I) replaced by scapolite (I) (TL-CP). **Abbreviations:** Qtz = quartz; Act = actinolite; Scp = scapolite; Pl = plagioclase; Bt = biotite; Ab =Albite; Mag = magnetite; Kfs = feldspar; Fe-parg = ferro pargasite; Ap = apatite.

The amydaloidal metabasalt is isotropic, aphanitic, and dark gray in color (Fig. 3 D). Intergranular and intersetal texture is composed of thin and dense ripiform albite-I crystals (Fig. 3 E), as well as relic tabular plagioclase crystals with well-developed polysynthetic twinning. The amygdales are infilled mainly by biotite, quartz and euhedric magnetite-II, in addition to smaller amounts of apatite-I (Fig. 3 F).

Metalapilli and metacrystal tuffs (Fig. 3 G and 3 I, respectively) were intensely hydrothermally altered. They are dark gray or brown due to their replacement by fine-grained biotite-I crystals, even in undeformed rocks. The metalapilli tuffs are matrix supported and have angular clasts smaller than 6 cm in diameter and intensely substituted by biotite-I (Fig. 3 H). The crystal tuff consists of more than 75% of plagioclase crystals, which are often deformed and also has fragments replaced by biotite-I (Fig. 3 J).

Metadiabase crosscut the metavolcanic and metavolcaniclastic rocks. It is dark green in color, phaneritic, fine- to medium-grained and usually isotropic (Fig. 3 K). Local porphyritic texture is made of plagioclase megacrysts strongly replaced by clinozoisite and sericite (Fig. 3 K). The subophitic and intergranular texture is characterized by the euhedral laths of plagioclase with cloudy appearance, replaced by albite-I, partially included in metamorphic actinolite-I (Fig. 3 L and 3 M). Fine magnetite-I crystals included in the actinolite denote the trellis-like texture (Fig. 7 A and 7 B). The actinolite-I has ferro-pargasite rims with strong bluish pleochroism and pale greenish cores. In turn, albite is partially to completely replaced by scapolite (Fig. 3 M). Interstitial crystals of ferro-pargasite and biotite make up the intergranular textural arrangement (Fig. 3 M).

Mylonitization within the Canaã Shear Zone

The development of the Canaã Shear Zone enables the regional fluid flow and extensive hydrothermal alteration zones with several hundred meters in the high-angle interface between the footwall and hanging wall zones. Shear features in the metarhyodacites (Fig. 4 A and Fig. 5) include mylonitic foliation, S-C pairs, almond-shaped albite or scapolite porphyroclasts involved by pressure shadows made of biotite, hastingsite (± actinolite) and quartz (Fig. 4 B), undulose extinction, subgrain formation in coronas, and grain boundary migration, which are often observed in the quartz blastophenocrysts. Quartz ribbons are present (Fig. 4 C), besides cataclasis of quartz megacrysts (Fig. 4D). (Scapolite)-actinolite-biotite mylonites are the main product of deformation of metarhyodacites within shear zones (Fig. 4 A).

In metabasalts (Fig. 4 E), magnetite replaces previous infilling minerals in amygdales and is involved by pressure shadows (Fig. 4F) composed of fine crystals of biotite, hastingsite (± actinolite) and quartz (Fig. 4G), and have asymmetric deformation tails composed of fine quartz and scapolite. Quartz and chalcedony occur as infilling of

stretched amygdales (Fig. 4 G). Scapolite-biotite-hastingsite mylonites represent strongly deformed and hydrothermally altered metabasalts.

Deformational features in metadiabase (Fig. 4 H) are represented by nematolepidoblastic texture made of hastingsite + chlorite (± actinolite), and subordinately fine sulfides, magnetite, titanite, and leucoxene (Fig. 4 I). In addition, microboudinage of these porphyroclasts and quartz ribbons are common (Fig. 4 I).

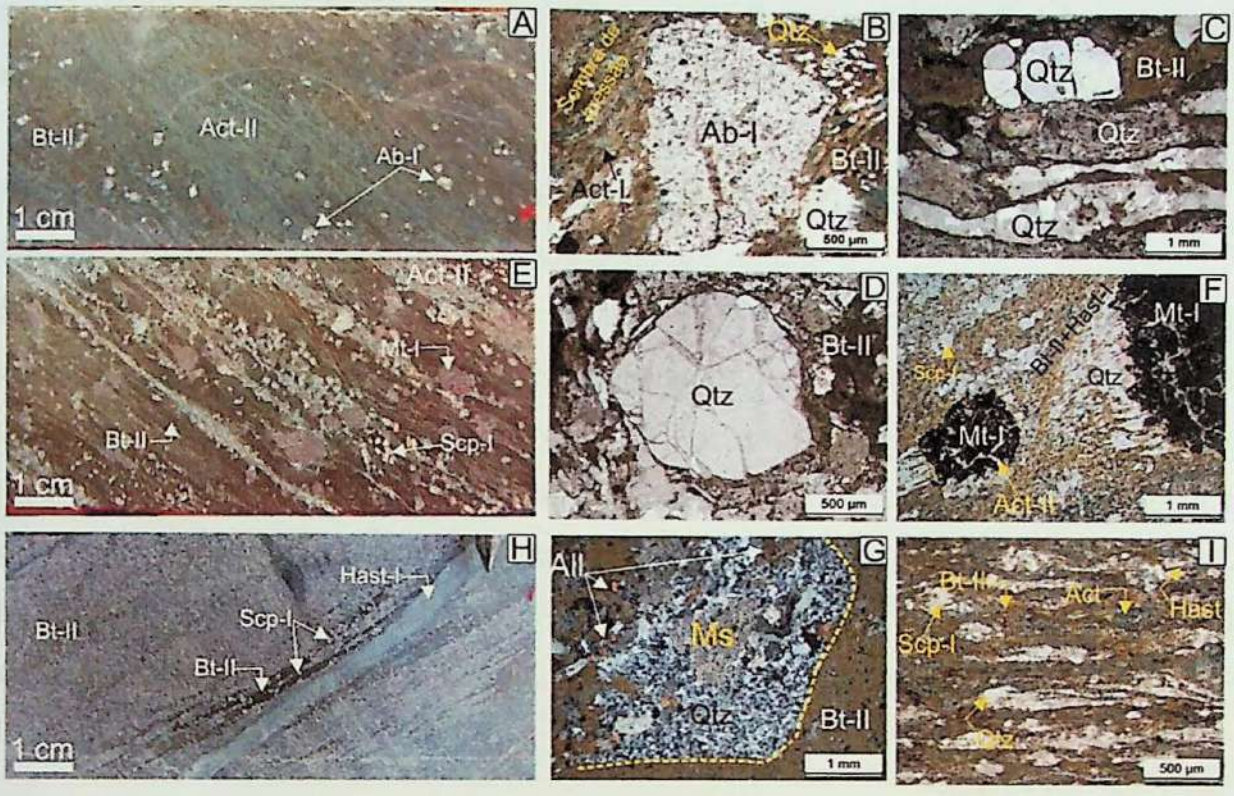

Figure 4. Macro and microscopic features of deformed and strongly hydrothermalized host rocks of the Jatobá deposit. **A to D**: features of deformed in metarhyodacite with; **A)** porphyritic metarhyodacite substituted by biotite (I) and by actinolite (II) fronts; **B)** deformed albite-I megacrystal with pressure shadow (TL-PP); **C)** preserved quartz blastophenocrysts and quartz ribbons associated with fine grained biotite (TL-PP); **D)** fractured quartz blastophenocrysts (TL-PP); **E and F:** features of deformed in amydaloidal metabasalt with; **E)** metabasalt replaced by scapolite (I) and biotite (II) and with magnetite infilling in amygdales; **F)** deformed magnetite (I) with pressure shadow in metabaslt (TL-PP); **G)** defomed quartz in recrystallized amygdale in metabasalt replaced by Cl-K-hastingsite (I) and biotite (II) (TL-PP); **H and I:** features of deformed in metadiabase with; **H)** metadiabase replaced by fine biotite (I) and scapolite (I) with overprinting of biotite (II) and hastingsite (I); **I)** quartz ribbons in foliated metadiabase, in which the subophitic texture was strongly obliterated (TL-PP). **Abbreviations:** Qtz = quartz; Act = actinolite; Cl-K-hast-I = hastingsite; Scp = escapolite; Bt = biotite; Ab = albite; Ms = muscovite; Mag = magnetite.

Hydrothermal alteration

Hydrothermal alteration was strongly controlled by the shear zone (Fig. 5), however strongly pervasive alteration was also developed in isotropic rocks.

Proximal and distal hydrothermal alteration halos towards copper mineralization zones, recurrence of alteration stages and telescoping were observed.

The hierarchy of hydrothermal alteration stages and paragenetic evolution was established on the basis of the relationship between mineral blastesis and microstructures, considering pre-, syn, and post-shearing structures (Fig. 5; Fig. 14).

EARLY PRE-SHEARING HYDROTHERMAL ALTERATION

Silicification associated with biotite, magnetite and apatite

In the undeformed metabasalts (Fig. 6 A), quartz occurs as infilling of amygdales associated with biotite (I), euhedral to subeuhedral magnetite (II; Fig. 7 C and D) and Cl-apatite (I) assemblage (Fig. 6 B to 6 D). In isotropic metabasic rocks, such as metadiabase, incipient silicification was accompanied by alteration of the magmatic magnetite (II), resulting in ilmenite lamellae replaced by leucoxene with a trellis texture. In the metarhyodacite, a similar mineral association (quartz-biotite-magnetite-apatite) was developed in pervasive alteration fronts that replace the rock matrix and occur as infills (Fig. 4 C).

Sodic alteration

Formation of albite (Ab - I): Sodic alteration is recognized in all host rocks and confers differentiated staining depending on the host rock nature: whitish pink in metabasic rocks and intense pink color in metarhyodacites, possibly due to the presence of very fine inclusions of hematite. The sodic alteration is well developed and selective. Cloudy albite occurs exclusively as replacement of preexisting igneous feldspars with geminate texture (Fig. 6 F to 6 G). In rocks affected by weak sodic alteration, the recognition of subophitic texture in metadiabase (Fig. 6 F to 6G) and porphyritic character of metarhyodacites is still possible (Fig. 6 J and 6K), even after the albite (I) formation. In the latter, however, pervasive fronts with clear subdioblastic albite-(quartz) are also common.

Scapolite formation (Scp I): Scapolite alteration comprises one of the most extensive types of hydrothermal alteration in the host rocks of the Jatobá deposit.

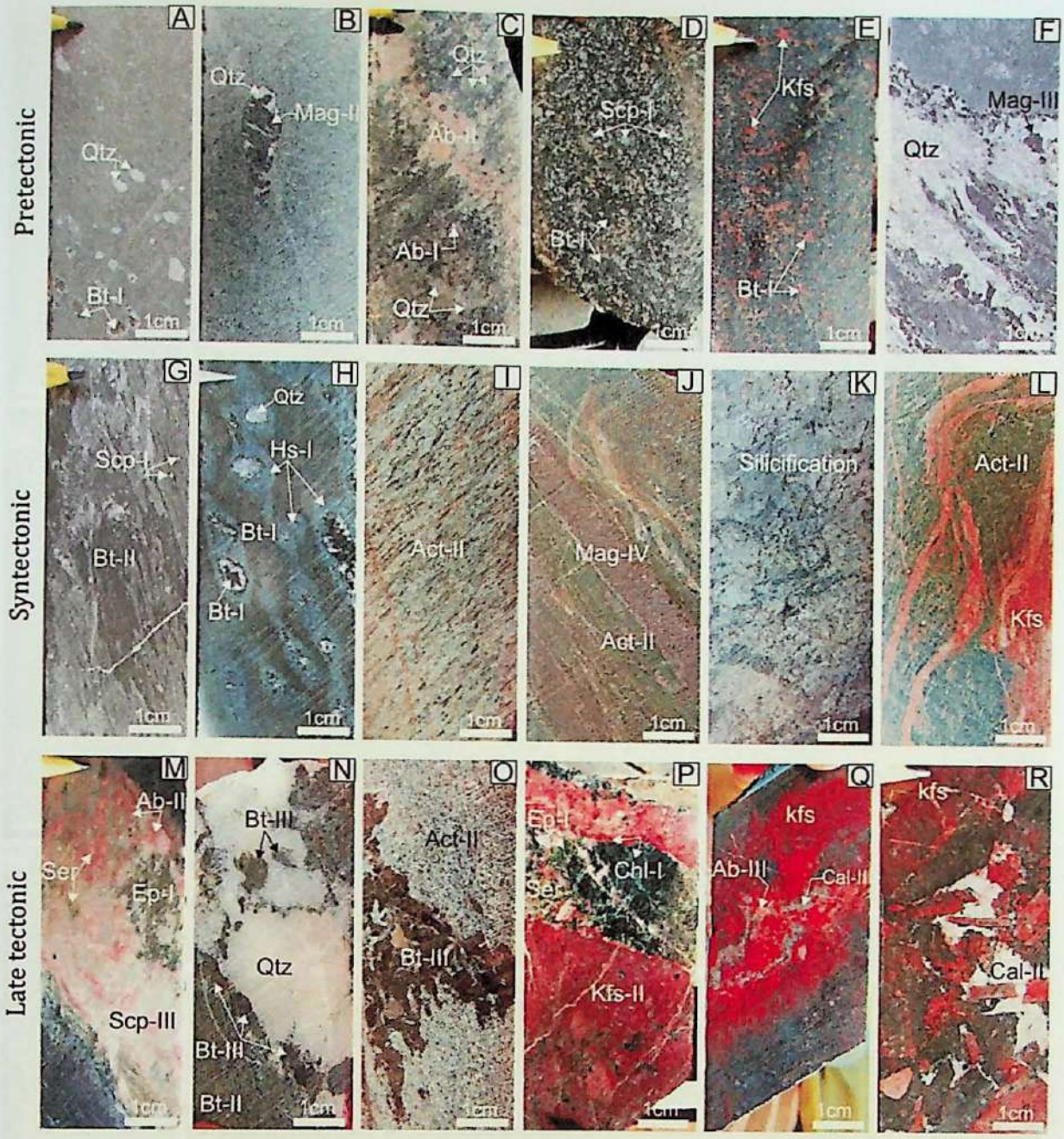

Figure 5. Distribution of pre-, syn-, and post-shearing types of hydrothermal alteration in the Jatobá deposit. A to F: features in isotropic rocks; **A)** metabasalt with amygdales infilled by quartz and partially replaced by biotite (I); **B)** amygdales with quartz and magnetite (II) that replace original infilling in metabasalt; **C)** Albite (II) alteration fronts in metarhyodacite; **D)** scapolite (I) and biotite (I) in metadiabase; **E)** K-feldspar replaces previous sacpolite (I) in metadiabase; **F)** quartz-magnetite vein in the metadiabase; G to L: hydrothermal alteration controlled by mylonitic foliation; **G)** metabasalt replaced by biotite (II) and scapolite; **H)** foliated amygdaloidal metabasalt with hastingsite (I) developed along the mylonitic foliation; **I)** metadiabase replaced by magnetite and hastingsite; **J)** metarhyodacite strongly replaced by actinolite (II); **K)** silicification associated with actinolite (II) in the metarhyodacite; **L)** metadiabase with potassic alteration with K-feldspar; M to R: fissural-controlled alteration; **M)** Vein infilled by fibrous scapolite (III) partilaly replaced by albite, epidote and sericite in the metadiabase; **N)** quartz vein with coarse biotite in the metadiabase (III); **O)** Metarhyodacite replaced by actinolite (II) and thereafter by coarse green biotite (III); **P)** chlorite (II) veinlets cut previous potassic alteration zone in the metarhyodacite; **Q)** potassic alteration with K-feldspar with intense red colour due to tiny hematite inclusions crosscut by calcite; **R)** breccia with fragments of potassic-altered rock involved by calcite. **Abbreviation:** Qtz = quartz; Act = actinolite; Cl-K-hast-I = hastingsite; Scp = scapolite; Bt = biotite; Ab = albite; Mag = magnetite.

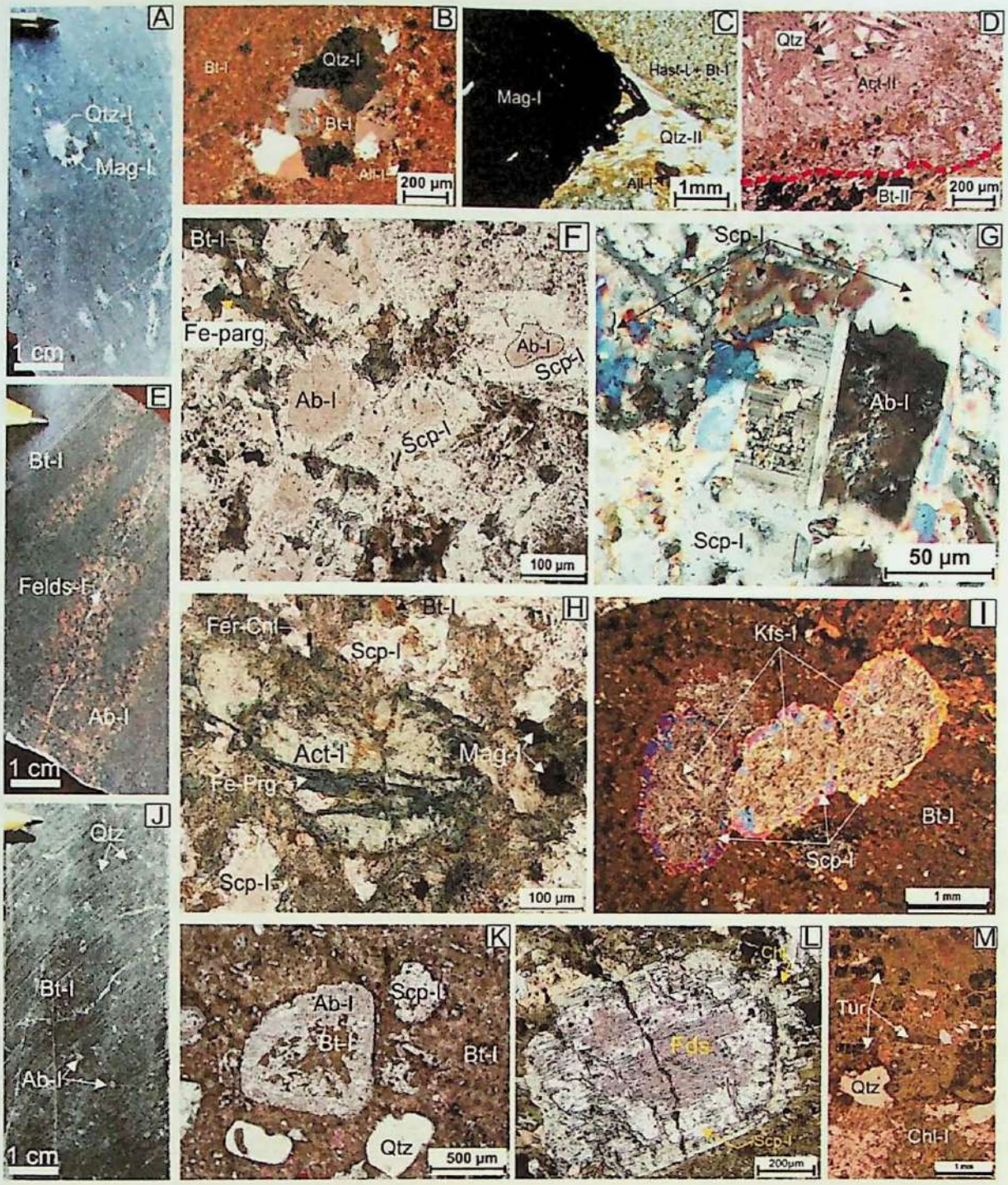

Figure 6. Main early pre-tectonic hydrothermal alteration in the Jatobá deposit. **A to D)** amydaloidal metabasalt with: **A)** amygdale infilled by quartz (I) and magnetite (I); **B)** pervasive potassic alteration with biotite (I) and amygdale with quartz and biotite (I); **C)** magnetite with pressure shadow in amygdale (TL-PP); **D)** actinolite (II) in amygdale (TL-PP); **E)** metadiabase with pervasive potassic alteration with biotite (I) and fissural albite (I) and K-feldspar (I) alteration; **F and G)** albite (I) in metadiabase partially replaced by scapolite (I) (TL-PP and TL-CP); **H)** Ferro-pargasite associated with scapolite (I) replacing actinolite (I) in metadiabase (TL-PP); **I)** previous albite (I) porphyroblasts replaced by scapolite (I) and K-feldspar (I) (TL-CP); **J and K)** porphyritic metarhyodacite with plagioclase and quartzo phenocrysts in matrix composed of fine biotite (I) (TL-PP); plagioclase was partially replaced by albite (I), scapolite (I) and biotite; **L)** metarhyodacite with scapolite (I) replaced by K-feldspar in its core and by chlorite in the rims (TL-PP); **M)** metarhyodacite with tourmaline associated with biotite (I) (TL-PP). **Abbreviations:** Qtz = quartz; Act = Actinolite; Cl-K-Hast-I = Cl-K-hastingsite; Scp = scapolite; Bt = Biotite; Ab = Albite; Mag = Magnetite.

This alteration type gives to the affected rocks a whitish to light cream color (Fig. 6 E). Scapolite (I) initially occurs on the edges of the cloudy albite (I) crystals. Locally, only albite cores involved by scapolite are recognized (Fig. 6 F and 6 G). In pervasive alteration zones, scapolite occurs as rounded, milimetric to sub-centimetric (up to 0.6 cm) porphyroblasts with irregular or reentrant rims or as amoeboid-shaped crystals dispersed in the matrix of rocks.

Sodic-calcic alteration

Ferro-pargasite formation: Ferro-pargasite is recognized in least-altered metadiabase portions. It has intense bluish pleochroism and occurs as fine crystals with pseudo-prismatic, replacing the borders of the metamorphic actinolite (act - I) (Fig. 6 H). It also occurs on the borders of scapolite (I) crystals.

Potassic alteration

Formation of biotite (Bt I): The initial formation of biotite (I) was coeval to silicification and associated magnetite-apatite formation. Biotite (I) is commonly recognized in metabasalts as infilling of old vesicles (Fig. 3 F and 6 B), which commonly occurs as infillings of amygdales. However, biotite (I) formation extended for longer and biotite also represents the main hydrothermal mineral phase in extensive alteration zones with weak silicification. Brown biotite occurs associated with subordinated magnetite (I), quartz, Ce-allanite (I), Cl-apatite (I), K-feldspar, and tourmaline (Fig. 6 M). In metadiabase, biotite (I) occurs as thin aggregates that replace actinolite (I) crystals (Fig. 6 H). In the metarhyodacites, biotite fronts replace the matrix, formerly substituted by silicification-biotite-magnetite-apatite. It also replaces partially albite megacrystals (Fig. 6K).

In the metarhyodacites, subdioblastic, fine to medium tourmaline crystals are associated with biotite (I; (Fig. 6M). Zoned crystals have brown rims with green-bluish cores, but crystals without zoning are predominantly dark green and/or brown (Fig. 6 K).

Formation of potassic feldspar: In metadiabase, K-feldspar is formed in expenses of the nuclei of the preexisting scapolite crystals (Fig. 6 I and 6 L), whereas in the metarhyodacite replacement of the pseudomorphic albite megacrysts is commonly observed, with remarkable association with allanite, clinozoisite and chlorite (I).

Potassic alteration fronts are composed of fine aggregates of K-feldspar crystals with a cloudy appearance, giving the rock an intense reddish-pink color due to tiny hematite inclusions.

Formation of early vein magnetite (Mt III + quartz): Veins and veinlets with coarse magnetite crystals and quartz (up to 1.5 cm) crosscut foliated and intensely altered rocks (Fig. 5 F). Superposed deformation is evidenced by the recrystallized texture of quartz and by microfraturation in both minerals. The veins are also composed of titanite (Tit - I), chlorite (Chl - II), fine adularia and ilmenite (Ilm - I) crystals. The latter is commonly replaced by titanite (Tit - II) and hematite, besides subordinate brookite/rutile and pseudobrookite. The coarse magnetite crystals exhibit, according to different crystallographic planes, distinct lamellae composed of ilmenite and hercinite. Fine chalcopyrite crystals occur as inclusions in the magnetite (Fig. 7 E and F).

Formation of Chlorite: The development of chlorite in the Jatobá deposit is recognized in all host rocks and is responsible by their characteristic green colour. Chlorite (I) replaces amphibole, scapolite, K-feldspar and biotite, even in least-deformed rocks (Fig. 8 C).

MAIN SYN-SHEARING HYDROTHERMAL ALTERATION

Sodic-(calcic) alteration (II)

Formation of scapolite (Scp - II): Scapolite (II) occurs on the borders of previous stretched porphyroclasts of scapolite (I), which has cores strongly replaced by K-feldspar and chlorite. This scapolite generation differs from the first due to its mode of occurrence and clear appearance (Fig. 8 B and C). The mineral was distinguished by its elevated refractive index and birefringence, and has composition intermediate in relation to that of the marialite-meionite end-members. In mylonitic rocks, scapolite (I) frequently behaves as porphyroclasts with pressure shadows composed of K-Cl-hastingsite and biotite, both conforming to each other (Fig. 8B, C).

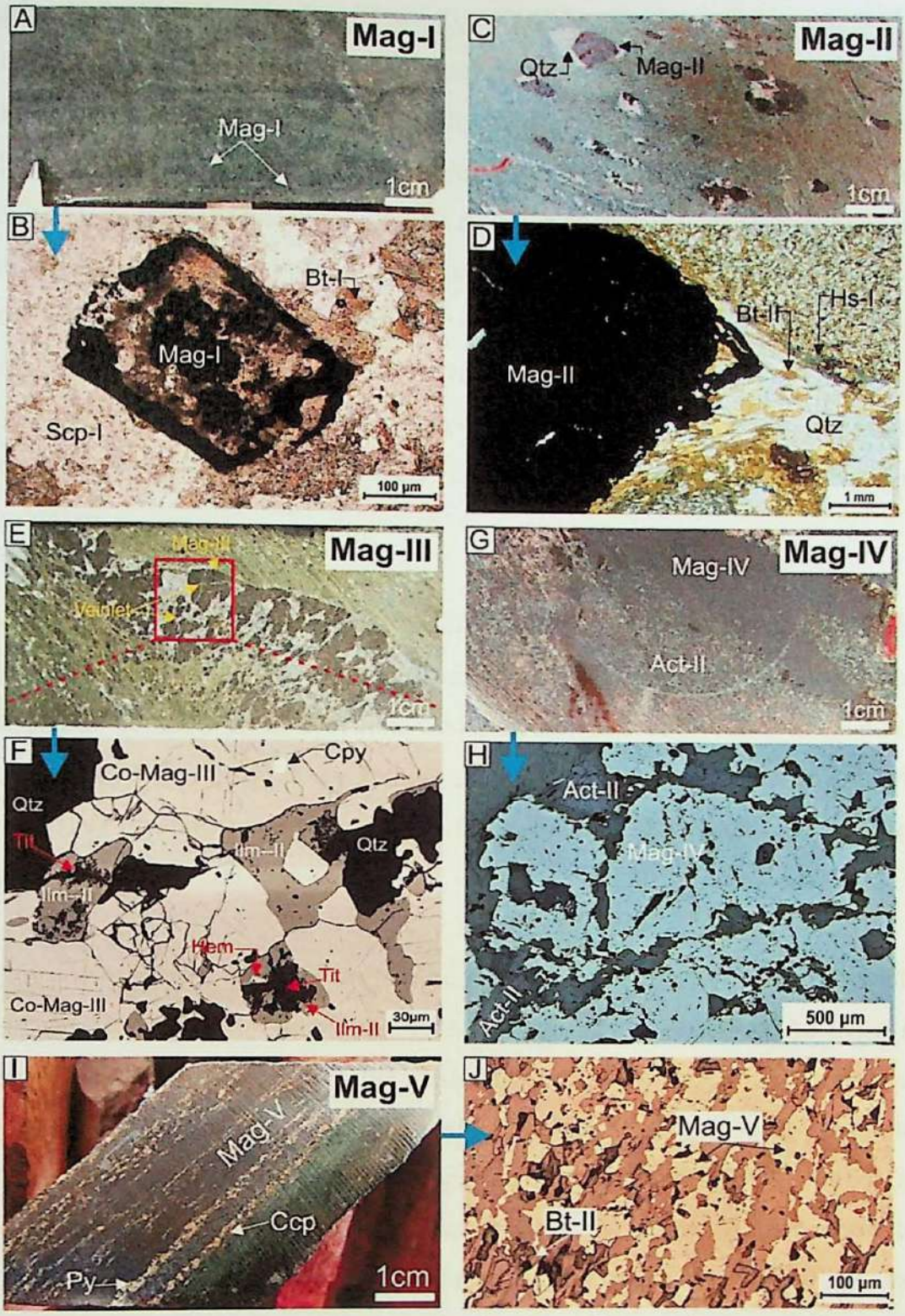

Figure 7. Distinct magnetite generations identified in the Jatobá deposit. A and B) magnetite in metadiabase; **A)** metadiabase with fine-grained magnetite (I); **B)** Igneous magnetite (I) partically altered in metadiabase; C and D) magnetite in metabasalt; **C)** Metabasalts with amygdale infilled by magnetite (II) and quartz; **D)** Metabasalts with amygdale infilled by magnetite (II) with pressure shadow composed of quartz (TL;CP); E and F) magnetite in metarhyodacite; **E)** Vein with coarse-grained euhedral to subhedral magnetite (III) and quartz; **F)** SEM image showing Co-rich magnetite (V) crystals with thin ilmenite lamellae cut by quartz and ilmenite, which is turn partilally replaced by titanite-hematite; G and H) magnetite in metarhyodacite; **G)** pervasive magnetite (IV) replacement front involved by actinolite (II); **H)** SEM image showing actinolite (II), apatite (II) and magnetite (IV); I and J) magnetite in metarhyodacite; I) syn-tectonic magnetite (V) associated with chalcopyrite and pyrite in metarhyodacite; **J)** syn-tectonic magnetite (V) and biotite (II). **Abbreviations:** Abbreviation: Qtz =quartz; Act = actinolite; Hs = hastingsite; Scp = scapolite; Bt = biotite; Mag = magnetite; Ilm = ilmenite; Ccp = chalcopyrite; Ttn = titanite; Hem = hematite.

Formation of Cl-K-hastingsite (Hs- I): Cl-K-hastingsite (I), associated with subordinated biotite, is recognized in mylonitic rocks in the hanging wall zone of the Jatobá deposit. It was developed mainly in hydrothermally altered mafic protoliths, both metadiabase and basalts, giving a green-bluish color to these rocks (Fig. 8 A and D, respectively). Its formation along mylonitic foliation in metarhyodacites is incipient. Cl-K-hastingsite (I) crystals have blue and bluish green pleochroism, prismatic habit, contacts with each other rectilinear and orientation along the mylonitic foliation, resulting in nematoblastic or decussate texture (Fig. 8 E and F). Locally Cl-K-hastingsite (I) crystals represent pseudomorphs after scapolite (I) and commonly are recognized in shadow pressures and deformational tails around scapolite (I) porphyroclasts.

Iron enrichment (Massive magnetite bodies - Mt IV): Massive magnetite bodies represent proximal envelopes of mineralized zones and are well develop along the contact zones between metarhyodacites and metabasalts and within the latter. The magnetitite may reach up to 60 m and is composed of coarse euhedral to subeuhedral magnetite (IV) crystals, commonly cut by fibrous actinolite (II) and apatite (Fig. 7 G and 7H).

Formation of Actinolite (Act II): Actinolite (II) is formed mainly in the footwall zone and replaces the mylonitic metarhyodacites, giving a greenish colour to these rocks. (Fig. 8 G). Bundles of fibrous and fine actinolite crystals associated with apatite define the mylonitic foliation (Fig. 9 G and H). Actinolite (II), associated with Cl-apatite (II), Ce-allanite (III), crosscut the massive magnetite (IV) zones (Fig. 9 G and H) and is closely related with the initial mineralization stage at Jatobá. Rare occurrences of fibrous actinolite (II) were identified in the metabasic rocks, notably in metabasalts, infilling older amygdales (Fig. 6 D; 8 J).

Formation of hornblende: Hornblende crystals are observed in metabasic rocks. They occur as euhedral crystals oriented along the mylonitic foliation with strong dark green and pale yellow pleochroism. Cummingtonite and magnesio-ferri-hornblende have also been identified in zones with well-developed Cl-K-hastingsite (I), but their occurrence is quite subordinate.

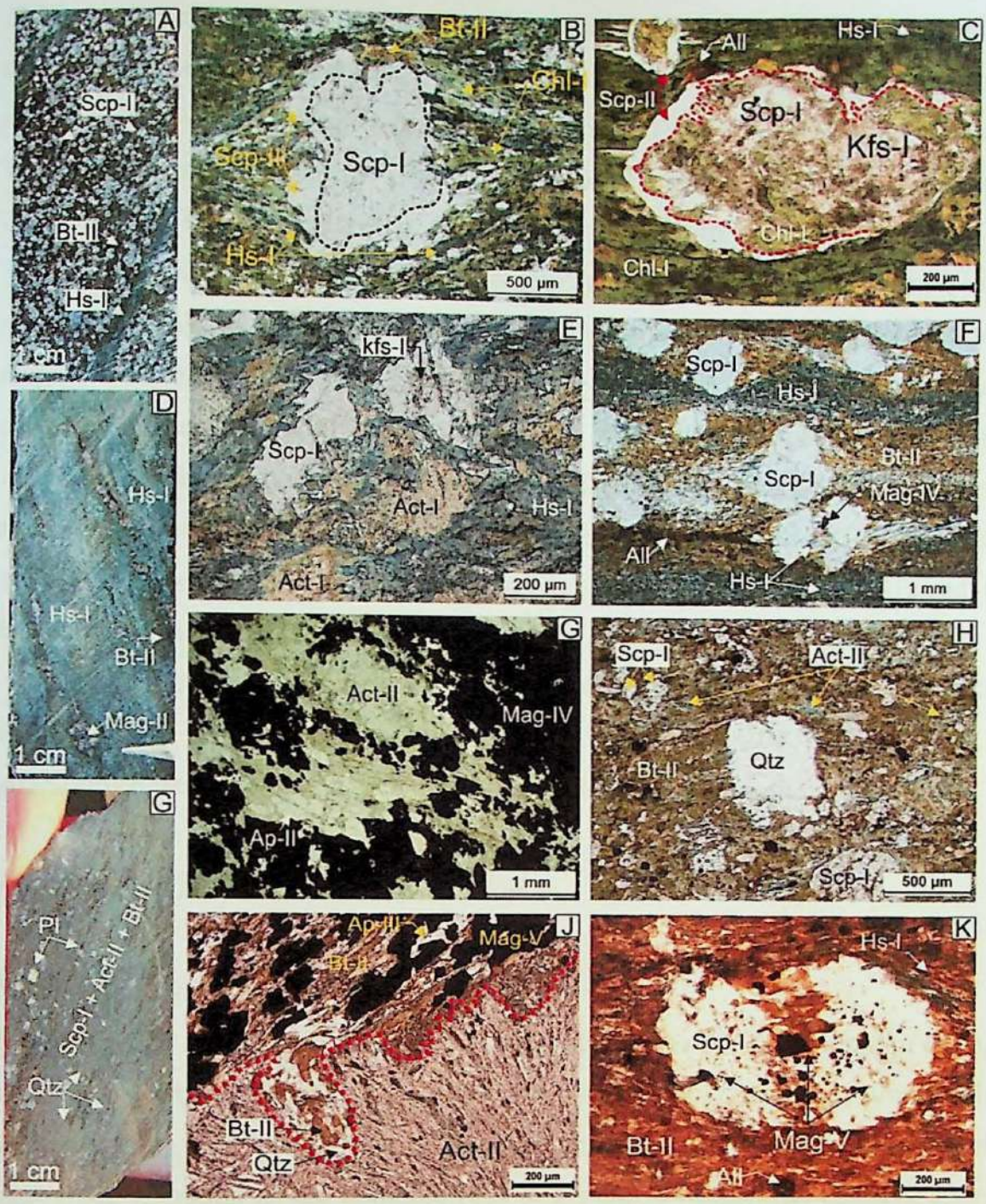

Figure 8. Main features of syn-tectonic hydrothermal alteration in the Jatobá deposit. **A to C**: metadiabase with sodic-calcic and potassic alteration; **A)** replacement of foliated metadiabase by biotite (II), hastingsite and scapolite (I); **B)** deformed scapolite (I) porphyroblast with scapolite (II) in its rim and pressure shadow with hastingstite (I) and quartz (TL-PP); **C)** clear scapolite (II) on the border of a stretched scapolite (I) crystal; scapolite (I) was replaced by K-feldspar and chlorite (TL-PP); **D to E**: metabasalt with sodic-calcic and potassic alteration; **D)** foliated metabasalt with stretched amygdales infilled by biotite (I) and quartz and mylonitic foliation defined by biotite (II) and Cl-K-hastingsite (I); **E)** Cl-K-hastingsite (I) involves and replaces previous actinolite (I) (TL-PP); **F)** scapolite (I) porphyroblasts with pressure shadow and foliation defined by Cl-K-hastingsite (I) and biotite (II) (TL-PP); **G to K**: porphyritic metarhyodacite; **G)** magnetite-rich rock replaced by actinolite (II) and apatite (II); **H)** Biotite (II) along the mylonitic foliation and relicts of actinolite (II) in the porphyritic metarhyodacite with deformed quartz blastophenocryst (TL-PP); **I)** deformed scapolite (I) porphyroblasts partially or totally replaced by euhedral hornblende and Cl-K-hastingsite (TL-PP); **J to K**: intense potassic alteration; **J)** metabasalt with amygdales infilled by actinolite (II) and mylonitic foliation defined by biotite (II), magnetite (IV), apatite (III) e ± quartz; **K)** boudin neck in scapolite (I) infilled by biotite (II) and magnetite (IV). **Abbreviation:** Qtz = quartz; Act = actinolite; Cl-K-hast-I = Cl-K-hastingsite; Scp = scapolite; Bt = biotite; Ab = albite; Mag = magnetite.

Potassic alteration (II) (Bt II and Kfs): The potassic alteration (II) is widespread in all the host rocks at Jatobá, including the metavolcaniclastic lithotypes. Pervasive fronts of potassic alteration (II) overprint the previous sodic and sodic-calcic (II) alteration zones. The mineral assemblage of the potassic alteration (II) comprises Cl-biotite (II), quartz, Co-magnetite (IV), Cl-apatite (III), and Ce-allanite (III) (Fig. 8 J and K).

Cl-biotite (II) has dark brown to reddish color, occurs in aggregates of fine anhedral crystals, and defines a lepidoblastic texture along the mylonitic foliation. Co-magnetite-IV grains have fine ilmenite inclusions on their edges. Allanite commonly occurs as coarse euhedral to subeuhedral crystals with strong compositional zoning.

This mineral association is also recognized in crystallization tails in pressure shadows, narrow subgrain mats, as well as ribbons and millimeter infills. Additionally, a distinct potassic alteration (II) assembly represented by Cl-biotite (II) and Cl-K-hastingsite (I) and quartz occurs preferentially in the mylonitized metabasic rocks.

Potassic alteration with K-feldspar is also partially controlled by mylonitic foliation (Fig. 5 L) and overprints alteration zones with Cl-K-hastingsite (I). This alteration confers intense red colour to the rock due to tiny hematite inclusions.

LATE HYDROTHERMAL ALTERATION

Sodic-calcic alteration (III)

Scapolite (III): Scapolite (III) occurs in thick veins (up to 1 m) composed of large, well developed prismatic or fibrous crystals, white to slightly creamy in colour, sectioning foliated rocks and previous hydrothermal alteration zones (Fig. 9 A). Incipient retrograde alteration of the scapolite (III) to sericite, pyrophyllite, chlorite, albite and carbonate (Fig. 9 B). In addition, these veins represent proximal regions in relation to the mineralized intervals associated with chloritization, which are characterized by chalcopyrite associated with chlorite-epidote ± albite ± calcite ± feldspar. Often these thick veins are crosscut by late veinlets with coarse crystals of biotite (III; Fig. 9 C).

Formation of Scapolite (IV) and Cl-K-Hastingsite (II): Late veinlets infilled by scapolite (IV) and Cl-K-hastingsite (II) and biotite (III; Fig. 9 D) replacement fronts with fibrous scapolite (III; (Fig. 9 F). Both minerals are oriented parallel to the veinlets walls. Cl-K-hastingsite (II) is prismatic and has dark blue to purple pleochroism.

Potassic alteration III and late alteration stages:

Formation of biotite (Bt III): The biotite (III) difers from the previous biotite generations due to its coarser crystals, paler brown or green colour, and occurrence in late barren or mineralized veins. Green biotite, scapolite (IV) and Cl-K-hastingsite (II) also occurs associated, cutting those areas of fibrous escapolite (III) veins (Fig. 9 E and 9 F). Veinlets composed of quartz, albite (IV) and fibrous-radiated stilpnomelane crystals are also identified (Fig. 9 G to 9 H). Fine late carbonate (III) veinlets cut all these veins (Fig. 9 I).

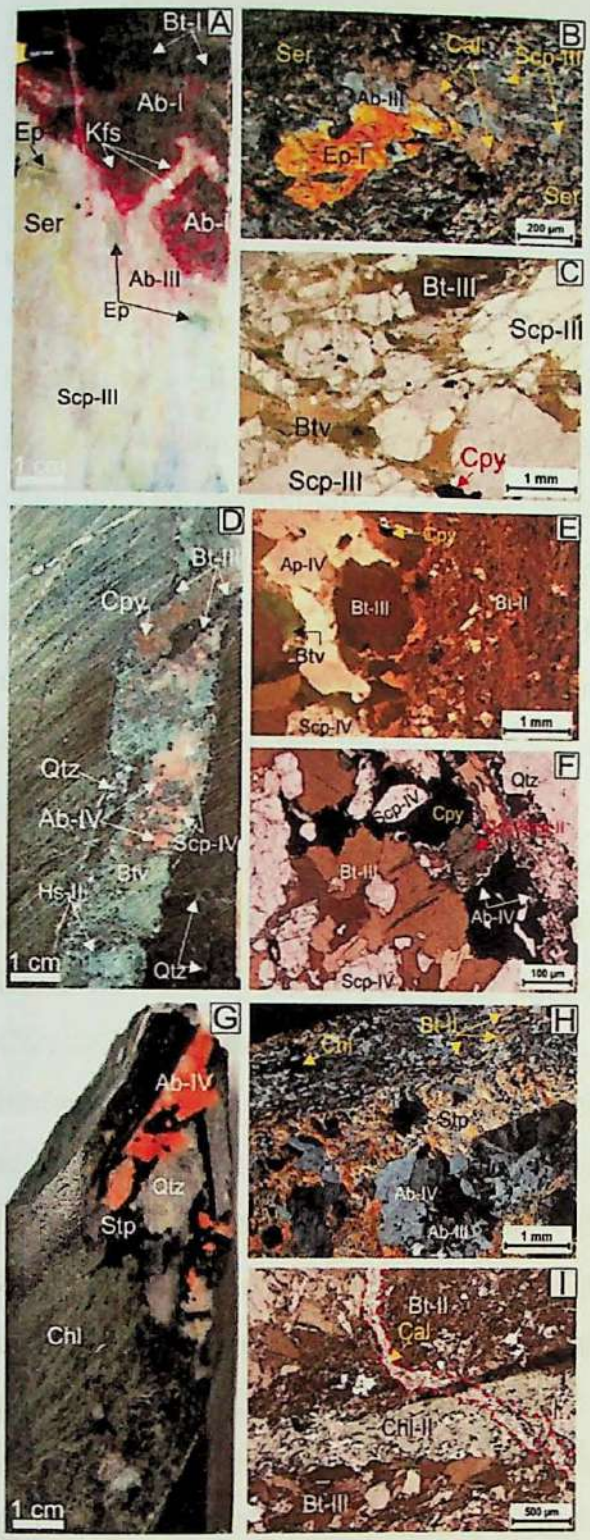

Figure 9. Main features of late tectonic hydrothermal alteration in the Jatobá deposit; **A to E**: porphyritic metarhyodacite; **A)** fibrous scapolite (III) vein with albite (II) and Kfeldspar in its rims; scapolite has retrograde alteration to sericite and epidote; **B)** scapolite (III) replaced by sericite, epidote (I) and carbonate (II); TL-CP); **C)** Brecciated scapolite (III) crystals associated with biotite (III) infill (TL-PP); **D)** vein infilled by Cl-K-hastingsite, biotite (III), albite (IV), scapolite (IV) and chalcopyrity; **E)** veinlet infilled by biotite (III), apatite (IV) and scapolite (IV) cutting the rock previouly replaced by biotite (II) (TL-PP); **F)** veinlet infilled by biotite (III), scapolite (IV), quartz and chalcopyrite (TL-PP); **G to I:** chlorite alteration in metabasalt; **H)** veinlet with quartz, stilpnomelane and albite (IV) cutting chlorite-rich zones (IV); **H)** detail of **G)** showing the stilpnomelane-albite (IV) association (TL-CP); **I)** late chlorite (II) alteration front replaces fine biotite (II) and coarse biotite (III) and thereafter cut by late calcite (II) veinlets (TL-PP). **Abbreviation:** Qtz =quartz; Hs = hastingsite; Scp = scapolite; Bt = biotite; Ab = albite; Ccp = chalcopyrite; Chl = chlorite; Stp = stilpnomelane; Cal = calcite; Ser = sericite; Ep = epidote; Kfs = K-feldspar.

Formation of K-feldspar: K-feldspar represents an infill of late veinlets and barren or mineralized veins. The K-feldspar has cloudy appearance, giving the rock an intense red color due to tiny hematite inclusions.

Formation of Chlorite: Chlorite (II) occurs in pervasive alteration fronts and veinlet systems crosscutting previously altered rocks (Fig. 9 I).

Calcite Formation: Calcite occurs in late veinlets that intercepts rocks with potassic (Bt II and Bt III – Kfs II) and chlorite alteration (II; Fig. 9 I) and in the matrix of breccias with fragments of potassic-altered rock.

Copper-gold mineralization

The copper-gold mineralized zones recognized in the Jatobá deposit comprise swarms of vertical to subvertical orebodies, with thicknesses ranging from 1.3 to 18.4 m. Mineralization styles include disseminations and massive ore in replacement fronts controlled by the mylonitic foliation, hydrothermal breccias, as well as stockworks, vein and veinlet systems. Spatial relationship among metadiabase dikes, contact between rhyodacites and metabasalts, and mineralized zones is documented at Jatobá. The mineralized zones, however, were formed in four distinctly temporally separated episodes, coeval to ductile and ductile-brittle deformational events (Fig. 10).

Mineralization (I) - (Min - I/Act - II): The initial mineralization stage at Jatobá (Fig. 10 A to 10 C; 11 A to E) was related to sodic-calcic alteration (II), especially to actinolite (II) formation in metarhyodacites controlled by the development of the Canaã dos Carajás Shear Zone (Fig.11 B and 11 C). Actinolite (II) conforms to massive magnetite bodies, sometimes promoting local brecciation in these bodies, evidencing its posterior temporal relation with these bodies (Fig. 11 D and 11 E). Actinolite (II) commonly occurs associated with coarse crystals of Cl-apatite (II), in addition to replacement fronts composed of Ni-pyrrhotite and Ni-pyrite, and subordinately, Co-chalcopyrite, Ce-allanite (II), Co-pentlandite, quartz and, Ce-monazite, which make up the ore paragenesis of this stage (Fig. 11 B to 11 E). Co-pentlandite occurs as probable exsolution lamellae in Ni-pyrrhotite. In addition, fine Ni-pyrrhotite crystals, actinolite (II), magnetite (IV) and subordinate quartz constitute replacement fronts and brecciated zones with up to 40 cm.

Mineralization II (Min - II/Bt - II): The second copper mineralization stage is temporal and spatially related to the development of the potassic alteration (II), which pervasively and indiscriminately affects the main host rocks of the Jatobá deposit (Fig. 10 D to 10 F; 11F to 11J). It was also related to the development of the Canaã Shear Zone. Mineralized zones are developed in portions were biotite (II) was formed at the expense of actinolite (II) in mylonitic rocks.

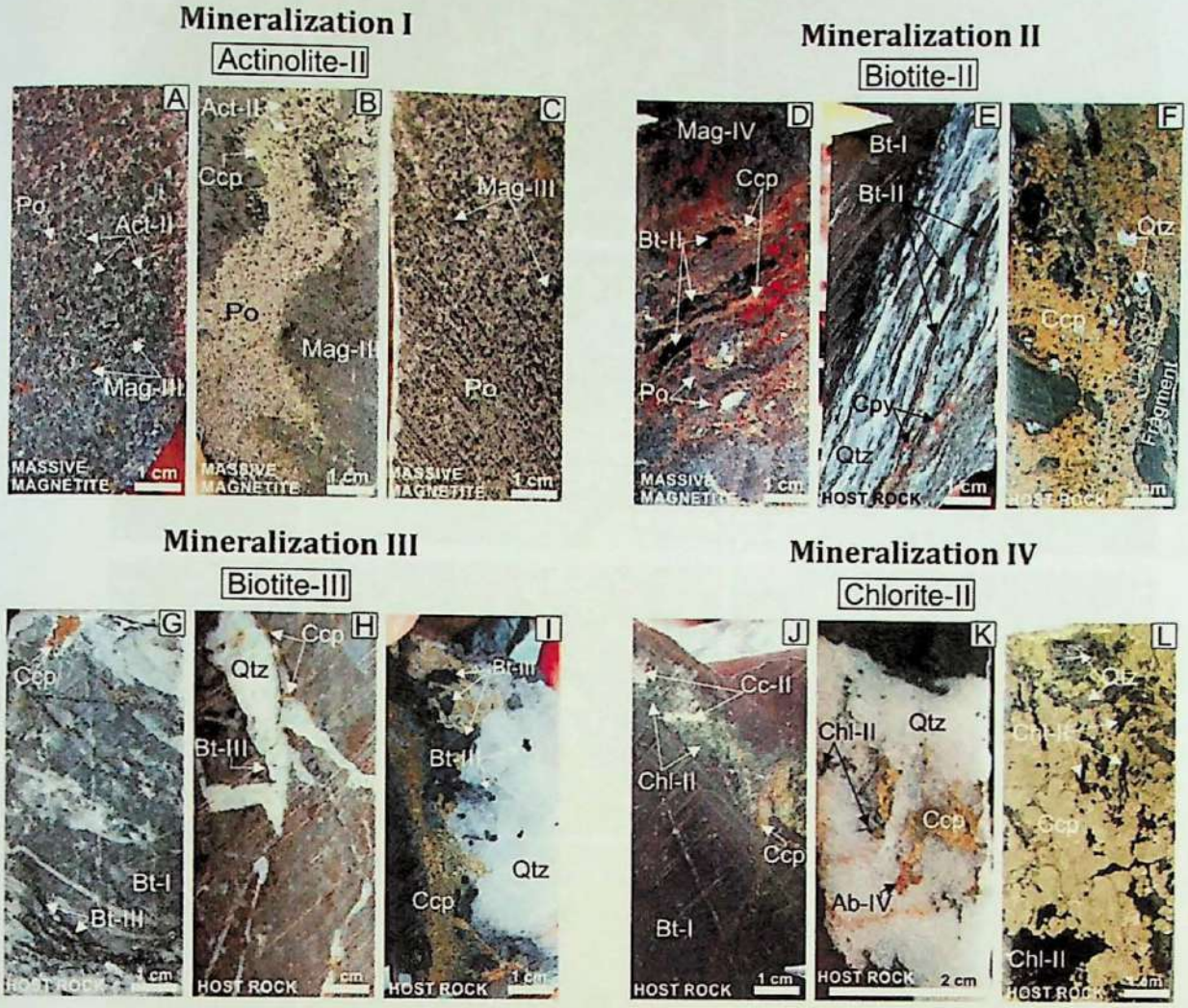

Figure 10. Distribution of the main macroscopic features of the different mineralization stages and styles of the Jatobá deposit. **A to C:** first mineralizing stage with progressive increase of pyrrhotite contents from: **A)** massive magnetite replaced by pyrrhotite and subordinate chalcopyrite and actinolite (II); **B)** massive magnetite with replacement front composed of pyrrhotite and subordinate chalcopyrite and actinolite (II); **C)** breccia with fragments of magnetite (III) and matrix of pyrrhotite; D to F: second mineralization stage; **D)** massive magnetite (III) cut by front with chalcopyrite, pyrrhotite, biotite (II) and minor quartz controlled by mylonitic foliation; **E)** chalcopyrite associate with quartz and biotite (II), which defines the mylonitic foliation; **F)** breccia with matrix composed of chalcopyrite, biotite (II) and quartz and fragments of metarhyodacite replaced by biotite (I); **G to I:** third mineralizing stage with veins and veinlets infilled by chalcopyrite associated with biotite (III) and quartz; **J to L:** fourth mineralizing stage represented by veins and breccias; **J)** veinlet infilled by chalcopyrite, chlorite (II), quartz and calcite; **K)** quarz vein with chalcopyrite and subordinate chlorite and albite; **L)** vein infilled by chalcopyrite, chlorite (II) and quartz. **Abbreviation:** Qtz = quartz; Bt = biotite; Ab = albite; Mag = magnetite; Ccp = chalcopyrite. Po = pyrrhotite.

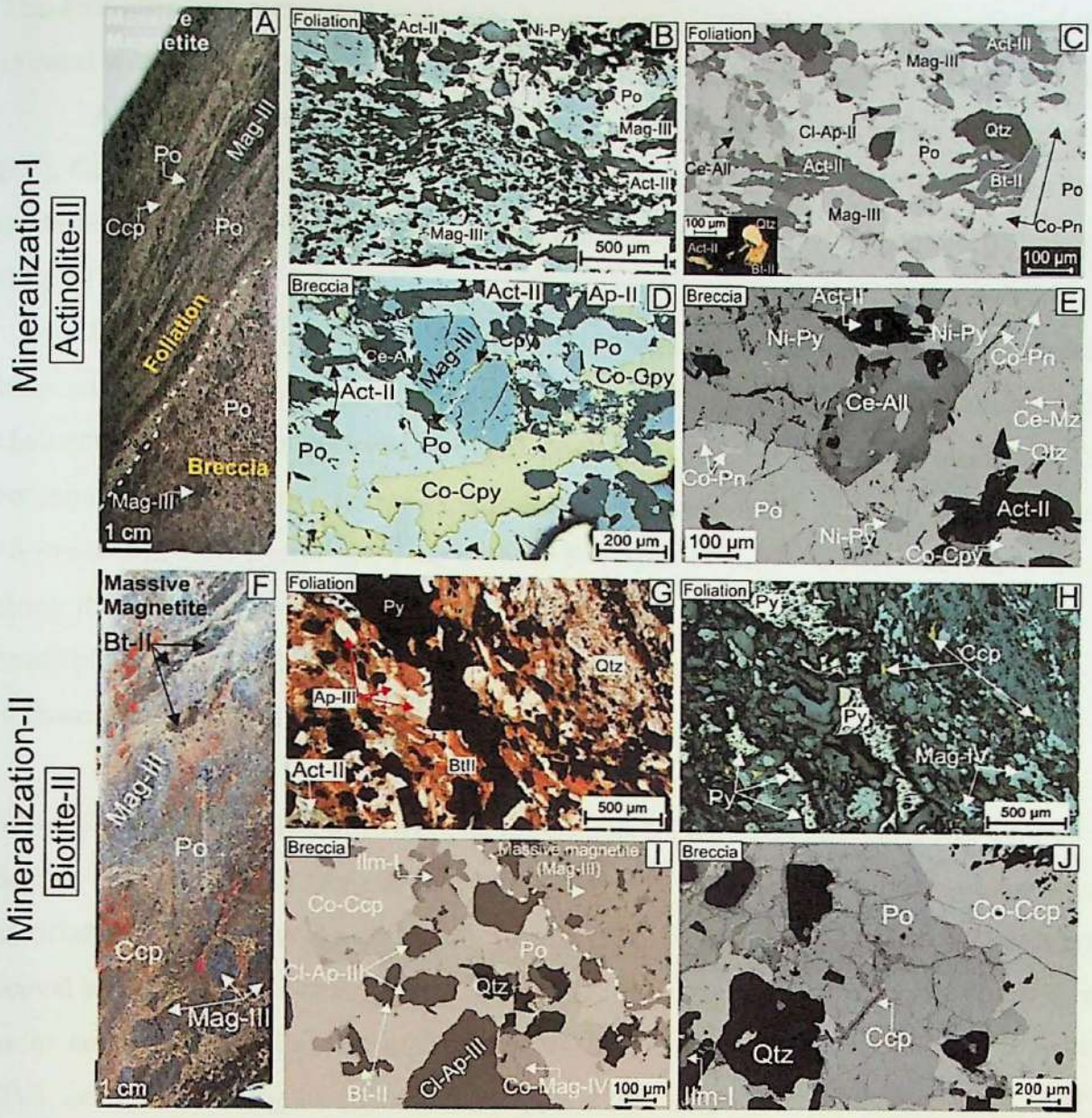

Figure 11. Distribution of the main macro and microscopic features of the mineralizing stages associated with ductile to ductile-brittle deformation of the Jatobá deposit. **A to E**: mineralization stage (I) with zones enriched in pyrrhotite that often crosscut massive magnetite bodies (Mag III); **A)** transition of foliated and brecciated domains with pyrrhotite and minor chalcopyrite; **B)** mylonitic foliation defined by streched magnetite (III), fine crystals of actinolite (II) and pyrrhotite (reflected light); **C)** SEM backscattered image showing actinolite (II), biotite (II), chalcopyrite, Ni-Py, Cl-apatite (II), Ce-allanite (II), Co-Pentlandite and quartz along the mylonitic foliation that contour the massive magnetite (III); Inset shows the same field under transmitted light, showing the association of actinolite and biotite; **D)** hydrothermal breccia with pyrrhotite associated with pyrrhotite, Co-chalcopyrite, actinolite (II), Cl-apatite and fragments of magnetite (III) (reflected light); **E)** SEM backscattered image showing Ce-allanite and Ce-monazite crystals and flames of Co-pentlandite in pyrrhotite; **F to J**, mineralization stage (II) with enrichment in chalcopyrite and, subordinately, in pyrrhotite, disseminated along mylonitic foliation associated with potassic alteration (Bt II); **F)** foliated and brecciated massive magnetitite, which was replaced by chalcopyrite and pyrrhotite; **G)** mylonitic foliation defined by biotite (Bt II), in addition to pyrite, chlorine-rich apatite and minor quartz and chalcopyrite (TL-PP); H) idem under reflected light; **I and J**: SEM backscattered image showing breccia zone with Co-rich chalcopyrite, Cl-apatite, pyrrhotite and fragments of magnetite (III). Abbreviation: Act = actinolite; Ap = apatite; All = allanite; Qtz = quartz; Bt = biotite; Co-Mag = Co-magnetite; Co-Ccp = Co-chalcopyrite; Co-Pn = Co-pentlandite; Po = pyrrhotite; Py = pyrite; Ni-Py = Ni-pyrite; Mz = monazite; Ilm = ilmenite.

The actinolite was converted to biotite, however, it is possible to identify relics of this mineral within biotite aggregates, commonly partially replaced by chlorite (Fig. 10 G).

A system of strongly oriented and interconnected bodies with Co-magnetite (IV), Cl-apatite (III), ilmenite (I), Ce-allanite (III) and quartz, besides discrete portions containing Ni-pyrite and Co-chalcopyrite, are associated with the biotite (II) domains (Fig. 11 G and 11 H).

In these domains, it is also possible to notice the development of mineralized breccias, but of localized occurrence (Fig. 11 I and 11 J). Expressive formation of Co-chalcopyrite, affecting the preexisting bodies of massive magnetite, is observed. The brechoid zones are associated with biotite (II), Cl-apatite (III), ilmenite (I), quartz and Ni-pyrite and ± Ni-pyrrhotite. Fine-grained Bt (II) and Cl-apatite (III) commonly occur along the edges of the magnetite crystals. Ilmenite, however, represents an important oxide phase (Fig. 11 I). The amounts of Ni-pyrrhotite and Ni-pyrite are lower compared to those of actinolite (II)-rich mineralized zones.

Mineralization III (Min III/Bt III): The third mineralizing stage recognized in the Jatobá deposit is distinguished from the others because it is controlled by brittle structures and associated with stockworks and vein systems (Fig. 10 G to 10 I; 12 A to 12 E). It was coeval to the paler brown or green biotite (III) formation in veins of up to 4 cm. These veins are composed of coarse quartz crystals, in addition to scapolite (IV), Cl-F-apatite (IV), and Cl-K hastingsite (II) and have typical open-sapce filling textures (Fig. 12 B). Co-chalcopyrite and siegenite are the dominant sulfides in veins. Cobaltiferous pyrite occurs as fine grains on the edges of siegenite crystals (Fig. 1 2 D). It is observed at this stage the drastic decrease in the magnetite content, which occurs only as microinclusions in chalcopyrite together with the thiny cassiterite crystals (Fig. 12 E).

Mineralization IV (Min IV/Chl II): Comprises the fourth and last mineralizing stage (Fig. 10 J to 10 L; Fig. 12 F to 12 J). It was coeval to widespread chlorite (II), quartz, epidote and calcite development. It occurs in a variety of branching veinlets, which cut out and isolate portions of rock that have been previously altered, thus giving a brechoid aspect to the rock.

In these chlorite-rich domains, the predominant Co-chalcopyrite has in its rims inclusions of subeuhedral cobaltiferous pyrite crystals. Sphalerite commonly occurs as inclusions in quartz and more rarely in chalcopyrite. Thiny molybdenite, uraninite and

monazite inclusions in chalcopyrite were also identified by using scanning electronic microscope (SEM) (Fig. 13 I and 12 J).

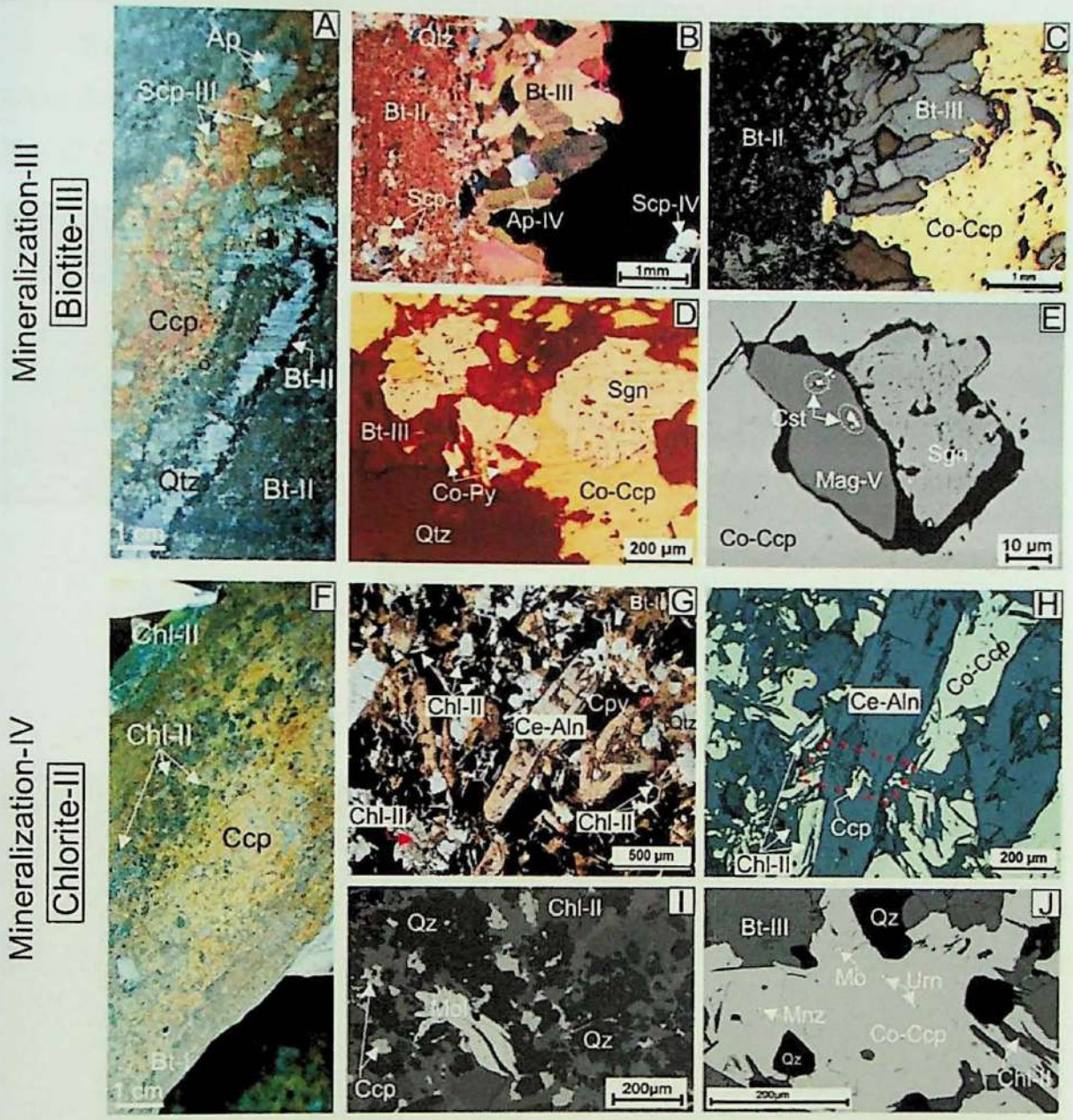

Figure 12. A to E: Mineralization stage (III) showing the relationship between coarse biotite (III) and chalcopyrite in veins controlled by brittle structures; **A)** vein with chalcopyrite, apatite, quartz and biotite (III); **B)** vein infilled by biotite (III), Co-chalcopyrite, apatite (IV) and scapolite (IV) crosscutting the metabasalt replaced by fine biotite (II) (TL-CP); **C)** Idem under reflected light; **D)** Siegenite and Co-pyrite associated with Co-chalcopyrite (reflected light); **E)** SEM backscattering image showing inclusion of siegenite and magnetite (V) in Co-chalcopyrite; tiny cassiterite inclusions occur in magnetite; **F to J:** Mineralization stage (IV) highlighting the association between chlorite (II) and chalcopyrite; F) Chlorite (II), chalcopyrite and quartz in breccia zone; **G)** Ce-allanite associated with chlorite (II) and chalcopyrite (TL-PP); **H)** Idem under reflected light; **I)** SEM image showing molybdenite associated with quartz and chlorite (II); **J)** SEM image showing tiny inclusions of uraninite, molybdenite and monazite in Co-chalcopyrite associated with chlorite (II) and relicts of biotite (III). **Abbreviation:** Ap = apatite; Ce-Aln = Ce-allanite; Qtz = quartz; Bt = biotite; Mag = magnetite; Co-Ccp = Co-chalcopyrite; Co-Py = Co-pyrite; Mz = monazite; Mo = molybdenite; Mnz = monazite; Urn = uraninite; Sgn = siegenite.

Variably deformed quartz-chalcopyrite-K-feldspar veins are expressive. Quartz has undulose extinction, deformation bands and sub-grain formation, whereas K-feldspar presents a clear appearance and is undeformed. In these veins, chalcopyrite, molybdenite, Co-pentlandite, and siegenite represent important mineral phases.

Eventual millimeter-wide veinlets consisting essentially of chlorite (Fig. 13 A, B) cut these rocks and present zoned textures, typically indicative of open-space filling (Fig. 13 C).

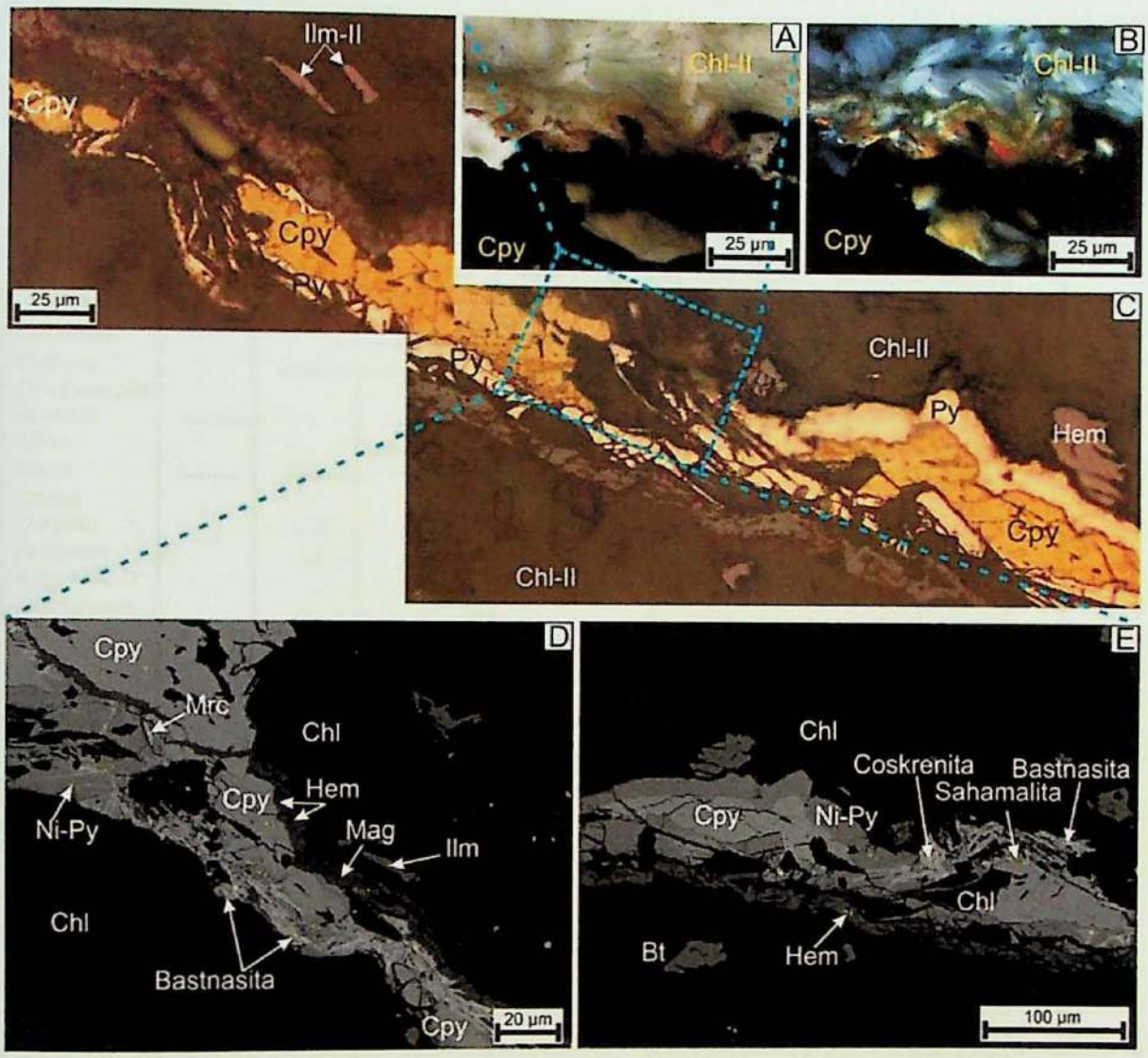

Figure 13. Main features of mineralization stage (IV) associated with chlorite (II) alteration. **A-B)** chalcopyrite, pyrite and quartz veinlets associated with proximal biotite (III) and distal chlorite (II); **C)** detail of **B)** showing veinlets with pyrite on the borders and chalcopyrite in its central portion; ilmenite and hematite are associated with chlorite (II); **D)** SEM image showing bastinäsite associated with Ni-pyrite and marcasite and magnetite-hematite on the border of chalcopyrite; **E)** SEM image showing bastinäsite, coskrenite and sahamalite associated with pyrite and chalcopyrite. **Abbreviations:** Mag = magnetite; Ilm = ilmenite; Cpy = chalcopyrite; Chl = chlorite; Hem = hematite; Chm = chamosite; Mrc = marcasite; Ni-Py = Ni-pyrite; Qz = quartz.

Magnetite is rare and represents fine grains on the border of these veinlets, not infrequently, being partial to completely replaced by W-bearing hematite (up to 1.6%

W, as indicated by EDS analyses). Rare earth carbonates, represented by bastnäsite, coskrenite and sahamalite, also occur in these borders (Fig. 13 D, E). Ni-pyrite and ilmenite occurs in the intermediate parts and presents alteration to marcasite, limonite and leucoxene. Chalcopyrite is the dominant sulfide and occupies the central portions of the veinlets associated with sphalerite crystals. Finally, fine inclusions of adularia in the cobalt pyrite were also identified (Fig. 13 D, E). The paragenetic evolution at Jatobá is shown in the Figure 14.

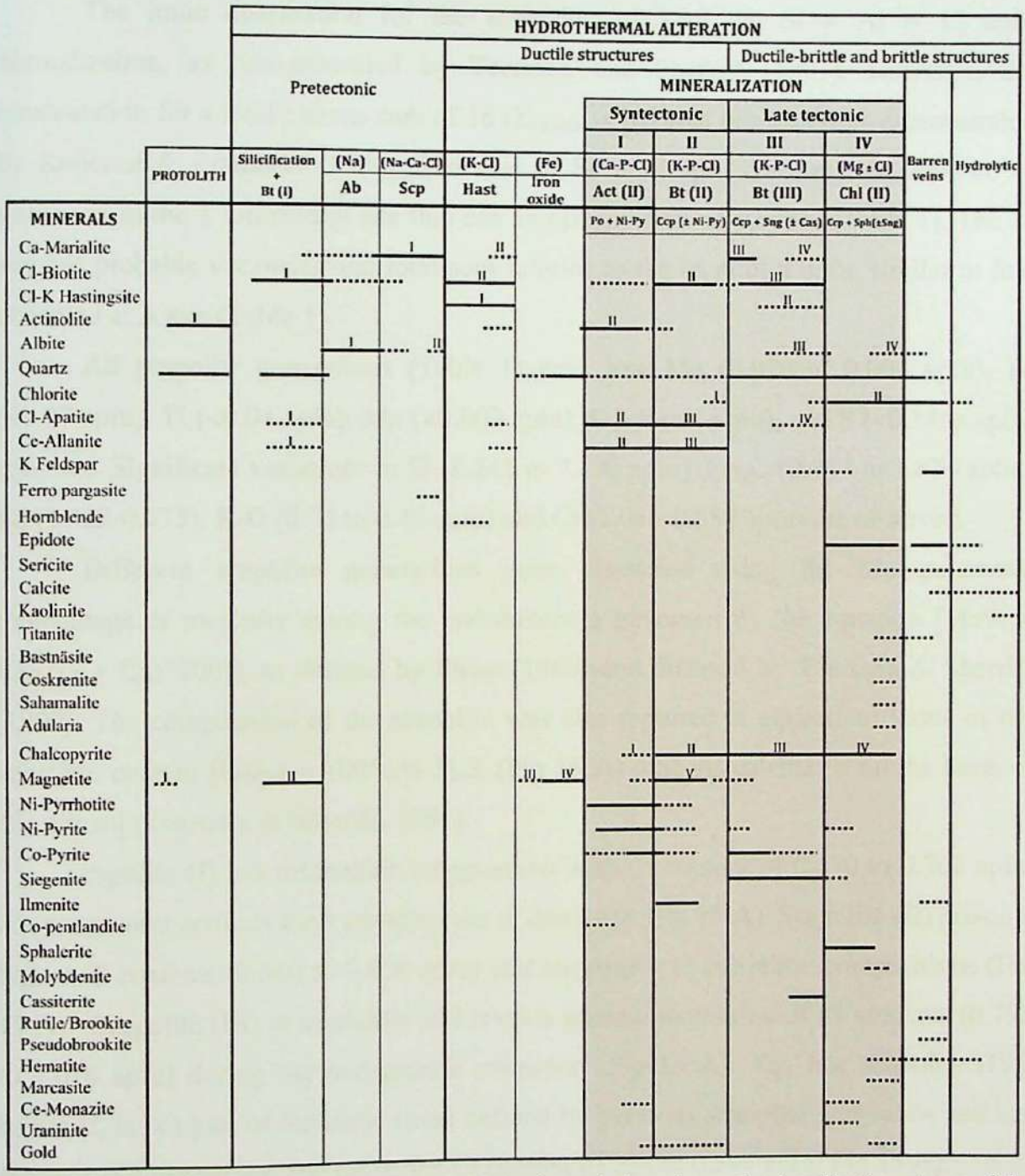

Figure 14. Paragenetic sequence showing the hydrothermal alteration and mineralization stages of the Jatobá deposit. The numbers represents the generations from which the minerals belong.

Mineral chemistry

Scapolite

Four scapolite generations (Scp I, Scp II, Scp III and Scp IV) have been identified in the Jatobá deposit (Table 1). The pre-tectonic scapolite (I) occurs in distal zones in relation to ore zones and replaces directly albite; syn-tectonic scapolite (II) represents overgrowth to the scapolite (I) porphyroclasts in mylonitic zones; post-tectonic fibrous scapolite (III) occurs in thick veins; and scapolite (IV) in late veinlets crosscutting fibrous scapolite (III).

The ionic distribution for the scapolite followed the Si + Al = 12 apfu normalization, as recommended by Teertstra and Sherriff (1997). However, the recalculation for a total cations sum of 16 ($\Sigma_{cations} = 16$) was necessary, as demonstrated by Kullerud & Erambert (1999). The sum of Si + Al apfu confirms the absence of vacancies in the T tetrahedral site that has an optimal sum of 12 apfu (Table 1). The M site has probable vacancies and total sum inferior to the ideal of 4 apfu, similar to that observed at A site (Table 1).

All scapolite generations (Table 1) have low Mg (0.070 to 0.003 apfu), Fe (<0.07 apfu), Ti (<0.04 apfu), Mn (<0.003 apfu), F (<0.051 apfu), and S (<0.14ap apfu) contents. Significant variations in Si (8.241 to 7.190 apfu), Na_2O (2.817 to 1.874 apfu), Ca (1.423-0.775), K_2O (0.74 to 0.43 apfu) and Cl (1.016-0.550 apfu) are observed.

Different scapolite generations were classified using the Me parameter (percentage of meionite among the end-members governed by the equation [Me% = Ca/(Na + Ca)*100]), as defined by Shaw (1960) and diffused by Teertstra & Sherriff (1997). The composition of the scapolite was also reported in equivalent terms of the anorthite content [EqAn = 100*(Al-3)/3, (Fig 15 A) with Al calculated on the basis of 16 cations] (Teertstra & Sherriff, 1997).

Scapolite (I) has mizzonitic composition with Cl content of 0.470 to 0.702 apfu, however, some outliers have composition of marialite (Fig 15 A). Scapolite (II) presents higher Cl contents (0.660 to 0.950 apfu) and mizzonitic to marialitic compositions (Fig 15 A). Scapolite (III) is marialitic and reveals gradual increasing of Cl contents (0.798 to 1.016 apfu) during the paragenetic evolution (Fig 15 A). The late scapolite (IV), however, is not part of the same trend defined by previous scapolite generatios and has mizzonitic composition and moderate Cl content (0.764 to 0.897 apfu; Fig 15 A).

Table 1. Representative chemical composition of scapolite from the Jatobá IOCG deposit.

Event	Pre-tectonic	Syn-tectonic	Late tectonic	
Sample	JATD-21 (64,80m)	JATD-28 (54,22m)	JATD-15 (87,63m)	JATD-15 (44,35m)
Rock	Metadiabase	Scp-Hs-Bt mylonite	Metabasalt	Metadiabase
Mineral	Scp I (Rim)	Scp II (Rim)	Scp (III)	Scp (IV)
SiO_2 wt%	52.39	60.74	56.34	55.95
Al_2O_3	24.63	21.10	22.94	23.44
TiO_2	00.00	00.00	0.04	0.01
Fe_3O_4	0.03	0.10	0.02	0.11
MnO	00.00	00.00	0.01	0.01
CaO	9.18	6.89	6.35	7.19
Na_2O	7.92	8.26	10.35	9.78
K_2O	0.30	0.27	0.26	0.38
SO_3	0.05	0.02	00.00	0.05
∑ Óxidos	94.50	97.36	96.31	96.93
F	0.01	00.00	00.00	00.00
Cl	2.35	2.64	3.50	3.09
O=Cl	0.530	0.596	0.790	0.697
TOTAL	96.323	99.427	99.021	99.323
Ions number on the basis of Si + Al = 12				
TSi *a.p.u.f.*	7.388	8.145	7.672	7.618
TAl^{IV}	4.612	3.855	4.328	4.382
∑T	12.00	12.000	12.000	12.000
$M^{+2}Al^{VI}$	-0.518	-0.520	-0.647	-6.210
$M^{+2}Fe^{+++}$	0.003	0.10	0.002	0.011
$M^{+2}Mn$	00.00	0.001	0.001	0.002
$M^{+2}Ti$	00.00	00.00	0.004	0.001
$M^{+2}Ca$	1.387	0.990	0.926	1.049
$M^{+}Na$	2.165	2.147	2.732	2.582
$M^{+}K$	0.054	0.046	0.046	0.067
∑M	3.091	2.674	3.064	3.090
AS	0.006	0.002	00.00	0.005
AF	0.024	0.600	0.808	0.713
ACl	0.562	0.014	00.00	0.019
∑A	0.591	0.616	0.808	0.737
Eq. An	53.718	28.497	44.283	46.071
Me %	39.0	31.6	25.3	28.9

In the Si versus Σ(Na + K) plot (Fig 15B) all scapolite generations are classified as calcic marialite, which few outliers. The increasing of Σ(Na + K) contents from scapolite (I) to (III) is similar to that observed for Cl, and analogously the late scapolite (IV) has intermediate Σ(Na + K) contents between those of scapolite (II) and (III) (Fig 15 B). This late scapolite generation also has intermediate Si, Na, Ca, and Al^{IV} contents in relation to scapolite (II) and (III) (Fig 15).

A similar pattern was observed for other major elements in relation to Cl contents (apfu). The content of Si and Na (apfu) define positive correlation with Cl contents for all scapolite generations (Fig 16), whereas Ca and Al^{IV} reveal negative correlation with Cl contents. Clear correlation trends between K (apfu) and Cl (apfu) were not observed, althought a set of outliers in other graphs appears to be aligned (Fig 16).

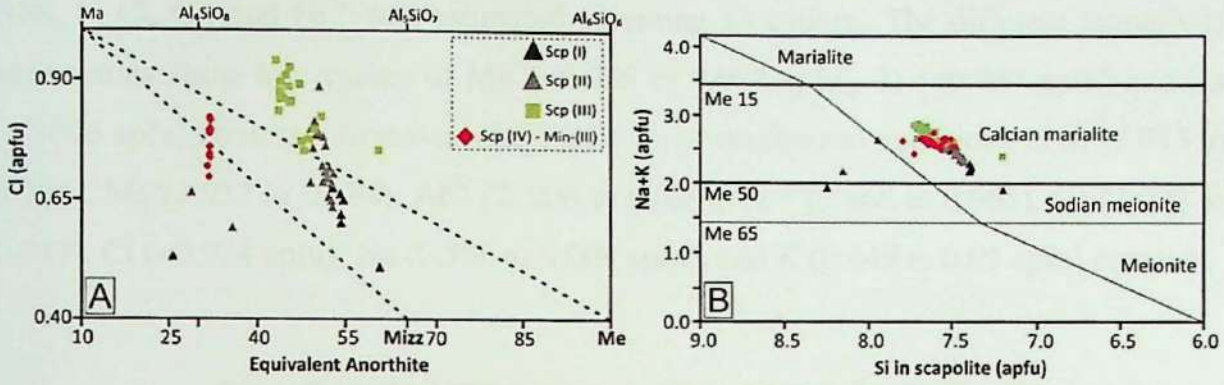

Figure 15. A) Cl versus Eq. Anorthite for scapolite generations recognized in the Jatobá deposit (Teertstra & Sherriff, 1997). The dashed lines show the stoichiometry of solid solutions proposed by Evans et al. (1969) for the fields of marialite, mizzonite and meionite. B) Correlation between Si versus Σ(Na + K) distributed among the three main trends of chemical composition in Meionite 15, 50 and 65 for each type of scapolite (Teertstra at al. 1999). Abbreviations: Scp (I) = scapolite (I); Scp (II) = syn-tectonic scapolite (II); Scp (III) = fibrous scapolite (III); Scp (IV) = late scapolite (IV) veinlet.

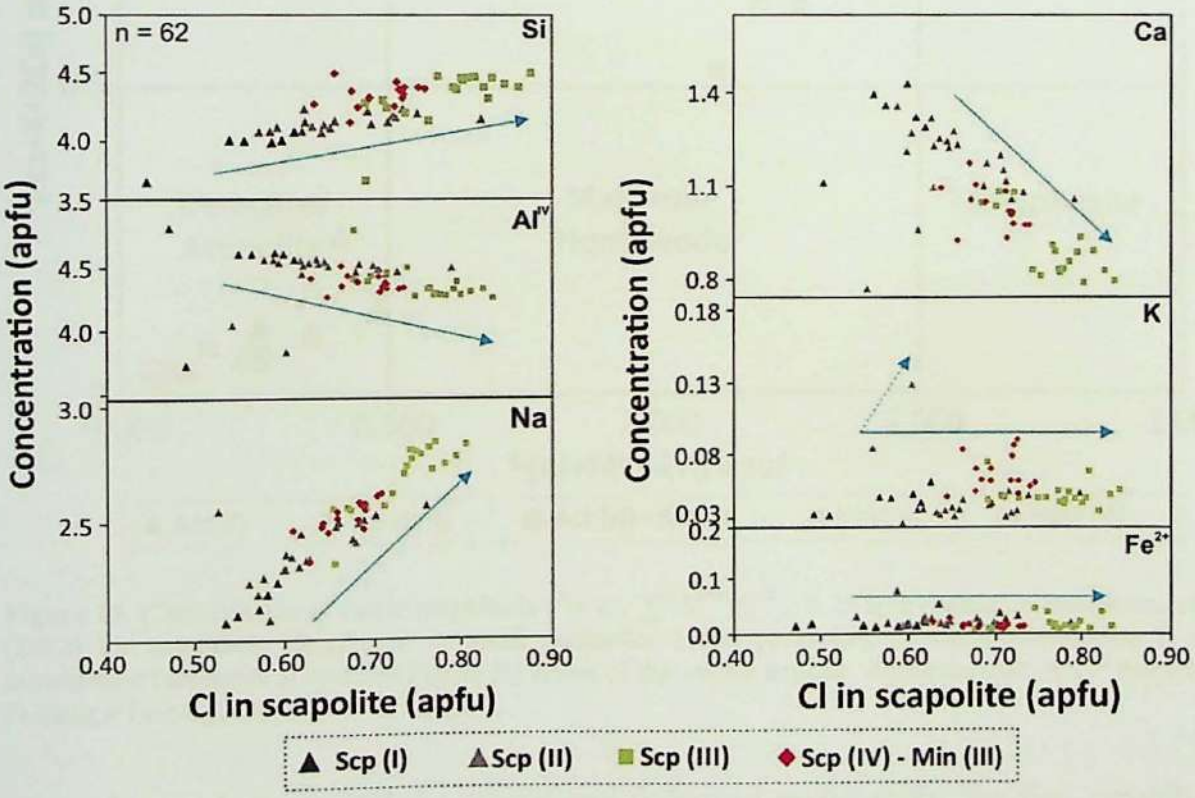

Figure 16. Compositional variations of major elements and chlorine in scapolite of the depósito Jatobá.

Amphibole

In the Jatobá deposit, amphibole was formed during low-grade metamorphism and in four sodic-calcic alteration stages developed in distal, proximal and mineralization zones. Its compositional variation and classification, based on Hawthorne et al. (2012), are shown in Table 2 and Figure 17.

The amphibole cationic distributions were calculated on the basis of 22 apfu (OH, F, Cl, O), and Fe^{3+} was estimated assuming 13 cations. The different amphibole generations show low values of Mn (<0.035 to 0.007 apfu), Ti (<0.037 apfu) and Zn (<0.006 apfu) contents. However, they show large continuous variations of Si (7.953 to 5.794), Mg (3.912 to 0.884), Al^{IV} (2. 206 to 0.029), Fe^{2+} (2.868 to 0.965), Ca (2.000 to 0.747), Cl (<0.924 apfu), Na (0.568 to 0.009 apfu), and K (0.449 to 0.01 apfu) contents.

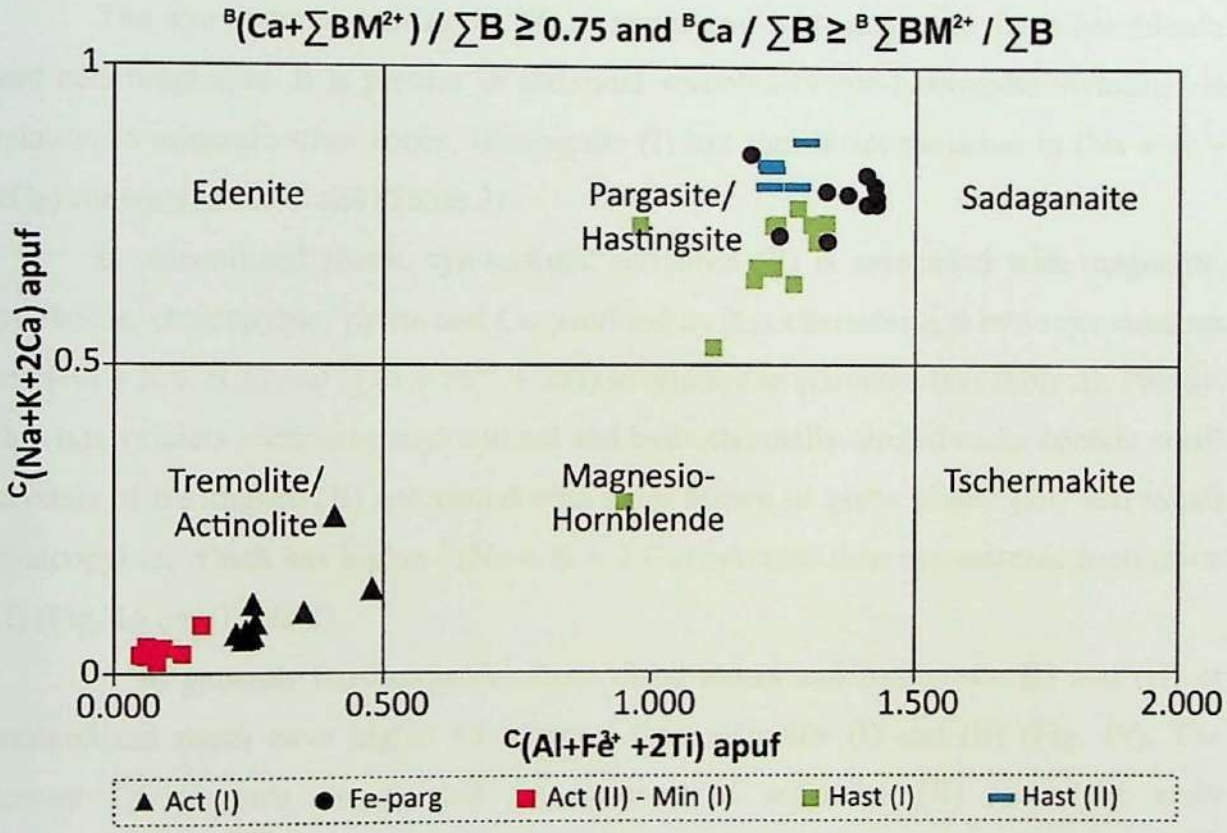

Figure 17. Classification of calcic amphibole [$^{B}(Ca + \sum^{B} M^{2+})/\sum^{B} \geq 0.75$ apfu] based on Hawthorne et al. (2012) for amphibole distributed in distal (actinolite I and pargasite), proximal (hastingsite I) and mineralized (actinolite II and hastingsite II) zones of the Jatobá deposit. Abbreviations: Act = actinolite; Fe-parg = Fe-pargasite; Hast = hastingsite.

In distal zones, in least-altered and deformed mafic rocks, the first amphibole generation is represented by actinolite (I) (Act I; Fig. 18). The second amphibole generation replaces the actinolite (I) rims and has ferro-pargasite (Fig. 18), K-ferro-

pargasite ferro-cannilloite and ferro-ferri-tschermakite compositions. It has higher contents of Fe^{2+}, Al^{IV}, Cl, Na, K and $Fe_t/(Fe_t + Mg)$ ratios and lower Mg contents in relation to actinolite (I), as shown in Fig. 17.

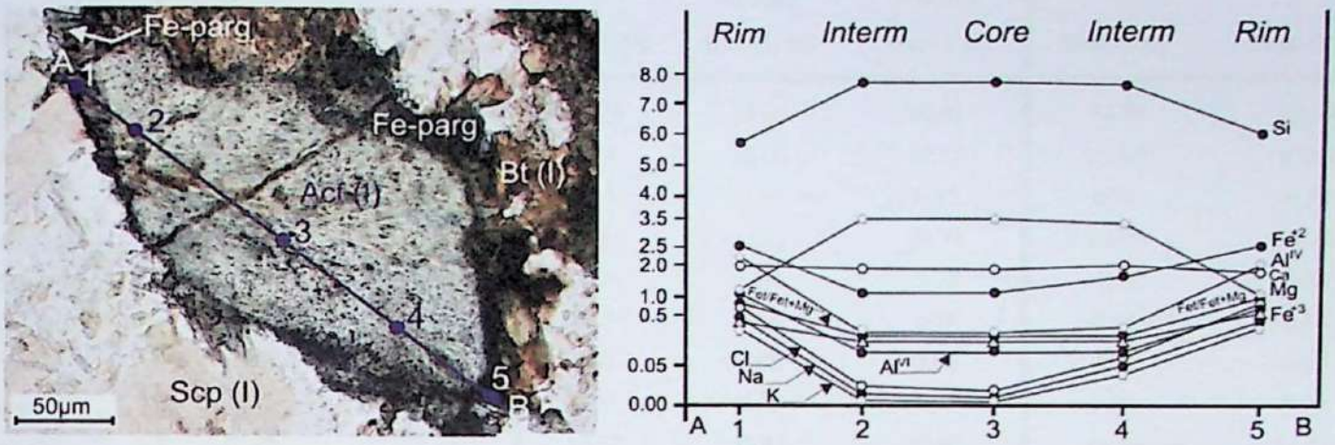

Figure 18. Chemical variations related to the replacement of actinolite (I) by ferro-pargasite in its rims.

The syn-tectonic hastingsite (I) is associated with magnesio ferro-hornblende and cummingtonite. It is present in proximal scapolite-biotite-hastingsite mylonites in relation to mineralization zones. Hastingsite (I) has significant variation in (Na + K + 2Ca) contents in the C site (Table 2).

In mineralized zones, syn-tectonic actinolite (II) is associated with magnetite, pyrrhotite, chalcopyrite, pyrite and Co-pentlandite. It is characterized by lower contents of $^{C}(Na + K + 2Ca)$ and $^{C}(Al + Fe^{3+} + 2Ti)$ in relation to actinolite (I) (Table 2). Finally, thin late veinlets sectioning mylonitized and hydrothermally altered rocks contain small crystals of hastingsite (II) associated with paler brown or green biotite (III) and minor chalcopyrite, which has higher $^{C}(Na + K + 2\ Ca)$ contents than syn-tectonic hastingsite (I) (Fig. 16 and Table 2).

In general, ferro-pargasite from distal zones and hastingsite (I) and (II) of mineralized zones have higher Cl contents than actinolite (I) and (II) (Fig. 19). The lowest Cl contents are related to syn-tectonic actinolite (II) from the early mineralization stage. Wider variation in Cl contents is observed in syn-tectonic hastingsite (I). General trends of negative correlation among Cl and Si, Mg and Ca are observed. However, ferro-pargasite reveals, in relation to Ca, inheritance from previous actinolite (I), which was replaced by this mineral phase (Fig 19). It makes its chemical evolution differentiated in relation to the other amphibole (Fig 19).

Table 2. Representative analysis of different amphibole generations in the Jatobá deposit.

Event	Pretectonic		Syn-tectonic			Late tectonic	
Sample	JATD-21 (64,80m)	JATD-21 (64,80m)	JATD-32 (383,00m)	JATD-28 (54,22m)	JATD-28 (54,22m)	JATD-15 (44,35m)	JATD-15 (44,35m)
Rock	Metadiabase	Metadiabase	Min-I	Scp-Hast-Bt-mylonite	Scp-Hast-Bt-mylonite	Metadiabase	Metadiabase
Mineral	Act (I)	Fe-parg	Act (II)/SZ	Hast (I)/SZ	Hast-I/SZ	Hast-II/LV	Hast-II/LV
SiO_2 wt%	51.48	37.33	56.24	39.44	40.01	37.76	37.49
Al_2O_3	4.57	15.22	0.24	13.00	12.49	13.09	12.97
TiO_2	0.18	0.24	0.03	0.10	0.32	0.24	0.17
$Fe_2O_{3(t)}$	13.79	23.60	10.84	24.83	24.78	26.89	27.26
MgO	14.59	4.85	18.36	5.67	5.77	4,17	3.88
MnO	0.07	0.11	0.10	0.10	0.08	0.11	0.10
NiO	0.00	0.00	0.03	0.00	0.00	0.00	0.00
ZnO	0.02	0.01	0.02	0.03	0.00	0.00	0.00
CaO	12.06	11.12	12.37	10.91	10.83	10.88	11.01
Na_2O	0.42	1.51	0.11	2.08	1.88	1.93	1.89
K_2O	0.33	1.89	0.00	1.03	1.03	1.39	1.51
∑ Óxidos	97.51	95.88	98.34	97.20	97.19	96.47	96.28
F	0.01	0.01	0.05	0.00	0.00	0.00	0.00
Cl	0.41	2.95	0.03	2.09	2.26	3.02	3.23
O=Cl, F	-0.10	-0.67	-0.03	-0.47	-0.51	-0.68	-0.73
TOTAL	97.83	98.17	98.40	98.82	98.94	98.81	98.78
	Ion number on the basis of 22 (OH, F, Cl, O)						
TSi *a.p.u.f.*	7.448	5.905	7.923	6.132	6.209	6.005	5.999
TAl^{IV}	0.552	2.095	0.041	1.868	1.791	1.995	2.001
TTi	0.00	0.00	0.003	0.00	0.00	0.00	0.00
TFe^{+3}	0.00	0.00	0.033	0.00	0.00	0.00	0.00
CAl^{VI}	0.227	0.743	0.00	0.514	0.494	0.459	0.445
CFe^{+2}	1.379	2.512	1.066	2.462	2.469	2.767	2.868
CFe^{+3}	0.226	0.572	0.073	0.694	0.664	0.757	0.741
CTi	0.019	0.029	0.00	0.012	0.037	0.029	0.020
CNi	0.00	0.00	0.003	0.00	0.00	0.00	0.00
CZn	0.003	0.001	0.002	0.004	0.00	0.00	0.00
CMg	3.147	1.144	3.856	1.314	1.335	0.989	0.926
BMn^{+2}	0.009	0.015	0.012	0.013	0.011	0.015	0.014
BFe^{+2}	0.064	0.039	0.105	0.072	0.082	0.053	0.039
BCa	1.689	1.885	1.867	1.817	1.801	1.854	1.888
BNa	0.058	0.061	0.016	0.097	0.106	0.078	0.060
ANa	0.059	0.402	0.016	0.530	0.460	0.517	0.526
AK	0.061	0.381	0.001	0.204	0.204	0.282	0.308
Cations	15.121	15.784	15.017	15.733	15.663	15.800	15.835
COH	1.896	1.203	1.970	1,449	1.406	1.186	1.124
CF	0.004	0.006	0.022	0.00	0.00	0.00	0.00
CCl	0.101	0.791	0.008	0.551	0.594	0.814	0.876
Mg/(Mg+Fe)	0.695	0.313	0.783	0.348	0.351	0.263	0.244
Fe/(Fe+Mg)	0.305	0.687	0.217	0.652	0.649	0.737	0.756
Na+K	0.120	0.783	0.017	0.734	0.664	0.799	0.834

Trends of positive correlation among Cl and Fe^{2+}, Al^{IV}, Fe^{3+}, K and Na are also identified. However, ferro-pargasite and hastingsite (II) are not well aligned along the same tendency of correlation of Cl in relation to Fe^{3+}, Na and K (Fig 19).

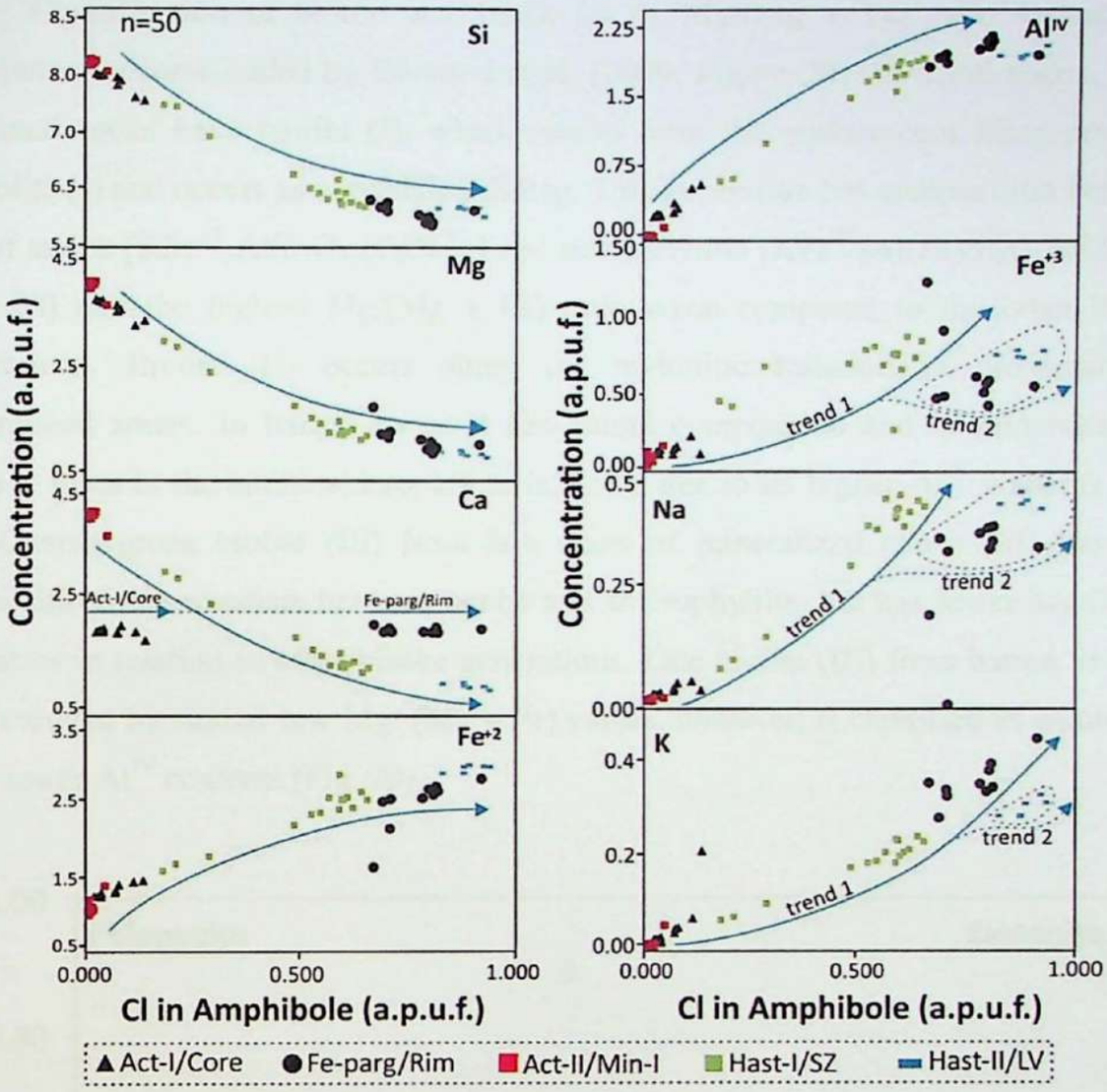

Figure 19. Compositional variations of amphibole in the Jatobá deposit.

Biotite

Biotite (I), (II) and (III) are associated with three potassic alteration stages clearly identified in the Jatobá deposit: pre-, syn- and late-tectonic in relation to the shear zone development. Representative biotite compositions are shown in Table 3 and Figure 20.

The cationic compositions of biotite were calculated on the basis of 20 apfu (OH, F, Cl, O). Different generations of biotite show extremely low values of Mn (<0.016 apfu), Zn (<0.009 *apfu*) and F (<0.008 apfu). Cu and Ba were not detected. However, significant compositional variations were identified in relation to contents of Si (6.152 to 5.113 apfu), Fe^{2+} (3.378 to 0.805 apfu), Al^{IV} (2.751 to 1.848 apfu), Mg

(2.816 to 1.024 apfu), K (1.972 to 0.943 apfu), Cl (0.885 to 0.219 apfu), Al^{VI} (1.354 to 0.00 apfu), Fe^{3+} (0.308 to 0.076 apfu), Ca (0.515 to 0.000 apfu), Ti (0.225 to 0.011 apfu) and Na (0.085 to 0.004 apfu).

Classification of biotite was based on its Mg/(Mg + Fe) ratio versus Al^{IV} contents, as recommended by Boomeri et al. (2009; Figure 20). In distal zones, least-deformed rocks have biotite (I), which results from the replacement from previous actinolite (I) and occurs as amygdale infilling. This generation has composition between that of annite [$KFe^{+2}{}_3AlSi_3O_{10}(F,OH)_2$] and siderophyllite [$KFe^{2+}{}_2Al(Al_2Si_2O_{10}(F,OH)_2$] (Fig. 20) and the highest Mg/(Mg + Fe) ratio when compared to the other biotite generations. Biotite (II) occurs along the mylonitic foliation in proximal and mineralized zones. In barren zones it has annite composition and in mineralization zones it plots in the annite-siderophillite interface due to its higher Al^{IV} contents (Fig. 20). Coarse green biotite (III) from late veins of mineralized zones (III) has also compositions intermediate between annite and siderophyllite, but has lower Mg/(Mg + Fe) ratios in relation to other biotite generations. Late biotite (III) from barren veins is characterized by similar low Mg/ (Mg + Fe) values, however, is classified as annite due to its lower Al^{IV} contents (Fig. 20).

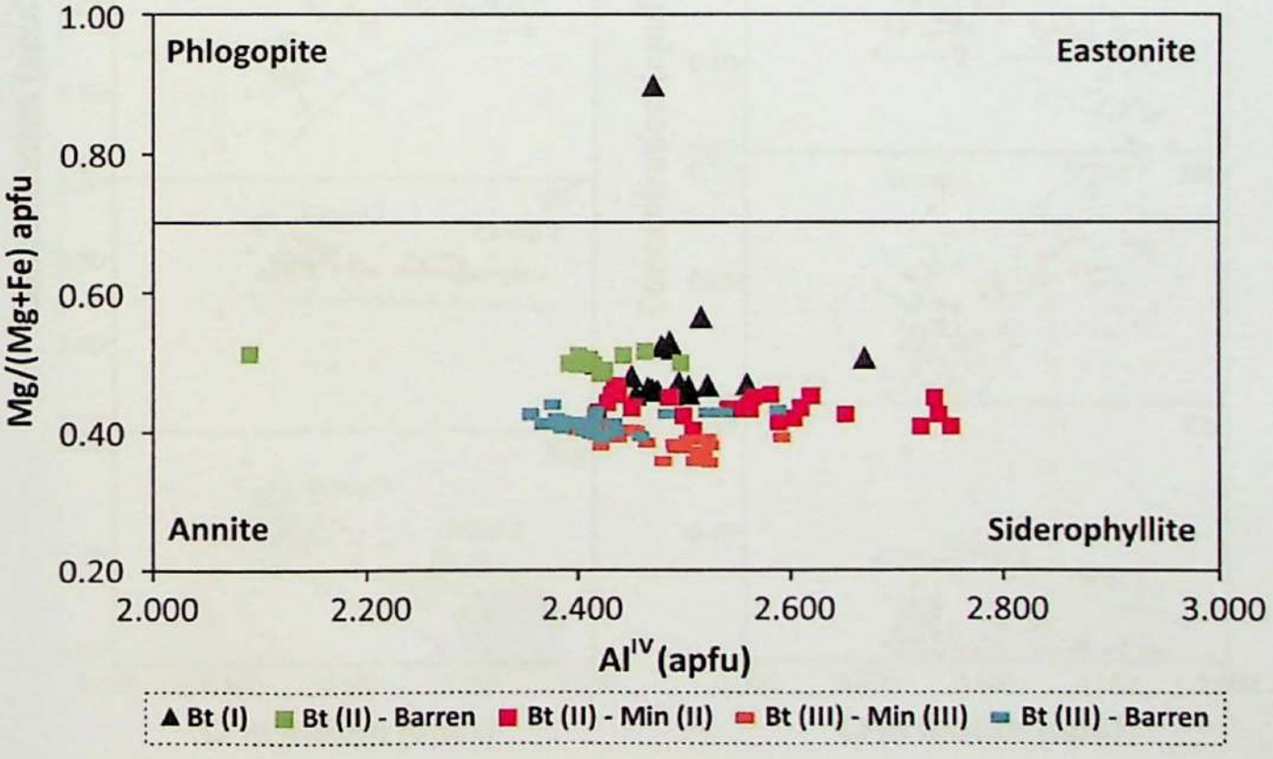

Figure 20. Classification, based on Boomeri *et al.* (2009), of biotite (I), (II) and (III) from distal, proximal and mineralized (Bt-II/Min-II and Bt-III/Min-III) zones.

The chlorine content in biotite defines two main groups for this mineral. The group 1 encompasses distal pre-tectonic biotite (I) and syn-tectonic biotite (II) from proximal and mineralization zones (Fig. 21). This group is characterized by its lower Cl and relatively higher Mg and Ti contents in relation to group 2, and trends of positive correlation among Cl, Si, and K (Fig. 21). However, biotite (II) in mineralized zones is distinct from biotite (II) from proximal domains due to its relatively high Cl contents and negative correlation between Cl and Fe^{2+} (Fig. 21). The group 2 comprises late biotite (III) from mineralized and barren zones, which has higher Cl, Na and Fe^{2+} contents (Fig. 21). Biotite (III) from barren zones, however, may be distinguished from biotite (III) from mineralized zones due to its lower Ti contents (Fig. 21). The samples of these two groups also define trends of negative correlation among Cl and Mg, Ca, and Al^{IV} (Fig. 21).

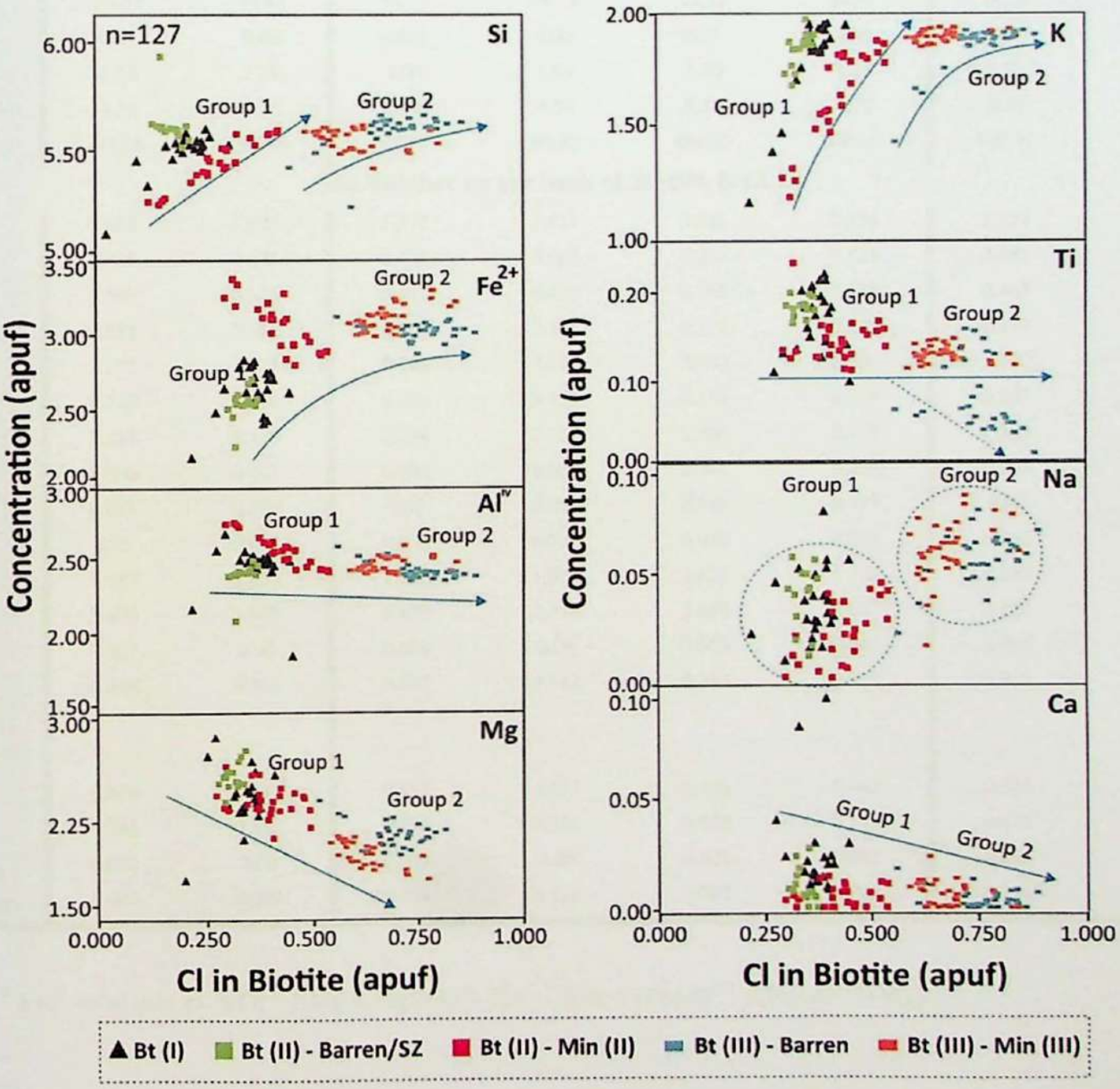

Figure 21. Compositional variations of biotite of the Jatobá deposit.

Table 3. Representative analysis of different biotite generations in the Jatobá deposit.

Event	Pre-tectonic		Syn-tectonic				Late tectonic	
Sample	JATD-21 (64.80m)	JATD-21 (64.80m)	JATD-28 (160.40m)	JATD-3 (130.05m)	JATD-28 (54.22m)	JATD-28 (54.22m)	JATD-21 (40.00m)	JATD-21 (40.00m)
Rock	Metadiabase	Metadiabase	Min (II)	Min (II)	Scp-Hast-Bt-mylonite	Scp-Hast-Bt-mylonite	Min (II)	Metadiabase
Mineral	Bt (I)	Bt (I)	Bt (II)	Bt (II)	Bt (II)/SZ	Bt (II)/SZ	Bt (III)	Bt (III)/ST
SiO_2 wt%	35.34	35.29	34.47	33.83	35.46	35.72	33.59	34.39
Al_2O_3	15.24	15.07	14.04	15.93	14.41	14.82	15.20	14.34
TiO_2	1.61	1.80	1.24	0.88	1.51	1.24	0.89	0.36
$Fe_2O_{3(t)}$	22.90	21.68	25.78	25.22	22.91	23.72	27.96	26.72
MgO	9.88	11.01	9.52	9.87	10.67	10.52	7.28	8.55
MnO	0.047	0.05	0.001	0.02	0.06	0.06	0.02	0.02
CaO	0.06	0.05	0.00	0.04	0.03	0.10	0.00	0.02
Na_2O	0.16	0.19	0.10	0.09	0.17	0.09	0.19	0.20
K_2O	9.11	9.28	9.04	8.84	9.31	8.60	9.06	9.04
∑ Oxides	94.37	94.42	94.19	94.73	94.52	94.57	94.19	93.63
F	0.01	0.00	0.001	0.00	0.01	0.01	0.01	0.01
Cl	1.38	1.49	1.96	1.63	1.30	1.23	3.02	3.01
O=Cl, F	0.31	0.34	0.44	0.37	0.30	0.28	0.69	0.68
TOTAL	99.86	99.95	99.75	99.92	100.03	100.07	100.01	99.78
Ion number on the basis of 20 (OH, F, Cl, O)								
Si *a.p.u.f.*	5.562	5.525	5.572	5.417	5.586	5.576	5.519	5.629
Al^{IV}	2.438	2.475	2.428	2.583	2.414	2.424	2.481	2.371
Al^{VI}	0.389	0.306	0.247	0.424	0.262	0.326	0.463	0.396
Ti	0.191	0.212	0.151	0.106	0.179	0.147	0.110	0.044
Fe^{+2}	2.571	2.425	2.896	2.842	2.542	2.602	3.220	2.991
Fe^{+3}	0.148	0.138	0.196	0.178	0.159	0.174	0.207	0.222
Mg	2.318	2.570	2.294	2.356	2.506	2.469	1.783	2.086
Mn	0.006	0.007	0.001	0.003	0.007	0.008	0.003	0.003
Ca	0.011	0.009	0.00	0.007	0.004	0.017	0.00	0.003
Na	0.05	0.056	0.030	0.029	0.050	0.029	0.060	0.062
K	1.829	1.853	1.864	1.806	1.871	1.727	1.899	1.887
OH	3.629	3.605	3.459	3.558	3.650	3.667	3.153	3.162
F	0.003	0.00	0.004	0.00	0.003	0.005	0.006	0.003
Cl	0.368	0.366	0.537	0.442	0.347	0.328	0.841	0.835
Parameters								
X_{ann} [d]								
XMg [b]	0.474	0.514	0.442	0.453	0.496	0.487	0.356	0.411
XFe [c]	0.561	0.515	0.578	0.581	0.528	0.543	0.674	0.619
F/(F+OH)	0.001	0.00	0.001	0.00	0.001	0.001	0.002	0.001
Cl/(Cl+OH)	0.092	0.099	0.134	0.111	0.087	0.082	0.211	0.209

[a] FeO, total iron as FeO; [b] XMg = Mg/(Mg + Fe); [c] XFe = $(Fe+Al^{(VI)})/(Fe+Al^{(VI)}+Mg)$.

Chlorite

Chlorite classification was based on the recommendations of the AIPEA (Association Internationale Pour l'Étude des Argiles; Guggenheim et al., 2006). Representative chlorite analyses are shown in Table 4 and Figure 22 A. The cationic distributions obtained for chlorite were carried out on the basis of 14 O.

Two chlorite generations were identified in the Jatobá deposit. Chlorite (I) replaces amphibole, scapolite and biotite. It has $Fe^{2+}/(Fe^{2+} + Mg)$ ratios between 0.62 and 0.68 and chamosite composition. Chlorite (II) occur in the mineralization (IV) zones and has considerably lower $Fe^{2+}/(Fe^{2+} + Mg)$ ratios, between 0.40 and 0.45 (Table 4) and clinochlore composition (Table 4 and 6; Fig. 22 B). Chlorine contents in both chlorite generations are distinctly lower (<0.03 apfu) compared to that of other hydrated silicates in the Jatobá deposit (Table 1; Table 2; Table 3).

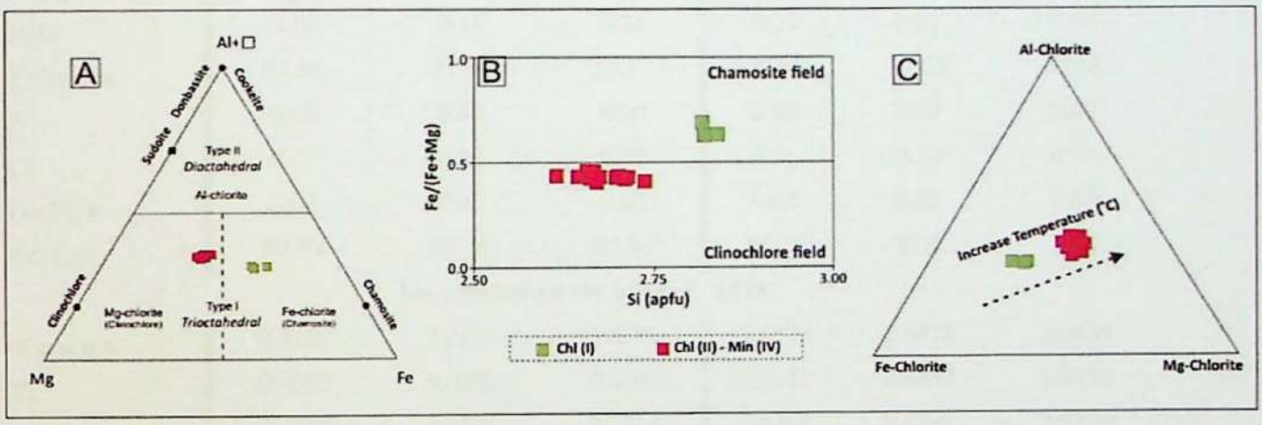

Figure 22. Compositional variation of chlorite from the Jatobá deposit. A) Ternary plot of Mg, Fe and Al + □ (Zane and Weiss, 1998); B) Plot of Fe/(Fe+Mg) ratio versus Si (apfu), showing the chamosite and clinochlore fields (Ruiz and Nieto, (2006); C) Ternary plot for Fe-chlorite, Mg-chlorite, and Al-chlorite (De Caritat *et al.*, 1993), showing trend of temperature increase from chlorite (I) to chlorite (II).

Temperature was estimated based on chlorite composition according to different geothermometers (Table 5). Although different calibrations have resulted in different temperatures, consistently the temperatures for chlorite II are higher (261 to 386 °C; Table 5) than those calculated for chlorite I formation (215 to 330 °C; Table 5).

Table 4. Representative analysis of different chlorite generations in the Jatobá deposit.

Event	Syn-tectonic			Late tectonic		
Sample	JATD-28 (166.40m)	JATD-28 (166.40m)	JATD-28 (166.40m)	JATD-03 (130.05m)	JATD-03 (130.05m)	JATD-03 (130.05m)
Rock	Scp-Hast-Bt mylonite	Scp-Hast-Bt mylonite	Scp-Hast-Bt mylonite	ZM (IV)	ZM (IV)	ZM (IV)
Mineral	Chl (I)	Chl (I)	Chl (I)	Chl (II)	Chl (II)	Chl (II)
SiO_2 wt%	25.17	25.56	25.65	25.46	25.95	25.62
TiO_2	0.00	0.00	0.01	0.18	0.06	0.08
Al_2O_3	17.06	17.52	17.10	21.35	21.01	21.01
FeO	36.15	32.93	33.47	24.49	23.07	23.06
MnO	0.04	0.03	0.03	0.04	0..03	0.04
ZnO	0.04	0.02	0.04	0.07	0.10	0.09
CaO	0.04	0.05	0.20	0.01	0.01	0.02
MgO	9.22	11.30	11.05	16.42	17.47	17.71
Na_2O	0.03	0.01	0.08	0.00	0.02	0.01
K_2O	0.10	0.17	0.14	0.02	0.01	0.03
∑ Oxides	87.86	87.64	87.77	88.05	87.73	87.66
F	0.00	0.00	0.00	0.00	0.00	0.00
Cl	0.09	0.08	0.09	0.21	0.10	0.14
O=Cl, F	0.02	0.02	0.02	0.05	0.03	0.03
TOTAL	87.93	87.70	87.84	88.20	87.8	87.8
	Ion number on the basis of 14 O					
Si *a.p.u.f.*	2.8180	2.8192	2.8395	2.6575	2.6978	2.6626
Ti	0.0000	0.0036	0.0006	0.0141	0.0045	0.0059
Al^{IV}	2.2511	2.2775	2.2311	2.6264	2.5743	2.5734
Al^{VI}	1.0691	1.0966	1.1605	1.3425	1.3022	1.3374
Fe^{+2}	3.3034	3.0000	3.0931	2.1136	1.9923	1.9237
Fe^{+3}	0.0813	0.0375	0.0055	0.0242	0.0134	0.0805
Mg	1.5389	1.8580	1.8236	2.5550	2.7076	2.7438
Mn	0.0036	0.0026	0.0032	0.0040	0.0026	0.0035
Ca	0.0048	0.0061	0.0234	0.0015	0.0007	0.0020
Na	0.0069	0.0029	0.0169	0.0002	0.0047	0.0013
K	0.0150	0.0244	0.0196	0.0029	0.0015	0.0040
F	0.0000	0.0000	0.0000	0.0000	0.0000	0.0000
Cl	0.0165	0.0142	0.0166	0.0368	0.0176	0.0240
OH	7.9835	7.9858	7.9834	7.9632	7.9824	7.9760
Fe(total)	3.3847	3.0374	3.0986	2.1378	2.0058	2.0042
Fe/(Fe+Mg)	0.6875	0.6205	0.6295	0.4555	0.4256	0.4221
$Mg/(Mg+Fe^{2+})$	0.3178	0.3825	0.3709	0.5473	0.5761	0.5879

Table 5. End-members and temperature (°C) estimated using chlorite composition and distinct geothermeters: [1] Cathelineau and Nieva (1985); [2] Cathelineau and Nieva (1985); [3] Kranidiotis and MacLean (1987); [4] Cathelineau (1988); [5] Kavalieris *et al.* (1990); [6] Jowett (1991); [7] Hiller and Velde (1991); [8] Zang and Fyfe (1995); [10] El-Sharkawy (2000).

Sample	JAT-28 (166.40)			JAT-03 (130.05)											
Rock	Scp-Hast-Bt mylonite			Ore (Mineralization stage IV)											
Mineral	Chl (I)			Chl (II)											
Zane and Weiss (1998)	Fe chlorite			Mg chlorite											
Wiewiora and Weiss (1990)	Chamosite			Clinochlore											
Geothermometer (°C)															
[1] **TCN85-Al^{IV}**	264	264	260	281	287	286	296	298	296	307	301	290	294	290	297
[2] **TCN85-OV**	281	281	281	281	281	281	281	281	281	281	281	281	281	281	281
[3] **TKML87-Al^{IV}**	320	314	311	316	322	322	334	336	330	344	337	326	330	326	333
[4] **TC88-Al^{IV}**	319	318	312	344	353	352	367	370	366	384	374	357	364	358	369
[5] **TK90-Si**	228	227	218	266	281	278	305	311	303	336	318	288	300	289	308
[6] **TJ91-Al^{IV}**	330	327	321	346	356	354	370	374	368	386	377	360	367	361	371
[7] **THV91-Al^{IV}**	265	264	254	304	318	316	340	345	338	366	351	325	335	326	342
[8] **TZF95-Al^{IV}**	236	242	237	279	284	282	290	292	294	303	297	286	291	287	294
[9] **TES00-Al^{IV}**	215	222	216	261	265	263	271	273	275	284	278	267	272	268	275
Temperature Interval	**215 to 330**			**261 to 386**											

Magnetite

Representative analyses of magnetite compositions are presented in the Table 6.

Magnetite occurs in five generations in the Jatobá deposit (Fig. 8). The first generation of magnetite (I) occurs in metadiabase with preserved subophitic texture and is characterized by its trellis texture. The pre-tectonic magnetite (II) infills amygdales and replaces the host rocks in pervasive alteration fronts. Magnetite (III) occurs as thick and deformed crystals in early veins, whereas magnetite (III) forms massive magnetite-(apatite) bodies. The syn-tectonic magnetite (IV) was coeval to the mineralization (I) stage.

The analytical results obtained for different generations of magnetite show variable Ti contents (Mag II = < 2059 ppm; Mag IV = 49 to 2741 ppm; Mag V = < 2224 ppm) with the highest values in magnetite from early veins (III; Ti = < 29,700 ppm). Values of chromium (up to 1045 ppm) are higher in syn-tectonic magnetite (V) in relation to other magnetite generations (Mag II = < 279 ppm; Mag III = < 357 ppm; Mag IV = < 325 ppm). The magnetite (V) has also the highest (Cr + Ni + Cu) contents (up to 1632 ppm). In addition, magnetite (IV) and (V) have higher vanadium contents (Mag IV = 2303 to 2343 ppm; Mag V = 1088 to 3200 ppm) in comparison with early magnetite (Mag II = 133 to 1654 ppm; Mag III = 1400 to 1936 ppm). Three samples associated with magnetite (V) have high Ti + V contents (48,944 - 49,145%) and were classified as ulvospinel, whereas two magnetite crystals have distinctly higher Ni/(Cr+Mn) ratios (5.706 – 6.611).

In the spider diagram (Fig. 23), the average composition of each magnetite generation of the Jatobá deposit indicates similarity between pre-tectonic magnetite (II) and syn-tectonic magnetite (V) in relation to Si, Al, Mn, Mg, K and Ti contents. The magnetite (III) has lower Mg and higher Ti and Ca than other magnetite generations at Jatobá. Its average Ca content is only similar to that of skarn deposits. Massive magnetite (IV) is distinct due to its high Si and Mg contents and values of Al, Ti and V comparable to those of Kiruna or iron oxide-apatite (IOA) deposits. All Jatobá magnetite generations have higher Ti contents than those typical of IOCG deposits, according to Dupuis & Beaudoin (2011).

The Figure 24 shows discriminant petrogenetic diagrams for magnetite distributed among the different deposit classes of Dupuis & Beaudoin (2011). The relationship between (Si+Mg) and (Ni+Cr) for Jatobá magnetite allows its distinction from that of magmatic Ni-Cu deposits (Fig. 24 A), which typically exhibits Ni + Cr

values above 0.1 wt.%. The Al/(Zn + Ca) *vs.* Cu/(Si + Ca) plot (Fig. 24 B) also distinguishes the Jatobá magnetite from that of volcanic-hosted massive sulfides (VMS). According to Dupuis & Beaudoin (2011), the magnetite of VMS deposits, commonly, presents high contents of Cu, Zn and Ca and low of Al. However, the magnetite samples of the Jatobá deposit have relatively high values of the Al/(Zn + Ca) ratio (Fig. 24B).

The Ni/(Cr + Mn) versus Ti + V plot (Fig. 24 C) compares the composition of the Jatobá magnetite with that of banded iron formation (BIF) and of Kiruna, IOCG, porphyry copper, and Fe-Ti-V deposits. The Jatobá magnetite has variable (Ti + V) contents (0.031 to 2.243 wt. %) and Ni/(Cr + Mn) ratios (<1.785), which are comparable with those of the high temperature magmatic-hydrothermal porphyry copper, Kiruna and IOCG deposits. The low (Ca + Al + Mn) contents (0.017 to 0.663 wt.%) of the Jatobá magnetite, however, have similarity only with those of the Kiruna magnetite field proposed by Dupuis & Beaudoin (2011) (Fig. 24 D).

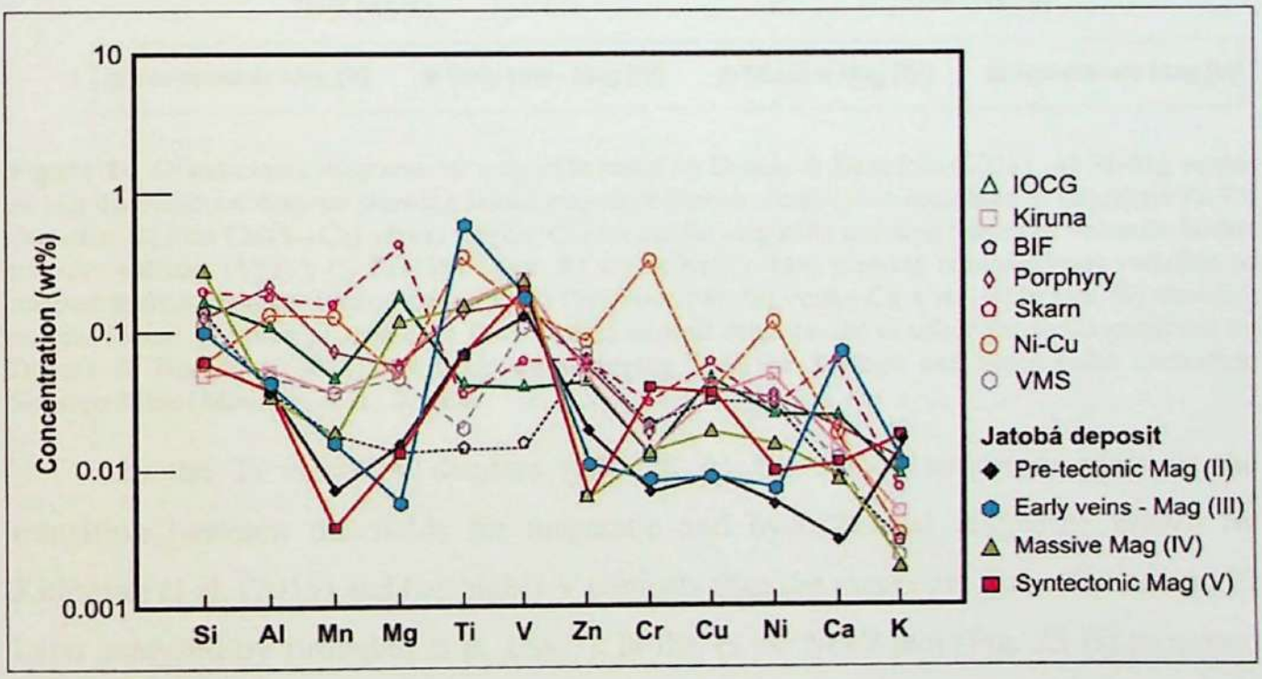

Figure 23. Spider diagram showing the average composition of distinct magnetite generations of the Jatobá deposit and from selected mineral deposits (Dupuis & Beaudoin, 2011).

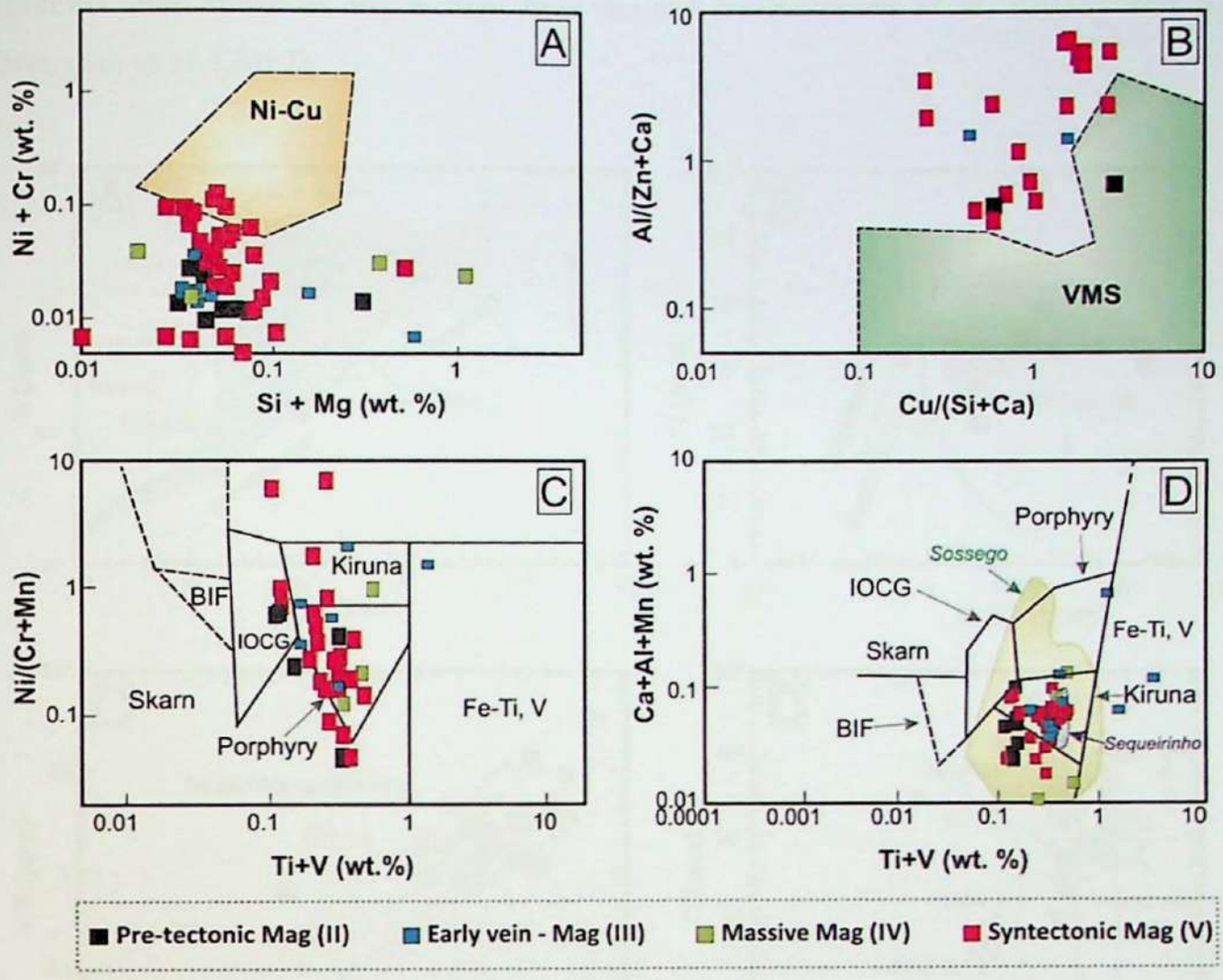

Figure 24. Discriminant diagrams for magnetite based on Dupuis & Beaudoin (2011). A) Si+Mg versus Ni+Cr discriminant diagram showing Jatobá magnetite deposit composition compared to magmatic Ni-Cu deposits; B) Plot Cu/(Si+Ca) versus Al/(Zn+Ca) for Jatobá magnetite and iron oxides of volcanic-hosted massive sulfides (VMS); C) Plot Ti+V (wt. %) versus Ni/(Cr+Mn) showing compositional variation of magnetite from distinct mineral deposits; D) Plot Ti+V (wt. %) versus Ca + Al + Mn (wt. %) showing compositional variation of magnetite from distinct mineral deposits, the discriminant fields proposed by Dupuis & Beaudoin (2011) and fields for magnetite from the Sossego and Sequeirinho orebodies, Sossego Mine (Monteiro et al., 2008b).

In the Ti versus V diagram (Fig. 25 A), the Jatobá magnetite plots in the transition between the fields for magmatic and hydrothermal magnetite drawn by Knipping et al. (2015) and has higher V contents than ore magnetite from Kiruna and El Laco analysed by Broughm et al. (2017). In the Ti vs. Ni/Cr plot (Fig. 25 B) proposed by Dare et al. (2014) to discriminate between magmatic and hydrothermal environments for magnetite formation, the Jatobá magnetite plots in the hydrothermal field. Its composition partially overlaps that of the Kiruna ore magnetite analysed by Broughm et al. (2017). The relationship between the V/Ti and Ni/Ti ratios (Fig. 25 C) for magnetite at Jatobá is also similar to that of magnetite-apatite ore field proposed by Loberg and Horndahl (1983) and to those of magnetite samples of Kiruna and El Laco reported by Broughm et al. (2017). However, the Jatobá magnetite has higher chromium (Fig. 25D)

contents than those of the Kiruna field defined by Knipping et al. (2015) and by Broughm et al. (2017).

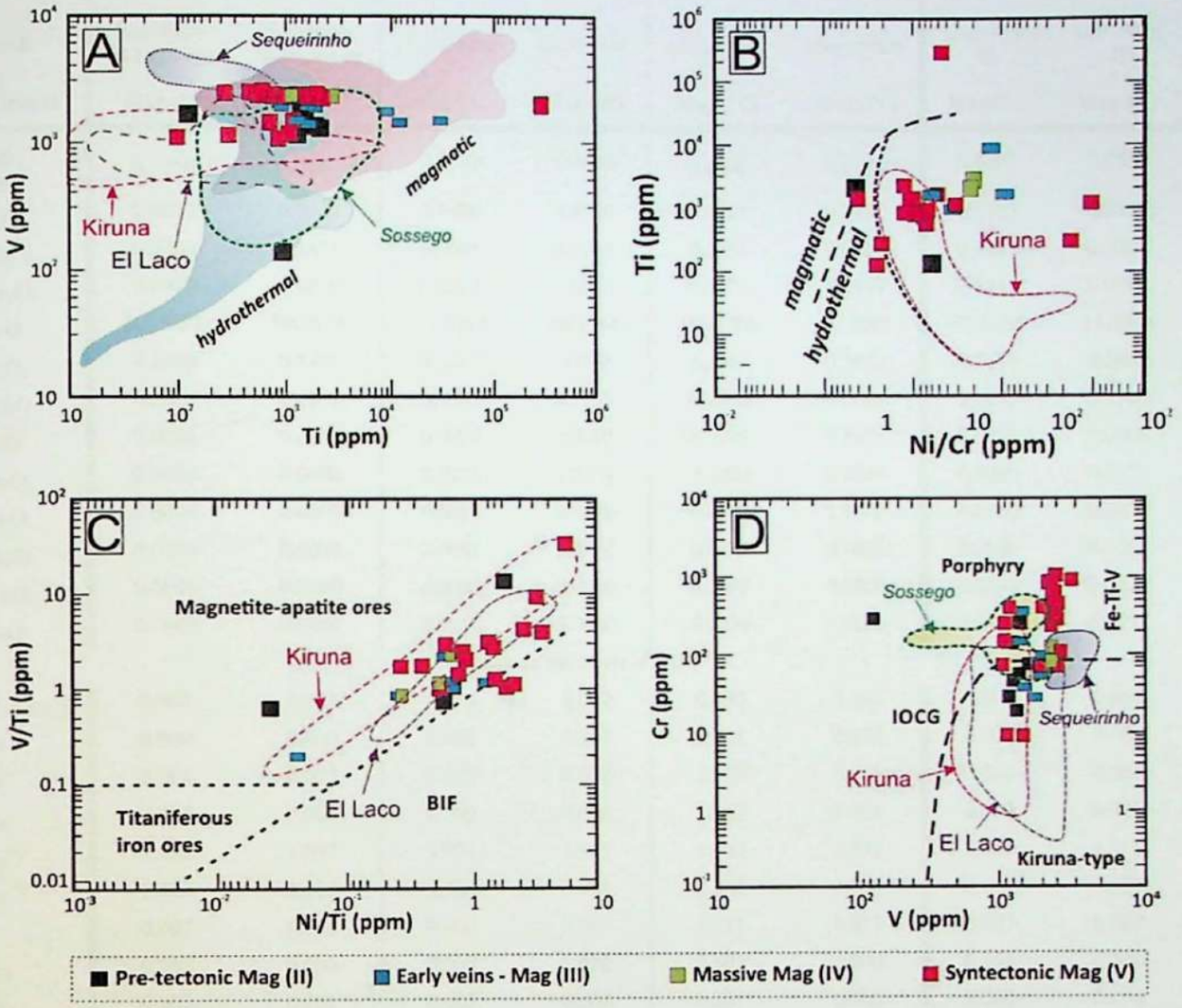

Figure 25. A) Ti vs. V plot showing distribution of Jatobá magnetite and fields for magmatic and hydrothermal magnetite drawn by Knipping et al. (2015); B) Ti vs. Ni/Cr plot proposed by Dare et al. (2014) to discriminate between magmatic and hydrothermal environments for magnetite formation with samples from this study plotted. The dotted blue line separates magnetite from intrusive rocks from the ore magnetite of Kiruna, according to Broughm *et al.* (2017); C) V/Ti vs. Ni/Ti plot with fields for magnetite-apatite ores, BIF and titaniferous iron ores proposed by Loberg and Horndahl (1983); D) Cr vs. V plot discriminating Kiruna type from IOCG, porphyry and titaniferous iron ore deposits by Knipping et al. (2015). The fields for Kiruna and El Laco ore magnetite identified by dotted lines were delimited by samples analysed by Broughm et al. (2017) and those for magnetite from the Sossego and Sequeirinho orebodies, Sossego Mine are from Monteiro et al. (2008b).

Table 6. Representative analysis of different magnetite generations in the Jatobá deposit.

Event	Pretectonic						Syn-tectonic	
Sample	JATD-28 (91,60m)	JATD-28 (91,60m)	JATD-28 (91,60m)	JATD-28 (91,60m)	JATD-32 (383,00m)	JATD-32 (383,00m)	JATD-28 (160,40m)	JATD-28 (160,40m)
Rock	Scp-Hast-Bt-mylonite	Scp-Hast-Bt-mylonite	Early vein	Early vein	Magnetitite	Magnetitite	Ore -Min II	Ore -Min II
Mineral	Mag (II)	Mag (II)	Mag (III)	Mag (III)	Mag (IV)	Mag (IV)	Mag (V)	Mag (V)
SiO_2 wt%	0.0766	0.0682	0.0780	0.0420	0.0000	0.0773	0.1067	0.0587
TiO_2	0.0000	0.0000	2.0300	4.9500	0.1715	0.4572	0.1957	48.8600
Al_2O_3	0.0764	0.1457	0.0698	0.0342	0.1054	0.0268	0.0289	0.0302
Cr_2O_3	0.0079	0.0026	0.0522	0.0055	0.0475	0.0119	0.0013	0.0099
FeO	93.3992	93.2013	91.4647	88.1444	93.7592	93.9031	93.3183	48.0043
V_2O_3	0.2040	0.1951	0.2117	0.2186	0.3447	0.3422	0.2187	0.2851
MnO	0.0075	0.0245	0.0303	0.1258	0.0346	0.0000	0.0023	0.1749
NiO	0.0086	0.0154	0.0000	0.0000	0.0093	0.0101	0.0238	0.0000
ZnO	0.0000	0.0000	0.0225	0.0269	0.0000	0.0049	0.0000	0.0171
CaO	0.0000	0.0000	0.0018	0.0000	0.0000	0.0000	0.0000	0.0000
MgO	0.0224	0.0000	0.0031	0.0428	0.0325	0.0020	0.0000	0.0161
CuO	0.0000	0.0000	0.0000	0.0000	0.0607	0.0000	0.0247	0.0125
K_2O	0.0000	0.0000	0.0113	0.0000	0.0034	0.0055	0.0428	0.0157
			Ions on the basis of 4 O					
Si *a.p.u.f.*	0.003	0.003	0.003	0.002	0.000	0.003	0.004	0.002
Ti	0.000	0.000	0.061	0.147	0.005	0.014	0.006	1.100
Al	0.004	0.007	0.003	0.002	0.005	0.001	0.001	0.001
Cr	0.000	0.000	0.002	0.000	0.002	0.000	0.000	0.000
Fe^{+3}	1.991	1.992	1.991	1.995	2.000	1.991	1.987	1.995
Fe^{+2}	0.405	0.400	0.320	0.195	0.382	0.389	0.402	-1.093
V	0.007	0.006	0.007	0.007	0.011	0.011	0.007	0.007
Cu	0.000	0.000	0.000	0.000	0.002	0.000	0.001	0.000
Mn	0.000	0.001	0.001	0.004	0.001	0.000	0.000	0.004
Ni	0.000	0.001	0.000	0.000	0.000	0.000	0.001	0.000
K	0.000	0.000	0.001	0.000	0.000	0.000	0.002	0.001
Ca	0.787	0.788	0.775	0.763	0.781	0.778	0.785	0.577
Mg	0.001	0.000	0.000	0.003	0.002	0.000	0.000	0.001
Zn	0.000	0.000	0.001	0.001	0.000	0.000	0.000	0.000
TOTAL	3.198	3.198	3.165	3.119	3.192	3.188	3.197	2.595

5. Discussion

Host Rocks

This contribution includes the first detailed studies on the geological characterization of the Jatobá deposit, including the nature of host rocks, the hydrothermal alteration patterns and mineralizing events, with emphasis on changes in mineral chemistry in an evolving mineral system.

The Jatobá deposit, in the Carajás Province, is located about 3 km north of the Sossego Mine, a world-class iron oxide-copper-gold deposit (IOCG), which is notable by its deep-intermediate and shallow-crustal level alteration zones (Monteiro et al, 2008a, 2008b) developed during Neoarchean and Paleoproterozoic metallogenetic events, respectively (Moreto et al., 2015a). Both deposits are associated with the WNW-ESE regional Canaã shear zone that defines the southern contact of the ca. 2.76 – 2.73 Ga metavolcanosedimentary Itacaiúnas Supergroup with Mesoarchean units, including ca. 2.97 Ga greenstone belts and TTG-like granitoids (e.g. ca. 3.0 Ga Sequeirinho Tonalite; Moreto et al., 2015a). Both the Itacaiúnas Supergroup and its basement are cut by ca. 2.74 Ga and ca. 1.88 Ga A-type granites and gabbros. However, there is an important difference regarding the geological setting of the Sossego and Jatobá deposits. While the first one is hosted by the Mesoarchaean units crosscut by Neoarchean intrusive rocks, the Jatobá deposit is essentially hosted by metavolcanosedimentary units and metadiabase.

The main host rocks of the Jatobá deposit comprise metarhyodacite and amygdaloidal metabasalt, in addition to felsic metavolcaniclastic breccias and mafic metatuffs, which are cut by metadiabase (Fig. 3). The metarhyodacite has bluish bipyramidal and embayed quartz blastophenocrysts (paramorphs after B-quartz) with features typically associated with their circulation in the magma chamber, causing dissolution and rotation of these crystallized phenocrysts in the warmer zones of the magma chamber (Fig. 3B and C).

The pyroclastic rocks are distributed in limited areas in the Jatobá deposit, suggesting that the eruption emitted alternately lavas and pyroclasts, forming alternated consolidated rock beds from lava and layers of pyroclastic material, usually loose. Regionally, the metabasalts are expressive and have a spatial relationship with banded iron formations, not recognized in the Jatobá area. This set of geological units can be correlated with those of the Neoarchean Itacaiúnas Supergroup (DOCEGEO, 1988), which hosts huge iron deposits at Carajás (e.g. S11D, N4).

This set of rocks was intensely modified by hydrothermal alteration previously and concomitant to the installation of the Canaã shear zone. Thus, the hydrothermal alteration in the Jatobá deposit has, in a large extent, an important structural control, which facilitated the channelized flow of hydrothermal fluids in the system. However, in regions farther away from the central focus of hydrothermalism, there are rocks without evidences of any deformation, but presenting intense metasomatism, suggesting

that hydrothermalism was not restricted to the main shear corridor, but represented a pervasive process.

Hydrothermal alteration and chemical evolution

The distribution of the hydrothermal alteration in the Jatobá deposit was governed by the nature of host rocks and hydrothermal fluids, and by the crustal level at which it was established, as well as observed in the IOCG deposits worldwide (Hitzman et al., 1992, Hitzman 2000). Usually, these deposits comprise alteration trends in a vertical pattern, in which deep (magnetite-rich) alteration zones are controlled by ductile shear zones and shallow (hematite-rich) zones are linked to brittle structures. In the Jatobá deposit, magnetite is predominant, but an evolving system resulted in pre-, syn, and post-tectonic alteration with telescoping characteristics. Late alteration encompasses stages controlled by ductile-brittle to brittle structures (Fig. 5)

Despite the general evolution from sodic, iron, (sodic)-calcic, potassic to chlorite alteration, the types and stages of hydrothermal alteration recognized in the Jatobá deposit have important differences in relation to those of the Sossego deposit (Rosa, 2006; Monteiro et al., 2008a, 2008b). The extensive syn-tectonic scapolite-hastingsite-biotite alteration zones at Jatobá are only recognized in the footwall zone of the Sossego deposit, in distal (and barren) portions in relation to orebodies (Monteiro *et al.* 2008a). Massive magnetite-(apatite) bodies enveloped by actinolite-rich zones were recognized Sequeirinho orebody (Sossego Mine) and Jatobá deposit, however their spatial relationship with nickel-enriched pyrrhotite-bearing mineralized zones was only identified at Jatobá.

In the Jatobá deposit, the least-altered and deformed rocks, mainly derived from mafic protoliths, possibly record effects of the lower greenschist facies metamorphism. Albite (I) and actinolite (I) represent early paragenesis in such rocks, and were formed from calcic plagioclase and pyroxene. The first generation of magnetite (I) occurs in metadiabase rocks with preserved subophitic texture and is characterized by its trellis texture.

Pre-tectonic hydrothermal alteration is represented by silicification and coeval biotite (I), apatite (I) and magnetite (II), mainly recognized in pervasive fronts in metarhyodacites and infilling of amygdales in metabasalts. In addition, incipient sodic-calcic alteration resulted in formation of albite (II), scapolite (I), and Cl-rich amphibole (ferro-pargasite, potassium-ferro-pargasite, ferri-cannilloite and ferro-ferri-

tschermakite) that replaces actinolite (I) along crystal rims. This generation of amphibole has higher contents of Fe^{2+}, Al^{IV}, Cl, Na, K and $Fe_t/(Fe_t + Mg)$ ratios and lower Mg contents in relation to actinolite (I). Calcic marialite (I) initially replaces preexisting igneous plagioclase that, in part, exercises control in scapolite composition (Kullerud, 1996), and hydrothermal albite. In this stage, amphibole has up to 2.95 % Cl and calcic marialite has 2.30 to 2.58% of Cl.

Due to the shear zone installation, the scapolite (I) crystals were deformed and occur as almond-shaped porphyroclasts envolved by pressure shadows. Scapolite (II) with calcic marialite compositions and higher Cl (2.34 to 3.38%) contents was formed in their rims. In metarhyodacite, pervasive calcic alteration resulted in development of actinolite (II) associated with Cl-apatite, Ce-allanite, and Ce-monazite. Actinolite (II), however, has low amounts of Cl (<0.03%), suggesting preferential partitioning of chlorine in apatite. In altered rocks derived from mafic protoliths, K-Cl-Hastingsite (I) was coeval to biotite (II), quartz, Co-magnetite, Cl-apatite and Ce-allanite. Both K-Cl-hastingsite (1.07 to 2.38% of Cl) and biotite (1.14 to 1.37 % of Cl) have significant chlorine contents.

The Jatobá deposit still records transitional conditions from a ductile structural regime to a dominantly ductile-brittle regime, which controlled the development of pervasive fronts of chlorite alteration and late vein systems. Late tectonic hydrothermal alteration is represented by expressive veins with fibrous scapolite (III) that has the highest Cl contents (3.12 – 3.60 %). These veins are cut by scapolite (IV; Cl = 2.71 – 3.18 %), Cl-K-hastingsite (II; Cl = 3.02 – 3.39 %) and biotite (III; Cl = 2.15 – 3.19 %) veinlets.

Overall, despite the recurrence and telescoping of hydrothermal alteration, the distinct mineral generations have significant differences in mineral chemistry. The pre-tectonic scapolite (I) from distal zones in relation to mineralized zones, the syn-tectonic scapolite (II) porfiroblasts in mylonitic zones, and the post-tectonic fibrous scapolite (III) from veins reveal gradual increasing of Cl (0.798-1.016 apfu), Si and Na contents during the paragenetic evolution. The scapolite (IV) from late veinlets, however, is not part of the same trend defined by previous scapolite generations and has intermediate Si, Na, Ca, Al^{IV} and Cl contents (Cl = 0.764-0.897 apfu).

According to Holland (1972) and Kullerud (1996), in an evolved system, chlorine is progressively enriched in the fluid phase whereas H_2O is incorporated in hydrated minerals, indicating that hipersaline fluids have participated in the alteration

process. This may explain the gradual increase of Cl contents in scapolite (I) to (III).

The expressive fibrous scapolite veins may be related to episodic influx of supersaturated fluids. This could indicate buffering of chlorine activities and low or no infiltration of diluted fluids during and posterior to shear zone development at Jatobá (Jiang *et al.* 1994; Mora & Valley 1989). According to experiments by Vanko & Bishop (1980) and Vanko (1982) on the stability of the marialite escapolite, hydrothermal solutions with temperatures of approximately 600 to 750 °C and pressures between 1.7 to 2.8 kbar could favour its formation. This may imply that high temperature also prevailed during the long-term system evolution.

Chlorine-bearing amphibole and biotite are also ubiquitous in the Jatobá deposit. In general, ferro-pargasite from distal zones and hastingsite (I) and (II) of mineralized zones have higher Cl contents than actinolite (I) and (II). The lowest Cl contents are related to actinolite (II) from early mineralization zones, which is spatially related to massive magnetite-(apatite) bodies.

The chlorine content in biotite defines two main groups for this mineral, allowing to separate biotite related to ductile and ductile-brittle to brittle structures. The group 1 encompasses distal pre-tectonic biotite (I) and syn-tectonic biotite (II) from proximal and mineralization zones. This group is characterized by its lower Cl and relatively higher Mg and Ti contents in relation to group 2. Its higher Ti contents are consistent with higher temperature of biotite formation from group I. The group 2 comprises late biotite (III) from mineralized and barren zones, which has higher Cl, Na and Fe^{2+} contents. Interestingly, in the two groups, biotite from barren and mineralized zones can be also differentiated. In group 1, biotite (II) from mineralized zones is distinct from biotite (II) from proximal domains due to its relatively high Cl contents and negative correlation between Cl and Fe^{2+}. In group 2, biotite (III) from barren zones has lower Ti contents, which may reflect lower temperature.

In general, the Cl content in amphibole and biotite is in accordance with the Mg-Cl avoidance rule (or Fe-F; Ramberg, 1952). This rule refers to the effect of the strong binding forces between Mg and F and the weak binding forces between Fe and F. In general, Fe-Cl bonds are strongly preferred over the Mg-Cl bonds in silicates (Munoz & Swenson 1981, Munoz 1984). This may explain the lower Cl contents in actinolite in relation to hastingsite and higher Cl contents in lower temperature Fe-richer biotite from group 2. However, this rule does not explain the negative correlation between Cl and

Fe^{2+} in biotite (II) from mineralized zones. Its composition may be controlled by the preferential Cl partitioning into coeval mineral phases.

Chlorite alteration developed in the transition from ductile structural regime to a dominantly ductile-brittle regime, resulting in chlorite from distal (I) and mineralized zones (II). The first is the product of replacement of scapolite, amphibole, and biotite and has chamosite composition and $Fe^{2+}/(Fe^{2+} + Mg)$ ratios between 0.62 and 0.68. The chlorite (II) is associated with the mineralization stage (IV) and has clinochlore composition with $Fe^{2+}/(Fe^{2+} + Mg)$ ratios between 0.40 and 0.45. Chlorite contents are low in both chlorite generations (0.08 to 0.21 % Cl) in accordance with the Mg-Cl avoidance rule. However, fluid dilution is also suggested by destabilization of preexinting scapolite (III) that shows retrograde alteration to sericite, pyrophyllite, chlorite, albite and carbonate.

Different chlorite geothermometers result in significant differences in estimated temperature, with maximum values of 330 °C for chlorite from distal zones and 386 °C for chlorite (II), according to Jowett (1991). This points to temperature decrease in late stages of the system evolution.

Hydrothermal iron oxides and massive magnetite formation

Minor elements in magnetite have been measured using EMPA method, which, according to Depuis & Beaudoin (2011), has a higher spatial resolution (<10 μm) compared to the lower spatial resolution for LA-ICP-MS analyses (>50 μm) and allows selecting analytical spot to avoid submicrometric inclusions.

The magnetite composition is controlled by the chemical environment in which it grows and by physico-chemical conditions during its formation (Beaudoin et al., 2007; Depuis & Beaudoin, 2007; Nadoll et al., 2014). Although the mechanisms of trace element partitioning between iron oxides and hydrothermal solutions are relatively little known, distinction of magmatic and hydrothermal magnetite has been attempted. Ti, V and Cr are the best discriminators as their depletion is often seen in magnetite from known hydrothermal deposits (Nadoll et al., 2014). Hydrothermal oxidized fluids could enhance the mobility of Cr^{6+} that may be transported out of the ore-forming system and lower Cr contents are expected in hydrothermal magnetite (Broughm et al. 2017).

Aluminiun and Ti are relatively immobile and their incorporation in magnetite is largely temperature controlled (Nielsen et al. 1994; Toplis and Carroll 1995), with

higher concentrations expected under high-temperature igneous conditions (Nadoll et al., 2014). According to Dare et al. (2014) and Nadoll et al. (2014a), in general only about 10% of the hydrothermal magnetite have more than 1 wt% of Ti. On the other hand, oxygen fugacity exerts a strong control on multivalent elements, such as Cr and V, which are preferably incorporated into the magnetite under reduced conditions.

Early iron oxide at Jatobá comprises igneous magnetite (I) with trellis texture in metadiabase and magnetite (II) in infilling of amygdales and pervasive alteration fronts. The latter is commonly stretched in deformed domains (Fig. 7). Early veins are infilled by quartz and magnetite (III), which occurs as large crystals in veins and veinlets. Commonly magnetite (III) is deformed and has ilmenite lamellae according to different crystallographic planes. In addition, magnetite is replaced by ilmenite, which in turn is substituted by titanite, hematite, brookite/rutile and pseudobrookite (Fig. 7).

Massive magnetite bodies (up to 60 m) formed by undeformed magnetite (IV) represent proximal envelopes of mineralized zones. They are well develop along the contact zones between metarhyodacites and metabasalts and within the latter. The bulk of magnetite (IV) is previous to copper-(nickel) mineralization. The massive magnetite bodies are cut and surrounded by fibrous actinolite (II), Cl-apatite and sulfides, which promote their brecciation.

The magnetite (V) is syn-tectonic, related to the shear zone development, and coeval to the early Ni-pyrrhotite and Ni-pyrite-bearing mineralization event. Ulvöspinel occurs associated with euhedric magnetite (V) crystals. Very subordinated magnetite also occurs in the subsequent copper mineralization events, coeval to biotite and chlorite formation, in decresing amounts.

In the Jatobá deposit, magnetite has variable Ti contents (Mag II = <LOD to 2059 ppm; Mag IV = 49 – 2741 ppm; Mt V = <LOD to 2224 ppm) with the highest values in magnetite from early veins (III; Ti = 0 – 29,700 ppm). Except in relation to the latter, all analyses indicate Ti contents typical of hydrothermal origin. However, Ti concentation in Jatobá magnetite is highly erratic and the coexistence of ulvölspinel and ilmenite, as lamellae in magnetite and individual grains, point to oxidation-exsolution mechanisms, accompanied by local redistribution of Ti and other elements.

Evidences of oxidation-exsolution are more common in magmatic magnetite because the continuous solid solution between magnetite and ulvöspinel exists when temperatures above 600 °C are achieved. When reaching temperatures below 600 °C extensive miscability gaps occur (Nesser, 2009; Nadoll, 2011). A diminishing

temperature also leads to the potential exsolution of ilmenite out of Ti-bearing magnetite, which results in lower levels of Ti in the concerned magnetite grain (Nesser, 2009). Thus, the coexistence of magnetite (IV)-ulvöspinel and magnetite (V)-ilmenite- could point to high-temperature (> 600 °C) conditions of formation and explain the data spreading.

In addition, the magnetite (V) has also the highest (Cr + Ni + Cu) contents (up to 1632 ppm), whereas magnetite (IV) and (V) are relatively enriched in vanadium (Mag IV = 2303 – 2343 ppm; Mag V = 1088 – 3200 ppm) in comparison with early magnetite (Mag II = 133 -1654 ppm; Mag III = 1400 – 1936 ppm). According to Nadoll et al. (2014), lower V concentrations are indicative of hydrothermal origin, because roughly 50% of hydrothermal magnetite has vanadium concentration below 1000 ppm. Often only in high-temperature hydrothermal fluids (about 500-700 °C) associated with a magmatic-hydrothermal source (e.g. porphyry and IOCG) the magnetite is enriched in the compatible elements Ni, V, Co, Zn, Mn and, Sn (Dare et al., 2014). Thus, the higher V and Cr concentration in Jatobá magnetite also point to higher temperature conditions even during the early nickel-enriched mineralization event, coeval to magnetite (V)-actinolite-apatite formation.

The use of discriminant petrogenetic diagrams for environment of magnetite formation should be done with caution. Recent studies conducted by Broughm et al. (2017) using the LA-ICP-MS technique showed distinct compositions for magnetite from the Kiruna and El Laco areas, when compared to those of the Kiruna field in the discriminant diagrams of Depuis & Beaudoin et al. (2011). Therefore in the present study the representative fields of the samples analysed by Broughm et al. (2017) were also considered.

The discriminant petrogenetic diagrams (Fig. 24) proposed by Depuis & Beaudoin et al. (2007) effectively allow the distinction of the Jatobá magnetite from that of magmatic Ni-Cu and Fe-Ti-V deposits, hydrothermal skarns and volcanic-hosted massive sulfide (VMS) deposits and banded iron formation. In addition, the Jatobá magnetite has similarities with that formed in high-temperature magmatic-hydrothermal porphyry copper, Kiruna-type apatite–magnetite deposits, and IOCG deposits (e.g., Ti + V contents = 0.031 to 2.243 wt. %; Ni/Cr + Mn contents up to 1.785). Its low Ca + Al + Mn contents (0.017 to 0.663 wt.%), however, are only comparable to those of the Kiruna magnetite (Fig. 24D). The comparison of Jatobá magnetite composition with that of iron oxide-apatite ore analysed by Broughm et al. (2017) in terms of V and Ti

contents and Ni/Cr, Ni/Ti and V/Ti ratios also underscores the similarity of Jatobá magnetite with that of Kiruna and El Laco areas (Fig. 24).

This could indicate that iron oxide and related copper-(nickel) mineralization at Jatobá were formed in deeper and hotter conditions than those typically related to copper precipitation in IOCG deposits. This is consistent with the model for the IOCG deposit class proposed by Hitzman et al. (1992), Barton and Johnson (1996), Hitzman (2000) and Sillitoe (2003), which considers that magnetite-apatite bodies may be formed in the roots of IOCG systems and magnetite-apatite ore deposits may represent an end-member of the IOCG clan. In this context, IOCG and IOA deposits would be formed by the replacement of the host rocks by iron-rich hydrothermal fluids (e.g., Hitzman et al. 1992; Rhodes and Oreskes 1999; Hitzman 2000; Dare et al. 2015).

However, the formation of magnetite-apatite deposits is even more controversial than that of IOCG deposits. Other genetic models for the formation of magnetite and apatite in IOA deposits include their crystallization from iron-rich melts that were immiscible from a parental silicate melt producing large volumes of massive magnetite (e.g., Henríquez and Martin 1978; Nyström et al. 2008; Martinsson 2016; Tornos et al. 2016). According to the magmatic model, the crystallization of iron-rich melts was accompanied by the exsolution of large amounts of magmatic-hydrothermal fluids (Tornos et al. 2016), resulting in the highly variable magnetite composition in IOA deposits.

In the Jatobá deposit, where a hydrothermal evolution is now well-documented, evidences for a linkage with immiscible iron-rich melts are missing. However, advances should be achieved in order to establish the relationship between the hydrothermal IOCG system at Carajás and the crystallization of a specific melt type, if one exists.

The Jatobá magnetite has intermediate composition in relation to that of magnetite from the Sequeirinho and Sossego orebodies of the Sossego mine (Monteiro *et al.*, 2008b), in terms of Ti, V, and Ca + Al + Mn contents (Fig. 24D). This is interesting because magnetite from the Sequeirinho orebody constitutes pre-mineralization massive magnetite bodies, similar to those identified at Jatobá, whereas Sossego magnetite represents early infill in chalcopyrite-bearing veins and breccias formed in shallow crustal conditions. In part, similarities of Jatobá and Sossego magnetite composition revealed by the spreading of Ti data may be explained by oxidation-exsolution reactions and retrograde alteration of magnetite. The highest Cr contents of the Jatobá magnetite, however, implies, in relatively more reducing

conditions, as also indicated by its higher pyrrhotite contents.

(Nickel)-copper mineralization

The copper-gold mineralized zones in the Jatobá deposit comprise swarms of vertical to subvertical orebodies spatially related to metadiabase dikes and contact zones between rhyodacites and metabasalts. Mineralization styles include disseminations, massive ore in replacement fronts controlled by the mylonitic foliation, hydrothermal breccias, stockworks, vein and veinlet systems. The mineralized zones were formed in four stages. The first two were controlled by ductile structures, evolving from replacement fronts controlled by mylonitic foliation to breccias. The last two stages were coeval to ductile-brittle and brittle deformational events.

The mineralization stage (I) was related to syn-tectonic calcic alteration (II), especially to actinolite formation in metarhyodacites, and is the nickel-richer stage at Jatobá. Replacement fronts and breccias have predominance of Ni-pyrrhotite and Ni-pyrite, and subordinately, Co-chalcopyrite, Ce-allanite, Co-pentlandite, quartz and Ce-monazite. In addition, fine Ni-pyrrhotite crystals, actinolite (III), magnetite (IV) and subordinate quartz constitute replacement fronts and brecciated zones with up to 40 cm. This mineralization stage is characterized by enrichment in Fe-Ni-(Cu)-Co-LREE and evidence hydrothermal nickel transport under relatively high fS_2, salinity and temperature conditions, compatible with those of magmatic-hydrothermal systems (Tian *et al.* 2012).

According to Tian et al. (2012), increasing salinity favors the formation of $NiCl_3^-$ complexes, which is believed to play an important role in Ni transport in Cl-rich hydrothermal fluids under high temperature conditions. In addition, according to these authors, the transition of Ni (II) chloride complexes from octahedral to tetrahedral is of major importance for nickel solubility in hydrothermal systems. This transition, however, occurs at higher temperature and/or salinity than the corresponding Co(II) complexes (Liu et al., 2011). Such differences can explain the sharp contrast in mobility of Ni and Co in hydrothermal brines, with much of the World's cobalt resources found in hydrothermal deposits while the vast majority of Ni resources are mined from higher temperature magmatic deposits (Tian et al., 2012). Thus, the relative nickel enrichment in the mineralization stage (I) may also reflect a particularly hot hydrothermal system.

In addition, the geological setting of the Jatobá deposit, which is close to the contact between the Neoarchean Itacaiúnas Supergroup and Mesoarchean greenstone belt, is highly favourable for metal leaching from mafic and mafic-ultramafic rocks.

The mineralization (II) stage was temporal and spatially related to the development of the syn-tectonic potassic alteration (II), which is pervasively developed in the main host rocks of the Jatobá deposit. This stage is represented by a system of strongly oriented and interconnected bodies with biotite (II), Cl-apatite, Co-magnetite, ilmenite, Ce-allanite, quartz, Ni-pyrite and Co-chalcopyrite controlled by mylonitic foliation. Hydrothermal breccia zones with expressive formation of Co-chalcopyrite (± Ni-pyrite ± Ni-pyrrhotite) affecting the preexisting bodies of massive magnetite are also observed.

The occurrence of the (nickel)-copper mineralization developed in the mylonitic zones in the Jatobá deposit may be in part attributed to the circulation of mineralizing fluids through the structural discontinuities (Sibson, 1994). However, in relatively deep crustal levels, such as in mylonitic zones, the porosity of the rocks is strongly reduced to make the system fertile. On the other hand, the circulation of mineralizing fluids and associated hydrothermal alterations, at deep levels, can also be given by altering the properties or composition of the circulating hydrothermal fluid. In this sense, the fluid-rock interaction (Groves & Phillips 1987), promotes the metal precipitation due to changes in the physical-chemical properties of a fluid.

The coexistence of hydrothermal breccias during the early mineralization stages could be related to episodic and localized decompression due to fluid overpressure and hydrofracture. This may imply in litostatic pressure probably lower than the pressure exerted by the hydrothermal fluids, which were being channeled in the shear corridor. In this sense, significant copper precipitation may be synchrounous to brecciation events.

The third mineralizing stage recognized in the Jatobá deposit is distinguished from the others because it is controlled by ductile-brittle and associated with veins. It was coeval to the late paler brown or green biotite (III), scapolite (IV), F-Cl-apatite (IV), and Cl-K hastingsite (II) associated with Co-chalcopyrite and siegenite (± Co-pyrite ± magnetite ± cassiterite). Even during this stage, scapolite stability indicates buffering of chlorine activities. Chlorine incorporation in scapolite and other minerals, however, may have contributed to lowering the fluid salinity and destabilize the chloride copper complexes, permitting chalcopyrite precipitation.

The late mineralization stage (IV) was synchronous to widespread chlorite (II), quartz, epidote, and calcite development. It occurs in a variety of branching veinlets and brechoid zones with Co-chalcopyrite, Co-pyrite, sphalerite, gold, molybdenite, uraninite and monazite. Other late vein types comprise those with quartz-chalcopyrite-K (±molybdenite, Co-pentlandite, and siegenite) and fine veinlets with chlorite-chalcopyrite, W-bearing hematite, rare earth carbonates (bastnäsite, coskrenite and sahamalite), Co- and Ni-pyrite, sphalerite, ilmenite, marcasite, leucoxene and adularia.

The decrease in temperature from > 600 °C to < 350 °C, indicated by chlorite geothermometry, likely promoted the precipitation of metals transported as chloride complexes from hydrothermal fluids. However, in depth, the temperature gradients across the structures within which the fluids are moving tend to be minimal and the precipitation of the metal will neither be efficient nor very restricted to a particular trap zone. Thus, a continuous evolution from mineralization stages (I) to (IV) is unlikely unless significant fluid mixing has occurred. However, the scapolite composition reflects a buffered system in respect to chlorine activity, without significant contribution of diluted, external derived fluids. Other mechanism is necessary to explain the sharp temperature decrease. Overpressuring associated with significant system exhumation may be associated with the bulk of copper precipitation.

The world-class Sossego deposit, located 3 km south the Jatobá deposit, records multiple hydrothermal events responsible for formation of ore at ca. 2.70 Ga-2.68 Ga (e.g. Sequeirinho and Pista orebodies) and ca. 1.88 Ga (e.g. Sossego orebody; Moreto et al., 2015a). The Neoarchean IOCG mineralization was formed in deeper crustal levels, whereas the Paleoproterozoic Sossego orebody was controlled by brittle structures. Precise geochronological data is still necessary to constrain the timing of copper-(nickel) mineralization at Jatobá. Its geological attributes may record a similar evolution to the Sossego deposit, in which late mineralization stage would represent the overprinting of a shallow-emplaced hydrothermal event. However, the Jatobá deposit may also reflect a protracted evolution in a single event.

6. Conclusions

The Jatobá deposit, in the Carajás Province, is hosted by a metavolcanosedimentary sequence, which encompasses metarhyodacite and amygdaloidal metabasalt, felsic metavolcaniclastic breccias, mafic metatuffs, and

metadiabase attributed to the Neoarchean Itacaiúnas Supergroup. An evolving hydrothermal system resulted in pre-, syn, and post-tectonic alteration with telescoping characteristics. Early alteration and mineralization stages (I-II) were developed in relatively deep crustal levels, controlled by the Canaã shear zone development. Post-tectonic alteration was associated with the mineralization stages (III-IV) after significant system exhumation.

Pre-tectonic hydrothermal alteration includes silicification, potassic, sodic-calcic alteration and iron metasomatism. It evolved from interaction of host rocks with hypersaline hydrothermal fluids and resulted in formation of massive magnetite-apatite bodies, which are spatially related to a system of magnetite-quartz veins. The early hydrothermal magnetite at Jatobá was formed in temperatures exceeding 600 °C and underwent oxidation-exsolution reactions, resulting in variations in the magnetite chemistry. Nevertheless, its composition is similar to that formed in high-temperature magmatic-hydrothermal systems (e.g. IOCG, porphyry copper and IOA deposits). This could indicate that iron oxide formation and related copper-(nickel) mineralization at Jatobá were formed in deeper and hotter conditions than those typically related to copper precipitation in IOCG deposits.

The main syn-tectonic hydrothermal alteration stages comprise sodic-calcic, calcic and potassic alteration controlled by the mylonitic foliation and resulted in extensive syn-tectonic scapolite-hastingsite-biotite alteration zones. The magnetitites are cut by fibrous actinolite, magnetite and Cl-apatite, which also promote their brecciation.

The early mineralization stages (I and II) were coeval to shear zone development and accompanied by actinolite and thereafter by high-temperature biotite formation. These stages reflect an evolving system resulting in decreasing contents of Ni and Co and pyrrhotite and actinolite amounts in ore zones. They also record the transition from replacement fronts controlled by mylonitic foliation to hydraulic breccia zones. Ore bodies comprise Ni-pyrrhotite, Ni-pyrite, and subordinately, Co-chalcopyrite, Co-pentlandite, Co-magnetite, Ce-allanite, monazite and Cl-apatite. These mineralization stages are characterized by enrichment in Fe-Ni-(Cu)-Co-LREE and evidence hydrothermal nickel transport under relatively high fS_2, salinity and temperature conditions. Hereupon, the nickel richer orebodies may be formed in the roots of the IOCG system, resulting from extensive interaction of hipersaline fluids with mafic and mafic-ultramafic rocks (e.g. greenstone belts).

The third and fourth mineralizing stages reflect a change in structural conditions and were controlled by ductile-brittle structures. These stages were coeval to low-temperature biotite and chlorite and have higher chalcopyrite contents and predominance of Co-bearing mineral phases instead of those nickel-bearing present in early mineralization stages. Ore zones are composed of Co-chalcopyrite, Co-pyrite, siegenite and subordinate cassiterite, sphalerite, molybdenite, uraninite, monazite, bastnäsite, coskrenite and sahamalite. Late hematite evidences higher fO_2 conditions in a colder hydrothermal system (< 380 °C).

Amphibole, scapolite and biotite indicate hipersalinity conditions even in late post-tectonic alteration stages. In addition, the chemical composition of biotite permits the distinction of its environment of formation. Biotite formed in early alteration and mineralization stage (II) has lower Cl and relatively higher Mg and Ti contents, reflecting its higher temperature. Biotite from barren and ore zones may be also distinguished based on mineral chemistry. In deeper alteration zones, syn-tectonic biotite from ore zones has higher Cl contents and negative correlation between Cl and Fe^{2+}. In late mineralization stage, biotite from barren zones has lower Ti contents than biotite from mineralized veins and breccias, reflecting its lower temperature.

High contents of Cl in scapolite indicate buffering of chlorine activities and low or no infiltration of diluted fluids during and posterior to shear zone development at Jatobá. This precludes extensive fluid mixing as the main mechanism of fluid evolution and chalcopyrite precipitation.

The Jatobá deposit reveals a protracted evolution, in which the main copper precipitation occurred in lower temperature conditions than the early stage after significant system exhumation. Precise geochronological data is still necessary to constrain the timing of mineralization at Jatobá, allowing correlating the main mineralization stage recorded in this deposit with the geological evolution of the Carajás Province.

ACKNOWLEDGEMENTS

We are very grateful to VALE for the continuous support, especially to geologists Fernando Matos, Sergio Bacelar Hunh, Benevides Aires, and Fabrício Franco. This research has been supported by the INCT Geociências da Amazônia (MCT/CNPq/Fapespa 573733/2008-2), National Council for Scientific and

Technological Development (CNPq Grant 481969/2013-6, 308365/2014-3), and CAPES Scholarship for the first author.

REFERENCES

Almeida, J.A.C., Dall'Agnol, R., Dias, S.B., Althoff, F.J. 2010. Origin of the Archean leucogranodiorite–granite suites: Evidence from the Rio Maria terrane and implications for granite magmatism in the Archean. Lithos **187**: 201-221

Almeida, J.A.C., Dall'Agnol, R., Oliveira, M.A., Macambira, M.J.B., Pimentel, M.M., Rämö, O.T., Guimarães, F.V., Leite, A.A.S. 2011. Zircon geochronology and geochemistry of the TTG suites of the Rio Maria granite-greenstone terrane: Implications for the growth of the Archean crust of Carajás Province, Brazil. Precambrian Research **120**: 235-257.

Almeida, J.A.C., Dall'Agnol, R., Leite, A.A.S. 2013. Geochemistry and zircon geochronology of the Archean granite suites of the Rio Maria granite-greenstone terrane, Carajás Province, Brazil. Journal of South American Earth Sciences. **42**:103–126

Althoff, F.J., Barbey P., Boullier A.M. 2000. 2.8-3.0 Ga plutonism and deformation in the SE Amazonian craton: the Archean granitoids of Marajoara (Carajás Mineral province, Brazil). Precambrian Research, 104:187-206.

Armstron, J.T. 1991. Quantitative Elemental Analysis of Individual Microparticles with Electron Beam Instruments. In: Heinrich K.F.J., Newbury D.E. (eds) Electron Probe Quantitation. Springer, Boston, MA. DOI: 10.1007/978-1-4899-2617-3_15.

Angélica, R.S. 1996. Mineralogia e geoquímica de gossans e lateritos auríferos da região de Carajás, Estado do Pará: os depósitos do Igarapé Bahia e Águas Claras. Tese de Doutorado, UFPA, 115 p.

Araújo, O. J. B. D., & Maia, R. G. N. 1991. Serra dos Carajás, folha SB. 22-ZA.

Augusto R.A., Monteiro L.V.S., Xavier R., Souza Filho C.R. 2008. Zonas de alteração hidrotermal e paragênese do minério de cobre do Alvo Bacaba, Província Mineral de Carajás (PA). Rev. Bras. Geoci., 38:263-277.

Avelar, V.G. 1996. Geocronologia Pb-Pb por evaporação em monocristal de zircão do magmatiwsmo da região de Tucumã, SE do Estado do Pará, Amazônia oriental. Dissertação de Mestrado, Universidade Federal do Pará, 149p.

Barbosa, J.P.O. 2004. Geologia Estrutural, Geoquímica, Petrografia e Geocronologia de granitóides da região do Igarapé Gelado, norte da Província Mineral de Carajás. Dissertação de Mestrado, UFPA, 96p.

Barros, C. D. M., Barbey, P., & Boullier, A. M. (2001). Role of magma pressure, tectonic stress and crystallization progress in the emplacement of syn-tectonic granites. The A-type Estrela Granite Complex (Carajás Mineral Province, Brazil). Tectonophysics, 343(1), 93-109.

Barton, M. D., & Johnson, D. A. 1996. Evaporitic-source model for igneous-related Fe oxide–(REE-Cu-Au-U) mineralization. Geology, 24(3), 259-262.

Beaudoin, G., Dupuis, C., Gosselin, P., & Jébrak, M. 2007. Mineral chemistry of iron oxides: application to mineral exploration. In Proceedings of the 9th Biennial SGA Meeting, Dublin, pp. 497-500.

Boomeri, M., Nakashima, K., & Lentz, D. R. (2009). The Miduk porphyry Cu deposit, Kerman, Iran: A geochemical analysis of the potassic zone including halogen

element systematics related to Cu mineralization processes. Journal of Geochemical Exploration, 103(1), 17-29.

Brito Neves, B.B. & Cordani, U.G. 1991. Tectonic evolution of South América during Late Proterozoic. Precambrian Research, 53: 23-40. Brito Neves, B. B. 1999. América do Sul: quatro fusões, quatro fissões e o processo acrescionário Andino. Revista Brasileira Geociências, 29(3):379-392

Broughm, S. G., Hanchar, J. M., Tornos, F., Westhues, A., & Attersley, S. (2017). Mineral chemistry of magnetite from magnetite-apatite mineralization and their host rocks: examples from Kiruna, Sweden, and El Laco, Chile. Mineralium Deposita, 1-22.

Cabral, A.R., Lehmann B., Kwitko-Ribeiro R. Costa, C.H.C. 2002a. Palladium and platinum minerals from the Serra Pelada Au-Pd-Pt Deposit, Carajás Mineral Province, Northern Brazil. Can. Mineral., 40:1451-1463.

Cabral, A.R., Lehmann B., Kwitko-Ribeiro R., Costa C.H.C. 2002b. The Serra Pelada Au-Pd-Pt Deposit, Carajás Mineral Province, Northern Brazil: reconnaissance mineralogy and chemistry of very high grade palladian gold mineralization. Econ. Geol., 97:1127–1138.

Carvalho, E. de R., Xavier R.P., Monteiro, L.V.S, Souza Filho, C.R. de, 2005 Geology and hydrothermal alteration of the Sossego iron oxide-copper-gold deposit, Carajás Mineral Province, Brazil. In: Simpósio Brasileiro de Metalogenia, 1, [CD-ROM].

Chiaradia, M., Banks, D., Cliff, R., Marschik, R., de Haller, A., 2006. Origin of fluids in iron oxide-copper-gold deposits: constraints from δ37Cl, 87Sr/86Sr and Cl/Br. Miner. Dep., 41: 565-573.

Cordeiro, A.A.C., Alves C.A., Fonseca L.R., de Nascimento J.A.S., Azevedo L.L., Santos F.F. 1984. Pesquisa geológica da jazida de wolframita de Pedra Preta, Rio Maria. In: SBG, Simp. Geol. Amaz., 2, Manaus, Anais, p. 374-390.

Silva, A. R., Villas, R. N. N., Lafon, J. M., Craveiro, G. S., & Ferreira, V. P. 2015. Stable isotope systematics and fluid inclusion studies in the Cu–Au Visconde deposit, Carajás Mineral Province, Brazil: implications for fluid source generation. Mineralium Deposita, 50(5), 547-569.

Dall'Agnol, R., Lafon J.M., Macambira M.J.B., 1994. Proterozoic anorogenic magmatism in the Central Amazonian Province, Amazonian Craton: geochronological, petrological and geochemical aspects, Miner. Petrol., 50: 113-138.

Dall'Agnol R.; Rämö, O.T.; Magalhães, M.S.; Macambira, M.J.B. 1999. Petrology of the anorogenic, oxidised Jamon and Musa granites, Amazonian craton: implications for the genesis of Proterozoic A-type granites. Lithos 46:431-462.

Dall'Agnol, R, Oliveira MA, Almeida JAC, Althoff FJ, Leite AAS, Oliveira DC, Barros CEM. 2006. Archean and paleoproterozoic granitoids of the Carajás Metallogenic Province, eastern Amazonian craton. In: Symposium on magmatism, crustal evolution and metallogenesis of the Amazoniam Craton, Belém, Excursion Guide, pp 99–150

Dall'Agnol, R. & Oliveira D. C. 2007. Oxidized, magnetite-series, rapakivi-type granites of Carajás, Brazil: Implications for classification and petrogenesis of A-type granites. Lithos 93: 215–233.

Dardenne, M.A. & Schobbenhaus C.S. 2001. Metalogênese do Brasil. Ed.UnB/CNPq, Brasília, 392 p.

Dare, S. A., Barnes, S. J., Beaudoin, G., Méric, J., Boutroy, E., & Potvin-Doucet, C. 2014. Trace elements in magnetite as petrogenetic indicators. Mineralium Deposita, 49(7), 785-796.

Dare, S. A., Barnes, S. J., & Beaudoin, G. 2015. Did the massive magnetite "lava flows" of El Laco (Chile) form by magmatic or hydrothermal processes? New constraints from magnetite composition by LA-ICP-MS. Mineralium Deposita, 50(5), 607-617.

De Oliveira, M. A., Dall'Agnol, R., & de Almeida, J. D. A. C. 2011. Petrology of the Mesoarchean Rio Maria suite and the discrimination of sanukitoid series. Lithos, 127(1), 192-209.

Dias, G.S., Macambira M.B., Dall'Ágno, R., Soare, A.D.V. Barro, C.E.M., 1996. Datações de zircões de sill de metagabro: comprovação de idade arqueana da Formação Águas Claras, Carajás, Pará. In: Simp. Geol. Amaz., 5, SBG, Belém, pp. 376-378.

DOCEGEO, 1988. Revisão litoestratigráfica da Província Mineral de Carajás – Litoestratigrafia e principais depósitos minerais. In: Cong. Bras. Geol., 35, SBG, p. 11-54.

Dreher A.M., Xavier R.P., Taylor B.E., Martini S. 2008. New geologic, fluid inclusion and stable isotope studies on the controversial Igarapé Bahia Cu–Au deposit, Carajás Province, Brazil. Mineralium Deposita, 43:161-184.

Dupuis, C., & Beaudoin, G. (2011). Discriminant diagrams for iron oxide trace element fingerprinting of mineral deposit types. Mineralium Deposita, 46(4), 319-335.

Feio GRL., Dall'Agnol R., Dantas E.L., Macambira M.J.B., Gomes A.S., Sardinha D.C., Oliveira D.c., Santos R.D., Santos P.A. 2012. Geochemistry, geochronology, and origin of the Neoarchean Planalto Granite suite, Carajás, Amazonian craton: A-type or hydrated charnockitic granites? Lithos. Online. http:// dx.doi.org/10.1016/j.lithos.2012.02.020

Feio, G. R. L., Dall'Agnol, R., Dantas, E. L., Macambira, M. J. B., Santos, J. O. S., Althoff, F. J., & Soares, J. E. B. 2013. Archean granitoid magmatism in the Canaã dos Carajás area: implications for crustal evolution of the Carajás province, Amazonian craton, Brazil. Precambrian Research, 227, 157-185.

Gabriel, E.O.; Oliveira D.C.; Galarza M.A. 2010. Petrografia e Geocronologia de granitoides do Complexo Xingu da região nordeste de Água Azul do Norte, Província Mineral de Carajás, In: SBG, Congresso Brasileiro de Geologia, 45, Anais, Belém, CDrom.

Galarza, M.A., Macambira, M.J.B., and Moura, C.A.V ., 2003, Geocronologia Pb-Pb e Sm–Nd das rochas máficas do depósito Igarapé Bahia, Província Mineral de Carajás (PA): Simpósio de Geologia da Amazônia, 7th, Belém, Sociedade Brasileira de Geologia, Proceedings [CD-ROM].

Groves, D. I., & Phillips, G. N. (1987). The genesis and tectonic control on Archaean gold deposits of the western Australian shield—a metamorphic replacement model. Ore Geology Reviews, 2(4), 287-322.

Groves, D.I., Bierlein F.P., Meinert L.D., Hitzman M.W. 2010. Iron Oxide Copper-Gold (IOCG) deposits through Earth history: implications for origin, lithospheric setting, and distinction from other epigenetic iron oxide deposits. Econ Geol. 105:641-654.

Guggenheim, S., Adams, J. M., Bain, D. C., Bergaya, F., Brigatti, M. F., Drits, V. A., ... & Stanjek, H. 2006. Summary of recommendations of nomenclature committees relevant to clay mineralogy: report of the Association Internationale pour l'Etude

des Argiles (AIPEA) Nomenclature Committee for 2006. Clays and Clay Minerals, 54(6), 761-772.

Hawthorne, F.C., Oberti, R., Harlow, G.E., Maresch, W.V., Martin, R.F., Schumacher, J.C., Welch, M.D. 2012. IMA report nomenclature of the amphibole supergroup. American Mineralogist, 97: 2031–2048.

Henriquez, F., & Martin, R. F. (1978). Crystal-growth textures in magnetite flows and feeder dykes, El Laco, Chile. The Canadian Mineralogist, 16(4), 581-589.

Hirata, W.K., Rigon J.C., Kadekaru K., Cordeiro A.A.C., Meireles E.A. 1982. Geologia Regional da Província Mineral de Carajás. In: Simp. Geol. Amaz., 1, Belém, SBG/NO, p. 100–110.

Hitzman, M.W., Oreskes, N., Einaudi, M.T., 1992, Geological characteristics and tectonic setting of Proterozoic iron oxide (Cu-U-Au-REE) deposits. Precamb. Res. 58:241–287.

Hitzman, M.W. 2000. Iron oxide-Cu-Au deposits: what, where, when and why?. In: Porter T.M. (ed.) Hydrothermal Iron-Oxide Copper-Gold and Related Deposits: A Global Perspective. PGC Publishing, Adelaide, pp. 9-25.

Holland, H. D. (1972). Granites, solutions, and base metal deposits. Economic Geology, 67(3), 281-301.

Huhn, S.R.B., Santos A.B.S., Amaral A.F., Ledsham E.J. Gouveia J.L., Martins L.B.P., Montalvão R.M.G., Costa V.G. 1988. O terreno granito greenstone da região de Rio Maria-sul do Pará. In: Cong. Bras. Geol., 35, Belém. Anais... SBG. v.3, p. 1438-1453.

Huhn, S.R.B. 1992. Geologia, controle estrutural e gênese do depósito aurífero Babaçu, região de Rio Maria, sul do Pará. Dissertação de Mestrado, IG/ UnB, 168p.

Huhn, SRB, Souza CIJ, Albuquerque MC, Leal ED, Brustolin V. 1999a. Descoberta do depósito Cu(Au) Cristalino: Geologia e mineralização associada região da Serra do Rabo - Carajás – PA. SBG/NO, Simpósio de Geologia da Amazônia, 6, pp 140-143

Huhn, S.R.B., Macambira M.J.B., Dall'Agnol R. 1999b. Geologia e geocronologia Pb-Pb do Granito Alcalino Planalto, Região da Serra do Rabo, Carajás-PA. In: SBG, Simp. Geol. Amaz., 6, Boletim de Resumos, p. 463-466.

Http://www.open.ac.uk/earth-research/tindle/AGT/AGT_Home_2010/Microprobe-.html

Jiang, S. Y., Palmer, M. R., Xue, C. J., & Li, Y. H. (1994). Halogen-rich scapolite-biotite rocks from the Tongmugou Pb-Zn deposit, Qinling, northwestern China: Implications for the ore-forming processes. Mineralogical Magazine, 58(393), 543-552.

Jorge João, X.S.; Neves, A.P.; Leal, J.W.L. 1982. Ouro da Serra Pelada: aspectos da geologia e garimpagem. In: Simpósio De Geologia Da Amazônia, 1., Belém. Anais... Belém: SBG–Núcleo Norte, v. 2, p. 52-62.

Jowett, E. C. (1991). Fitting iron and magnesium into the hydrothermal chlorite geothermometer. In GAC/MAC/SEG Joint Annual Meeting, Toronto, May 27-29, 1991, Program with Abstracts 16.

Justo, A.P., Freitas-Silva, F.H., Schorscher J.H.D., Nascimento, J.A.S., Dantas, E.L. 2015. Derrames komatiíticos do greenstone belt a sul da serra sul, Província Mineral de Carajás, Pará, Brasil. 14° Simp. Geol. Amaz, [CD-ROM].

Klein, E.L. & Carvalho J.M. de A. 2008. Recursos Minerais. In: M.L Vasquez & L.T. Rosa-Costa. (Orgs) Geologia e Recursos Minerais do Estado do Pará: SIG: Texto explicativo dos Mapas Geológico e Tectônico e de Recursos Minerais do Estado do Pará. Escala 1:1.000.000. Belém: CPRM.

Knipping, J. L., Bilenker, L. D., Simon, A. C., Reich, M., Barra, F., Deditius, A. P., ... & Munizaga, R. (2015). Trace elements in magnetite from massive iron oxide-apatite deposits indicate a combined formation by igneous and magmatic-hydrothermal processes. Geochimica et Cosmochimica Acta, 171, 15-38.

Kotschoubey B. & Lemos V.P. 1985. Considerações sobre a origem e a gênese das bauxitas da Serra dos Carajás. In: SBG, Simp. Geol. Amaz., 3, Belém, Anais, v. 3, p. 48-61.

Kullerud, K. (1996). Chlorine-rich amphiboles: interplay between amphibole composition and an evolving fluid. European Journal of Mineralogy, 355-370.

Kullerud, K., & Erambert, M. (1999). Cl-scapolite, Cl-amphibole, and plagioclase equilibria in ductile shear zones at Nusfjord, Lofoten, Norway: Implications for fluid compositional evolution during fluid-mineral interaction in the deep crust. Geochimica et Cosmochimica Acta, 63(22), 3829-3844.

Lafon, J. M., Macambira, M. J. B., & Pidgeon, R. T. 2000. Zircon U-Pb SHRIMP dating of Neoarchean magmatism in the southwestern part of the Carajás Province (eastern Amazonian Craton, Brazil). In International Geological Congress, 31, Abstracts..., Rio de Janeiro (Vol. 1).

Lancaster J.O., Fanton J., Almeida A.J., Leveille R.A. Vieira S. 2000. Discovery and geology of the Sossego copper-gold deposit, Carajás District, Pará State, Brazil. In: Inter. Geol. Congr., 31, Abstracts, RJ, [CDROM].

Leonardos, O.H., Santos M.D., Giuliani G., Araújo L.R. 1991. The Cumaru mesothermal granodiorite-hosted gold mineralization, Amazon Craton, Brazil. In: E.A. Ladeira (ed.) Brazil gold'91, the economics geology geochemistry and genesis of gold deposits. Belo Horizonte, Proceedings, Rotterdam, Balkema, p. 557-562.

Leite, A.A.S. 2001. Geoquímica, petrogênese e evolução estrutural dos granitóides arqueanos da região de Xinguara, SE do Cráton Amazônico. Belém, Universidade Federal do Pará, Centro de Geociências. (Tese de Doutorado).

Lindenmayer, Z.G., 2003. Depósito de Cu-Au do Salobo, Serra dos Carajás: Uma revisão, in Ronchi, L.H., Althoff, F.J., (eds.), Caracterização e modelamento de depósitos minerais, Ed. Unisinos, pp. 69-98.

Liu, W., Borg, S. J., Testemale, D., Etschmann, B., Hazemann, J. L., & Brugger, J. (2011). Speciation and thermodynamic properties for cobalt chloride complexes in hydrothermal fluids at 35–440 C and 600bar: an in-situ XAS study. Geochimica et Cosmochimica Acta, 75(5), 1227-1248.

Locock, A. J. 2014. An Excel spreadsheet to classify chemical analyses of amphiboles following the IMA 2012 recommendations. Computers and Geosciences, 62: 1-11.

Lobato, L.M., Rosière C.A., Silva R.C.F., Zucchetti M., Baars F.J., Sedane J.C.S., Javier Rios F., Pimentel M., Mendes G.E., Monteiro A.M. 2005. A mineralização hidrotermal de ferro da Província Mineral de Carajás – controle estrutural e contexto na evolução metalogenética da província. In: Marini, O.J., Queiroz, E.T., Ramos, B.W. (Eds.). Caracterização de Depósitos Minerais em Distritos Mineiros da Amazônia, DNPM-CT-Mineral-FINEP-ADIMB, pp. 25-92.

Loberg, B. E., & Horndahl, A. K. (1983). Ferride geochemistry of Swedish Precambrian iron ores. Mineralium Deposita, 18(3), 487-504.

Macambira, E.M.B. & Vale A.G. 1997. Programa Levantamentos Geológicos Básicos do Brasil. São Felix do Xingu. Folha SB.22-Y-B. Estado do Pará. DNPM/ CPRM. Brasília, 384p.

Machado, N., Lindenmayer, Z., Krogh, T. E., & Lindenmayer, D. (1991). U-Pb geochronology of Archean magmatism and basement reactivation in the Carajás area, Amazon shield, Brazil. Precambrian Research, 49(3-4), 329-354.

Martinsson, O., Billström, K., Broman, C., Weihed, P., & Wanhainen, C. 2016. Metallogeny of the northern Norrbotten ore province, northern Fennoscandian Shield with emphasis on IOCG and apatite-iron ore deposits. Ore Geology Reviews, 78, 447-492.

Melo, G. H. C., Monteiro, L. V., Xavier, R. P., Moreto, C. P., Santiago, E. S., Dufrane, S. A., ... & Santos, A. F. 2017. Temporal evolution of the giant Salobo IOCG deposit, Carajás Province (Brazil): constraints from paragenesis of hydrothermal alteration and U-Pb geochronology. Mineralium Deposita, 52(5), 709-732.

Meireles, E.M. & Silva A.R.B. 1988. Depósito de ouro de Serra Pelada, Marabá, Pará. In: C. Schobbenhaus, C.E.S. Coelho (eds) Principais Depósitos Minerais do Brasil, Brasília, DNPM/CVRD, v. 3, pp. 547-557. McCulloch M.T. & Chappell B.W. 1982. Nd isotopic characteristics of S- and I-type granites. Earth and Planetary Science Letters 58, 51–64.

Melo, G. H. C. D. (2014). Evolução temporal do depósito de óxido de ferro-cobre-ouro de Salobo, Província Carajás.

Monteiro, L.V.S. Xavier, R.P. Souza Filho, C.R . Moreto, C.P.N 2014. Metalogêmese das Províncias Tectônicas Brasileiras: Província Carajás. CPRM, Belo Horizonte, 589p.

Monteiro, L. V., Xavier, R. P., de Carvalho, E. R., Hitzman, M. W., Johnson, C. A., de Souza Filho, C. R., & Torresi, I. 2008a. Spatial and temporal zoning of hydrothermal alteration and mineralization in the Sossego iron oxide–copper–gold deposit, Carajás Mineral Province, Brazil: paragenesis and stable isotope constraints. Mineralium Deposita, 43(2), 129-159.

Monteiro, L. V. S., Xavier, R. P., Hitzman, M. W., Juliani, C., de Souza Filho, C. R., & Carvalho, E. D. R. 2008b. Mineral chemistry of ore and hydrothermal alteration at the Sossego iron oxide–copper–gold deposit, Carajás Mineral Province, Brazil. Ore Geology Reviews, 34(3), 317-336.

Moreto, C.P.N., Monteiro L.V.S., Xavier R.P., Amaral W.S., Santos T.J.S., Juliani C., Souza Filho C.R. 2011. Mesoarchean (3.0 and 2.86 Ga) host rocks of the iron oxide-Cu-Au Bacaba deposit, Carajas Mineral Province: U-Pb geochronology and metallogenetic implications. Miner. Dep., 46: 789-811.

Moreto, C. P., Monteiro, L. V., Xavier, R. P., Creaser, R. A., DuFrane, S. A., Melo, G. H., ... & Sato, K. 2015a. Timing of multiple hydrothermal events in the iron oxide–copper–gold deposits of the Southern Copper Belt, Carajás Province, Brazil. Mineralium Deposita, 50(5), 517-546.

Moreto, C. P. N., Monteiro, L. V. S., Xavier, R. P., Creaser, R. A., DuFrane, S. A., Tassinari, C. C. G., ... & Amaral, W. S. 2015b. Neoarchean and Paleoproterozoic iron oxide-copper-gold events at the Sossego Deposit, Carajás Province, Brazil: Re-Os and U-Pb geochronological evidence. Economic Geology, 110(3), 809-835.

Moroni, M., Girardi V.A.V., Ferrario A. 2001. The Serra Pelada Au–PGE deposit, Serra dos Carajás (Pará State, Brazil): geological and geochemical indications for a composite mineralising process. Min. Depos., 36:768-785.

Mougeot, R., Respaut J.P., Briqueu L., Ledru P., Milesi J.P., Macambira M.J.B., Huhn S.B. 1996. Geochronological constrains for the age of the Águas Claras Formation (Carajás Province, Pará, Brazil). In: Cong. Bras. Geol, 39, Anais., Salvador, SBG. 6:579-581.

Mora, C. I., & Valley, J. W. 1989. Halogen-rich scapolite and biotite; implications for metamorphic fluid-rock interaction. American Mineralogist, 74(7-8), 721-737.

Munoz, J. L., & Swenson, A. 1981. Chloride-hydroxyl exchange in biotite and estimation of relative HCl/HF activities in hydrothermal fluids. Economic Geology, 76(8), 2212-2221.

Munoz, J. L. 1984. F-OH and Cl-OH exchange in micas with applications to hydrothermal ore deposits. Reviews in Mineralogy and Geochemistry, 13(1), 469-493.

Nadoll, P., & Koenig, A. E. (2011). LA-ICP-MS of magnetite: methods and reference materials. Journal of Analytical Atomic Spectrometry, 26(9), 1872-1877.

Nadoll, P., Angerer, T., Mauk, J. L., French, D., & Walshe, J. (2014). The chemistry of hydrothermal magnetite: a review. Ore Geology Reviews, 61, 1-32.

NCL Brasil, 2005. Revision de La Estimación de Recursos del Proyecto Cristalino. Vale S.A Internal Report, 1-103.

Nielsen, R. L., Forsythe, L. M., Gallahan, W. E., & Fisk, M. R. (1994). Major-and trace-element magnetite-melt equilibria. Chemical Geology, 117(1-4), 167-191.

Nogueira, A.C.R., Truckenbrodt, W., Pinheiro, R.V.L. 1995. Formação Águas Claras, Pré-Cambriano da Serra dos Carajás: redescrição e redefinição litoestratigráfica. Bol. Mus. Par. Em. Goeldi, Ciênc. da Terra, (7), pg. 177-277.

Nyström, J. O., Billström, K., Henríquez, F., Fallick, A. E., & Naslund, H. R. (2008). Oxygen isotope composition of magnetite in iron ores of the Kiruna type in Chile and Sweden. Gff, 130(4), 177-188.

Oliveira, C.G. & Leonardos O.H. 1990. Gold mineralization in the Diadema shear belt, northern Brazil. Econ. Geol., 85:1034-1043.

Pestilho A.L.S. 2011. Sistemática de isótopos estáveis aplicada à caracterização da evolução dos paleosistemas hidrotermais associados aos depósitos cupríferos Alvo Bacaba e Alvo Castanha, Província Mineral de Carajás, PA. Dissertação de Mestrado, UNICAMP

Pidgeon R.T., Macambira M.J.B., Lafon J.M. 2000. Th– U–Pb isotopic systems and internal structures of complex zircons from an enderbite from the Pium Complex, Carajás Province, Brazil: evidence for the ages of granulite facies metamorphism and the protolith of the enderbite. Chem. Geol., 166:159–171.

Pimentel, M.M., Machado, N. 1994. Geocronologia U-Pb dos Terrenos granito-greenstone de Rio Maria, Pará. In: Congresso Brasileiro de Geologia, 38, Camboriú, 1988. Boletim de Resumos Expandidos. Camboriú, SBG. p. 390-391.

Porto, C.G., Imbernon R.A.L., Toledo M.C.M., Menezes R.O.G., Souza J.J., Borges C.E.P. 2010. Depósitos de Cu-Au lateríticos do Brasil: casos de Chapada (GO), Igarapé Bahia e Salobo (Carajás, PA). In: R.S.C. Brito, M.G. Silva, R.M. Kuyumjian. (Org.). Modelos de depósitos de cobre do Brasil e sua resposta ao intemperismo. Brasilia: CPRM, 2010, p. 191213.

Ramberg, H. 1952. Chemical bonds and the distribution of cations in silicates. J. Geol., 60 (1952), pp. 331-355

Réquia, K., Stein, H., Fontboté, L. Chiaradia, M. 2003. Re-Os and Pb-Pb geochronology of the Archean Salobo iron oxide copper–gold deposit, Carajás Mineral Province, northern Brazil. Miner. Dep., 38: 727-738.

Rigon, J.C., Munaro P., Santos L.A., Nascimento J.A.S., Barreira C.F. 2000 Alvo 118 copper–gold deposit – geology and mineralization, Serra dos Carajás, Para, Brazil. In: IUGS, International Geological Congress, 31 [CD-ROM]

Rios, F..J., Villas R.N., Fuzikawa K., Sial A.N., Mariano G. 1998. Isótopos de oxigênio e temperatura de formação dos veios mineralizados com wolframita da jazida Pedra Preta, sul do Pará. Rev. Bras. Geoc., 28:253-256.

Rhodes, A. L., & Oreskes, N. (1999). Sheets, SA.(1999) Geology and rare earth element (REE) geochemistry of magnetite deposits at El Laco, Chile. Geology and Ore Deposits of the Central Andes, Brian J. Skinner, ed., Society of Economic Geologists Special Publication, 7, 299-332.

Rosa, A.G.N. 2006. Rochas encaixantes, alteração hidrotermal e caracterização dos fluidos relacionados à formação do Corpo Sequeirinho do Depósito Cu-Au do Sossego, região de Carajás. Dissertação de Mestrado, UFPA.

Santos, J.O.S., Hartmann, L.A., Gaudette, H.E., Groves, D.I., Mcnaughton, N.J., Fletcher, I.R., 2000. A new understanding of the provinces of the Amazonian Craton based on integration of field mapping and U-Pb and Sm-Nd geochronology. Gondwana Research, 3, 453-488.

Santos, J.O.S. 2003. Geotectônica do Escudo das Guianas e Brasil-Central. In: Bizzi, L.A. (Ed.). Geologia, tectônica e recursos minerais do Brasil: texto, mapas e SIG. Brasília: CPRM, p. 169-226.

Sardinha, A.S; Barros, C.E.M.; Krymsky, R. S.; Macambira, M.J.B. 2001. Petrografia e geocronologia U-Pb em zircão do Granito Serra do Rabo, Província Mineral de Carajás, Pará. In: Simpósio de Geologia da Amazônia, 7, Belém. Resumos expandidos...Belém: SBG-Núcleo Norte, 2001. 1 CD-ROM.

Shaw, D. M. (1960). The geochemistry of scapolite part I. Previous work and general mineralogy. Journal of Petrology, 1(1), 218-260.

Shaw, D. M. (1960). The Geochemistry of Scapolite: Part II. Trace Elements, Petrology, and General Geochemistry. Journal of Petrology, 1(1), 261-285.

Sibson, R. H. (1994). Crustal stress, faulting and fluid flow. Geological Society, London, Special Publications, 78(1), 69-84.

Siepierski, L., & Ferreira Filho, C. F. 2016. Spinifex-textured komatiites in the south border of the Carajas ridge, Selva Greenstone belt, Carajás Province, Brazil. Journal of South American Earth Sciences, 66, 41-55.

Sillitoe, R. H. (2003). Iron oxide-copper-gold deposits: an Andean view. Mineralium Deposita, 38(7), 787-812.

Silva, K. S. 2016. Geologia, petrologia, geocronologia e mineralizações sulfetadas do Complexo Ézio, província mineral de carajás, Brasil.

Souza, S.R.B., Macambira M.J.B., Sheller T. 1996. Novos dados geocronológicos para os granitos deformados do Rio Itacaiúnas (Serra dos Carajás, PA), implicações estratigráficas. In: Simp. Geol. Amaz., 5, Belém, Anais, 380–383.

Souza, Z.S., Potrel A., Lafon J.M., Althoff F.J., Pimentel M.M., Dall'Agnol R., Oliveira C.G., 2001. Nd, Pb and Sr isotopes in the Identidade Belt, an Archean greenstone belt of Rio Maria region (Carajás Province, Brazil): implications for the geodynamic evolution of the Amazonian Craton. Precambrian Research 109: 293–315.

Sousa, S.D.; Oliveira, D.C.; Gabriel, E.O.; Macambira, M.J.B. 2010. Geologia, Petrografia e Geocronologia das rochas granitoides do Complexo Xingu da porção a leste da cidade de Água Azul do Norte (PA) - PMC. In: SBG, Congresso Brasileiro de Geologia, 45, Anais, Belém, CDrom.

Tallarico, F.H.B., Coimbra C.R., Costa C.H.C. 2000. The Serra Leste Sediment-Hosted Au-(Pd-Pt) Mineralization, Carajás Province. Rev. Bras. Geoc., 30:226229.

Tallarico, F.H.B. 2003. O cinturão cupro-aurífero de Carajás, Brasil. Tese de Doutorado, UNICAMP, 229p

Tallarico, F.H.B., Figueiredo B.R., Groves D.I., Kositcin N., McNaughton N.J., Fletcher I.R., Rego J.L. 2005. Geology and SHRIMP U–Pb geochronology of the Igarapé Bahia deposit, Carajás copper–gold belt, Brazil: an Archean (2.57 Ga) example of iron–oxide Cu–Au–(U– REE) mineralization. Econ Geol 100:7–28.

Tassinari, C.C.G. 1996. O mapa geocronológico do Cráton Amazônico no Brasil: revisão dos dados isotópicos. Tese de Livre Docência, IG-USP, 139p. Tassinari C.C.G., Macambira M.J.B. 1999. Geochronological Provinces of the Amazonian Craton. Episodes, 22:174-182.

Tassinari, C.C.G. & Macambira M.J.B. 1999. Geochronological Provinces of the Amazonian Craton. Episodes, 22:174-182.

Tassinari, C.C.G., Mellito, M.K., and Babinski, M., 2003, Age and origin of the Cu (Au-Mo-Ag) Salobo 3A ore deposit, Carajás mineral province, Amazonian craton, northern Brazil: Episodes, v. 26, p. 2–9

Tassinari, C.C.G. and Macambira, M.J.B., 2004. A evolução tectônica do Cráton Amazônico. In: MantessoNeto, V., Bartorelli, A., Carneiro, C.D.R. and Brito Neves, B.B. (Eds.) Geologia do Continente SulAmericano: Evolução da Obra de Fernando Flávio Marques de Almeida. pp. 471-485.

Tassinari, T., Tachibana J., Tulio M., Lívio R., Gaia C. 2005. Geologia isotópica aplicada nas mineralizações de Cu-Au do greenstone belt da Serra dos Gradaús, Província Mineral de Carajás, 190 Cráton Amazônico: exemplo de mineralizações policíclicas. In: SIMPÓSIO BRASILEIRO DE METALOGENIA, 1., Gramado, RS. Resumos... Porto Alegre: SBG/SEG/SGMTM-MME, 2005. 1 CD-ROM.

Teertstra, D. K., & Sherriff, B. L. (1997). Substitutional mechanisms, compositional trends and the end-member formulae of scapolite. Chemical Geology, 136(3-4), 233-260.

Teixeira, W., Tassinari, C.C.G., Cordani, U.G., Kawashita, K. 1989. A review of the geochronological of the Amazonian Craton: tectonic implications. Precamb. Res., 42: 213-227.

Tian, Y., Etschmann, B., Liu, W., Borg, S., Mei, Y., Testemale, D., ... & Johannessen, B. (2012). Speciation of nickel (II) chloride complexes in hydrothermal fluids: In situ XAS study. Chemical Geology, 334, 345-363.

The Open University Electron Microprobe Laboratory. 2010. Free Structural Formula Calculators. Available in http://www.open.ac.uk/earth-research/tindle/AGT/AGT_Home_2010/Microprobe-2.html

Tornos, F., Velasco, F., & Hanchar, J. M. (2016). Iron-rich melts, magmatic magnetite, and superheated hydrothermal systems: The El Laco deposit, Chile. Geology, 44(6), 427-430.

Toplis, M. J., & Carroll, M. R. 1995. An experimental study of the influence of oxygen fugacity on Fe-Ti oxide stability, phase relations, and mineral—melt equilibria in ferro-basaltic systems. Journal of Petrology, 36(5), 1137-1170.

Torresi I, Bortholoto D.F.A., Xavier R.P., Monteiro L.V.S. 2012. Hydrothermal alteration, fluid inclusions and stable isotope systematics of the Alvo 118 iron oxide–copper–gold deposit, Carajás Mineral Province (Brazil): implications for ore genesis. Miner Deposita, 47: 299-323.

Vale S.A. 2010. Projeto Furnas, Relatório Final de Pesquisa. DNPM.

Vale. 2012. Vale obtains operation license for Salobo. http:// saladeimprensa.vale.com /en/release/interna.asp?id= 22000. Accessed in february 04, 2013.

Vale. 2013. Projeto Jatobá. Internal report (Unpublished).

Vale. 2014. Projeto Jatobá. Internal report (Unpublished).

Vanko, D., & Bishop, F. (1980). Experimental determination of NaCl-rich scapolite stability. In Geol. Soc. Am. Abstr. Prog (p. 540).

Vanko, D. A., & Bishop, F. C. (1982). Occurrence and origin of marialitic scapolite in the Humboldt Lopolith, NW Nevada. Contributions to Mineralogy and Petrology, 81(4), 277-289.

Vasquez, L.V., Rosa-Costa L.R., Silva C.G., Ricci P.F., Barbosa J.O., Klein E.L., Lopes E.S., Macambira E.B., Chaves C.L., Carvalho J.M., Oliveira J.G., Anjos G.C., Silva H.R.. 2008 Geologia e Recursos Minerais do Estado do Pará: Sistema de Informações Geográficas —SIG: texto explicativo dos mapas Geológico e Tectônico e de Recursos Minerais do Estado do Pará 1:1.000.000. CPRM, Belém, p328.

Villas, R.N. & Santos M.D. 2001. Gold deposits of the Carajás Mineral Province: deposit types and metallogenesis. Miner. Dep., 36:300-331.

Villas R.N., Lima L.F.O., Neves M.P., Sousa F.D.S., Lamarão C.N., Fanton J., Morais R. 2005. Relações entre deformação, alteração hidrotermal e mineralização no depósito Cu-Au do Sossego, Província Mineral de Carajás. In: Simp. Bras. Metalogenia, 1,[CD-ROM]

Villas R.N., Neves M.P , Moura C.V., Toro M.A.G., Aires B., Maurity C. 2006. Estudos isotópicos (Pb, C e O) no depósito Cu-Au do Sossego, Província Mineral de Carajás. In: SBG/Núcleo Norte, IX Simpósio de Geologia da Amazônia, Resumos [CD-ROM].

Xavier R.P., Monteiro L.V.S., Souza Filho C.R., Torresi I., Carvalho E.R., Dreher A.M., Wiedenbeck M., Trumbull R.B., Pestilho A.L.S., Moreto C.P.N. 2010. The iron oxide copper-gold deposits of the Carajás Mineral Province, Brazil: an updated and critical review. In: T.M. Porter (ed) Hydrothermal Iron Oxide Copper-Gold & Related Deposits: A Global Perspective. Australian Miner. Fund, Adelaide, Vol 3, pp. 285306.

Xavier R.P., Monteiro L.V.S., Souza Filho C.R., Torresi I., Carvalho E.R., Dreher A.M., Wiedenbeck M., Trumbull R.B., Pestilho A.L.S., Moreto C.P.N. 2010. The iron oxide copper–gold deposits of the Carajás Mineral Province, Brazil: an updated and critical review. In: Porter TM (ed) Hydrothermal Iron Oxide Copper-Gold & Related Deposits: A Global Perspective. Australian Miner. Fund, Adelaide, Vol 3, pp. 285-306.

Xavier, R.P., Monteiro, L.V.S., Moreto, C.P.N., Pestilho, A.L.S., Melo, G.H.C., Silva, M.A.D. da ; Aires, B., Ribeiro, C., Freitas e Silva, F.H. 2012. The Iron Oxide Copper-Gold systems of the Carajás Mineral Province. In: J. Hedenquist, M. Harris, F. Camus. (Org.). SEG Special Publication 16, Geology and Genesis of Major Copper Deposits and Districts of the World: A Tribute to Richard H. Sillitoe. 1ed.Littleton: Society of Economic Geologists, v. 1, p. 433-454

Xavier, R.P., Wiedenbeck, M., Trumbull, R.B., Dreher, A.M., Monteiro, L.V.S., Rhede, D., Araújo, C.E.G., Torresi, I. 2008. Tourmaline B-isotopes fingerprint marine evaporites as the source of high-salinity ore fluids in iron oxide-copper-gold deposits, Carajás Mineral Province (Brazil). Geology, 36: 743-746.

Xavier, R.P., Rusk, B., Emsbo, P., Monteiro, 2009. Composition and source of salinity of ore-bearing fluids in Cu-Au systems of the Carajás Mineral Province, Brazil. In: SGA Biennial Meeting, 10, pp. 272-274.

Yavuz, F., Kumral, M., Karakaya, N., Karakaya, M. Ç., Yıldırıma, D.K. 2015. A Windows program for chlorite calculation and classification. Computers & Geosciences, 81: 101-113.

Wirth, K.R. Gibbs A.K. Olszewski,W.J.Jr. 1986. U–Pb ages of zircons from the Grão Pará Group and Serra dos Carajás granite, Pará, Brasil. Rev. Bras. Geoci. 16: 195–200.

Zang, W. & Fyfe W.S. 1995. Chloritization of the hydrothermally altered bedrock at the Igarapé Bahia gold deposit, Carajás, Brazil. Miner. Dep., 30:30-38.

ANEXO II

The iron oxide–copper–gold (IOCG) Jatobá deposit, Carajás Mineral Province, Brazil: isotope geochemistry (O, H, S, and Pb), and lithochemical constraints on the mineral system evolution

Angela Suélem Rocha Veloso [(1)], Lena Virginia Soares Monteiro [(1)], Caetano Juliani [(1)], Roberto Pérez Xavier [(2)]

(1) Geosciences Institute, University of São Paulo (USP), São Paulo, Brazil

(2) Geosciences Institute, State University of Campinas (UNICAMP), São Paulo, Brazil

Abstract

The Jatobá deposit is part of a cluster of iron oxide–copper–gold (IOCG) deposits recognized in the Southern Copper Belt, in the Carajás Province. These deposits are located in subsidiary structures within the E-W and WNW–ESE-trending Canaã shear zone. The host rocks at Jatobá comprise metadiabase, metabasalt, mafic metatuff, felsic volcaniclastic rocks and metarhyodacite (LA–ICP–MS U–Pb zircon; 2,700 ±16 Ma; MSWD = 22), which are attributed to the Itacaiúnas Supergroup.

The Jatobá deposit is notable for its extensive pre-mineralization scapolite-biotite-hastingsite alteration and intense iron metasomatism (magnetite-apatite). The mineralization stage (I) was coeval to syn-tectonic calcic alteration (actinolite-apatite) and resulted in replacement fronts and breccias with Ni-pyrrhotite (±Ni-pyrite ± Co-chalcopyrite) in the matrix. The mineralization stage (II), related to syn-tectonic potassic alteration (biotite–Cl-apatite), comprises Ni-pyrite–Co-chalcopyrite ± Ni-pyrrhotite. The ensuing mineralizing stages (III) and (IV) were accompanied by biotite and chlorite, respectively. The latter was the most expressive copper mineralization stage and encompasses branching veins with Co-chalcopyrite and siegenite (± Co-pyrite ± magnetite ± cassiterite ± sphalerite ± molybdenite ± uraninite ± monazite ± REE carbonates).

The early mineralization stage (I) is characterized by the highest contents of Fe_2O_3 (71.49 to 63.91 wt. %), Ni (3930 to 1270 ppm), Co (2320 to 670 ppm), V (740 to 590 ppm), Pd (81 to 372 ppb) and Pt (2 to 17 ppb) contents, which decrease with the paragenetic evolution. An opposite trend is observed in relation to copper, gold, zinc,

REE and LILE (P, U, Th, Sn, W, and Nb). Highest contents of ΣREE (up to 6773.92 ppm), U (up to 48.50 ppm), Th (up to 23.30 ppm), P_2O_5 (up to 7.97 wt. %), Sn (up to 24 ppm), Nb (up to 7.50 ppm), W (up to 322.50), Zn (up to 482 ppm), gold (up to 1310.80 ppm) were characterized in ore samples formed during the mineralization stage (IV).

Temperature decrease from the pre-mineralization iron metasomatism (558 °C) to mineralization stages (II = 507 °C; III = 422 °C; IV = 327 °C) was accompanied by a relatively narrow variation of calculated $\delta^{18}O_{H2O}$ values (9.53‰ to 5.41‰). The $\delta^{18}O_{H2O}$ and δD_{H2O} (–44.88‰ to –30.25‰) values overlap with those of primary magmatic waters and felsic magmatic water and could imply that fluid mixing involving externally-derived fluids was limited at Jatobá.

The $\delta^{34}S_{sulfide}$ values of Jatobá sulfides (0.27‰ to 1.80‰) also point to magmatic sulfur sources. Increasing of $\delta^{34}S_{sulfide}$ values during the paragenetic evolution was accompanied by decrease of Ni + Co and V contents and increase of Sn + W + Nb content in ore samples, suggesting that part of the sulfur and metals may have been leached from mafic-(ultramafic) rocks.

The highly radiogenic Pb isotope composition of Jatobá chalcopyrite ($^{206}Pb/^{204}Pb$ = 99.35 to 245.73; $^{207}Pb/^{204}Pb$ = 32.53 to 62.24; $^{208}Pb/^{204}Pb$ = 55.58 to 172. 76) point to imprecise Archean ages for the last mineralization stage (IV). Highly radiogenic lead signatures may have resulted from striking disturbance due to high U contents in the hydrothermal fluids and to incorporation of radiogenic Pb (or U) into the sulfide from an external source after its formation.

The Jatobá deposit was formed in the roots of a wider Archean IOCG mineral system from focused magmatic-derived fluids. The Jatobá ore signature may reflect evolution closely related to the ca. 2.74 Ga widespread alkaline magmatism, with inheritance of both A-type granites and gabbros, due to intense fluid-rock interaction involving residual alkaline-rich fluids.

Keywords: Jatobá deposit, Iron-oxide-copper-gold deposit, Carajás Province, Brazil, stable isotopes, lithochemical.

Introduction

The Jatobá deposit, located in the Carajás Province (Santos et al. 2000, Santos 2003; Fig. 1), in the Amazonian Craton, is part of a cluster of iron oxide–copper–gold (IOCG) deposits recognized in the Southern Copper Belt at Carajás (Monteiro et al., 2011; Moreto et al., 2015b). These deposits are distributed over a belt of more than 60 km within the E–W and WNW–ESE-trending Canaã shear zone.

The Southern Copper Belt is located in the contact zone between units of the former Carajás basin, represented by Neoarchean metavolcanosedimentary and sedimentary sequences, and its basement that comprises Mesoarchean TTG ortogneisses, granitoids and greenstone belts.

The Jatobá deposit, under evaluation, is the closest to the world-class Sossego Mine (355 Mt @ 1.5 % Cu and 0.28 g/t Au; Lancaster et al., 2000). However, according to Veloso et al. (Submitted), these deposits have distinct geological setting. While the Sossego deposit is hosted by the ca. 3.0 Ga Sequeirinho granite, ca. 2.97 Ga greenstone belt and Neoarchean intrusive rocks (ca. 2.74 Ga gabbronorite and granophyric granite; Moreto et al., 2015a), the Jatobá deposit is essentially hosted by metavolcanosedimentary units and metadiabase.

The Jatobá deposit is also notable for its extensive scapolite-biotite-hastingsite alteration zones, massive magnetite-(apatite) bodies and spatially related nickel-rich pyrrhotite breccias, which may represent the roots of the IOCG system. The bulk of copper mineralization at Jatobá, however, is associated with late chlorite alteration (Veloso et al. Submitted).

The geological attributes of the Jatobá deposit may reflect an evolving system that records a single or multiple hydrothermal events. Its evolution may be analogous to that reported by Monteiro et al. (2008a) for the Sossego mine, which has deep-intermediate and shallow-crustal level alteration zones (Monteiro et al, 2008a, 2008b) developed during Neoarchean (ca. 2.70Ga – 2.68 Ga; U–Pb LA–MC–ICPMS in monazite and Re–Os NTIMS in molybdenite) and Paleoproterozoic (ca. 1.90 – 1.87 Ga; U–Pb LA–MC–ICPMS in monazite) metallogenetic events, respectively (Moreto et al. 2015a). However, the recognition of these deposits as distinct portions of a larger mineral system depends on the identification of similar sources and processes.

Stable isotope studies may enable the identification of the nature of fluid and sulfur sources for the Jatobá copper ore. In addition, whole-rock lithochemical

signatures of the Jatobá ore may reflect fluid-interaction process and the nature of leached rocks. Thus, this contribution integrates U–Pb geochronology, oxygen, hydrogen, sulfur, and lead isotope data, and lithochemistry, aiming to unravel the nature and mechanisms of fluid evolution and the fluid flow paths. This study also may contribute to the identification of mechanisms that permitted the genesis of world-class and minor copper deposits in a complex multi-episodic mineral system.

1. Methods

Detailed descriptions of cores from eight drill holes (JATD-01, JATD-02, JATD-03, JATD-15, JATFD-21, JATFD-28, JATD-32 e JATD-33) was integrated to petrographic studies under transmitted and reflect light and using a scanning electronic microscope (SEM), LEO 440I model, coupled to an Oxford Energy Dispersive X-Ray Spectrometry (EDS) were carried out in the Electronic Microscope Laboratory of the Geoscience Institute, University of São Paulo (USP).

U–Pb geochronology

For geochronological studies, zircon concentration from the host rocks (mafic and felsic metavolcanic rocks, mafic metatuff, and metadiabase) was attempted. Zircon was satisfactorily extracted from approximately 1 kg of a metarhyodacite sample. Conventional techniques were used, involving crushing, granulometric separation by sieving (<250 mesh), concentration of dense minerals in Wiffley table, elimination of magnetic minerals using hand magnet and Frantz electromagnetic separator and zircon concentration using high density solutions (bromoform and methylene iodide), in accordance with the sample preparation procedures adopted in Loios (2009). Zircon grains were collected and manually selected using a Stereomicroscope Olympus DF Plan 1.5x and assembled in blocks with 4 ml of resin and 0.5 ml of healer, resulting in a mount with 23 zircon grains.

The U–Pb analyses in zircon were performed on a Thermo Neptune laser ablation multi-collector inductively coupled plasma mass spectrometer (LA-ICP-MS) with spatial analytical resolution obtained in a Laser Excimer with ArF 193ηm (6Hz frequency), with spot production of 32 μm and ablation time of 40s. The correction for the common Pb was made based on the zircon Gj-1 (age-reference of 608.5 +/- 0.4 Ma; TIMS; Jackson et al., 2004). The analytical data were processed in Excel spreadsheets, and the isotopic ratios were reported in level 1σ. Age calculation was performed using

the ISOPLOT/Ex 4.15 software (Ludwing, 2009). The LA-ICP-MS U–Pb isotopic analyses of zircon were performed at the Geochronological Research Center (CPGeo) of the University of São Paulo, following the analytical procedures presented in Sato (2008).

Pb–Pb isotope analysis

Pb–Pb isotope analyses were carried out on sulfide concentrates adopting the analytical procedures recommended by Magdaleno and Ruiz (2009). The analyses include the use of a clean class 10.000 (ISO N° 7) laboratory equipped with laminar flow hoods class 100 (ISO N°5), following the reference standard ABNT NBR ISSO 14644-1. The technique requires care in the purification of reagents and handling of materials in order to avoid probable contaminations by Pb. The total dissolution of the sulfide sample was obtained by acid digestion in a SAVILLEX using HCl + HNO_3 at different stages, at a temperature of 100 °C. The Pb isotopic ratios were obtained by thermal ionization mass spectrometry (TIMS), using the FINNIGAN MAT 262 spectrometer at the Center for Geochronological Research of the Institute of Geosciences of the University of São Paulo (CPGeo - USP). Isotopic ratios were corrected for bulk fractionation of 0.12%/u.m.a ($^{207}Pb/^{204}Pb$ ratio) and 0.13%/u.m.a ($^{206}Pb/^{204}Pb$ and $^{208}Pb/^{204}Pb$ ratios). Error 2SD (Standard deviation) is reported in 2σ level for an average number of measurements of 60. Total white during analysis were of 77 pg. Mean value of the isotopic ratios of the NBS-981 standard between April/2015 and March/2016 was value ± standard deviation (1σ): $^{206}Pb/^{204}Pb$ = 16,894 ±0.006; $^{207}Pb/^{204}Pb$ = 15,433 ±0.008 and $^{208}Pb/^{204}Pb$ = 36,518 ±0.026.

Stable isotope analysis

Mineral concentrates with a purity of more than 95% were obtained using a hand-drill, milling in stainless steel mortar, sieving and manual sorting under a stereomicroscope. Sulfur stable isotope analyses were carried out in the Geochronology Laboratory of the Institute of Geosciences, University of Brasília, Brazil. For sulfur isotope analysis, SO_2 production was obtained from the combustion of sulfides with excess oxygen in tin capsules at 1080 °C. The gas produced from the combustion was brought through a stream of helium to tungsten and zirconium catalysts for reduction in a high purity copper filament. The separation of SO_2 took place in a gas chromatograph. Stable isotope ratios were analyzed using a LA-MC-ICP-MS (Laser Ablation Multi

Collector – Inductively Coupled Plasma Mass Spectrometer). The data processing, as well as the control of the mass spectrometer and its peripherals were performed by software Isodat 3.0 (Sharp, 2007). The $\delta^{34}S$ values have an accuracy of 0.01 ‰ and were reported in relation to the Canyon Diablo Troilite (CDT) standard.

Oxygen and hydrogen isotope analyses were carried out on silicates and oxides in the Stable Isotope Analytical Service of the University of Salamanca, Spain, under supervision of the Prof. Dr. Clemente Récio Hernández. Mass spectrometric measurements for the $^{18}O/^{16}O$ isotopic ratios were performed based on Sharp (1990), using the original Clayton and Mayeda (1963) techniques using a SIRA-II mass spectrometer. The method consisted of the release of O_2 by laser ablation (CO_2 laser SYNRAD 25W) in an atmosphere of ClF_3. The water and H_2 reduction and determination of D/H ratios were performed according to Godfrey (1962) in a Dual Inlet gas source mass spectrometer (2 SIRA-II spectrometers + 1 SIRA-10 spectrometer). The results of the oxygen and hydrogen isotopes are expressed in conventional delta (δ) notation per thousand (‰), and are reported in relation to the Vienna Standard Mean Ocean Water (VSMOW) standards. The reproducibility of the analyses was ±0.2 ‰ for $\delta^{18}O$ and ±5 ‰ for δD.

Lithochemical analyses

Whole rock chemical analyses were performed on mineralized samples of the Jatobá deposit. The sample preparation was done in the Treatment Laboratory of the Institute of Geosciences, University of São Paulo. Rock powders were prepared in a tungsten carbide ring mill and analyzed after lithium metaborate or tetraborate fusion. The chemical analyses were carried out in the ACME Analytical Laboratories Ltd. and the ALS Australian Laboratory Services Pty Ltd. Major elements were analyzed by ICP-AES (Inductively Coupled Plasma Atomic Emission Spectroscopy), whereas minor (MnO, TiO_2, P_2O5, Cr_2O_3), traces (Ba, Be, Co, Ga, Nb, Ni, Rb, Sc, Sn, Sr, V, W, Y, Zr, Ag, As, Au, Bi, Cd, Cu, Hg, Mo, Ni, Pb, Sb, Si, Tl, Zn), ultra-traces (Cs, Hf, Ta, Th, U) and REE were determined by ICP-MS (Inductively Coupled Plasma Mass Spectrometry). The results were treated using Excel spreadsheets and the GCDKit software (Janoušek et al., 2006).

2. Geological setting of the Carajás Province

The Carajás Province (Santos *et al.* 2000; Santos 2003; Fig. 1), located in the Amazonian Craton (Teixeira *et al.* 1989; Brito Neves and Cordani, 1991; Tassinari, 1996; Tassinari and Macambira, 1999; 2004), comprises a well-preserved Archean nuclei. It is divided into two tectonic domains: Rio Maria, in the south, and the Carajás Domain, in the north. The Rio Maria Domain represents a typical granitoid-greenstone terrain. It evolved from the amalgamation of intra-oceanic arcs in two stages (3.05 Ga to 2.90 Ga; 2.88 Ga to 2.82 Ga; Leite, 2001; Souza *et al.*, 2001; Santos, 2003; Tassinari *et al.*, 2005; Vasquez *et al.*, 2008; Almeida *et al.*, 2011), accompanied by compressive regime and crustal shortening in the N-S direction until its stabilization at ca. 2.85 Ga.

The Carajás Domain (Figure 1) comprises an outstanding metallogenetic province in Brazil and concentrated the known iron and copper-gold deposits at Carajás. This domain is characterized by a regional E-W and WNW-ESE-trending sigmoidal structure and by expressive transcurrent shear zones (e.g. Cinzento, Carajás and Canaã; Araújo and Maia; 1991; Pinheiro and Holdsworth, 1997; Pinheiros, 2013).

The Mesoarchean basement is recognized outwards the limits of the Carajás sigmoidal structure. It comprises: i) gneisses and migmatites of the Xingu Complex; ii) granulites of the Chicrim Cateté Ortogranulite (or Pium Complex; 3.0 Ga; Pidgeon *et al.*, 2000); iii) ca. 3.0 Ga granitoids (e.g. Sequeirinho and Bacaba tonalites; Moreto *et al.* 2011a; 2015a); iv) ca. 2.96 to 2.93 Ga Canaã dos Carajás Granite (Feio *et al.*, 2013); and v) ca. 2.88 to 2.84 Ga granitoids (e.g. Água Azul; Água Limpa, Serra Dourada, Cruzadão, Rio Verde, Campina Verde, Bom Jesus; Gabriel *et al.*, 2010; Sousa *et al.*, 2010; Moreto *et al.*, 2011; Feio *et al.*, 2012a, 2013).

Greenstone belt sequences (ca. 2.97 Ga; U–Pb SHRIMP zircon; Moreto *et al.* 2015a) define the southern boundary of the sigmoidal structure, close to the contact between Mesoarchean granitoids and Neoarchean metavolcano-sedimentary units (e.g. Selva greenstone belt; Sequeirinho Group; Siepierski et al., 2016; Justo et al., 2015). They include metaultramafic (talc schist, serpentinite and spinifex-textured komatiite), mafic (actinolite-chlorite-quartz-albite schist), intermediate (metadacite) and metasedimentary units (quartz-chlorite schists).

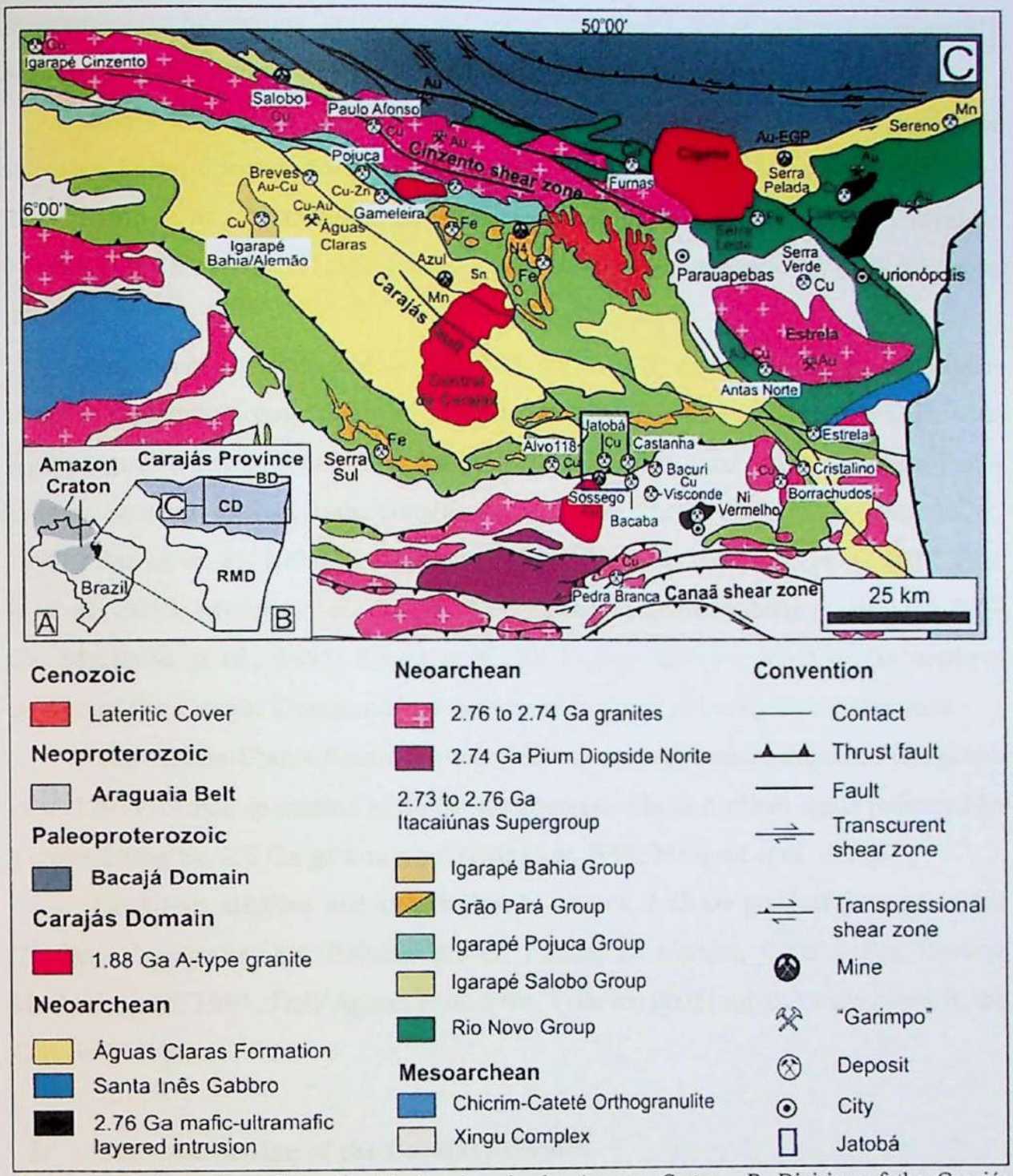

Figure 1. A. Location of the Carajás Province in the Amazon Craton. B. Division of the Carajás Province into the Rio Maria (RMD) and Carajás (CD) domains, and its north limit with the Paleoproterozoic Bacajá Domain (DB). C. Geological map of the Carajás Domain (Vasquez *et al.*, 2008b).

The inner part of the sigmoidal structure is represented by metavolcano-sedimentary and metasedimentary units, which are referred to as the former Carajás basin. The ca. 2.76 to 2.73 Ga Itacaiúnas Supergroup (Wirth *et al.*, 1986, DOCEGEO1988, Machado *et al.* 1991) and Rio Novo Group (Hirata *et al.* 1982) comprise mafic and felsic metavolcanic and metavolcaniclastic rocks, banded iron formation, metagraywackes and quartzites. The Itacaiúnas Supergroup was divided into the Igarapé Salobo, Igarapé Pojuca, Grão Pará, and Igarapé Bahia groups that have

predominance of distinct volcanic and sedimentar facies. These volcano-sedimentary sequences underwent low greenschist to amphibolite facies metamorphism.

Mafic-ultramafic intrusions (e.g. Luanga Complex; Ézio Complex Jorge; Cateté Intrusive Suite; Jorge João *et al.,* 1982; Machado *et al.*, 1991; Macambira and Vale, 1997; Lafon *et al.,* 2000; Silva, 2016) and gabbros, norites and diorites (e.g. Diopsídio Norito Pium; Cristalino Diorite; Huhn *et al.,* 1999b) were emplaced in ca. 2.76 Ga to 2.70 Ga.

Expressive granitegenesis (ca. 2.75 Ga to 2.70 Ga), synchronous to mafic-ultramafic intrusion emplacement, is represented by foliated alkaline to metaluminous A_2-type granites (e.g. Planalto; Estrela; Plaquê; Serra do Rabo; Igarapé Gelado Pedra Branca; Sossego Granophyric Granite; Avelar, 1996; Huhn *et al.,* 1999a; Huhn *et al.*, 1999b; Barros et. al. 2004; Sardinha *et al.*, 2001; Barbosa, 2004; Feio *et al.*, 2012, Feio *et al.* al., 2013; Moreto *et al.,* 2015a). The Old Salobo and Itacaiúnas granites (ca. 2.57 Ga; Machado *et al.,* 1991; Souza *et al.,* 1996) were also identified in the northern portion of the Carajás Domain, close to the northern limit of the sigmoidal structure.

The Águas Claras Formation represents a metasedimentary sequence (Nogueira *et al.* 1995) formed in marine to fluvial environment, whose Archean age is indicated by a crosscutting ca. 2.6 Ga gabbroic sill (Dias *et al.* 1996; Mougeot *et al.* 1996).

Orosirian alkaline and subalkaline A_2-type ca. 1.88 Ga granites (e.g. Serra dos Carajás, Young Salobo, Pojuca, Breves, Central de Carajás, Cigano; Rio Branco; Machado *et al.* 1991, Dall'Agnoll *et al.* 1994, Tallarico 2003) are also widespread in the Carajás Province.

3. Tectonic setting of the Carajás Province

The origin of the Carajás sigmoidal structure is controversial. According to Tavares (2015), it results from the installation of an active continental margin in ca. 2.87 to 2.83 Ga, which evolved to the amalgamation of the Rio Maria and Carajás domains, leading to crustal thickening, high-grade metamorphic processes and migmatization recorded in the Xingu Complex rocks (ca. 2.86 Ga; Machado et al., 1991; Delinardo et al., 2015).

Araújo and Maia (1991), however, interpreted the sigmoidal mega-structuring as a result of thrusts and transcurrent fault systems, developed in an oblique compressive regime with shortening in the NW-SE direction. According this model, a dextral transtension of the basement rocks led to the formation of a pull-apart basin, controlled

by the anastomosed geometry of the main lineaments, resulting in the development of the Carajás and Cinzento fault systems.

In addition, Pinheiro and Holdsworth (1997) considered that the tectonic reactivation of Mesoarchean ductile shear zones was responsible for the complex structuring of the Carajás Domain. Between ca. 2.85 and 2.76 Ga, the basement rocks became intensely deformed, as evidenced by the subvertical E-W-trending mylonitic foliation imprinted on these rocks. Subsequently, an intracratonic basin developed under conditions of high-temperature regional sinistral transpression regime. Dextral transtension lead to the deposition of the Itacaiúnas Supergroup and the Águas Claras Formation in a wide intracratonic basin, followed by the establishment of the Cinzento and Carajás transcurrent shear zones.

Gibbs et al. (1986), Wirth et al. (1986), DOCEGEO (1988), Olszewski et al. (1989), Tallarico et al. (2005) and Tavares et al. (2015) attributed the formation of the Carajás Basin to the opening of a continental rift marked by the ascension of asthenospheric mantle in an extensional environment. Underplating of mafic magma at the base of the lower crust leaded to its melting and generation of different magmatic chambers, including those that would have originated the ca. 2.75 to 2.70 Ga mafic-ultramafic intrusions and the bimodal volcanism of the Itacaiúnas Supergroup (Tallarico et al., 2005; Ferreira Filho et al., 2007).

However, the Neoarchean A_2-type granites, synchronous to the ca. 2.75 to 2.70 Ga magmatism, are typically foliated and their emplacement is considered syn-tectonic in relation to a regional transpressive event (Barros et al., 2001, 2004, 2009). Alternatively, Tavares (2015) interpreted that reactivation of Mesoarchean basement faults during the Neoarchean rift resulted in conduits to emplacement of these magmas.

Additionally, another evolutionary model is defended by Meirelles (1986), Dardenne *et al.* (1988), Meirelles and Dardenne (1991), Teixeira and Eggler (1994), Teixeira, (1994), Silva *et al.*, (2005), Lindenmayer *et al.*, (2005), Lobato *et al.* (2005) and Teixeira *et al.* (2010). This model proposes the formation of a volcano-sedimentary basin in an active margin environment, whose evolution would be related to the subduction of oceanic plate, followed by continent-continent collision in ca. 2.76 to 2.74 Ga leading to amalgamation of the Rio Maria and Carajás domains. The high K calc-alkaline affinity of the Itacaiúnas Supergroup basalts is considered an evidence for this model. Zucchetti (2007) considered that such characteristics could reflect volcanism extravasated on continental crust in a back arc environment developed in ca. 2.76 Ga.

Regardless of the model adopted for the generation of the Carajás basin, its tectonic inversion in ca. 2.70 Ga to 2.60 Ga is suggested (Pinheiro e Holdsworth, 1997; Domingos, 2009). The oldest IOCG metallogenetic events at Carajás (e.g. Sequeirinho orebody, Sossego Mine; Moreto et al., 2015a) were developed during this stage. Thereafter an important tectonic event at ca. 2.57 Ga, coeval to the formation of the Salobo and Igarapé Bahia IOCG deposits (Réquia et al., 2003; Tallarico et al., 2005), is recognized in the north limit of the Carajás Domain and related to the reactivation of the Cinzento fault system (Melo et al., 2017).

A Paleoproterozoic collisional system (Carajás-Bacajá Orogen; ca. 2.09 to 2.07 Ga) was related to the Riacian agglutination process that led to the collage of the Carajás Province with the Bacajá Domain (Tavares, 2015). The ensuing Orosirian Sereno tectono-thermal event (ca. 2.0 Ga) was restricted to the eastern edge of the Carajás Domain (Tavares, 2015) and comprises a shear-dominated compressive system with vergence towards north-northwest to west-northwest. A hydrothermal event dated in ca. 2.05 Ga was identified by Moreto et al. (2015b) in the Bacaba deposit, located in the Southern Copper Belt. The main copper mineralization at Bacaba was formed at ca. 2.70 Ga to 2.68 Ga, but the record of Paleoproterozoic hydrothermal activity in ca. 2.05 Ga may be linked with an overprinting related to the Paleoproterozoic tectonic events (e.g. Carajás-Bacajá Orogen or Sereno event).

The collapse of the Paleoproterozoic orogen was followed by the development of ENE-WSW and WNW-ESSE ductile-brittle and brittle structures related to the emplacement of ca. 1.88 Ga A-type granite and formation of younger IOCG deposits or orebodies (ca. Alvo 118; Sossego orebody, Sossego Mine; Tallarico, 2003; Moreto et al., 2015b).

4. The Jatobá iron-oxide-copper-gold (IOCG) deposit

The Jatobá deposit is located about 3 km north of the Sossego Mine (Fig. 2), a world-class iron oxide–copper–gold deposit (IOCG), in the Carajás Mineral Province. Both deposits are associated with the WNW-ESE regional Canaã shear zone that defines the southern contact of the ca. 2.76 to 2.73 Ga Itacaiúnas Supergroup with Mesoarchean units, including ca. 2.97 Ga greenstone belts and ca. 3.0 Ga TTG-like granitoids.

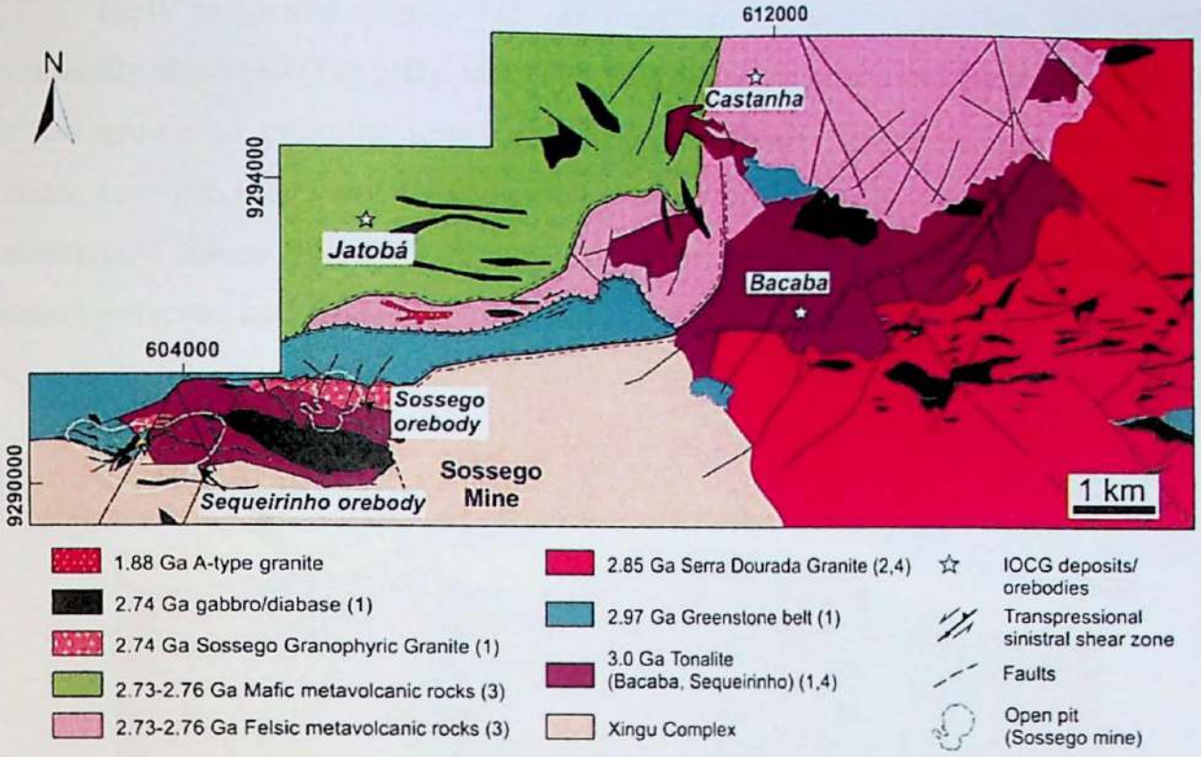

Figure 2. Geological map of part of the Southern Copper Belt in the Carajás Domain, showing the location of IOCG deposits (VALE, 2014; Moreto *et al.*, 2015b). Geochronological data soure: (1) Moreto et al. (2015a); (2) Moreto et al. (2015b); (3) Machado et al. (1991); (4) Moreto et al. (2011).

According to Veloso et al. (Submitted), the main host rocks of the Jatobá deposit comprise metarhyodacite and amygdaloidal metabasalt, in addition to felsic metavolcaniclastic breccias and mafic metalapilli and metacrystal metatuffs, which are cut by metadiabase dikes (Fig. 3 and 4). The least-altered and deformed rocks, mainly derived from mafic protoliths, record effects of lower greenschist facies metamorphism. Sodic plagioclase and actinolite (I) represent the metamorphic paragenesis in rocks with blastosubophitic texture and magnetite (I) with trellis texture.

Hydrothermal alteration was controlled by the Canaã shear zone development, however intense alteration also was developed pervasively in isotropic rocks (Fig 5). Early pre-tectonic hydrothermal alteration encompasses pervasive silicification, sodic (albite, scapolite I, Ce-allanite), sodic-calcic (ferro-pargasite), and potassic (biotite I, tourmaline, Cl-apatite) alteration (Fig 6 A and 6 B). Almond-shaped albite or scapolite (I) porphyroclasts involved by pressure shadows occur in mylonitic rocks (Fig 6 B). Distal hydrothermal alteration resulted in replacement of preexisting minerals that filled amygdales in metabasalts by biotite (I), euhedral magnetite (II) and quartz (Fig 5 A). In more deformed domains, the amygdales are stretched and pressure shadows are also developed around magnetite (II) crystals.

Early magnetite-quartz veins are composed of coarse magnetite (III) crystals, commonly stretched (Fig 5 D). Magnetite (III) has tiny ilmenite exsolution lamellae and is intergrown to granular ilmenite and quartz crystals. Towards the mineralization zones, massive magnetite bodies (IV; up to 60 m) represent proximal envelopes of mineralized zones (Fig 5 E) and are well develop along the contact zones between metarhyodacites and metabasalts and within the latter.

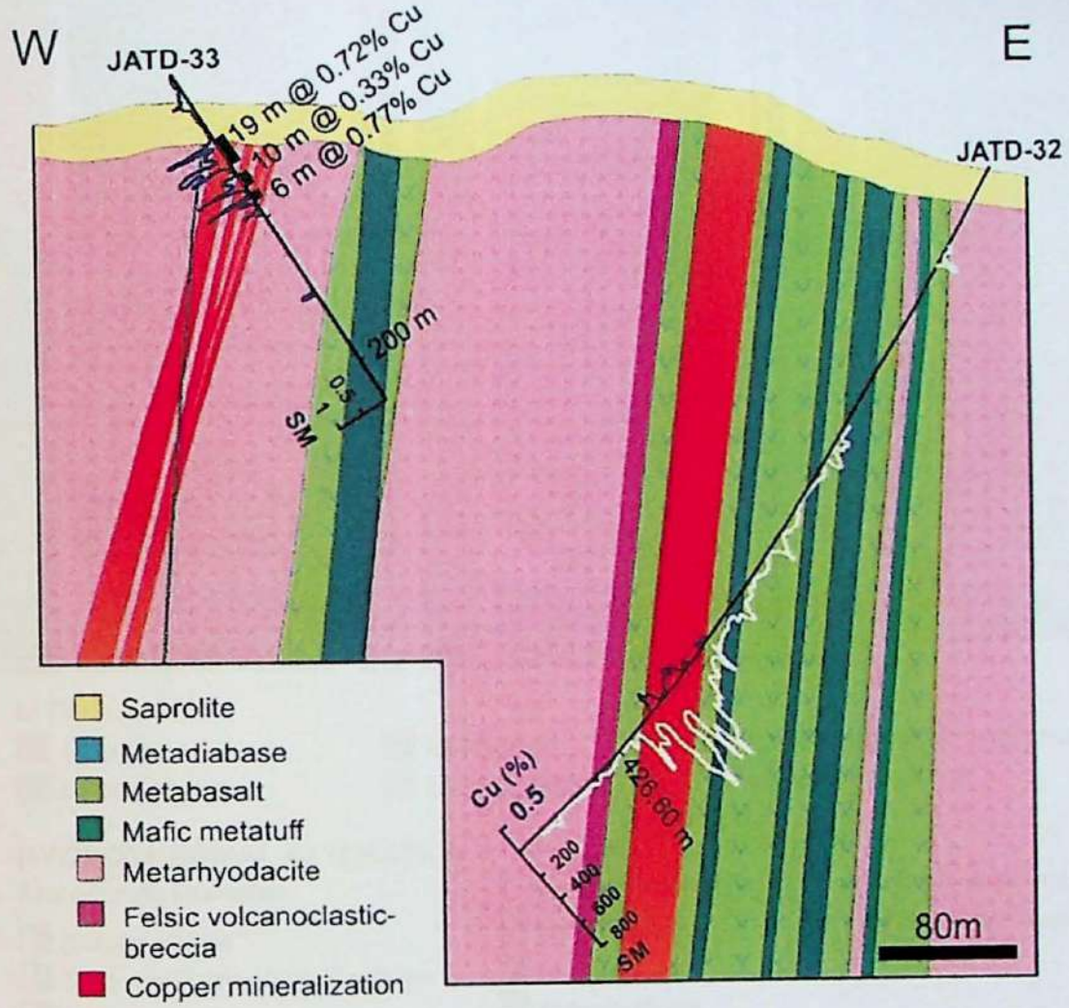

Figure 3. Simplified cross-section of the Jatobá deposit (VALE, 2014), showing magnetite-rich zones in the drill-hole JATD-32, identified by high magnetitic susceptibility (SM), and intercepts of copper mineralization.

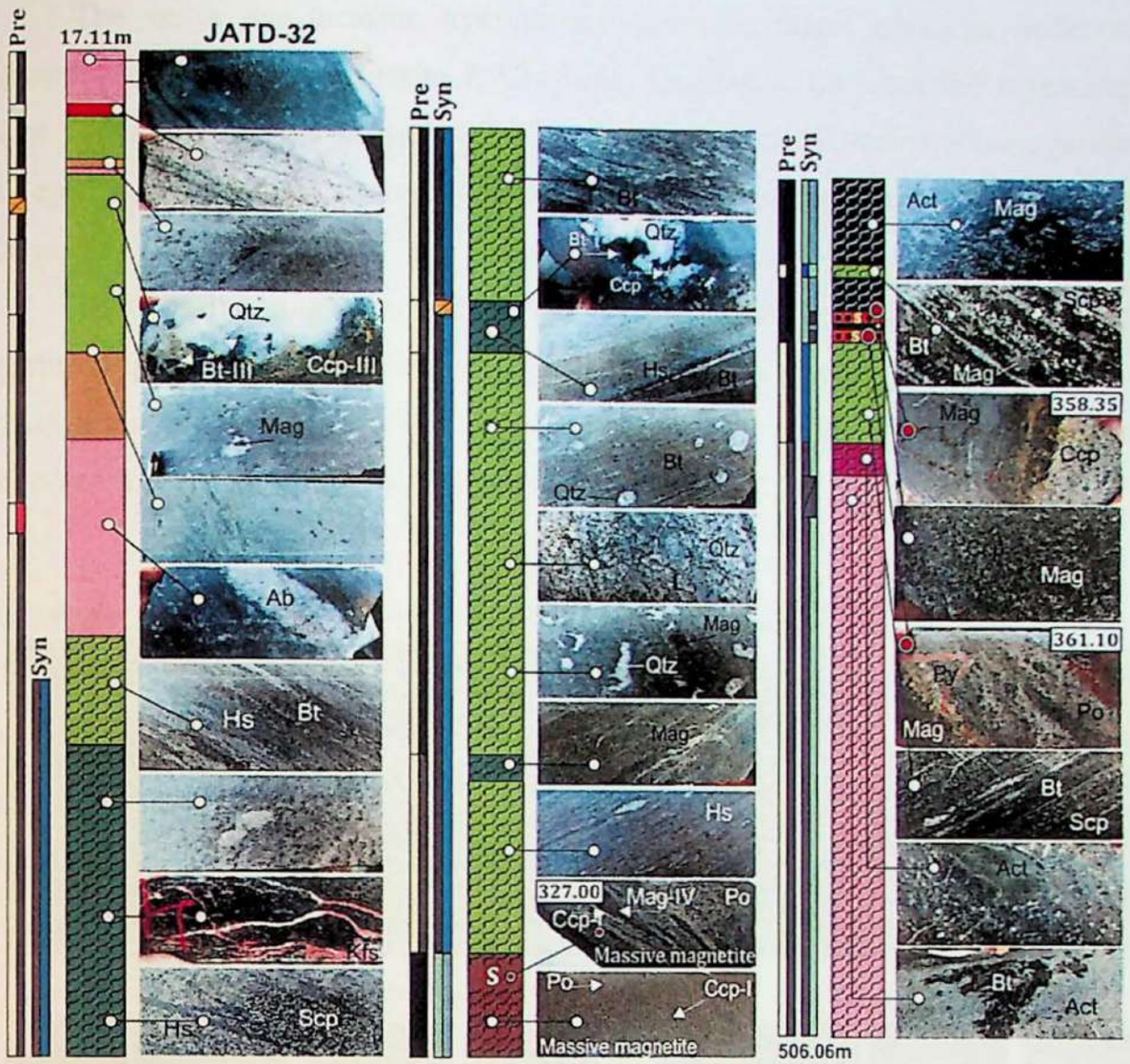

LITHOLOGY

- Granite
- Metadiabase
- Metabasalt
- Metarhyodacite
- Felsic metavolcaniclastic rock
- Mafic metalapilli tuff

HYDROTHERMAL ALTERATION

Pretectonic alteration

- Scapolite/Albite
- Scapolite/Quartz-Magnetite-Biotite
- Scapolite/Biotite
- Massive magnetite bodies

Syntectonic alteration

- Biotite/Hastingsite
- Actinolite/Apatite
- Actinolite/Biotite
- Hastingsite/Actinolite

Late tectonic (veins)

- Biotite and Quartz
- Chlorite

- Late veinlet
- Breccia
- Mylonitic foliation
- S Pyrrohtite sample for S isotope

ORE

Syntectonic mineralization

- Massive magnetite (Pyrrhotite >> Chalcopyrite)
- Massive magnetite (Chalcopyrite > Pyrrhotite)

Late tectonic mineralization

- Biotite - Quartz Chalcopyrite

Figure 4. Schematic profile of the JATD-32 drill hole of the Jatobá deposit, showing characteristic host rocks. Thin columns, at left, represent types of pre-tectonic (PRE) and syn-tectonic (SYN) hydrothermal alteration and main alteration zones.

The main syn-tectonic hydrothermal alteration stages comprise sodic-calcic (scapolite II), calcic (actinolite I, Cl-apatite, Ce-allanite, Ce-monazite, magnetite V; Figs. 5 F and 6 D) and potassic (Cl-K-hastingsite I, biotite II, quartz, Co-magnetite V, Cl-apatite, Ce-allanite) alteration controlled by the development of mylonitic foliation (Figs. 5 H and 6 C).

The massive magnetite bodies (Mag IV; Fig 5 E) are cut by fibrous actinolite, Cl-apatite (Fig 6 D) and subordinated magnetite (V; Fig 5 G). Actinolite also surrounds the massive magnetite bodies (Fig 5 F), sometimes promoting their brecciation, evidencing its posterior temporal relation with these bodies (Fig 5 E).

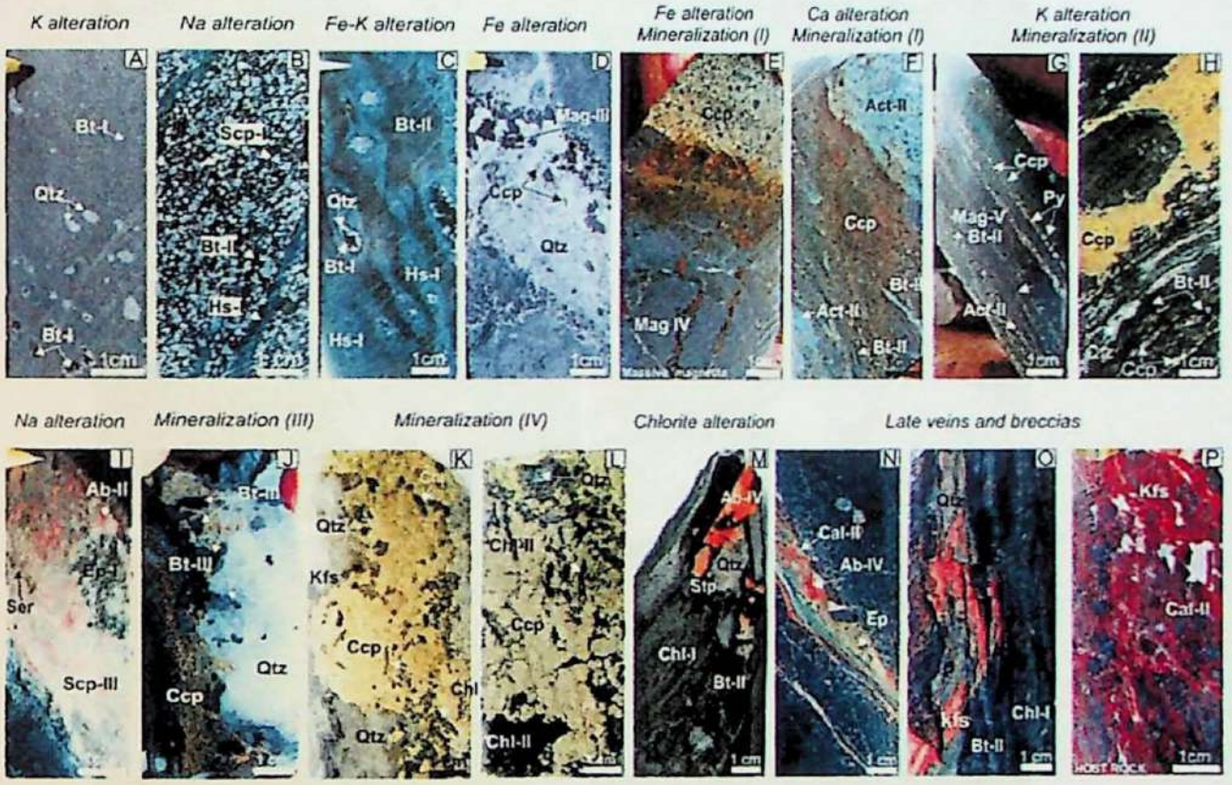

Figure 5. Main features of hydrothermal alteration in the Jatobá deposit, showing its general temporal evolution. A) Metabasalt with pervasive potassic alteration represented by fine biotite (I), which also replaced the amygdale infill; B) Metadiabase with pervasive sodic alteration (scapolite I) followed by syn-tectonic potassic alteration with biotite (II) and thereafter by hastingsite; C) Hastingsite alteration fronts developed along the mylonitic foliation in metabasalt overprinting biotite (I) and (II); D) early magnetite-quartz veins in metabasalt; E) Massive magnetitite replaced and cut by chalcopyrite; F) Metarhyodacite replaced by actinolite (II), chalcopyrite, pyrrhotite, and biotite (II); G) Magnetite (V) associated with biotite (II) and sulfides (chalcopyrite and pyrite); H) Foliated metabasalt replaced by biotite (II) and chalcopyrite; I) Vein infilled with scapolite (III) replaced by retrograde albite, sericite and epidote; J) Vein with quartz, chalcopyrite and coarse green biotite (III); K) Mineralized zone with chalcopyrite and quartz; L) Mineralized zone composed of chalcopyrite, chlorite (II) and quartz; M) Chlorite-altered metabasalt cut by stilpnomelane-quartz-albite (IV) veinlet; N) Porphyritic metadiabase cut by late calcite, albite (IV) and epidote veinlets; O) Foliated metarhyodacite replaced by K-feldspar and quartz and cut by microfaults; P) Breccia zone with K-feldspar and calcite. Abbreviation: Act = actinolite; Hs = hastingsite; Qtz = quartz; Scp = scapolite; Bt = biotite; Stp = stilpnomelane Chl = chlorite; Kfs = K-feldspar; Ep = epidote; Ser = sericite; Cal = calcite; Mag = magnetite; Ccp = chalcopyrite; Py = pyrite.

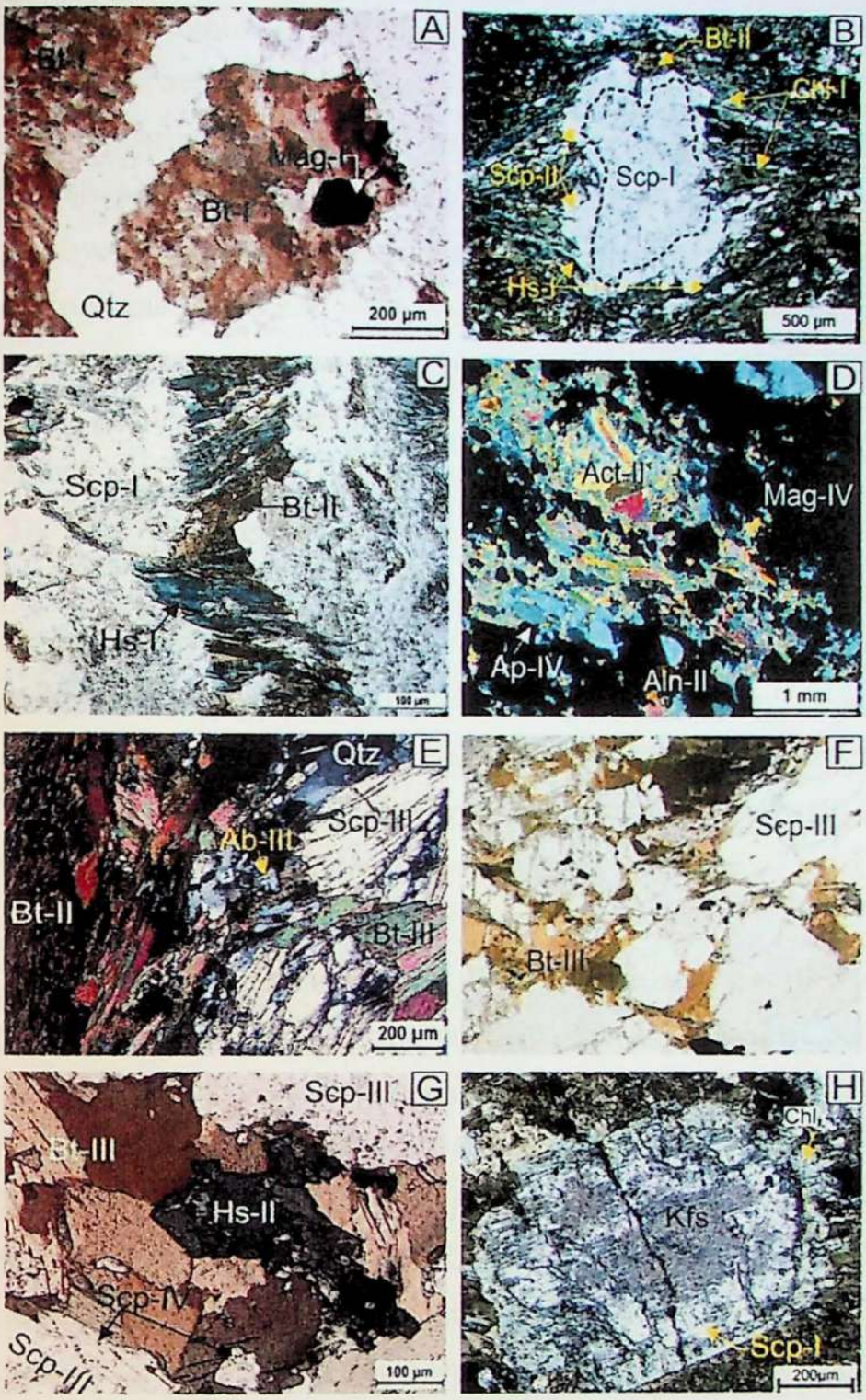

Figure 6. A) Metabasalt with amygdale infilled by biotite (I), magnetite (I) and quartz (TL; PP); **B)** Foliated metadiabase with porphyroclasts of scapolite (I) with scapolite (II) rim involved by mylonitic foliation defined by hastingsite (I) and biotite (II) (TL; PP); **C)** Hastingsite (I) and biotite (II) in a boudin neck in a scapolite (I) crystal (TL; PP); **D)** Actinolite (II), apatite (IV) , allanite (II) and magnetite (IV) (TL; PP); **E)** Metabasalt replaced by biotite (II) and cut by vein infilled by fibrous scapolite (III), which is in turn crosscut by coarse biotite (III) (TL; CP); **F)** Coarse green biotite (III) occurs as infill involving scapolite (III) crystals; **G)** Scapolite (IV), biotite (III) and hastingsite (II) crosscut fibrous scapolite (III); TL; PP); **H)** Scapolite (I) porphyroblast with retrograde alteration (K-feldspar and chlorite) (TL; PP). Abbreviation: Scp = scapolite; Act = actinolite; Hs = hastingsite; Bt = biotite; Chl = clorite; Kfs = K-Feldspar; Ap = apatite; Aln = allanite; Qtz = quartz; Mag = magnetite.

Late tectonic hydrothermal alteration is represented by pervasive chlorite alteration and late scapolite (III) veins (Fig 6 E), which are cut by scapolite (IV), Cl-K-

hastingsite (II) and biotite (III) veinlets (Fig 6 F and 6 G). Ilmenite (II)-titanite-chlorite (II)-adularia veins are formed in magnetite-rich domains.

The copper-gold mineralized zones in the Jatobá deposit comprise swarms of vertical to subvertical orebodies spatially related to metadiabase dikes and contact zones between rhyodacites and metabasalts (Fig 3). Mineralization styles include disseminations, massive ore in replacement fronts controlled by the mylonitic foliation, hydrothermal breccias, stockworks, vein and veinlet systems (Fig 7). The mineralized zones were formed in four distinct stages, coeval to ductile and ductile-brittle deformational events (Fig 7).

The first two stages are syn-tectonic and spatially related to massive magnetite bodies (Fig 7 A). The mineralization stage (I) was related to syn-tectonic calcic alteration, especially to actinolite (II) formation in metarhyodacites. Replacement fronts and breccias have predominance of Ni-pyrrhotite, Ni-pyrite and Cl-apatite (II), and subordinately, Co-chalcopyrite, Ce-allanite (II), Co-pentlandite, quartz and Ce-monazite (Fig 7 B and 7 C). In addition, fine Ni-pyrrhotite crystals, actinolite (II), magnetite (V) and subordinate quartz constitute replacement fronts and brecciated zones with up to 40 cm.

The mineralization stage (II) was temporal and spatially related to the development of the syn-tectonic potassic alteration, which pervasively and indiscriminately affects the main host rocks of the Jatobá deposit. Mineralized zones are developed in portions were biotite (II) was formed at the expense of actinolite (II) in mylonitic rocks (Fig 7 D). These are represented by a system of strongly oriented and interconnected bodies with biotite (II), Cl-apatite (III), Co-magnetite (IV), ilmenite (I), Ce-allanite (III) and quartz, besides discrete portions containing Ni-pyrite and Co-chalcopyrite (Fig 7 F). Breccia zones with expressive formation of biotite (II) and Co-chalcopyrite (± Ni-pyrite ± Ni-pyrrhotite) affecting the preexisting bodies of massive magnetite are also observed (Fig 7 E).

The mineralizing (III) and (IV) stages at Jatobá are distinguished from the others because they are controlled by ductile-brittle structures and associated with veins (Fig 7 G). The third stage was coeval to the late paler brown or green biotite (III), scapolite (IV), Cl-F-apatite (IV), and Cl-K hastingsite (II) and comprises Co-chalcopyrite and siegenite I (± Co-pyrite, ± magnetite, ± cassiterite; (Fig 7 H to 7 I). The late mineralization stage (IV) was the most expressive and coeval to widespread chlorite (II), quartz, epidote and calcite development (Fig 7).

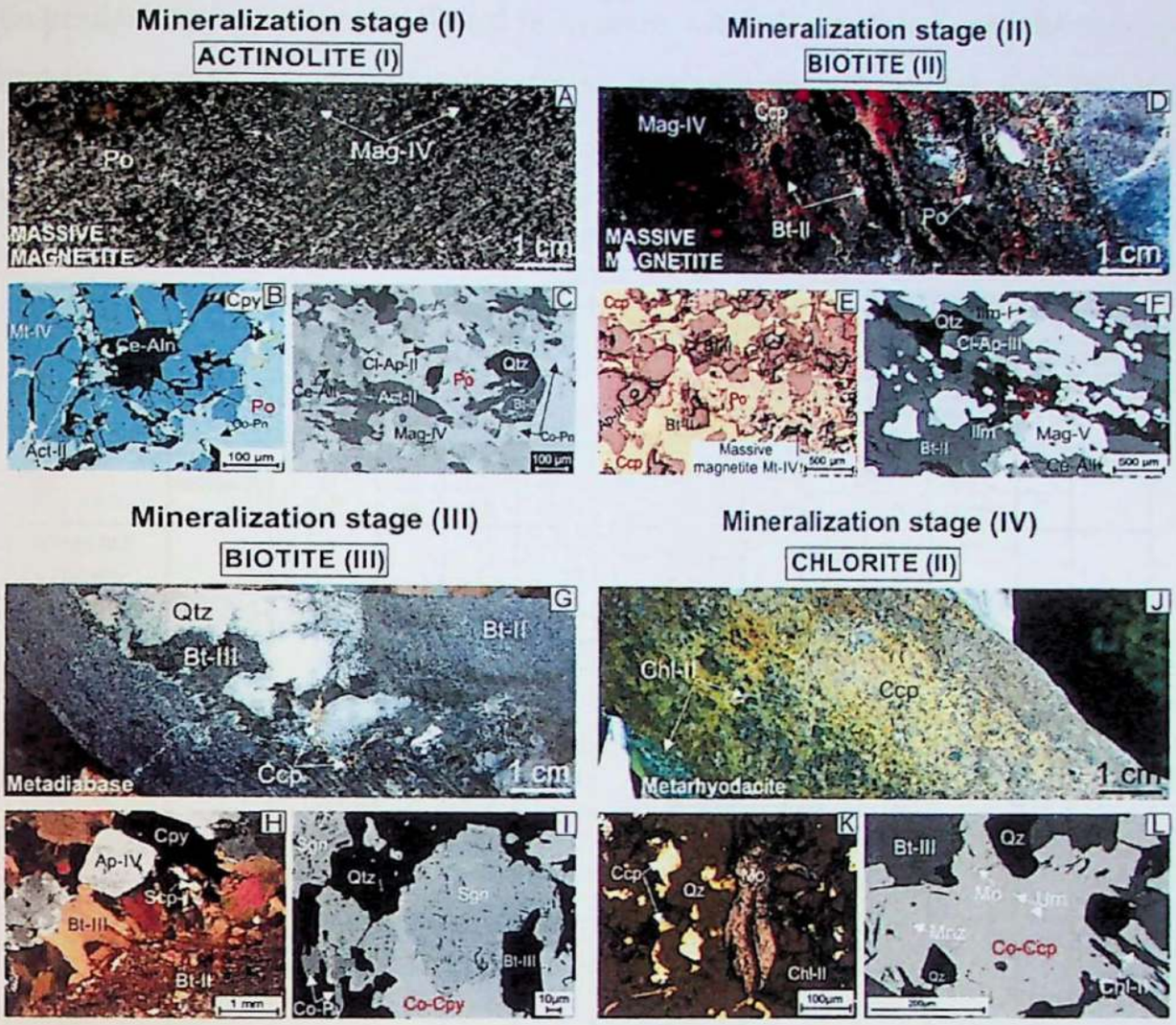

Figure 7. Mineralization stages in the Jatobá depost. **A)** Mineralization stage (I) represented by pyrrhotite-rich breccia; **B)** Magnetite (IV) with infill of pyrrhotite, actinolite (II) and allanite (reflected light); **C)** SEM image showing foliated magnetitite cut by pyrrhotite, actinolite (II), biotite (II), Cl-apatite and allanite; **D)** Foliated magnetitite composed of magnetite (IV) and replaced by syn-tectonic biotite (II), pyrrhotite, chalcopyrite; **E)** Chalcopyrite, pyrrhotite, apatite, biotite (II) and apatite in brecciated magnetitite (reflected light); **F)** SEM image showing syn-tectonic magnetite (V), biotite (II), Cl-apatite (III) and quartz along the mylonitic foliation; **G)** Metadiabase replaced by biotite (II) and cut by late quartz-biotite (III) vein with subordinate chalcopyrite; **H)** Detail of the quartz-biotite (III) vein, showing the association of chalcopyrite and apatite, and distinct texture of biotite (II) and (III) (TL; CP); **I)** SEM image showing detail of the Co-chalcopyrite-siegenite-quartz association of the mineralizing stage (III); **J)** Mineralization stage (IV) represented by chalcopyrite-chlorite alteration front in altered metarhyodacite; **K)** Molybdenite associated with chalcopyrite, K-feldspar, chlorite and quartz (reflected light); **L)** SEM image showing Co-chalcopyrite with uraninite and monazite microinclusions and associated biotite (III), quartz and chlorite (II). **Abbreviation:** Act = actinolite; Cl-Ap = Cl-Apatite; Aln = allanite; Qtz = quartz; Bt = biotite; Mag = magnetite; Co-Ccp = Co-chalcopyrite; Co-Pn = Co-pentlandite; Po = pyrrhotite; Py = pyrite; Ni-Py = Ni-pyrite; Mnz = monazite; Ilm = ilmenite; Urn = uraninite; Mo = molybdenite.

Mineralization (IV) occur as a variety of branching veinlets, which cut out and isolate portions of rock that have been previously altered, thus giving a brechoid aspect to the rock (Fig 7 J). In these chlorite-rich domains, veinlets with Co-chalcopyrite, ± Co-pyrite, sphalerite, molybdenite, uraninite and monazite occur (Fig 7 K and 7 L).

Other late vein types comprise those with quartz-chalcopyrite-K (± molybdenite, Co-pentlandite, and siegenite II) and fine veinlets with chlorite-chalcopyrite, W-bearing hematite, rare earth carbonates (bastnäsite, coskrenite and sahamalite), Co- and Ni-pyrite, sphalerite, ilmenite, marcasite, leucoxene and adularia. The paragenetic evolution of the Jatobá deposit is presented in Figure 8.

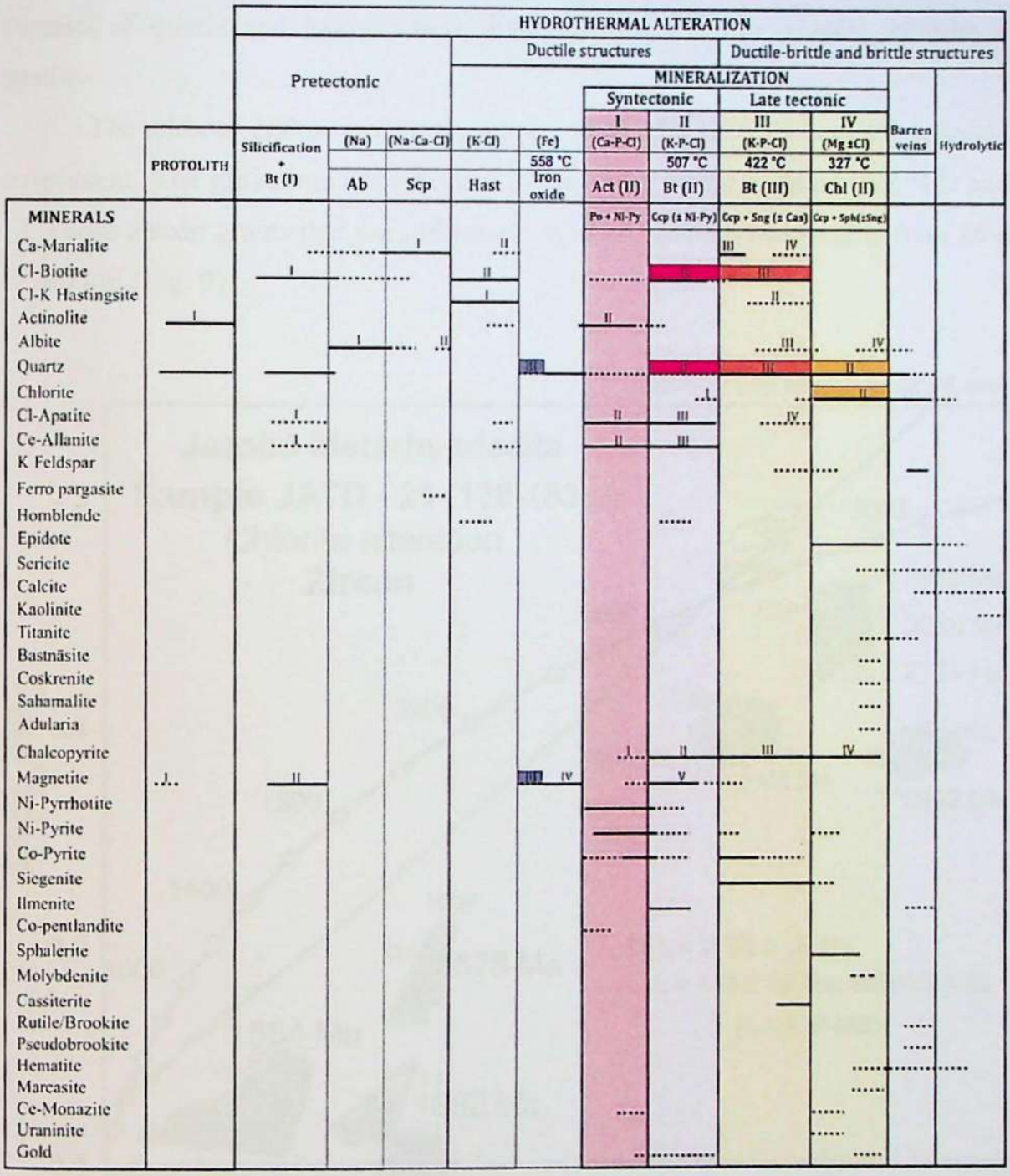

Figure 8. Paragenetic evolution of the Jatobá deposit. The colored rectangles represent the relative temporal position of mineral pairs chosen for stable isotope analysis.

5. Results

LA-ICP-MS U–Pb age in zircon

Least-altered portions of the host metarhyodacite (sample JATD-21; 178-183 m) were selected for geochronological studies. The rock is light gray, fine-grained, massive and porphyritic with bipyramidal quartz (β-quartz) and euhedral plagioclase blastophenocrists. The matrix is fine-grained, equigranular to inequigranular, and consists of quartz and hydrothermal albite, microcline, biotite, epidote, chlorite and apatite.

The zircon grains are murky brown to pinkish in color and transparent to translucent. The grains are often broken and few have prismatic shape (Fig. 9 D and 9 E). Those zircon grains that are still preserved have crystal lengths ranging from 80 μm to 240 μm (Fig. 9).

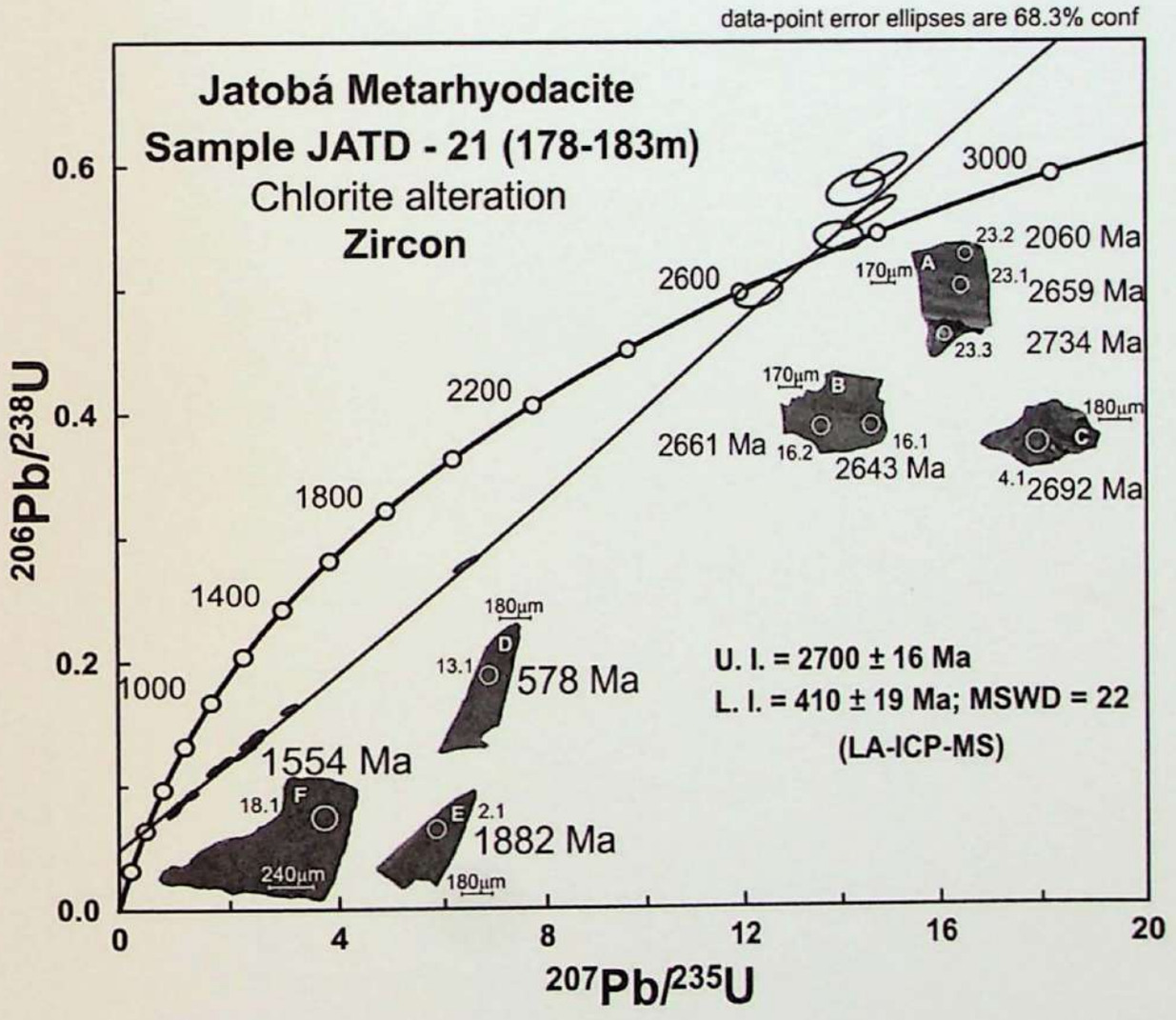

Figure 9. $^{206}Pb/^{238}U$ vs. $^{207}Pb/^{235}U$ Concordia diagram for the Jatobá metarhyodacite host rock (sample JAT – 21/178 -183 m), showing cathodoluminescence images of highly metamict zircon grains.

The cathodoluminescence images show typically low luminescence and homogeneity of zircon grains. These are highly metamict (Fig. 9A to 9 C) and have high U contents (between 246 and 664 ppm; Table). A total of 23 grains were analyzed, with $^{232}Th/^{238}U$ ratios ranging from 1.49 to 0.36 (Table 1). Three grains have concordant $^{207}Pb/^{206}Pb$ ratios (97–113% concordance) indicating an age of ca. 2.7 Ga, but the bulk of analyzed grains reflect intense Pb loss (Table 1). An upper intercept age of 2,700 ±16 Ma (MSWD = 22) was estimated using a total of 23 grains and considered as the crystallization age (Fig. 9).

Table 1. Summary of U-Pb LA–ICPMS zircon data from the host metarhyodacite (sample JATD 21/178-183) of the Jatobá deposit.

Spot	Pb total %	Pb rad (ppm)	Th (ppm)	U (ppm)	Th/U	$^{207}Pb/^{235}U$	1s	$^{206}Pb/^{238}U$	1s	$^{238}U/^{206}Pb$	1s	$^{207}Pb/^{206}Pb$	1s	$^{208}Pb/^{206}Pb$	1s	$^{206}Pb/^{238}U$	1s	$^{207}Pb/^{206}Pb$	1s	% concordance
16.2	0.15	17	13	19	0.69	12.3435	0.3161	0.4951	0.0074	2.0199	0.0302	0.1808	0.0036	0.2190	0.0037	2.593	0.032	2.661	0.032	97
11.1	0.36	108	225	246	0.92	6.4251	0.1469	0.2785	0.0036	3.5907	0.0462	0.1673	0.0028	0.2283	0.0036	1.584	0.018	2.531	0.028	62
23.2	1.23	61	234	299	0.78	2.1906	0.0599	0.1249	0.0019	8.0058	0.1237	0.1272	0.0030	0.2711	0.0059	0.759	0.011	2.060	0.039	36
5.1	0.99	77	271	313	0.87	2.5011	0.0636	0.1414	0.0019	7.0726	0.0975	0.1283	0.0025	0.3130	0.0066	0.853	0.011	2.075	0.034	41
22.1	0.52	74	270	321	0.84	2.3256	0.0612	0.1343	0.0020	7.4446	0.1117	0.1256	0.0027	0.2921	0.0048	0.812	0.011	2.037	0.037	39
7.1	1.01	81	271	330	0.82	3.0892	0.0736	0.1622	0.0021	6.1666	0.0807	0.1382	0.0025	0.2901	0.0069	0.969	0.012	2.204	0.032	43
15.1	0.15	63	253	333	0.76	1.7060	0.0480	0.1131	0.0018	8.8398	0.1384	0.1094	0.0024	0.2692	0.0037	0.691	0.010	1.789	0.041	38
19.1	1.29	48	308	345	0.89	1.0797	0.0314	0.0852	0.0013	11.7353	0.1828	0.0919	0.0023	0.3337	0.0072	0.527	0.008	1.465	0.048	35
14.1	0.86	69	303	357	0.85	1.9197	0.0523	0.1196	0.0018	8.3606	0.1273	0.1164	0.0026	0.3054	0.0091	0.728	0.010	1.902	0.039	38
21.1	1.03	64	594	398	1.49	1.3300	0.0371	0.0933	0.0014	10.7234	0.1640	0.1034	0.0025	0.5169	0.0126	0.575	0.008	1.687	0.044	34
20.1	1.23	54	343	400	0.86	0.9666	0.0303	0.0795	0.0013	12.5783	0.2035	0.0882	0.0023	0.3300	0.0051	0.493	0.008	1.386	0.051	35
18.1	1.36	56	334	405	0.82	1.1618	0.0330	0.0875	0.0014	11.4293	0.1767	0.0963	0.0024	0.3266	0.0056	0.541	0.008	1.554	0.047	34
2.1	0.98	76	450	405	1.11	1.8007	0.0447	0.1134	0.0015	8.8148	0.1169	0.1151	0.0022	0.3221	0.0055	0.693	0.009	1.882	0.035	36
12.1	1.16	54	488	408	1.19	1.0028	0.0275	0.0793	0.0011	12.6087	0.1698	0.0917	0.0020	0.3520	0.0057	0.492	0.006	1.461	0.042	33
9.1	1.31	48	393	410	0.96	0.9575	0.0276	0.0779	0.0011	12.8353	0.1792	0.0891	0.0022	0.3407	0.0054	0.484	0.006	1.407	0.048	34
17.1	0.36	103	485	469	1.03	2.4660	0.0608	0.1360	0.0019	7.3537	0.1047	0.1315	0.0026	0.2987	0.0116	0.822	0.011	2.118	0.034	38
3.1	1.35	73	504	559	0.90	1.0566	0.0268	0.0828	0.0011	12.0761	0.1536	0.0925	0.0019	0.3252	0.0049	0.513	0.006	1.479	0.039	34
10.1	0.79	94	708	566	1.25	1.2823	0.0311	0.0933	0.0012	10.7212	0.1348	0.0997	0.0019	0.4469	0.0049	0.575	0.007	1.619	0.036	35
6.1	0.71	150	964	664	1.45	2.3664	0.0524	0.1305	0.0016	7.6628	0.0928	0.1315	0.0021	0.4290	0.0037	0.791	0.009	2.118	0.028	37
23.3	0.33	74	32	89	0.36	14.5922	0.3675	0.5599	0.0086	1.7860	0.0275	0.1890	0.0038	0.1370	0.0069	2.866	0.036	2.734	0.033	104
8.1	0.18	34	25	41	0.61	13.9796	0.3220	0.5419	0.0073	1.8454	0.0247	0.1871	0.0033	0.1982	0.0175	2.791	0.030	2.717	0.029	102
4.1	-0.76	-6	-8	-10	0.76	12.0160	0.2540	0.4729	0.0057	2.1148	0.0253	0.1843	0.0029	0.1921	0.0070	2.496	0.025	2.692	0.026	92
1.1	2.95	25	34	45	0.76	7.8785	0.1762	0.3425	0.0044	2.9196	0.0376	0.1668	0.0027	0.3224	0.0689	1.899	0.021	2.526	0.026	75
16.1	0.29	26	17	28	0.61	14.3281	0.3896	0.5809	0.0093	1.7215	0.0274	0.1789	0.0039	0.2181	0.0054	2.952	0.038	2.643	0.035	111
23.1	0.11	24	11	26	0.40	14.8310	0.3560	0.5952	0.0084	1.6800	0.0237	0.1807	0.0038	0.1817	0.0129	3.011	0.035	2.659	0.033	113
13.1	0.81	55	9	526	0.02	0.7886	0.0225	0.0964	0.0012	10.3690	0.1323	0.0593	0.0014	0.0062	0.0044	0.594	0.007	0.578	0.052	102

Lithochemistry

Ten representative ore samples of the mineralization stages (I), (II), and (IV) of the Jatobá deposit were analyzed for major, minor and trace elements. All samples have Cu contents exceeding 10,000 ppm, except those of the mineralization stage (I) that present much lower values (590 to 1360 ppm; Appendix). Pyrrhotite-rich ore samples from the mineralization stages (I), spatially related to massive magnetite, have the highest Fe_2O_3 (71.49 to 63.91 wt. %), Ni (3930 to 1270 ppm), Co (2320 to 670 ppm), V (740 to 590 ppm), Pd (81 to 372 ppb) and Pt (2 to 17 ppb) contents. In general, ore samples from stage (II) have intermediate composition in relation to those of the mineralization stages (I) and (IV). Its contents of Fe_2O_3 reaches 50.45 wt.%, whereas those of the late mineralization stage vary from 34.19 wt.% to 21.00 wt.%. In consequence, nickel and cobalt contents are positively correlated to Fe_2O_3 and V (Fig. 10A and 10B). In the other hand, Ni + Co are negatively correlated to rare metals (Sn, W, Be), zinc, and gold (Fig. 10D, 11C to 11D), which are enriched in samples of the mineralization stage (IV). In the latter, Sn (up to 24 ppm), Nb (7.50 ppm), W (up to 322.50) and Zn (up to 482 ppm) contents were reported. Gold contents are markedly lower in the mineralization stages (I) samples (7 to 14 ppm) in relation to those of stage (II) with 282 to 1263 ppm and (IV) with 116 to 1310.80 ppm (Fig. 11C and 11D).

In addition, the variation of other oxides and minor elements do not have a clear relationship with the paragenetic evolution of the Jatobá deposit, but they are correlated with each other, such as U, Th, P_2O_5 and REE (Fig. 10C, 10F; 11A and B). The highest and lowest values of these elements/oxides were found in samples of the mineralization (IV), which have U (0.20 to 48.50 ppm), Th (1.10 to 23.30 ppm) and P_2O_5 (0.07 to 7.97 wt. %) contents (Fig. 11A and 11B).

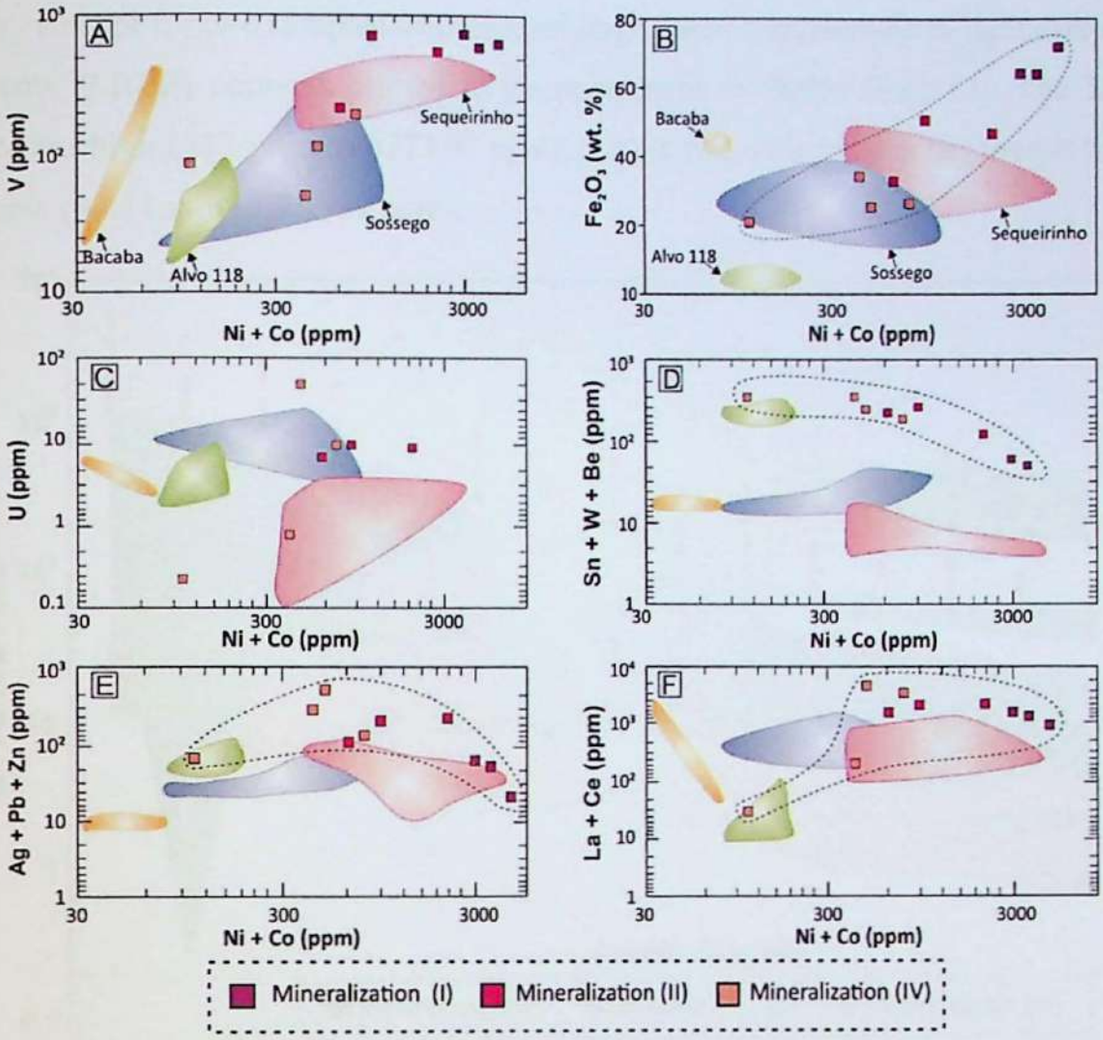

Figure 10. Bivariant diagrams for ore samples related to the mineralization stages (I), (II), and (IV). Lithochemistry data source: Sossego (Sequeirinho and Sossego orebody, Carvalho, 2009); Bacaba (Roscito, 2009); and Alvo 118 (Moreto et al. 2009).

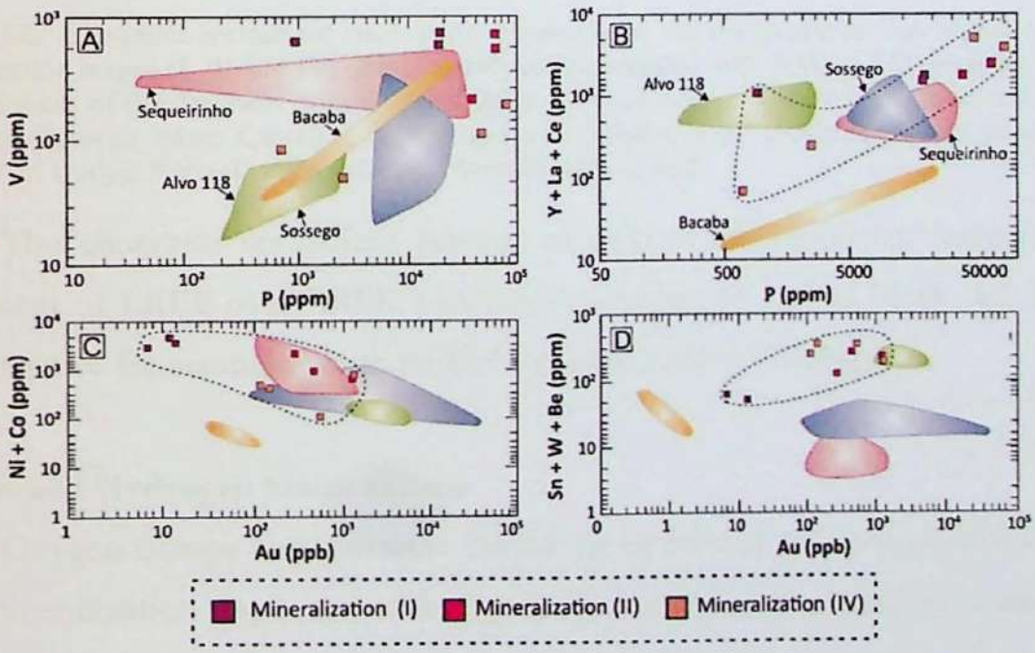

Figure 11. Bivariant diagrams for ore samples related to the mineralization stages (I), (II), and (IV). Lithochemistry data source: Sossego (Sequeirinho and Sossego orebody, Carvalho, 2009) Bacaba (Roscito, 2009) and Alvo 118 (Moreto et al. 2009).

Except for two samples from the last stage, there is an increase in light rare earth elements (LREE) contents related to the paragenetic evolution (Fig. 12). The ΣREE values are high (957 ppm to 6773.92 ppm), but the two outliers have the lowest ΣREE contents (64.11ppm to 318.89 ppm).

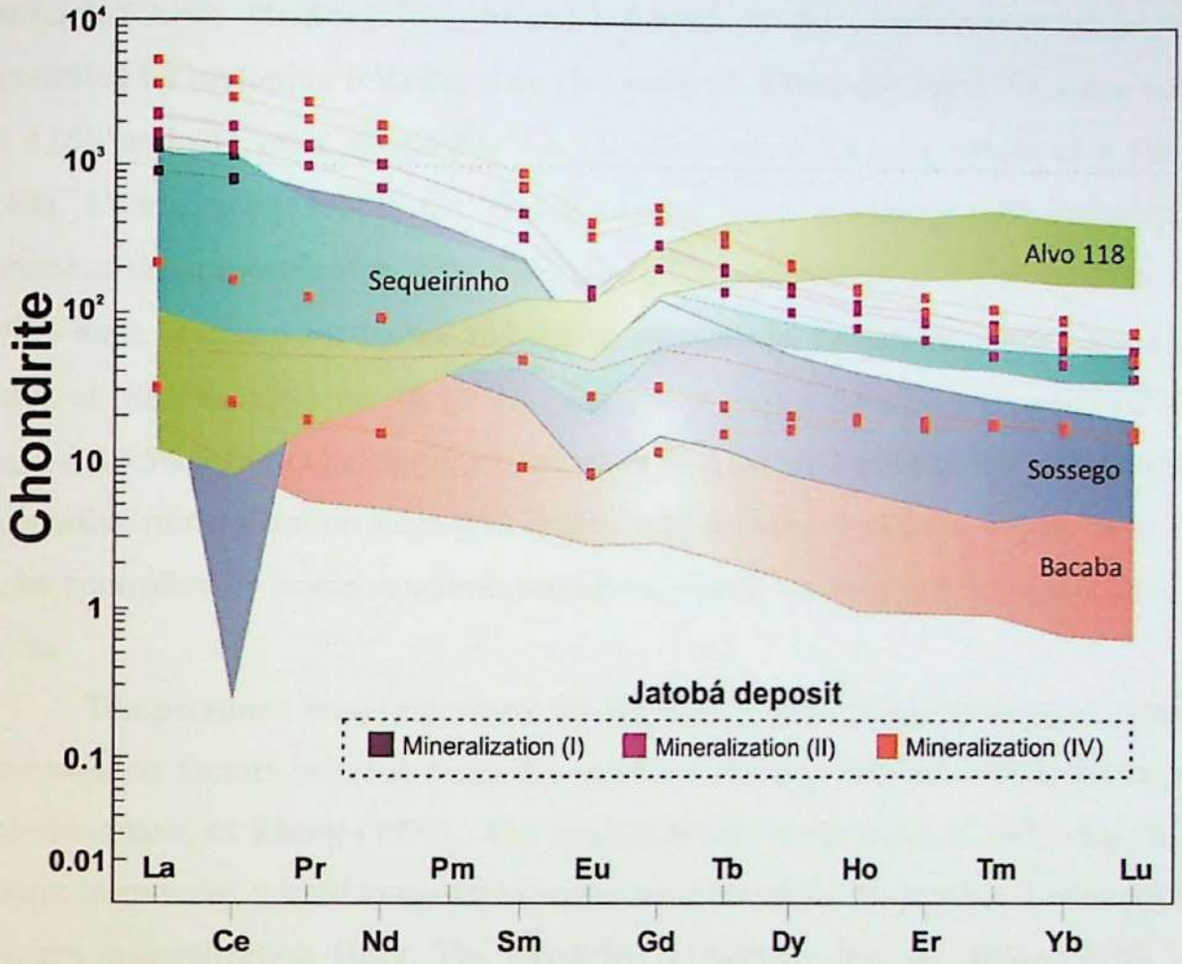

Figure 12. Chondrite-normalized rare earth element plot of representative ore samples of the mineralization stages (I, III and IV) of the Jatobá deposit compared with fields of REE patterns for other IOCG deposits of the Southern Copper Belt, Carajás Province. Source of data: Sequeirinho and Sossego orebodies (Sossego mine; Carvalho, 2009); Alvo 118 (Moreto et al., 2009); Bacaba (Roscito, 2009); Jatobá (This study). Normalization values are from Boynton (1984).

The chondrite normalized patterns of REE in the Jatobá ore samples show enrichment of LREE over HREE with $(La/Yb)_N$ values of 1.69 to 74.93. All samples show negative Eu anomalies with Eu/Eu* values of 0.36 to 0.79 (Fig. 12).

Oxygen and Hydrogen Stable isotope

Oxygen isotope analyses were carried out on mineral pairs representative of the main mineralization stages at Jatobá (Fig. 8). The selection of mineral pairs was based on evidence of textural equilibrium and absence of features indicative of retrograde alteration. Hydrogen isotope analyses were obtained for the same hydrated mineral

phases analyzed for oxygen isotopes. Oxygen and hydrogen isotope compositions for these mineral pair are presented in Table 2.

Magnetite (III) and quartz from early veins related to iron metasomatism have $\delta^{18}O_{V\text{-}SMOW}$ values of 3.7‰ and 11‰, respectively. Syn-tectonic biotite (II) and quartz associated with chalcopyrite-(pyrrhotite) formed in the mineralization stage (II) controlled by mylonitic foliation were also analyzed. Biotite (II) has $\delta^{18}O_{V\text{-}SMOW}$ value of 4.0‰ and δD value of -64.2‰. Coeval quartz has $\delta^{18}O_{V\text{-}SMOW}$ values of 8.5‰ to 8.6‰. Coarse green biotite (III) and quartz that occur associated with chalcopyrite represent the mineralization stage (III). The $\delta^{18}O_{V\text{-}SMOW}$ values of 4.4‰ to 4.6‰ and 9.9‰ were obtained for biotite and quartz, respectively. In addition, biotite has a δD value of -88.4‰. Chlorite (II) ($\delta^{18}O_{V\text{-}SMOW}$ = 4.8‰; δD = -59.6‰) and quartz ($\delta^{18}O_{V\text{-}SMOW}$ = 10.5‰) from chalcopyrite-bearing ore breccias are typical of the late and most expressive mineralization stage (IV) in the Jatobá deposit. In addition, calcite from late veins controlled by brittle structures was also analyzed, resulting in $\delta^{18}O_{V\text{-}SMOW}$ value of 8.7‰.

Temperatures were calculated for the chosen pairs using the oxygen isotope fractionation factors between magnetite-quartz of Zheng (1991) and biotite-quartz and chlorite-quartz of Zheng (1993). The oxygen isotope composition of early magnetite-quartz from veins related to massive magnetite permitted the temperature estimation for the pre-mineralization stage. The calculated temperature was the highest (558 °C) recorded at Jatobá. Conditions for the mineralizing stages (II), (III) and (IV) were estimated based on the isotope composition of biotite (II)-quartz (507 °C), biotite (III)-quartz (422 °C) and chlorite-quartz (327 °C) reflecting temperature decreasing during the paragenetic evolution (Table 2 and Fig. 13 A).

Oxygen isotope composition of fluids were estimated based on oxygen isotope fractionation factors between mineral-H_2O of Bottinga and Javoy (1973) for magnetite-H_2O and biotite-H_2O; Matsuhisa et al. (1979) for quartz-H_2O; Cole (1985) for chlorite-H_2O; and Golyshev et al. (1981) for calcite-H_2O. Hydrogen isotope composition of fluids was estimated based on hydrogen isotope fractionation factors between biotite-H_2O of Suzuoki and Epstein (1976) and chlorite- H_2O of Graham et al. (1987).

Table 2. Oxygen and hydrogen isotope compositions for minerals, calculated isotope compositions of hydrothermal fluids and calculated temperatures based on oxygen isotope fractionation factors of Zheng (1991, 1993).

Sample	Mineral	Stage	$\delta^{18}O_{SMOW}$ ‰	δD_{SMOW} ‰	Temperature (°C)	$\delta^{18}O_{H2O}$ ‰	δD_{H2O} ‰
JAT-32 (259.35)	Mag (III)	Early Fe metasomatism	3.7		558.4	9.53	
JAT-32 (259.35)	Qtz	Early Fe metasomatism	11.0		558.4	9.18	
JAT-28 (160.40)	Bt (II)	Mineralization stage (II)	4.0	-64.2	506.6	6.44	-30.25
JAT-28 (160.40)	Qtz	Mineralization stage (II)	8.5		506.6	6.37	
JAT-28 (160.40)	Qtz	Mineralization stage (II)	8.5		506.6		
JAT-28 (160.40)	Qtz	Mineralization stage (II)	8.6		506.6		
JAT-21 (40.00)	Bt (III)	Mineralization stage (III)	4.4	-88.4	421.5	6.77	-44.88
JAT-21 (40.00)	Bt (III)	Mineralization stage (III)	4.6		421.5		
JAT-21 (40.00)	Qtz	Mineralization stage (III)	9.9		421.5	6.79	
JAT-28 (128.10)	Chl (II)	Mineralization stage (IV)	4.8	-59.6	327.1	5.41	-31.6
JAT-28 (128.10)	Qtz	Mineralization stage (IV)	10.5		327.1	5.95	
JAT-3 (221.75)	Cal	Barren veins	8.7		280.0	4.48	

Oxygen isotope composition of fluids were estimated based oxygen isotope fractionation factors between mineral-H_2O of Bottinga and Javoy (1973) for magnetite-H_2O and biotite-H_2O; Matsuhisa et al. (1979) for quartz-H_2O; Cole (1985) for chlorite-H_2O; and Golyshev et al. (1981) for calcite-H_2O. Hydrogen isotope composition of fluids was estimated based hydrogen isotope fractionation factors between biotite-H_2O of Suzuoki and Epstein (1976) and chlorite- H_2O of Graham et al. (1987). Abbreviations: Mag = magnetite; Bt = biotite; Chl = chlorite; Qtz = quartz; Cal = calcite.

Hydrothermal fluids in equilibrium with magnetite-quartz have $\delta^{18}O_{H2O}$ values of 9.18 to 9.53‰, at 558 °C. Lower $\delta^{18}O_{H2O}$ values (6.37 to 6.44‰) were estimated for fluids in equilibrium with biotite (II) and quartz of the mineralization stage (II), at 507 °C. Calculated hydrogen isotope composition of fluids in equilibrium with biotite, at this same temperature, is -30.25‰. Similar $\delta^{18}O_{H2O}$ values were estimated, at 422 °C, for the mineralization stage (III) from biotite (III) (6.77‰) and quartz (6.79‰) (Fig. 13 B and 14). At this stage, hydrothermal fluids have δD_{H2O} values of -44.88‰ (Fig. 14).

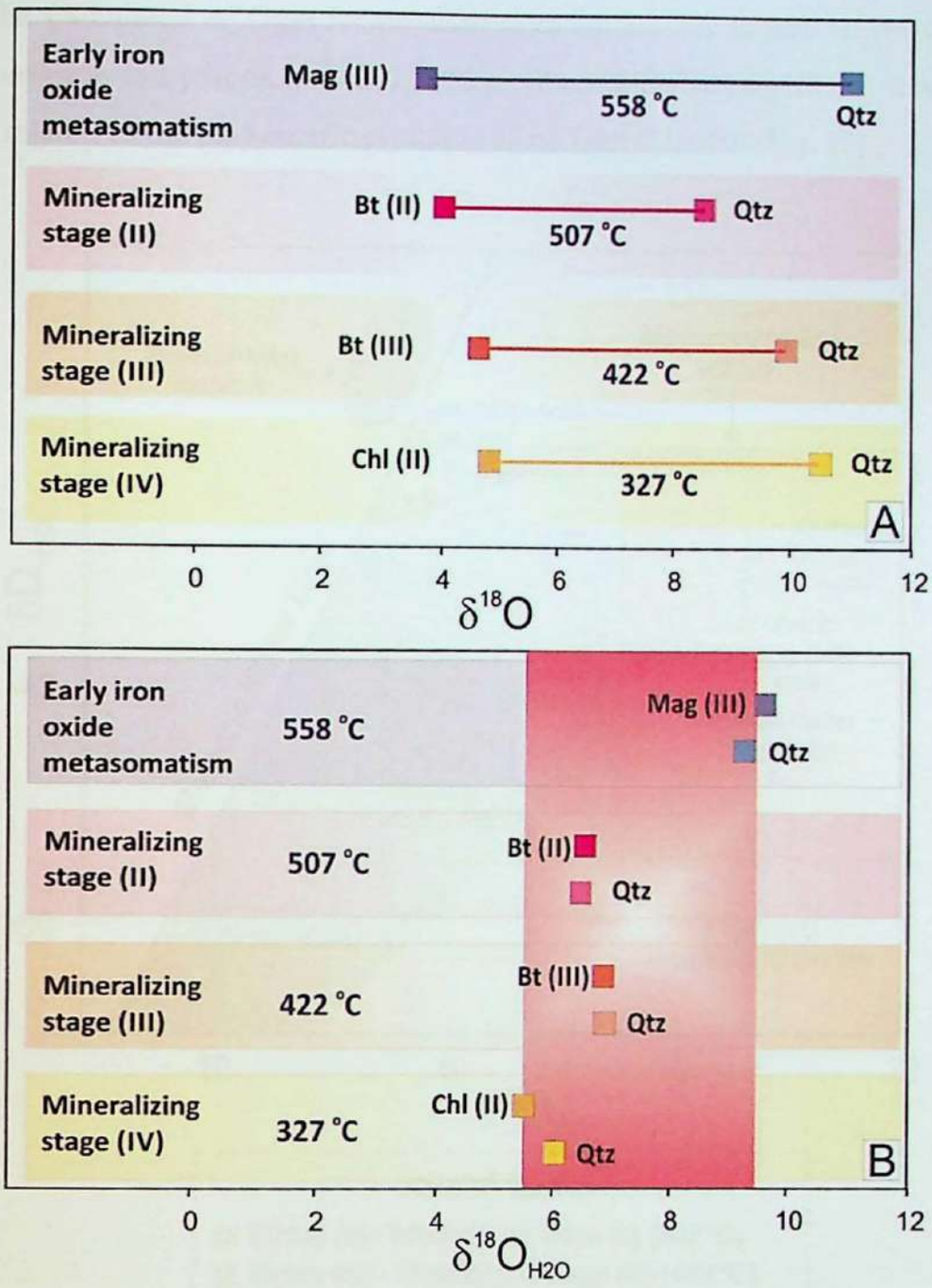

Figure 13. A) Calculated temperatures based on oxygen isotope fractionation factors of Zheng (1991, 1993) for mineral pairs representative of distinct alteration and mineralization stages in the Jatobá deposit. B) Oxygen isotope composition of fluids in equilibrium with magnetite, biotite, chlorite and quartz of the Jatobá deposit. $\delta^{18}O_{H2O}$ values were estimated based oxygen isotope fractionation factors between mineral-H_2O of Bottinga and Javoy (1973) for magnetite-H_2O and biotite-H_2O; Matsuhisa et al. (1979) for quartz-H_2O; Cole (1985) for chlorite-H_2O. The reddish area represents the field of primary magmatic waters (Taylor, 1974) and felsic magmatic water field from Taylor (1992).

Hydrothermal fluids associated chlorite (II) and quartz from the main mineralization stage (IV) show $\delta^{18}O_{H2O}$ (5.95‰ to 5.41‰) and δD_{H2O} (-31.6‰) values, (Fig. 14) at 327 °C. Oxygen isotope composition of fluids in equilibrium with calcite from late barren veins is 4.48‰, at 280 °C.

The calculated $\delta^{18}O_{H2O}$ for pre-mineralization and ore-related stages reveals a narrow variation in hydrothermal fluid isotope composition and significant temperature decrease related to the paragenetic evolution of the Jatobá deposit (Fig. 15).

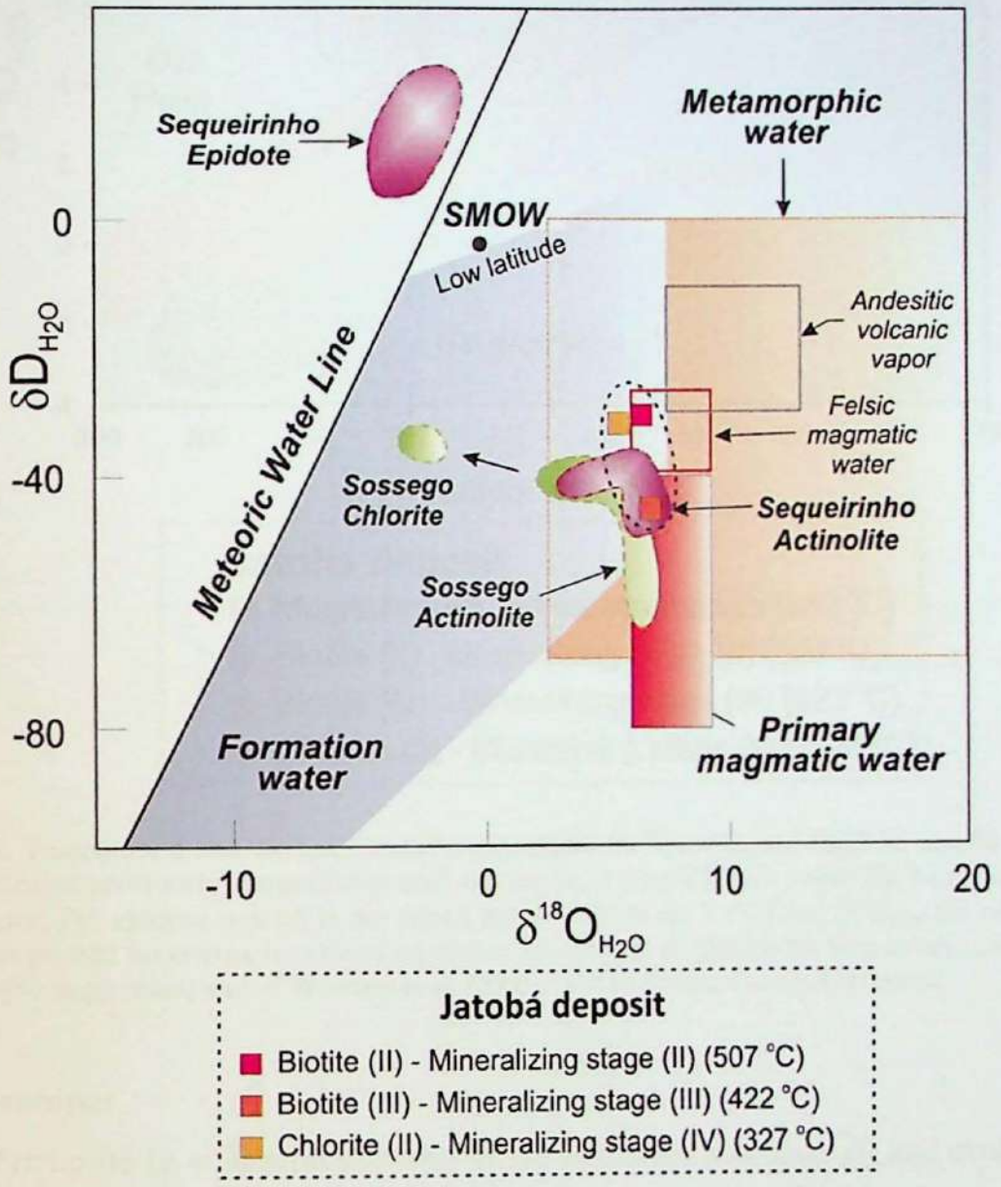

Figure 14. Oxygen and hydrothermal isotope composition of fluids in equilibrium with biotite (II) and (III) and chlorite (II), which are representative of the mineralization stages (II), (III) and (IV) of the Jatobá deposit. Fields for the Sossego mine (Sossego and Sequeirinho orebodies) are based on data of Monteiro et al. (2008a). Andesitic volcanic vapor field is from Giggenbach (1992); felsic magmatic water field is from Taylor (1992); primary magmatic water field is from Taylor (1974).

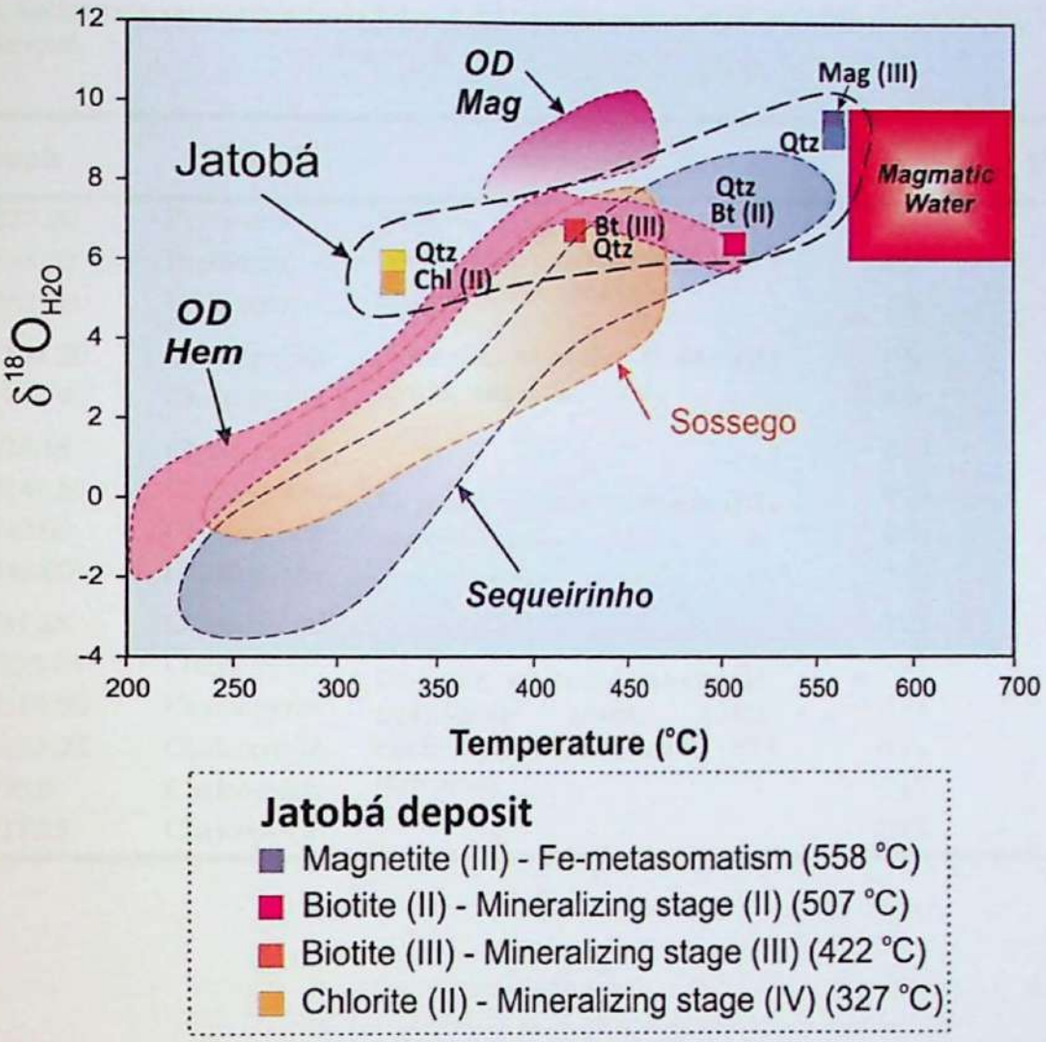

Figure 15. Temperature and oxygen isotope compositions for hydrothermal fluids in equilibrium with minerals formed previously (magnetite-quartz) and coeval to mineralization stages (II: biotite-quartz; III: biotite-quartz; IV: chlorite-quartz) in the Jatobá deposit. Fields for T (°C) and $\delta^{18}O_{fluid}$ for other IOCG deposits are plotted for comparison based on data of Monteiro et al. (2008a) for Sequeirinho and Sossego orebodies (Sossego mine) and of Williams et al. (2005) for the Olympic Dam (OD) deposit.

Sulfur Isotopes

Pyrrhotite (n = 3) representative of the mineralization stage (I) and chalcopyrite (n = 12) formed in the mineralization stages (II) to (IV) were chosen for sulfur isotope analysis (Table 3 and Fig. 16).

The sulfur isotope compositions of pyrrhotite and chalcopyrite of the Jatobá deposit indicate lower values ($\delta^{34}S$ = 0.27 to 0.85‰) for sulfides from the mineralization stages (I) and II) in relation to those of the mineralization stages (III) and (IV). The latter have $\delta^{34}S$ values of 0.78 to 1.80‰ (Table 3). Despite the increasing of $\delta^{34}S$ values related to the paragenetic evolution of the Jatobá deposit, its sulfides record a narrow variation of sulfur isotope compositions.

Table 3. Sulfur isotope compositions for sulfides representative of mineralization stages (I) to (IV) of the Jatobá deposit.

Sample	Mineral	Association	Mineralization Stage	$\delta^{34}S$ (‰)
JAT32/327.00	Pyrrhotite	Ni-pyrite, Co-pentlandite, Co-chalcopyrite, **Actinolite (II)**, allanite, apatite, monazite	(I)	0.85
JAT32/358.35	Pyrrhotite		(I)	0.63
JAT32/361.10	Pyrrhotite		(I)	0.27
JAT-15/194.20	Chalcopyrite	Pyrrhotite, Ni-pyrite, **Biotite (II)**, apatite, magnetite, allanite	(II)	0.69
JAT-28/160.40	Chalcopyrite		(II)	0.77
JAT-15/73.18	Chalcopyrite	Siegenite, Cassiterite, **Biotite (III)**, scapolite, apatite	(III)	1.04
JAT-15/147.65	Chalcopyrite		(III)	1.02
JAT-21/40.00	Chalcopyrite		(III)	1.02
JAT-21/46.00	Chalcopyrite		(III)	1.04
JAT 03/81.65	Chalcopyrite	Co-pyrite, sphalerite, **Chlorite (II)**, molybdenite quartz, epidote, calcite, uraninite, monazite, ETR carbonates	(IV)	0.90
JAT 03/130.05	Chalcopyrite		(IV)	1.80
JAT-28/119.00	Chalcopyrite		(IV)	1.20
JAT-15/185.22	Chalcopyrite		(IV)	0.78
JAT 02/78.6	Chalcopyrite		(IV)	1.60
JAT 02/172.5	Chalcopyrite		(IV)	1.80

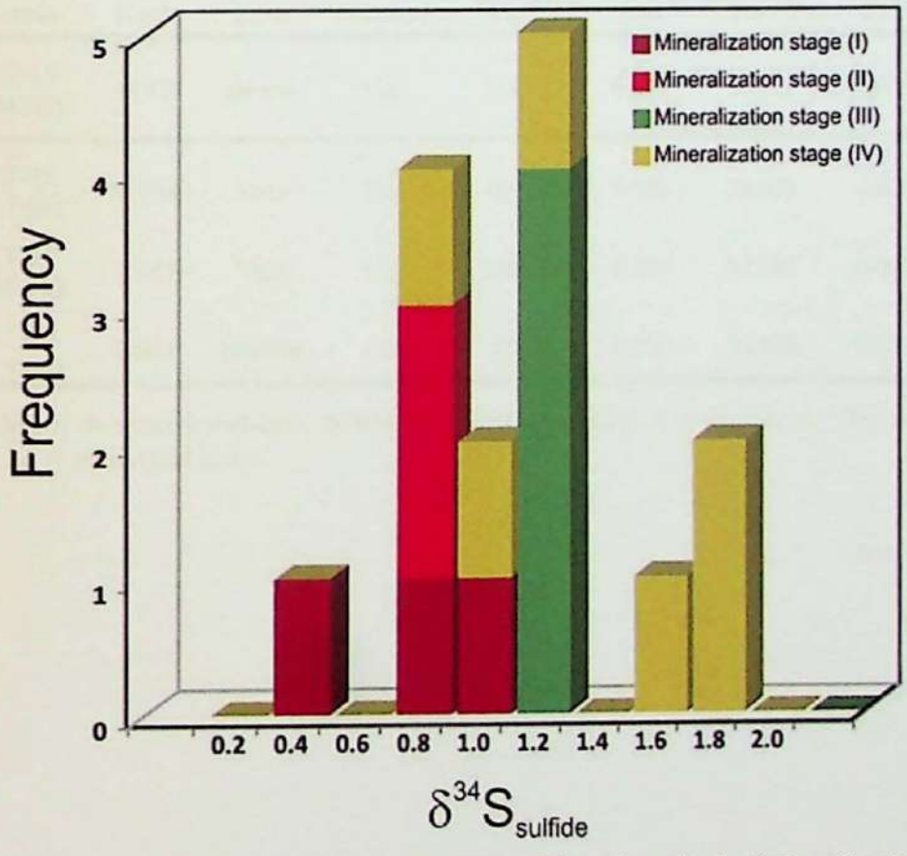

Figure 16. Histogram showing the sulfur isotope composition of pyrrhotite (mineralization stage I) and chalcopyrite (mineralization stages II to IV) of the Jatobá deposit.

Pb–Pb isotopes

Lead isotope analyses using total dissolution were carried out on chalcopyrite formed in the mineralization stages (II) and (IV). The obtained $^{206}Pb/^{204}Pb$ (99.35 to 245.728), $^{207}Pb/^{204}Pb$ (32.528 to 62.240) and $^{208}Pb/^{204}Pb$ (55.581 to 172. 755; (Table 4) ratios are strongly radiogenic. In the $^{207}Pb/^{204}Pb$ vs. $^{206}Pb/^{204}Pb$; Fig. 18) plot, three chalcopyrite samples of the mineralization stage (IV) show approximately collinear scattering, whereas the chalcopyrite formed in the mineralization stage (IV) does not line up with the others. The line defined for the scattering of the three chalcopyrite samples from the mineralization stage (IV) has an inclination corresponding to an age of 2,822 ±700 Ma (MSWD = 6170; Fig. 17A). Two chalcopyrite samples define a Pb–Pb age of 2786.1 ± 5.4 Ma.

Estimates of the μ ratio, which represents a petrogenetic parameter, was made using the simple stage model, based on Tatsumato et al. (1973). The calculated μ ratio for chalcopyrite of the mineralization stage (II) is 121.06, whereas μ ratios between 87.27 and 229.13 were estimated for chalcopyrite of the mineralization.

Table 4. Pb isotope data of chalcopyrite formed in the mineralization stages (II) and (IV) of the Jatobá deposit.

Stage	Sample	Rock	Style	Mineral	$^{206}Pb/^{204}Pb$	2SD	$^{207}Pb/^{204}Pb$	2SD	$^{208}Pb/^{204}Pb$
II	JAT-15 (194.20)	MVF	Brecia	Ccp	134.220	0.064	33.211	0.019	55.581
IV	JAT-15 (147.65)	MVM	Vein	Ccp	105.279	0.070	34.831	0.028	92.982
	JAT-15 (185.22)	BDO	Vein	Ccp	245.728	0.350	62.240	0.090	172.755
	JAT-28 (119.00)	DBO	Breccia	Ccp	99.35	0.356	32.528	0.011	81.229

Host rocks: MVF = metarhyodacite; MVM = metabasalt; BDO = metadiabase; Ore mineral: Ccp = chalcopyrite. 2σ = analytical error.

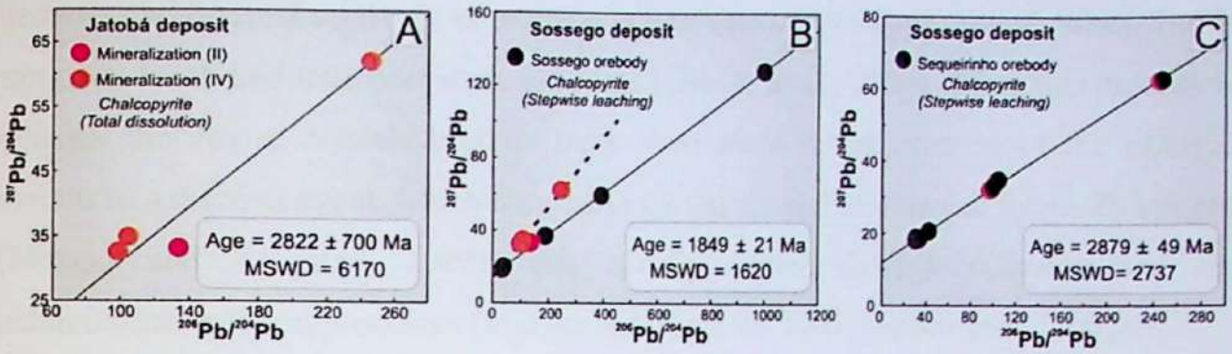

Figure 17. A) $^{207}Pb/^{204}Pb$ and $^{206}Pb/^{204}Pb$ correlation diagram and age for chalcopyrite of the mineralization stage (IV) from the Jatobá deposit using the model 1 of Ludwig (2000). The chalcopyrite sample of the mineralization (II) was not considered in age calculation and is plotted only for comparison of its $^{207}Pb/^{204}Pb$ ratios; B) Pb–Pb age estimated for chalcopyrite from the Sossego orebody (Sossego deposit) based on data of Lima da Silva (2017). Data of Jatobá chalcopyrite was not used for age estimates; C) $^{207}Pb/^{204}Pb$ and $^{206}Pb/^{204}Pb$ correlation diagram for chalcopyrite from the Sequeirinho orebody (Sossego deposit; Lima da Silva, 2017) and Jatobá (this study). The estimated age was obtained for the plotted sample set.

6. Discussions

Age of Host rocks

The Jatobá deposit is hosted by a metavolcanosedimentary sequence composed of felsic and mafic metavolcanic rocks and subordinate metavolcaniclastic rocks. LA-ICP-MS U–Pb zircon dating for a least-altered host metarhyodacite yielded an upper intercept age of 2,700 ±16 Ma (MSWD = 22). This was considered as its crystallization age (Fig. 9), despite the evidences of metamictization and intense Pb loss.

This age is similar to that obtained for the Igarapé Pojuca Group of the Itacaiúnas Supergroup by the Pb–Pb zircon method (2,705 ±2 Ma; Galarza and Macambira (2002b). However, these ages are significantly younger than those yielded by U–Pb zircon dating for the Itacaiúnas Supergroup (2.732 ± 5Ma, 2.761 ±3 Ma; Machado et al. 1991; 2.748 ±34 Ma; Tallarico et al. 2005; 2.745 ±1 Ma; Galarza and Macambira 2002a; 2.776 ±12 Ma; Galarza et al. 2003).

The apparent rejuvenation of U–Pb zircon ages in hydrothermally altered rocks in IOCG deposits of the Carajás Province was previously reported by Melo et al. (2017). Some authors have argued that the mobility of uranium, lead and zirconium in hydrothermal systems can be significant at high temperatures and acid pH (e.g. Rubin et al., 1993, Geisler et al., 2002, Geisler et al., 2007, Rubatto et al., 2008). In the presence of alkaline hydrothermal fluids, the zircon can develop granular texture or have recrystallized microdomains (Rubatto et al., 2008). The process of metamictization

destroys the internal structure of a zircon crystal and creates gaps through which fluids can pass, leach and transport some elements (Geisler et al., 2007). When this process is intense, the zircon crystals become more susceptible to the opening of the isotopic system in a thermal event, which may cause partial or total resetting of the U–Pb system (Mezger and Krogstad, 1997). This usually occurs through diffusion and re-precipitation reaction processes (Mezger and Krogstad 1997, Geisler et al., 2007).

Partial resetting produces discordant U–Pb ages, with upper intercepts representing the age of zircon crystallization. However, total resetting masks the age of crystallization and the age obtained reflects the last thermal event as a consequence of a drastic change in the U–Pb system (eg. Mezger and Krogstad 1997). In addition, the re-precipitation of hydrothermal zircon in the midst of preexisting zircon gaps may result in hybrid ages. Although total resetting is unlikely at Jatobá, some influence of hydrothermalism resulting in a hybrid age could explain the slightly younger age of the host metarhyodacite in relation to those of the Neoarchean Itacaiúnas Supergroup.

Chemical signature of the IOCG ore

Overall, pyrrhotite-rich ore samples of the mineralization stage (I) have the lowest copper contents (590 to 1360 ppm) and the highest Fe_2O_3 (71.49 to 63.91 wt. %), Ni (3930 to 1270 ppm), Co (2320 to 670 ppm), V (740 to 590 ppm), Pd (81 to 372 ppb) and Pt (2 to 17 ppb) values. These values are associated with the presence of Ni-pyrrhotite, Ni-pyrite, Co-chalcopyrite, siegenite and Co-pentlandite, which are closely spatially related to massive magnetite.

These values are also the highest when compared with those of ore samples from other IOCG deposits of the Southern Copper Belt of the Carajás Province (e.g. Sequeirinho and Sossego orebodies, Sossego mine; Bacaba, and Alvo 118; Fig. 10 A and 10 B) based on data from Carvalho (2009), Roscito (2009) and Moreto et al. (2009). It is interesting to note that the decreasing in Fe_2O_3, Ni, Co, and V contents related to the paragenetic evolution at Jatobá samples is wider than those observed in other single deposits or orebodies at Carajás. The highest contents of these elements were observed in the Neoarchean Sequeirinho ore samples and the lowest in the Paleoproterozoic Alvo 118 deposit. On the other hand, the highest Sn + W + Nb contents of ore samples of the mineralization stage (IV) are close to that of the Alvo 118 deposit. In addition, all Jatobá ore samples have Zn and (Zr + Nb + Ce + Y) contents and (10^4*Ga/Al) ratios similar to that expected for A-type granites (Whalen et al., 1987).

Except for two samples from the last stage, there is an increase in light rare earth elements (LREE) contents related to the paragenetic evolution (Fig. 13). The chondrite normalized patterns of REE of the Jatobá ore samples [$(La/Yb)_N$ values = 1.69 to 74.93] is similar to those of the others IOCG deposits at Carajás, except the Paleoproterozoic Alvo 118 deposit. The latter has an opposite pattern of REE distribution [$(La/Yb)_N$ values = 0.07 to 0.22]. All Jatobá samples show negative Eu anomalies (Eu/Eu^* = 0.36 to 0.79), which are typical of alkaline granites.

The ΣREE contents of Jatobá samples (up to 6,773.92 ppm) are higher than those reported for other IOCG deposits at Carajás (Fig. 13). These high ΣREE values are comparable to those from hematite-rich breccias of the giant Olympic Dam IOCG deposit, which have average REE of 5,000 ppm (Oreskes and Einaudi, 1990). At Jatobá, the main REE mineral phases are monazite, Ce-allanite, bastnäsite, coskrenite and sahamalite. As previously reported for the Olympic Dam deposit, extensive transport and deposition of REE and incompatible elements by Cl-, F-, CO_2-rich hydrothermal fluids are also evidenced in the Jatobá deposit.

The comparison of the Jatobá ore signature with those of other IOCG deposits from the Carajás Province evidence the great contribution of metals leached from mafic-(ultramafic) rocks at Jatobá and in the Neoarchean Sequeirinho orebody. On the other hand, its high REE and LILE (P, U, Th, Sn, W, and Nb) contents point to affinity with anorogenic alkaline magmatism (A-type granites and coeval gabbros) and suggested an evolution from residual alkali-rich fluids. The higher contents of Sn and W related to the paragenetic evolution at Jatobá may be explained by the decrease of their solubility during the fluid evolution due to fO_2 and/or pH increase and decrease in temperature (Pirajno, 2009). The fO_2 and pH increase are evidenced by hematite-calcite formation in late stages. The latter may also explain the apparent positive correlation between $\delta^{34}S$ values and LILE contents (Fig. 12).

Fluid evolution and sulfur sources in the Jatobá deposit

Significant temperature decrease was indicated by estimates using oxygen isotope fractionation factors for mineral pairs from the pre-mineralization iron metasomatism (558 °C) and mineralization stages (II = 507 °C; III = 422 °C; IV = 327 °C; Fig. 14A). Considering the imprecision of geothermometric calculations based on stable isotope calculation (±50 °C), the highest temperatures are close to those evidenced by ilmenite lamellae in magnetite (III), which points to its formation at

temperature exceeding 600 °C followed by oxidation-exsolution reactions at lower temperatures (Veloso et al., Submitted). High temperature for massive magnetite at Jatobá is also suggested by its elevated contents of Ti, V, and Cr, which are in part similar to those of magnetite from Kiruna-type magnetite-apatite ores (Veloso et al., Submitted).

The mineralization stage (II) was associated with the Canaã shear zone development, at 507 °C, and comprises chalcopyrite-(pyrrhotite-siegenite) oriented along the mylonitic foliation. The temperature estimated for this stage is consistent with a relatively deep crustal level, in which ductile structures are developed.

The stages (III) and (IV) record a change in structural styles of mineralization controlled by ductile-brittle and result in the main copper orebodies at Jatobá. The sharp temperature decrease from 422 °C in stage (III) to 327 °C in the stage (IV) appears to have exerted important control on chalcopyrite precipitation. The temperature estimated using oxygen isotope fractionation are within the interval of 261 to 386 °C obtained by distinct chlorite geothermometers based on mineral chemistry (Veloso et al., Submitted).

Calculation of oxygen isotope compositions for hydrothermal fluids in equilibrium with mineral pairs result in very close $\delta^{18}O_{H2O}$ values in each stage, evidencing that isotope equilibrium was achieved and maintained (Fig. 14B). There is also a trend of decreasing of $\delta^{18}O_{H2O}$ values from 9.53‰ for the pre-mineralization iron metasomatism to 5.41‰ for the mineralization stage (IV). A lower $\delta^{18}O_{H2O}$ value (4.48‰, at 280 °C) was also estimated for calcite from late barren veins. However, for the latter there is great uncertainty about temperature. The used value was that of similar calcite veins in nearby IOCG deposits at Carajás (Monteiro et al., 2008a). Even so, considering this significantly lower temperature, the obtained $\delta^{18}O_{H2O}$ value deviates little in relation to those estimated from the chlorite-quartz pair.

The δD_{H2O} and $\delta^{18}O_{H2O}$ values for the hydrothermal fluids associated with the mineralization stages of the Jatobá deposit plot in the fields of primary magmatic water (Taylor, 1968) and felsic magmatic water (Taylor et al., 1992), in the area in which these fields overlap with those of formational or low-temperature metamorphic fluids (Fig. 15). In addition, the relationship between temperature and oxygen isotope composition of fluids shown in Fig. 16 could also suggest that the hydrothermal system at Jatobá evolved essentially from magmatic-hydrothermal fluids.

Oxygen and hydrogen isotope composition of fluids in equilibrium with Jatobá biotite and chlorite is also close to that of hydrothermal fluids in equilibrium with actinolite from the Sequeirinho orebody of the Sossego mine (Fig. 15).

However, the Sequeirinho and Sossego orebodies have a wider variation of $\delta^{18}O_{H2O}$, reaching values lower than –5‰ in the mineralization stages (Fig. 16). In the deeper Sequeirinho orebody, ore-related actinolite, apatite, epidote, and quartz were formed by ^{18}O-depleted fluids (3.0‰ to –5.4‰) at 350 °C to 250 °C (Monteiro et al., 2008a). In the Sossego orebody, temperatures decreased from >450°C in the potassic to >300°C in the mineralization stage. As temperature decreased, $\delta^{18}O_{H2O}$ evolved from 10 to 6.8‰ in the early vein and breccia infilling to –0.6‰ to –6‰ in the mineralization stage and hydrolytic alteration stage. The sharp temperature decrease and $\delta^{18}O_{H2O}$ variation during the paragenetic evolution in these orebodies was interpreted as an evidence of extensive fluid mixing involving externally-derived fluids (Monteiro et al., 2008a).

This mechanism was also highlighted in the giant Olympic Dam deposit, Austrália, in which mixing of surficial-derived fluids surficial fluid with low $\delta^{18}O_{H2O}$ values (–2 to +6‰) and hotter, more saline, deep-seated fluid was considered of major importance for hematite–bornite–chalcocite precipitation (Oreskes and Einaudi 1992).

In the Jatobá deposit, despite its protracted evolution, significant temperature decrease related to the paragenetic evolution of the Jatobá deposit was accompanied by a relatively narrow variation of $\delta^{18}O_{H2O}$ values (Fig. 16). This could imply that fluid mixing involving isotopically distinct fluids does not play an important role at Jatobá. This is consistent with the scapolite formation even in late alteration stages in the Jatobá deposit, indicating limited fluid dilution and system buffering in respect to chlorine activities (Mora and Valley, 1989; Veloso et al., Submitted).

Despite the increasing of $\delta^{34}S$ values from 0.27‰ in the mineralization (I) to 1.80‰ in the mineralization stage (IV), Jatobá sulfides record a narrower variation of sulfur isotope compositions when compared with chalcopyrite from other IOCG deposits located in the Southern Copper Belt, such as the Sequeirinho and Sossego orebodies (Sossego Mine), Alvo 118, and Visconde (Fig. 18). Its sulfur composition, especially that of chalcopyrite from the mineralization stage (IV), is comparable with the $\delta^{34}S$ values of the Cristalino deposit (Ribeiro, 2008; Fig. 18).

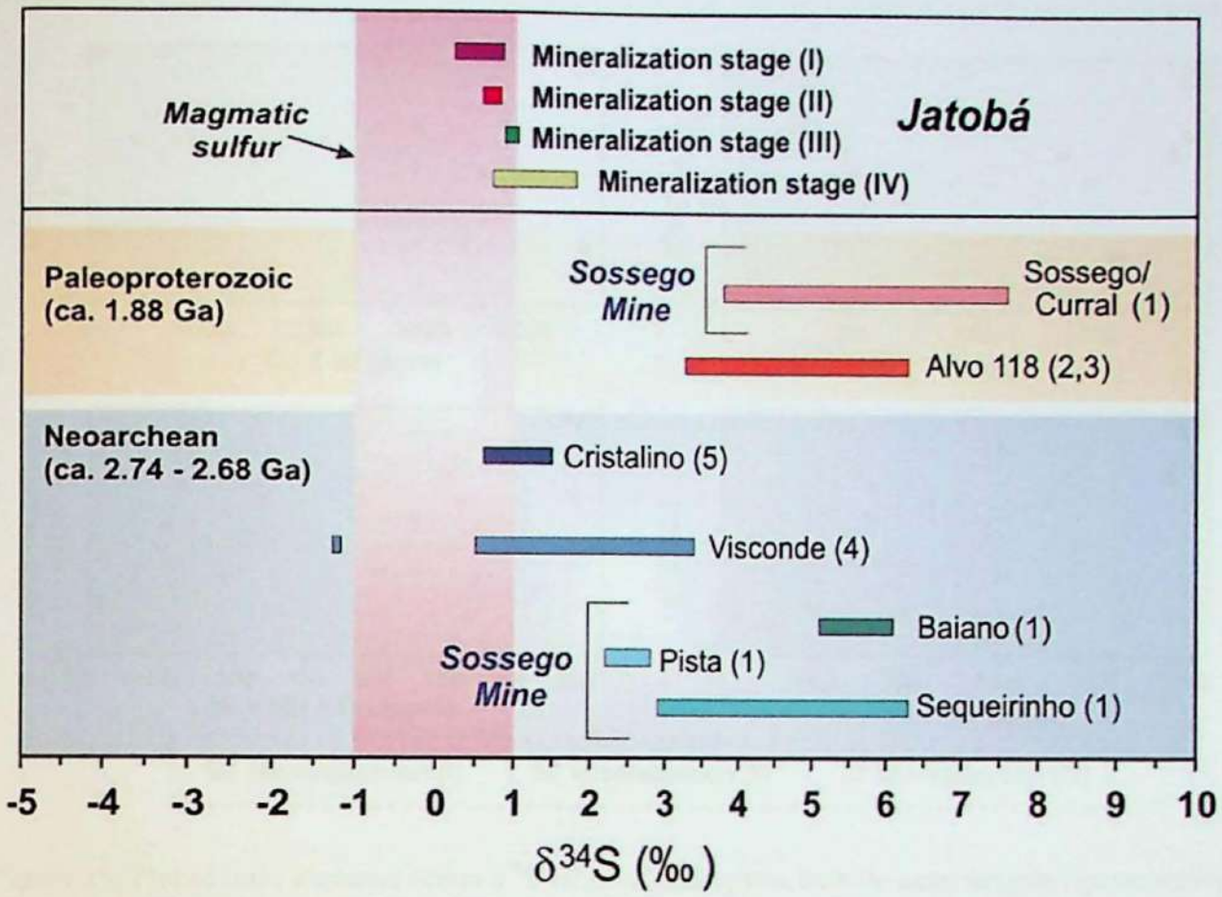

Figure 18. Sulfur isotope composition of pyrrhotite (mineralization stage I) and chalcopyrite (mineralization stages II to IV) of the Jatobá deposit compared to sulfur isotope variations recorded in another deposits in the Carajás Província. Isotopic data soure separated by age: (1) Sossego mine (Monteiro et al., (2008a), (2) Alvo 118 (Torresi et al., 2012), (3) Alvo 118 (Torresi et al., (012), (4) Visconde (Silva, 2013), (5) Cristalino (Ribeiro 2008). The reddish area represents the mantle sulfur (Eldridge et al. 1991).

The presence of pyrrhotite in the early mineralization stage (I) indicate that the mineralizing fluid was in the H_2S predominant field. In this case, the pyrrhotite $\delta^{34}S$ values (0.27‰ to 0.85‰) would be expected to closely reflect the sulfur source ($\delta^{34}S_{\Sigma S}$). Thus, the $\delta^{34}S$ values close to 0‰ point to magmatic sources ($\delta^{34}S = 0 \pm 1‰$; Eldridge et al. 1991). Increase of pH during the fluid evolution may result in slightly higher $\delta^{34}S$ values in chalcopyrite in the mineralization stage (IV) (Ohmoto and Rye, 1974). Alternatively, additional sulfur from leached magmatic rocks may have contributed to the hydrothermal system. The negative correlation among Fe_2O_3, Ni, Co, V and $\delta^{34}S$ values in chalcopyrite (Fig. 19A and 19B) may suggest that sulfur and metals were, at least in part, leached from mafic-(ultramafic) rocks.

The highest contents of Fe_2O_3, Ni, Co, and V were observed in samples with the lowest values of $\delta^{34}S$ in chalcopyrite (Fig. 19A and 19B). The opposite relation is observed among $\delta^{34}S$ and (Sn + W + Nb) and (La + Ce), although for the latter this trend is less clear (Fig. 19C and 19D).

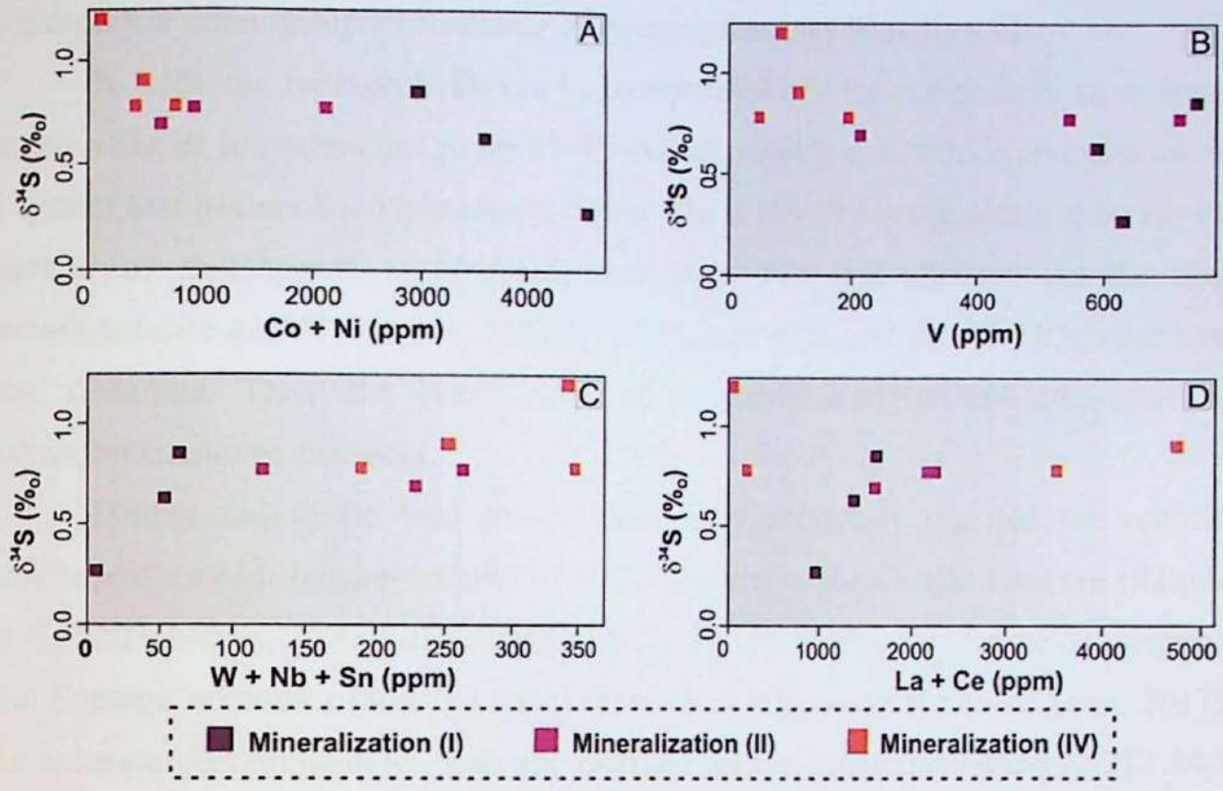

Figure 19. Plot of trace elements versus $\delta^{34}S$ values of chalcopyrite from the same samples representative of the mineralization stages (I, III and IV) of the Jatobá deposit.

Pb isotope signature and its implications

Lead isotope data for Jatobá chalcopyrite is highly radiogenic. Its high $^{206}Pb/^{204}Pb$ (99.35 to 245.73), $^{207}Pb/^{204}Pb$ (32.53 to 62.240) and ($^{208}Pb/^{204}Pb$ = 55.58 to 172.76) values cannot be plotted in the plumbotectonic diagrams of Doe and Zartman (1979), Zartman and Doe (1981) and Zartman (1988). The points analyzed would project far beyond the right border of the diagrams and well above the Pb evolution curve of the upper continental crust. This even corroborates the essentially hydrothermal environment for precipitation of chalcopyrite.

The highly radiogenic Pb isotope signatures of Jatobá chalcopyrite, in addition, may reflect mechanisms of the system evolution. The lead isotopic composition of any ore is characteristic of the source from which the lead was derived and is independent of the mode of ore deposition (Richards, 1971). Very radiogenic lead isotope signatures may result from higher U contents in relation to Pb at the time of chalcopyrite precipitation and/or U incorporation into the sulfide structure or within inclusions (McNaugton and Groves, 1996). In this study, these possibilities are corroborated by the fine uraninite inclusions in chalcopyrite of mineralization stage (IV). This is expected due to the U-rich nature of the oxidized hydrothermal fluids in IOCG systems. If those

fluids were exsolved from magmas, as indicated by their oxygen and hydrogen isotope signatures, a relationship with alkaline A-type magmas may be suggested.

In addition, radiogenic Pb can be incorporated into the sulfide from an external source after its formation due to the Pb–Pb system opening or to sulfide precipitation in a system that has not been completely closed. The 2,786 ±9 Ma age obtained by Pb–Pb method in chalcopyrite is unreliable and older than that obtained for the host metarhyodacite (2,700 ±16 Ma; MSWD = 22), indicating that the Pb–Pb system was also disturbed. Thus, the incorporation of radiogenic lead (or uranium) after its formation cannot be ruled out.

Highly radiogenic lead compositions were previously reported for sulfides (chalcopyrite or chalcocite–bornite) of IOCG deposits of the Carajás Province (Réquia et al., 2003; Neves, 2006; Lima da Silva, 2017). The Pb isotope data for the Sequeirinho and Sossego orebodies (Sossego mine) show some differences (Lima da Silva, 2017). As accurate geochronological data are available for the Sequeirinho–Pista (2,712 ±4.7 Ma; MSWD = 1.6; U–Pb LA–MC–ICP–MS in monazite; 2,685 ±11 Ma; 2,710 ±11 Ma; Re–Os NTIMS in molybdenite; Moreto et al., 2015a) and Sossego (1,879 ±4.1; 1,904 ±5.2; 1,890 ±8.5 Ma; U–Pb LA–MC–ICP–MS in monazite; Moreto et al., 2015a) orebodies, their Pb isotope data may be better evaluated. The Sequeirinho chalcopyrite is significantly less radiogenic than chalcopyrite from the Sossego orebody (Fig. 19B and 19C). The scattering of Pb isotope data on the $^{207}Pb/^{204}Pb$ versus $^{206}Pb/^{204}Pb$ plot indicates a disturbed system, resulting in very imprecise ages (2,727 ±380 Ma; MSWD = 465). On the other hand, the highly radiogenic Pb isotope data for the Sossego orebody result in Paleoproterozoic Pb–Pb ages (1849 ±21 Ma; MSWD = 1620; Lima da Silva, 2017).

The Jatobá chalcopyrite samples from the mineralization stage (IV), associated with chlorite alteration, are less radiogenic than Sossego chalcopyrite. The Jatobá chalcopyrite samples are aligned, but according to a trend that does not fit with that defined by the Paleoproterozic Sossego samples (Fig. 15B). On the other hand, these samples fit the line defined by the scattering of Sequeirinho chalcopyrite samples, defining an age of 2879 ±49 Ma (MSWD = 2737).

Overall, these data suggest that chalcopyrite from the late mineralization stage (IV) at Jatobá was formed during the Archean in a system that was opened in the ensuing hydrothermal events recorded in the Carajás Province (e.g. 2.57 Ga; 2.01 Ga or

1.88 Ga?). Although the age of copper mineralization at Jatobá is still uncertain, it is possible that it has evolved into a single event.

Models of origin and evolution of saline fluids

The presence of chlorine in mineral phases is ubiquitous in the Jatobá deposit (e.g. scapolite, biotite, apatite; Veloso et al., Submitted) and in other IOCG deposits of the Carajás Province, such as the Salobo deposit (Guimarães, 1987, Lindenmayer, 1990; Melo et al., 2017), Cristalino (Huhn et al., 1999), Igarapé Bahia (Zang and Fyfe, 1995; Dreher, 2004; Dreher et al., 2008), Sossego (Monteiro et al., 2008b), Castanha and Bacaba (Pestilho, 2011) and Bacuri (Moreto et al., 2015b).

The Cl is a halogen of wide interest in the studies of the IOCG deposits, as it acts as an important complexing agent, responsible for transport of Cu, Au, Fe and other metals (Rickard and Luther, 2006). Holland (1972) has shown that the solubility of many metals in a magmatic fluid is strongly dependent on the concentration of Cl, as well as other parameters such as temperature, pH, and variation of oxygen and sulfur fugacity. Henley (1973) proposed that chloride complexes are efficient in transporting gold at temperatures above 400 °C.

The precipitation of metals occurs when the solubility capacity of the complexes is decreased until their destabilization. The basic principles that control ore precipitation are summarized in Seward & Barnes (1997). The precipitation of polymetallic ore in IOCG deposits can occur in any of the hydrothermal alteration phases recognized in the deposits, but is usually synchronous to the potassic alteration (Hitzman et al., 1992; Hitzman et al., 2005; Skirrow, 2011).

In the Jatobá deposit, precipitation of copper ore occurred in four stages, encompassing calcic, potassic (biotite II–biotite III) and chlorite alteration, which reflect sharp temperature decrease (507 °C to 327 °C) related to increase of copper contents.

The importance of hypersaline fluids is recognized in IOCG deposits worldwide. However, the origin of fluids and salinity remains controversial. According to Barton and Johnson (1996, 2004), non-magmatic models include Cl-enriched metamorphic fluids that interacted with rocks derived from evaporitic sources or derived from deep basins. Metamorphic fluids do not require a heat source, although intrusions may be present and contribute to the system heating, as well as favor the supply of Cu and Fe for fluids, as proposed for the Osborne deposit, Australia (Fisher and Kendrick, 2008).

The evaporitic source model would be related to intrusive bodies as responsible

for the non-magmatic brine thermal convection, allowing the generation of high salinity hydrothermal systems on a regional scale. The salinity of these fluids would probably be due to the evaporation of surface water in hot and arid conditions and/or the interaction of hydrothermal fluids with preexisting evaporitic deposits, or would be caused by the breakdown of Cl-rich silicates, such as scapolite. However, the source of metals would be provided by the leaching of the adjacent igneous rocks and their transport would be effected by chloride complexes supplied by the evaporitic source itself.

According to Pollard (2001, 2006), the magmatic model is justified by the presence of highly saline fluids and the expressive presence of CO_2 identified in fluid inclusions in IOCG ores. In this sense, Cloke and Kesler (1979) already attributed to primary siliceous magmas the origin of sufficiently high Cl contents in fluid that would be needed to stabilize scapolite, due to its concentration in a separated fluid phase from a magmatic supercritical fluid. According to Pollard (2001, 2006), the presence of volatile CO_2 would also play an important role in the release of saline fluids. Evidences of the greatest contribution of magmatic fluids (Sillitoe, 2003) were identified in the Candelaria and Mantoverde deposits (Rieger et al. 2013, Marschik and Kendrick, 2014) and in El Espino deposit (Lopez et al., 2014), in Chile.

In the Carajás Mineral Province, non-magmatic saline sources have been related to metaexhalites (Villas *et al.* 2005; Rosa, 2006; Villas *et al.* 2005; Sousa, 2007) and evaporites associated with the metavolcanosedimentary sequence of the Neoarchean Itacaiúnas Supergroup (Dreher e Xavier, 2006; Xavier *et al.*, 2008). Evidences of extensive mixing with externally-derived fluids (e.g. meteoric water, seawater) is well-documented in world-class IOCG deposits at Carajás (Villas *et al.*, 2006; Rosa, 2006; Dreher *et al.*, 2008; Carvalho, 2009; Monteiro *et al.*, 2008a; Torresi *et al.*, 2012; Melo *et al.*, 2013; Silva *et al.*, 2015).

However, stable isotope data obtained in this study indicate that the Jatobá deposit was not formed in a hybrid system. The Jatobá deposit is part of an Archean IOCG system formed from focused magmatic-derived fluids. It may represent the magmatic-derived end member of a cluster of copper-gold deposits with variable attributes related to the local processes of fluid flow path and fluid-rock interaction.

7. Conclusions

The host rocks at Jatobá comprise metadiabase, metabasalt, mafic metatuff, felsic volcaniclastic rocks and metarhyodacite, which are attributed to the Itacaiúnas Supergroup. The LA–ICP–MS U–Pb zircon age of 2,700 ±16 Ma (MSWD = 22) was interpreted as indicative of the crystallization timing of metarhyodacite. However, this age may reflect influence of hydrothermal processes recorded in hybrid zircon grains with re-precipitation of hydrothermal zircon in the midst of preexisting zircon gaps.

Early mineralization stages at Jatobá are characterized by the highest Fe_2O_3, Ni, Co, V, Pd, and Pt values, which decrease in relation to the paragenetic evolution. Ore samples comprise Ni-pyrrhotite, Ni-pyrite, Co-chalcopyrite, siegenite and Co-pentlandite, which are closely related to syn-tectonic actinolite and biotite alteration that overprinted the early massive magnetite bodies. This association between intense iron metasomatism and nickel and cobalt enrichment is a characteristic of the Neoarchean IOCG deposits of the Southern Copper Belt in the Carajás Province.

The late mineralization stages at Jatobá reveal increasing of copper, gold, zinc, REE and LILE (P, U, Th, Sn, W, and Nb) contents related to the paragenetic evolution. The main mineralization stage (IV) was developed late during this evolution and was accompanied by extensive chlorite alteration. Late ore bodies are composed of chalcopyrite, pyrite, Co-pentlandite, siegenite, sphalerite, molybdenite, W-bearing hematite, REE carbonates (bastnäsite, coskrenite and sahamalite), allanite, monazite, and uraninite.

Significant temperature decrease from 558 °C (iron metasomatism) to 327 °C (mineralization stage IV) was accompanied by a narrow variation of $\delta^{18}O_{H2O}$ values (9.53‰ to 5.41‰). This may suggest that limited fluid mixing occurred at Jatobá. The sharp decrease in temperature, coupled with fO_2 and/or pH increase, likely had an important role in destabilization of chlorinated complexes and metal precipitation in late stages of mineralization.

The δD_{H2O} and $\delta^{18}O_{H2O}$ values for the hydrothermal fluids associated with the mineralization stages of the Jatobá deposit plot in the fields of primary magmatic water and felsic magmatic water. An evolution from residual alkali-rich magmatic fluids is also consistent with the high REE and LILE (P, U, Th, Sn, W, and Nb) contents of Jatobá ore.

The $\delta^{34}S$ values in pyrrhotite and chalcopyrite (0.27‰ to 1.80‰) are close to

those expected for mantle source ($\delta^{34}S = 0 \pm 1‰$; Eldridge et al. 1991). Sulfur may be sourced by magmatic fluids or leached from igneous rocks, which likely provide Ni, Co and V to the hydrothermal system.

Highly radiogenic lead isotope composition of chalcopyrite from the late mineralization stage (IV) points to its formation during the Archean in a system that was opened in the ensuing hydrothermal events recorded in the Carajás Province (e.g. 2.57 Ga; 2.01 Ga or 1.88 Ga?).

The Jatobá deposit represents a specific portion of a wider mineral system and was formed in the roots of an Archean IOCG system from focused magmatic-derived fluids. The Jatobá ore signature may reflect evolution closely related to the ca. 2.74 Ga widespread alkaline magmatism, with inheritance of both A-type granites and gabbros, due to intense fluid-rock interaction involving residual alkaline-rich fluids.

Acknowledgements

We are very grateful to VALE for the continuous support, especially to geologists Fernando Matos, Sergio Bacelar Hunh, Benevides Aires, and Fabrício Franco. This research has been supported by the INCT Geociências da Amazônia (MCT/CNPq/Fapespa 573733/2008-2), National Council for Scientific and Technological Development (CNPq Grant 481969/2013-6, 308365/2014-3), and CAPES Scholarship for the first author.

REFERENCES

Almeida, J.A.C., Dall'Agnol, R., Oliveira, M.A., Macambira, M.J.B., Pimentel, M.M., Rämö, O.T., Guimarães, F.V., Leite, A.A.S. 2011. Zircon geochronology and geochemistry of the TTG suites of the Rio Maria granite-greenstone terrane: Implications for the growth of the Archean crust of Carajás Province, Brazil. Precambrian Research **120**: 235-257.

Avelar, V.G. 1996. Geocronologia Pb-Pb por evaporação em monocristal de zircão do magmatiwsmo da região de Tucumã, SE do Estado do Pará, Amazônia oriental. Dissertação de Mestrado, Universidade Federal do Pará, 149p.

Araújo, O.J.B., Maia R.G.N., Jorge-João, X.S. Costa, J.B.S., 1988. A megaestruturação da folha Serra dos Carajás. In: Congr. Latino Am. Geol., 7, pp. 324-333.

Barbosa, J.P.O. 2004. Geologia Estrutural, Geoquímica, Petrografia e Geocronologia de granitóides da região do Igarapé Gelado, norte da Província Mineral de Carajás. Dissertação de Mestrado, UFPA, 96p.

Barnes, H. L. (Ed.). (1997). *Geochemistry of hydrothermal ore deposits* (Vol. 1). John Wiley & Sons.

Barros, C. D. M., Barbey, P., & Boullier, A. M. (2001). Role of magma pressure, tectonic stress and crystallization progress in the emplacement of syn-tectonic

granites. The A-type Estrela Granite Complex (Carajás Mineral Province, Brazil). Tectonophysics, 343(1), 93-109.

Barros, C.E.M., Macambira, M.J.B., Barbey P., and Scheller, T., 2004, Dados isotópicos Pb–Pb em zircão (evaporação) e Sm–Nd do Complexo Granítico Estrela, Província Mineral de Carajás, Brasil: implicações petrológicas e tectônicas. Rev. Brasil. Geoci. 34, 531–538.

Barros, C.E.M., Sardinha A.S., Barbosa J.P.O., Macambira M.J.B. 2009. Structure, Petrology, Geochemistry and zircon U/Pb and Pb/Pb geochronology of the synkinematic Archean (2.7 Ga) A-type granites from the Carajás Metallogenic Province, northern Brazil, The Canadian Mineralogist. 47: 1423-1440

Barton MD, Johnson DA (1996) Evaporitic-source model for igneousrelated Fe oxide–(REE–Cu–Au–U) mineralization. Geology 24: 259–262.

Barton, M. D., & Johnson, D. A. (2004). Footprints of Fe-oxide (-Cu-Au) systems. *University of Western Australia Special Publication*, *33*, 112-116. Boynton, W.V. 1984. Geochemistry of the rare earth elements: meteorite studies. In: HENDERSON, P. (ed), Rare Earth Element Geochemistry, Elsevier, 63–114.

Brito Neves, B.B. & Cordani, U.G. 1991. Tectonic evolution of South América during Late Proterozoic. Precambrian Research, 53: 23-40. Brito Neves, B. B. 1999. América do Sul: quatro fusões, quatro fissões e o processo acrescionário Andino. Revista Brasileira Geociências, 29 (3):379-392

Broughm, S. G., Hanchar, J. M., Tornos, F., Westhues, A., & Attersley, S. 2017. Mineral chemistry of magnetite from magnetite-apatite mineralization and their host rocks: examples from Kiruna, Sweden, and El Laco, Chile. Mineralium Deposita. https://doi.org/10.1007/s00126-017-0718-8.

Carvalho, E. de R., Xavier R.P., Monteiro, L.V.S, Souza Filho, C.R. de, 2005 Geology and hydrothermal alteration of the Sossego iron oxide-copper-gold deposit, Carajás Mineral Province, Brazil. In: Simpósio Brasileiro de Metalogenia, 1, [CD-ROM].

Carvalho, E.R., 2009. Caracterização geológica e gênese das mineralizações de óxido de Fe–Cu–Au e metais associados na Província Mineral de Carajás: estudo de caso do depósito de Sossego. Tese de Doutorado. UNICAMP, 141p.

Clayton, R. N., & Mayeda, T. K. (1963). The use of bromine pentafluoride in the extraction of oxygen from oxides and silicates for isotopic analysis. *Geochimica et* cosmochimica acta, 27(1), 43-52.

Cole, D.R. 1985. A preliminary evaluation of oxygen isotopic exchange between chlorite and water; Geol. Soc. America Abstr. with Programs, 17, p. 550

Cloke, P. L., & Kesler, S. E. (1979). The halite trend in hydrothermal solutions. *Economic Geology*, *74*(8), 1823-1831.

Silva, A. R., Villas, R. N. N., Lafon, J. M., Craveiro, G. S., & Ferreira, V. P. 2015. Stable isotope systematics and fluid inclusion studies in the Cu–Au Visconde deposit, Carajás Mineral Province, Brazil: implications for fluid source generation. Mineralium Deposita, 50(5), 547-569.

Dall'Agnol, R., Lafon J.M., Macambira M.J.B., 1994. Proterozoic anorogenic magmatism in the Central Amazonian Province, Amazonian Craton: geochronological, petrological and geochemical aspects, Miner. Petrol., 50: 113-138.

Dias, G.S., Macambira M.B., Dall'Ágno, R., Soare, A.D.V. Barro, C.E.M., 1996. Datações de zircões de sill de metagabro: comprovação de idade arqueana da Formação Águas Claras, Carajás, Pará. In: Simp. Geol. Amaz., 5, SBG, Belém, pp. 376-378.

DOCEGEO, 1988. Revisão litoestratigráfica da Província Mineral de Carajás – Litoestratigrafia e principais depósitos minerais. In: Cong. Bras. Geol., 35, SBG, p. 11-54.

Doe, B. R., & Zartman, R. E. (1979). Plumbotectonics, the phanerozoic. *Geochemistry of hydrothermal ore deposits*, *2*, 22-70.

Domingos, F.H.G., 2009, The structural setting of the Canaã dos Carajás region and Sossego-Sequeirinho deposits, Carajás, Brazil: Unpublished Ph.D. dissertation, Durhan, United Kingdom, Durham University, 483 p.

Dreher A.M. 2004. O depósito primário de Cu-Au de Igarapé Bahia, Carajás: Rochas fragmentárias, fluidos mineralizantes e modelo metalogenético. Tese de Doutorado, Universidade Estadual de Campinas, Campinas, São Paulo. 211p.

Dreher, A. M., Xavier, R. P., Taylor, B. E., & Martini, S. L. 2008. New geologic, fluid inclusion and stable isotope studies on the controversial Igarapé Bahia Cu–Au deposit, Carajás Province, Brazil. *Mineralium Deposita*, *43*(2), 161-184.

Eldridge CS, Compston W, Williams IS, Harris JW, Bristow JW. 1991. Isotope evidence for the involvement of recycled sediments in diamond formation. Nature 353:649–653.

Feio GRL., Dall'Agnol R., Dantas E.L., Macambira M.J.B., Gomes A.S., Sardinha D.C., Oliveira D.c., Santos R.D., Santos P.A. 2012. Geochemistry, geochronology, and origin of the Neoarchean Planalto Granite suite, Carajás, Amazonian craton: A-type or hydrated charnockitic granites? Lithos. Online. http:// dx.doi.org/10.1016/j.lithos.2012.02.020

Feio, G. R. L., Dall'Agnol, R., Dantas, E. L., Macambira, M. J. B., Santos, J. O. S., Althoff, F. J., & Soares, J. E. B. 2013. Archean granitoid magmatism in the Canaã dos Carajás area: implications for crustal evolution of the Carajás province, Amazonian craton, Brazil. Precambrian Research, 227, 157-185.

Ferreira Filho, C.F., Cançado, F., Correa, C., Macambira, E.M.B., Junqueira-Brod, T.C., Siepierski, L. 2007. Mineralizações estratiformes de PGE-Ni associadas a complexos acamadados em Carajás: os exemplos de Luanga e Serra da Onça. In: Rosa-Costa, L. T., Klein, E.L., Viglio, E.P. (Ed.). Contribuições à geologia da Amazônia. Belém: SBG-Núcleo Norte, v. 5, p. 1-14.

Fisher, L. A., & Kendrick, M. A. (2008). Metamorphic fluid origins in the Osborne Fe oxide–Cu–Au deposit, Australia: evidence from noble gases and halogens. *Mineralium Deposita*, *43*(5), 483-497.

Galarza, M. A., & Macambira, M. J. B. 2002. Geocronologia e evolução crustal da área do depósito de Cu-Au Gameleira, Província Mineral de Carajás (Pará), Brasil. Geologia USP. Série Científica, 2, 143-159.

Galarza, T. M. A., Macambira, M. J. B., & Moura, C. A. V. 2003. Geocronologia Pb-Pb e Sm-Nd das rochas máficas do depósito Igarapé Bahia, Província Mineral de Carajás (PA). *SBG, Simp. Geol. Amazônia*, *7*.

Geisler, T., Pidgeon, R. T., Van Bronswijk, W., Kurtz, R. 2002. Transport of uranium, thorium, and lead in metamict zircon under low-temperature hydrothermal conditions.

Geisler, T., Schaltegger U., Tomaschek F. 2007. Re-equilibration of zircon in aqueous fluids and melts. Elements, 3:43–50. Chemical Geology, 191: 141 – 154.

Gibbs, A.K., Wirth K.R., Hirata W.K., Olszewski Jr., W.J., 1986. Age and composition of the Grão Pará Group volcanics, Serra dos Carajás. Rev. Bras. Geoc. 16: 201–211. Gomes C.B. & Girardi V.A.V. 1973. Princípios e aplicações da microssonda eletrônica. Ciência e Cultura (SBPC), 25(8): 711-722.

Godfrey, J. D. (1962). The deuterium content of hydrous minerals from the east-central Sierra Nevada and Yosemite National Park. *Geochimica et Cosmochimica Acta*, *26*(12), 1215-1245.

Giggenbach, WF. 1992. Magma degassing and mineral deposition in hydrothermal systems along convergent plate boundaries. Economic Geology 87: 1927–1944.

Golyshev, S.I.; Padalko, N.L.; Pechenkin, S.A. 1981. Fractionation of stable isotopes in carbonate systems; Geochem. Int'l. 10, 85-99

Graham, C.M.; Viglino, J.A.; Harmon, R.S. 1987. Experimental study of hydrogen-isotope exchange between aluminous chlorite and water and of hydrogen diffusion in chlorite; Amer. Mineral. 72, 566-579

Guimarães, I. G. (1987). *Petrologia da formação ferrífera na área Salobo 3_-Província Mineral de Carajás, PA. Instituto de Geociências, Universidade de São Paulo, São Paulo* (Doctoral dissertation, Dissertação de Mestrado).

Henley, R. W. (1973). Solubility of gold in hydrothermal chloride solutions. *Chemical Geology*, *11*(2), 73-87.

Hirata, W.K., Rigon J.C., Kadekaru K., Cordeiro A.A.C., Meireles E.A. 1982. Geologia Regional da Província Mineral de Carajás. In: Simp. Geol. Amaz., 1, Belém, SBG/NO, p. 100–110.

Hitzman, M.W., Oreskes, N., Einaudi, M.T., 1992, Geological characteristics and tectonic setting of Proterozoic iron oxide (Cu-U-Au-REE) deposits. Precamb. Res. 58:241–287.

Hitzman, M. W., & Valenta, R. K. (2005). Uranium in iron oxide-copper-gold (IOCG) systems. *Economic Geology*, *100*(8), 1657-1661.Holland, H. D. (1972). Granites, solutions, and base metal deposits. *Economic Geology*, *67*(3), 281-301.

Huhn, SRB, Souza CIJ, Albuquerque MC, Leal ED, Brustolin V. 1999a. Descoberta do depósito Cu(Au) Cristalino: Geologia e mineralização associada região da Serra do Rabo - Carajás – PA. SBG/NO, Simpósio de Geologia da Amazônia, 6, pp 140-143

Huhn, S.R.B., Macambira M.J.B., Dall'Agnol R. 1999b. Geologia e geocronologia Pb-Pb do Granito Alcalino Planalto, Região da Serra do Rabo, Carajás-PA. In: SBG, Simp. Geol. Amaz., 6, Boletim de Resumos, p. 463-466.

Jackson, S. E., Pearson, N. J., Griffin, W. L., & Belousova, E. A. (2004). The application of laser ablation-inductively coupled plasma-mass spectrometry to in situ U–Pb zircon geochronology. *chemical Geology*, *211*(1), 47-69.

Janoušek, V., Farrow, C. M., & Erban, V. 2006. Interpretation of whole-rock geochemical data in igneous geochemistry: introducing Geochemical Data Toolkit (GCDkit). Journal of Petrology, 47(6), 1255-1259.

Jorge João, X.S.; Neves, A.P.; Leal, J.W.L. 1982. Ouro da Serra Pelada: aspectos da geologia e garimpagem. In: Simpósio De Geologia Da Amazônia, 1., Belém. Anais... Belém: SBG–Núcleo Norte, v. 2, p. 52-62.

Justo, A.P., Freitas-Silva, F.H., Schorscher J.H.D., Nascimento, J.A.S., Dantas, E.L. 2015. Derrames komatiíticos do greenstone belt a sul da serra sul, Província Mineral de Carajás, Pará, Brasil. 14° Simp. Geol. Amaz, [CD-ROM].

Lafon, J. M., Macambira, M. J. B., & Pidgeon, R. T. 2000. Zircon U-Pb SHRIMP dating of Neoarchean magmatism in the southwestern part of the Carajás Province (eastern Amazonian Craton, Brazil). In International Geological Congress, 31, Abstracts..., Rio de Janeiro (Vol. 1).

Lancaster J.O., Fanton J., Almeida A.J., Leveille R.A. Vieira S. 2000. Discovery and geology of the Sossego copper-gold deposit, Carajás District, Pará State, Brazil. In: Inter. Geol. Congr., 31, Abstracts, RJ, [CDROM].

Leite, A.A.S. 2001. Geoquímica, petrogênese e evolução estrutural dos granitóides arqueanos da região de Xinguara, SE do Cráton Amazônico. Belém, Universidade Federal do Pará, Centro de Geociências. (Tese de Doutorado).

Lima da Silva, C. D. 2017. Estudo isotópico de rochas e minério do depósito cupro-aurífero do Sossego (Carajás-PA). (Doctoral dissertation).

Lindenmayer, Z. G. 1990. Salobo Sequence, Carajás, Brazil: geology, geochemistry and metamorphism.

Lindenmayer, Z. G., Fleck, A., Gomes, C.H., Santos, A.B.S., Caron, R., Paula, F.C., Laux, J.H., Pimentel, M.M., and Sardinha, A.S. 2005. Caracterização geológica do alvo estrela (Cu-Au), Serra dos Carajás, Pará In: Caracterização de Depósitos Minerais em Distritos Mineiros da Amazônia. DNPM, CT-Mineral / FINEP, ADIMB, CD-ROM, 2005, cap. IV, 1, 137-205.

Lobato, L.M., Rosière C.A., Silva R.C.F., Zucchetti M., Baars F.J., Sedane J.C.S., Javier Rios F., Pimentel M., Mendes G.E., Monteiro A.M. 2005. A mineralização hidrotermal de ferro da Província Mineral de Carajás – controle estrutural e contexto na evolução metalogenética da província. In: Marini, O.J., Queiroz, E.T., Ramos, B.W. (Eds.). Caracterização de Depósitos Minerais em Distritos Mineiros da Amazônia, DNPM-CT-Mineral-FINEP-ADIMB, pp. 25-92.

Loios, V.A.P. 2009. Método de preparação e separação de minerais no CPGeo-IGc-USP. In: Boletim de resumos expandidos. Simpósio 45 anos de Geocronologia no Brasil. 330p. Lopez G. P. & Hitzman M. W. & Nelson E. P. 2014. Alteration patterns and structural controls of the El Espino IOCG mining district, Chile. Miner Deposita (2014) 49:235–259

Lopez G. P. & Hitzman M. W. & Nelson E. P. 2014. Alteration patterns and structural controls of the El Espino IOCG mining district, Chile. Miner Deposita (2014) 49:235–25

Ludwig, K. R. 2000. Decay constant errors in U–Pb concordia-intercept ages. *Chemical Geology*, *166*(3), 315-318.

Macambira, E.M.B. & Vale A.G. 1997. Programa Levantamentos Geológicos Básicos do Brasil. São Felix do Xingu. Folha SB.22-Y-B. Estado do Pará. DNPM/ CPRM. Brasília, 384p.

Machado, N., Lindenmayer, Z., Krogh, T. E., & Lindenmayer, D. (1991). U-Pb geochronology of Archean magmatism and basement reactivation in the Carajás area, Amazon shield, Brazil. Precambrian Research, 49(3-4), 329-354.

McNaughton, N.J. & Groves, D.I. 1996. A review of Pb-isotope constraints on the genesis of lode-gold deposits in the Yilgarn Craton, Western Australia. Jour. Royal Soc. Western Australia. **79:** 123-129

Magdaleno, G.B., Ruiz, I.R. 2009. Metodologia Isotópica Pb-Pb no CPGeo-USP. Boletim de Resumos Expandidos. In: simpósio 45 anos de geocronologia no Brasil. São Paulo: Instituto de Ciências Exatas. Centro de Pesquisas Geocronológicas – CPGeo.

Marschik R. & Kendrick M.A. 2014. Noble gas and halogen constraints on fluid sources in iron oxidecopper-gold mineralization: Mantoverde and La Candelaria, Northern Chile. Miner Deposita DOI 10.1007/s00126-014-0548-x

Matsuhisa, Y.; Goldsmith, J.R.; and Clayton, R.N. 1979. Oxygen isotopic fractionation in the system quartz-albite-anorthite-water; Geochim. Cosmochim. Acta 43, 1131-1140.

Melo, G.H.C. de, Monteiro, L.V.S., Xavier, R.P., Moreto, C.P.N., Santiago, E.S., Dufrane, S.A., Aires, B., Santos, A.F.F. 2017. Temporal evolution of the giant Salobo IOCG deposit, Carajás Province (Brazil): constraints from paragenesis of

hydrothermal alteration and U–Pb geochronology. Mineralium Deposita, 52: pp. 709–732. DOI: 10.1007/s00126-016-0693-5.

Meirelles, M.R. 1986. Geoquímica e petrologia dos jaspilitos e rochas vulcânicas associadas, Grupo Grão-Pará, Serra dos Carajás. Dissertação de Mestrado, UnB, pp.

Meirelles, M.R., Dardenne, M.A., 1991 - Vulcanismo basáltico de afinidade shoshonítica em ambiente de arco arqueano, Grupo Grão Pará, Serra dos Carajás, Pa. Rev. Bras. Geoc., 21: 41-50.

Mezger, K., Krogstad, E.J., 1997. Interpretation of discordant U–Pb zircon ages: an evaluation: Journal of Metamorphic Geology, 15: 127–140.

Monteiro, L. V., Xavier, R. P., de Carvalho, E. R., Hitzman, M. W., Johnson, C. A., de Souza Filho, C. R., & Torresi, I. 2008a. Spatial and temporal zoning of hydrothermal alteration and mineralization in the Sossego iron oxide–copper–gold deposit, Carajás Mineral Province, Brazil: paragenesis and stable isotope constraints. Mineralium Deposita, 43(2), 129-159.

Monteiro, L. V. S., Xavier, R. P., Hitzman, M. W., Juliani, C., de Souza Filho, C. R., & Carvalho, E. D. R. 2008b. Mineral chemistry of ore and hydrothermal alteration at the Sossego iron oxide–copper–gold deposit, Carajás Mineral Province, Brazil. Ore Geology Reviews, 34(3), 317-336.

Mora C.I. and Valley J.W. 1989. Halogen-rich scapolite and biotite: Implications for metamorphic fluid-rock interactions. Am. Mineral., 74: 721–737.

Moreto, C.P.N.; Monteiro, L.V.S; Xavier, R.P; Torresi, I; Souza Filho, CR. 2009. Caracterização Geoquímica do Minério e das Zonas de Alteração Hidrotermal do Depósito de Óxido de Ferro-Cobre-Ouro Alvo 118, Província Mineral de Carajás. In: II Simpósio Brasileiro de Metalogênese, Anais (CD-ROM).

Moreto, C. P., Monteiro, L. V., Xavier, R. P., Creaser, R. A., DuFrane, S. A., Melo, G. H., ... & Sato, K. 2015a. Timing of multiple hydrothermal events in the iron oxide–copper–gold deposits of the Southern Copper Belt, Carajás Province, Brazil. Mineralium Deposita, 50(5), 517-546.

Mougeot, R., Respaut J.P., Briqueu L., Ledru P., Milesi J.P., Macambira M.J.B., Huhn S.B. 1996. Geochronological constrains for the age of the Águas Claras Formation (Carajás Province, Pará, Brazil). In: Cong. Bras. Geol, 39, Anais., Salvador, SBG. 6:579-581.

Neves, M. P. 2006. Estudos isotópicos (Pb-Pb, Sm-Nd, C e O) do depósito Cu-Au do Sossego, Província Mineral de Carajás. *Centro de Geociências, UFPA (dissertação de mestrado), 104p.*

Nogueira, A.C.R., Truckenbrodt, W., Pinheiro, R.V.L. 1995. Formação Águas Claras, Pré-Cambriano da Serra dos Carajás: redescrição e redefinição litoestratigráfica. Bol. Mus. Par. Em. Goeldi, Ciênc. da Terra, (7), pg. 177-277.

Ohmoto, H., Rye, R. O. 1974. Sulfur and Carbon Isotopes and Ore Genesis: A Review. Economic Geology, 69, 826-842.

Olszewski, W.J., Wirth, K.R., Gibbs, A.K, and Gaudette, H.E., 1989, The age, origin, and tectonics of the Grão Pará Group and associated rocks, Serra dos Carajás, Brazil: Archean continental volcanism and rifting: Precambrian Research, v. 42, p. 229–254.

Oreskes N, Einaudi MT (1992) Origin of hydrothermal fluids at Olympic Dam: preliminary results from fluid inclusions and stable isotopes. Economic Geology 87:64–90.

Oreskes, N., Einaudi, M.T. 1990. Origin of rare earth element-enriched hematite breccias at the Olympic Dam Cu-U-Au-Ag deposit, Roxby Downs, South

Australia. Economic Geology and the Bulletin of the Society of Economic Geologists, 85(1): pp.1-28.

Pestilho, A. L. S. (2011). Sistemática de isótopos estáveis aplicada à caracterização da evolução dos paleo-sistemas hidrotermais associados aos depósitos cupríferos Alvo Bacada e Alvo Castanha, Província Mineral do Carajás, PA.

Pinheiro, R.V.L., Holdsworth R.E., 1997. Reactivation of Archaean strike-slip fault systems, Amazon region, Brazil. Journal of the Geological Society of London 154, 99–103.

Pinheiro R.V.L., Kiyoshi, K., Viana, S.A., Cantidiano, F., Nunes, F.S., Viera, F.M. 2013. Carajás, Brazil – A short tectonic review. In: Simp. Geol. Amaz., 13, Belém, Anais, [CDROM]

Pirajno, F. (2009). Hydrothermal processes associated with meteorite impacts. In *Hydrothermal processes and mineral systems* (pp. 1097-1130). Springer Netherlands.

Pollard, P. J. (2001). Sodic (–calcic) alteration in Fe-oxide–Cu–Au districts: an origin via unmixing of magmatic H2O–CO2–NaCl±CaCl2–KCl fluids. *Mineralium Deposita*, *36*(1), 93-100.

Pollard, P. J. (2006). An intrusion-related origin for Cu–Au mineralization in iron oxide–copper–gold (IOCG) provinces. *Mineralium Deposita*, *41*(2), 179.

Ribeiro, A. A. 2008. Litogeoquímica e geologia isotópica estável (C, S, O) do depósito cupro-aurífero do alvo cristalino sul, província mineral de Carajás, Pará.

Réquia K, Stein H, Fontboté L, Chiaradia M. 2003. Re–Os and Pb–Pb geochronology of the Archean Salobo iron oxide copper–gold deposit, Carajá mineral province, northern Brazil. Mineralium Deposita 38:727–738

Ribeiro, A.A., 2008. Litogeoquímica e geologia isotópica estável (C, S, O) do Depósito Cupro-aurífero do Alvo Cristalino Sul, Província Mineral de Carajás, Pará. Dissertação de Mestrado, UFOP, 127p.

Richards, J. R. (1971). Major lead orebodies, mantle origin?. *Economic geology*, *66*(3), 425-434.

Rickard, D., & Luther, G. W. (2006). Metal sulfide complexes and clusters. *Reviews in Mineralogy and Geochemistry*, *61*(1), 421-504.

Rieger A.A., Marschik R. & Díaz M. 2013. The evolution of the hydrothermal IOCG system in the Mantoverde district, northern Chile: new evidence from microthermometry and stable isotope geochemistry. Miner Deposita (2012) 47:359–369

Rosa, A.G.N. 2006. Rochas encaixantes, alteração hidrotermal e caracterização dos fluidos relacionados à formação do Corpo Sequeirinho do Depósito Cu-Au do Sossego, região de Carajás. Dissertação de Mestrado, UFPA.

Roscito, F.G. 2009. Caracterização geoquímica e balanço de massa das zonas de alteração hidrotermal do depósito cuprífero de Alvo Bacaba, Província Mineral de Carajás. Undergraduation Monograph. State University of Campinas.

Rubatto, D., Muntener, O., Barnhoorn, A., Gregory, C. 2008 Dissolution-reprecipitation of zircon at low-temperature, high-pressure conditions (Lanzo Massif, Italy). American Mineralogist 93: 1519–1529.

Rubin, J.N., Henry, C.D., Price, J.G. 1993. The mobility of zirconium and other "immobile" elements during hydrothermal alteration. Chemical Geology, 110: 29 – 47.

Santos, J.O.S., Hartmann, L.A., Gaudette, H.E., Groves, D.I., Mcnaughton, N.J., Fletcher, I.R., 2000. A new understanding of the provinces of the Amazonian

Craton based on integration of field mapping and U-Pb and Sm-Nd geochronology. Gondwana Research, 3, 453-488.

Santos, J.O.S. 2003. Geotectônica do Escudo das Guianas e Brasil-Central. In: Bizzi, L.A. (Ed.). Geologia, tectônica e recursos minerais do Brasil: texto, mapas e SIG. Brasília: CPRM, p. 169-226.

Sardinha, A.S; Barros, C.E.M.; Krymsky, R. S.; Macambira, M.J.B. 2001. Petrografia e geocronologia U-Pb em zircão do Granito Serra do Rabo, Província Mineral de Carajás, Pará. In: Simpósio de Geologia da Amazônia, 7, Belém. Resumos expandidos...Belém: SBG-Núcleo Norte, 2001. 1 CD-ROM.

Sato, K., Basei, M. A. S., Júnior, O. S., Sproesser, W. M., & Passarelli, C. R. (2008). Novas técnicas aplicadas ao método U-Pb no CPGeo-IGc/USP: avanços na digestão química, espectrometria de massa (TIMS) e exemplos de aplicação integrada com SHRIMP. *Geologia USP. Série Científica*, *8*(2), 76-99.

Sharp, Z. D. (1990). A laser-based microanalytical method for the in situ determination of oxygen isotope ratios of silicates and oxides. *Geochimica et Cosmochimica Acta*, *54*(5), 1353-1357.

Sharp, Z. D. Principles of Stable Isotope Geochemistry. New Jersey: Pearson Prentice Hall, 2007. 344 p.

Silva, A. R. D. C. 2013. *Estudos isotópicos (Pb, O, H, S) em zonas alteradas e mineralizadas do depósito cupro-aurífero Visconde, Província Mineral de Carajás* (Doctoral dissertation).

Skirrow R. G., 2011. Controls on uranium in iron oxide copper-gold systems: insights from Proterozoic and Paleozoic deposits in southern Australia. Proceedings of Society for the Geology Applied to Ore Deposits 11th Biennial Meeting, Antofagasta, Chile, 26-29th September 2011.

Sillitoe, R. H. (2003). Iron oxide-copper-gold deposits: an Andean view. *Mineralium Deposita*, *38*(7), 787-812.

Souza, Z.S., Potrel A., Lafon J.M., Althoff F.J., Pimentel M.M., Dall'Agnol R., Oliveira C.G., 2001. Nd, Pb and Sr isotopes in the Identidade Belt, an Archean greenstone belt of Rio Maria region (Carajás Province, Brazil): implications for the geodynamic evolution of the Amazonian Craton. Precambrian Research 109: 293–315.

Siepierski, L., Ferreira Filho, C.F. 2016. Spinifex-textured komatiites in the south border of the Sousa F.D.S. 2007. Estudo da alteração hidrotermal, com ênfase no metassomatismo sódico, de rochas granitóides e máficas da região de Canaã de Carajás, Província Mineral de Carajás. Dissertação de Mestrado, Universidade Federal do Pará. Carajas Ridge, Selva Greenstone Belt, Carajás Province, Brazil. Journal of South American Earth Sciences, 66:41–55.

Silva, A.R.C. 2013. Estudos isotópicos (Pb, O, H, S) em zonas alteradas e mineralizadas do depósito Cupro-Aurifero Visconde, Província Mineral de Carajás. Dissertação de Mestrado, Universidade Federal do Pará, Belém. 73 p.

Sousa F.D.S. 2007. Estudo da alteração hidrotermal, com ênfase no metassomatismo sódico, de rochas granitóides e máficas da região de Canaã de Carajás, Província Mineral de Carajás. Dissertação de Mestrado, Universidade Federal do ParáSuzuoki, T.; Epstein, S. 1976. Hydrogen isotope fractionation between OH-bearing minerals and water; Geochim. Cosmochim Acta 40, 1229-1240

Tallarico, F.H.B. 2003. O cinturão cupro-aurífero de Carajás, Brasil. Tese de Doutorado, UNICAMP, 229p

Tallarico, F.H.B., Figueiredo B.R., Groves D.I., Kositcin N., McNaughton N.J., Fletcher I.R., Rego J.L. 2005. Geology and SHRIMP U–Pb geochronology of the

Igarapé Bahia deposit, Carajás copper–gold belt, Brazil: an Archean (2.57 Ga) example of iron–oxide Cu–Au–(U– REE) mineralization. Econ Geol 100:7–28.

Tassinari, C.C.G. 1996. O mapa geocronológico do Cráton Amazônico no Brasil: revisão dos dados isotópicos. Tese de Livre Docência, IG-USP, 139p. Tassinari C.C.G., Macambira M.J.B. 1999. Geochronological Provinces of the Amazonian Craton. Episodes, 22:174-182.

Tassinari, C.C.G. & Macambira M.J.B. 1999. Geochronological Provinces of the Amazonian Craton. Episodes, 22:174-182.

Tassinari, C.C.G. and Macambira, M.J.B., 2004. A evolução tectônica do Cráton Amazônico. In: MantessoNeto, V., Bartorelli, A., Carneiro, C.D.R. and Brito Neves, B.B. (Eds.) Geologia do Continente SulAmericano: Evolução da Obra de Fernando Flávio Marques de Almeida. pp. 471-485.

Tassinari, T., Tachibana J., Tulio M., Lívio R., Gaia C. 2005. Geologia isotópica aplicada nas mineralizações de Cu-Au do greenstone belt da Serra dos Gradaús, Província Mineral de Carajás, 190 Cráton Amazônico: exemplo de mineralizações policíclicas. In: SIMPÓSIO BRASILEIRO DE METALOGENIA, 1., Gramado, RS. Resumos... Porto Alegre: SBG/SEG/SGMTM-MME, 2005. 1 CD-ROM.

Teixeira, W., Tassinari, C.C.G., Cordani, U.G., Kawashita, K. 1989. A review of the geochronological of the Amazonian Craton: tectonic implications. Precamb. Res., 42: 213-227.

Teixeira, J.B.G., Eggler, D.H., 1994. Petrology, geochemistry, and tectonic setting of Archean basaltic and dioritic rocks from the N4 iron deposit, Serra dos Carajás, Pará, Brazil. Acta Geology Leopoldensia 17, 71-114.

Tavares, F. M. 2015. Evolução geotectônica do nordeste da Província Carajás. Tese de Doutorado. Universidade Federal do Rio de Janeiro.

Taylor, B. E. 1992. Degassing of H_2O from rhyolitic magma during eruption and shallow intrusion, and the isotopic composition of magmatic water in hydrothermal systems. Geological Survey of Japan Report 279: 190–194.

Taylor, H. P. (1968). The oxygen isotope geochemistry of igneous rocks. *Contributions to mineralogy and Petrology*, *19*(1), 1-71.

Taylor, H.P. Jr. 1997. Oxygen and hydrogen isotope relationships in hydrothermal mineral deposits. In: Barnes HL (ed.) Geochemistry of Hydrothermal Ore Deposits, 3rd edn., pp. 229–302. New York, NY: Wiley.

Torresi, I., Xavier, R. P., Bortholoto, D. F., & Monteiro, L. V. 2012. Hydrothermal alteration, fluid inclusions and stable isotope systematics of the Alvo 118 iron oxide–copper–gold deposit, Carajás Mineral Province (Brazil): implications for ore genesis. *Mineralium Deposita*, *47*(3), 299-323.

Vale. 2014. Projeto Jatobá. Internal report (Unpublished).

Vasquez, L.V., Rosa-Costa L.R., Silva C.G., Ricci P.F., Barbosa J.O., Klein E.L., Lopes E.S., Macambira E.B., Chaves C.L., Carvalho J.M., Oliveira J.G., Anjos G.C., Silva H.R.. 2008 Geologia e Recursos Minerais do Estado do Pará: Sistema de Informações Geográficas —SIG: texto explicativo dos mapas Geológico e Tectônico e de Recursos Minerais do Estado do Pará 1:1.000.000. CPRM, Belém, p328.

Veloso, A.S.R. Monteiro, L. V. S., Juliani, C. (Submitted). The iron oxide-copper-gold (IOCG) Jatobá deposit, Carajás Mineral Province, Brazil: Geology, hydrothermal alteration, mineralization and mineral chemistry.

Villas, R.N., Lima L.F.O., Neves M.P., Sousa F.D.S., Lamarão C.N., Fanton J., Morais R. 2005. Relações entre deformação, alteração hidrotermal e mineralização no

depósito Cu-Au do Sossego, Província Mineral de Carajás. In: Simpósio Brasileiro de Metalogenia, 1, CD-Rom.

Villas, R.N., Neves M.P , Moura C.V., Toro M.A.G., Aires B., Maurity C. 2006. Estudos isotópicos (Pb, C e O) no depósito Cu-Au do Sossego, Província Mineral de Carajás. In: SBG/Núcleo Norte, Simpósio de Geologia da Amazônia, 9, Resumos, CD-Rom.

Villas, R.N., Neves M.P., Rosa A.G.N., 2006. The Fe oxide-Cu-Au Sossego deposit, Carajás Mineral Province, Brasil: dating of the mineralization and fluid characteristics. In: Dall'Agnol R, Rosa-Costa LT, Klein EL (eds.) Symposium on magmatism, crustal evolution, and metallogenesis of the Amazonian Craton. Abstracts Volume. Belém, PRONEX-UFPA-SBG, p 33.

Xavier R.P., Wiedenbeck, M., Trumbull, R.B., Dreher, A.M., Monteiro, L.V.S., Rhede, D., Araujo, C.E.G., Torresi, I. 2008. Tourmaline B-isotopes fingerprint marine evaporites as the source of high-salinity ore fluids in iron oxide-copper-gold deposits, Carajas Mineral Province (Brazil). Geology, 36: 743-746. Xavier

Wirth, K.R. Gibbs A.K. Olszewski,W.J.Jr. 1986. U–Pb ages of zircons from the Grão Pará Group and Serra dos Carajás granite, Pará, Brasil. Rev. Bras. Geoci. 16: 195–200.

Whalen, J.B., Curie, K.L., Chappell, B.W. 1987. A-type granites: geochemical characteristics, discrimination and petrogenesis. Contributions to Mineralogy and Petrology 95(4):407-419.

Williams, P.J., Barton, M.B., Johnson, D.A., Fontboté, L., Haller, A., Mark, G., Oliver, N.H., Marschik, R., 2005. Iron oxide copper-gold deposits: geology, space-time distribution, and possible modes of origin. Economic Geology 100 th Anniversary Volume, pp. 371-405.

Zang, W., & Fyfe, W. S. 1995. Chloritization of the hydrothermally altered bedrock at the Igarapé Bahia gold deposit, Carajás, Brazil. *Mineralium Deposita*, *30*(1), 30-38.

Zartman, R. E., & Doe, B. R. (1981). Plumbotectonics—the model. *Tectonophysics*, *75*(1-2), 135-162.

Zartman, R. E., & Haines, S. M. (1988). The plumbotectonic model for Pb isotopic systematics among major terrestrial reservoirs—a case for bi-directional transport. *Geochimica et Cosmochimica Acta*, *52*(6), 1327-1339.

Zheng, Y.F. 1991. Calculation of oxygen isotope fractionation in metal oxides; Geochim. Cosmochim. Acta 55, 2299-2307

Zheng, Y.F. 1993 Calculation of oxygen isotope fractionation in hydroxyl-bearing silicates; Earth. Plan. Sci. Lett. 120, 247-263.

Zucchetti, M. 2007. Rochas máficas do Grupo Grão Pará e sua relação com a mineralização de ferro dos depósitos N4 E N5, Carajás, PA. Tese de Doutorado, UFMG, 165p.

CONCLUSÕES

O depósito Jatobá é parte de um conjunto de depósitos de óxido de ferro-cobre-ouro reconhecidos no Cinturão Sul do Cobre, na Província Carajás, que representam partes específicas de um amplo sistema mineral. Esses depósitos, que incluem Sossego, Cristalino, Alvo 118, Bacaba, Castanha, Bacuri, Visconde e outros, vinculam-se a estruturas subsidiárias associadas ao desenvolvimento da Zona de Cisalhamento Canãa de direção E-W e WNW-ESSE e às suas reativações. Alguns dos importantes depósitos do Cinturão Sul do Cobre, como o depósito Sossego, são hospedados por rochas mesoarqueanas, que incluem gnaisses, granitoides e faixas de *greenstone belts*. Contudo, o depósito Jatobá é hospedado por uma sequência metavulcanossedimentar que inclui metadiabásio, metabasalto amigdaloidal, brechas metavolcaniclásticas félsicas, metalapilli tufos máficos e metariodacito porfirítico (LA-ICP-MS U-Pb em zircão, 2.700 ± 16 Ma, MSWD = 22), Grupo Grão Pará, atribuída ao Supergrupo Itacaiúnas, neoarqueano.

As rochas hospedeiras menos alteradas derivadas de protólitos máficos registram paragênese metamórfica de fácies xisto verde inferior (albita-actinolita I). A intensa e pervasiva alteração hidrotermal foi prévia, sin-tectônica e tardia em relação ao desenvolvimento da zona de cisalhamento Canaã. A alteração hidrotermal precoce abrange silicificação, alteração sódica (albita I, scapolita I), sódica-cálcica (ferro-pargasita) e potássica (biotita I, turmalina, Cl-apatita I, Ce-allanita I). Os porfiroclastos de albita (I) e escapolita (I) são amendoados e apresentam sombra de pressão nas rochas miloníticas, indicando a sua blastese anterior ao desenvolvimento da zona de cisalhamento.

Os principais estágios de alteração hidrotermal sin-tectônica compreendem alteração sódico-cálcica (escapolita II), cálcico (actinolita II, Cl-apatita II, Ce-allanita II, quartzo) e potássica (Cl-K-hastingsita I, biotita II, quartz, Co-magnetita IV, Cl-apatita III, Ce-allanita III) controlada pela foliação milonítica.

O intenso metassomatismo de ferro resultou na formação de veios com magnetita (III)-quartzo e corpos de magnetita maciça (IV), que representam envelopes proximais de zonas mineralizadas. A concentração elevada de Ti, V, Ni e Cr na estrutura da magnetita do depósito Jatobá aponta para condições de alta temperatura (> 500 °C) durante a sua formação, semelhante à dos sistemas magmático-hidrotermais

(por exemplo, IOCG, óxido de ferro-apatita (IOA) do tipo Kiruna e depósitos de cobre do tipo pórfiro). As composições de isótopos de oxigênio em par magnetita-quartzo com evidências de equilíbrio textural são também condizentes com elevadas temperaturas (558 °C) durante o estágio de metassomatismo de ferro pré-mineralização.

Os magnetititos são cortados por actinolita fibrosa (II), magnetita (V) e Cl-apatita, que também promoveram a sua brechação. A alteração hidrotermal tardi tectônica é representada por cloritização e por veios de escapolita (III), que por sua vez são cortadas por vênulas com escapolita (IV), Cl-K-hastingsita (II) e biotita (III).

As zonas mineralizadas em cobre-ouro-(níquel) no depósito de Jatobá compreendem corpos de minério verticais a subverticais espacialmente relacionados a diques de metadiabásio e zonas de contato entre metariodacitos e metabasaltos. As zonas mineralizadas foram formadas em quatro estágios.

O estágio de mineralização (I) é espacialmente relacionado a corpos de magnetita maciça e à alteração cálcica sin-tectônica (actinolita II-magnetita V). Durante esse estágio frentes de substituição controladas pela foliação milonítica evoluíram para domínios mais fortemente mineralizados com predominância de brechas hidráulicas. O estágio (I) caracteriza-se pela associação de Ni-pirrtotita, Ni-pirita e Cl-apatita (II), e subordinadamente, Co-calcopirita, Ce-allanita II, Co-pentlandita, quartzo e Ce-monazita. Análises químicas de rocha total de amostras de minério desse estágio inicial de mineralização mostraram os conteúdos mais elevados de Fe_2O_3 (71,49 a 63,91%), Ni (3930 a 1270 ppm), Co (2320 a 670 ppm), V (740 a 590 ppm), Pd (81 a 372 ppb) e Pt (2 a 17 ppb). Os conteúdos de níquel no estágio inicial de evolução do sistema evidenciam transporte hidrotermal de níquel em condições de fS_2, salinidade e temperatura elevadas.

A transição para o estágio de mineralização (II) foi acompanhada por diminuição dos teores de Ni e Co e da quantidade de pirrotita e actinolita. O estilo de mineralização evoluiu de frentes de substituição controladas pela foliação milonítica a zonas de brechas hidráulicas. O estágio de mineralização (II) foi relacionado ao desenvolvimento da alteração potássica sin-tectônica (II) e representado por um sistema de corpos fortemente orientados e interligados com biotita (II), Cl-apatita (III), Co-magnetita (IV), Ilmenita (I), Ce-allanita (III) e quartzo, além de porções discretas contendo Ni-pirita e Co-calcopirita. Brechas com matriz constituída de biotita (II) e Co-calcopirita (± Ni-pirita ± Ni-pirrotita) e fragmentos de magnetita maciça representam os corpos mais ricos em cobre formados nesse estágio.

O terceiro estágio de mineralização do depósito de Jatobá se distingue dos demais por seu controle estrutural exercido por estruturas dúcteis-rúpteis. Esse estágio foi sincrônico à alteração hidrotermal com biotita mais clara ou verde (III), escapolita (IV), F-Cl-apatita (IV), Cl-K hastingsita (II), Co-calcopirita e siegenita I (± Co-pirita, ± Co-magnetita ± cassiterita).

O estágio de mineralização tardia (IV), o mais expressivo no depósito Jatobá, foi concomitante à formação de clorita (II), quartzo, epidoto e calcita. Ocorre em uma variedade de veios ramificados e brechas com Co-calcopirita, Co-pirita, esfalerita, molibdenita, uraninita e monazita. Outros tipos de veios tardios compreendem aqueles com quartzo-calcopirita-feldspato potássico (± molibdenita, Co-pentlandita e siegenita II) e vênulas finas com clorita-calcopirita, hematita, carbonatos de terras raras (bastnäsita, coskrenita e sahamalita), pirita, esfalerita, ilmenita, marcassita, leucoxênio e adulária. Os conteúdos mais alto de ΣETR (até 6773,92 ppm), U (até 48,50 ppm), Th (até 23,30 ppm), P_2O_5 (até 7,97%), Sn (até 24 ppm), Nb (até 7,50 Ppm), W (até 322,50), Zn (até 482 ppm) e ouro (até 1310,80 ppm) foram caracterizados em amostras de minério formadas durante esse estágio de mineralização. A presença de hematita e carbonatos no estágio mais tardio de mineralização evidencia o aumento da fO_2 e de pH no sistema, que podem ter contribuído para a deposição dos metais transportados por complexos cloretados.

Os dados de isótopos de oxigênio apontam para a diminuição da temperatura durante os estágios de mineralização (II = 507 °C; III = 422 °C; IV = 327 °C). No entanto, uma variação relativamente pequena dos valores calculados de $\delta^{18}O_{H2O}$ (9,53 ‰ a 5,41 ‰) foi registrada durante a evolução paragenética do depósito Jatobá. Os valores de $\delta^{18}O_{H2O}$ e δD_{H2O} (-44,88 ‰ a -30,25 ‰) se sobrepõem ao das águas magmáticas primárias e água magmática félsica. O aumento gradual do conteúdo de Cl na estrutura da escapolita (I) a (III) também indica uma evolução progressiva a partir de fluidos hipersalinos de alta temperatura e tamponamento das atividades de cloro no sistema. A composição química da escapolita, juntamente aos dados de isótopos estáveis, pode apontar para limitada mistura de fluidos envolvendo fluidos externamente derivados.

Os valores de $\delta^{34}S$ de sulfetos (0,27 ‰ a 1,80 ‰) indicam fontes magmáticas de enxofre. O aumento dos valores de $\delta^{34}S_{sulfetos}$ durante a evolução paragenética foi acompanhado da diminuição dos teores de Ni + Co e V e aumento do teor de Sn + W +

Nb em amostras de minério, sugerindo que parte do enxofre e metais podem ter sido lixiviados de rochas máficas-(ultramáficas).

A composição altamente radiogênica dos isótopos de Pb em calcopirita ($^{206}Pb/^{204}Pb$ = 99,35 a 245,73; $^{207}Pb/^{204}Pb$ = 32,53 a 62,24; $^{208}Pb/^{204}Pb$ = 55,58 a 172,6) sugerem idade arqueana para o último estágio de mineralização (IV). Tais assinaturas podem ter resultado de perturbações no sistema devido ao alto conteúdo de U nos fluidos hidrotermais e à incorporação de Pb (ou U) radiogênicos no sulfeto a partir de uma fonte externa após a sua formação.

O conjunto de dados indica que o depósito de Jatobá foi formado nas raízes de um sistema mineral IOCG arqueano a partir de fluxo canalizado de fluidos magmáticos. A assinatura de minério de Jatobá pode refletir evolução estreitamente relacionada com o extensivo magmatismo alcalino reconhecido na Província Carajás em ca. 2,74 Ga, com herança de granitos tipo A e gabros, a partir de intensos processos de interação fluido-rocha envolvendo fluidos alcalinos residuais. O principal estágio de mineralização, contudo, foi associado com significativa exhumação do sistema hidrotermal.

Dados geocronológicos precisos ainda são necessários para estabelecer se o depósito Jatobá registra uma evolução em um único evento hidrotermal ou se sobreposição de eventos hidrotermais, reconhecida no depósito de classe mundial Sossego, também pode ser reconhecida nesse depósito. Contudo, no depósito Jatobá não foram identificadas evidências de contribuição de fluidos superficiais externamente derivados (por exemplo, água meteórica ou do mar) ou enxofre isotopicamente mais pesado, que caracterizam os depósitos com minério formado no Paleoproterozoico, após o Grande Evento de Oxigenação.

REFERÊNCIAS

Almeida, J.A.C., Dall'Agnol, R., Dias, S.B., Althoff, F.J. 2010. Origin of the Archean leucogranodiorite–granite suites: Evidence from the Rio Maria terrane and implications for granite magmatism in the Archean. Lithos **187**: 201-221

Almeida, J.A.C., Dall'Agnol, R., Oliveira, M.A., Macambira, M.J.B., Pimentel, M.M., Rämö, O.T., Guimarães, F.V., Leite, A.A.S. 2011. Zircon geochronology and geochemistry of the TTG suites of the Rio Maria granite-greenstone terrane: Implications for the growth of the Archean crust of Carajás Province, Brazil. Precambrian Research **120**: 235-257.

Almeida, J.A.C., Dall'Agnol, R., Leite, A.A.S. 2013. Geochemistry and zircon geochronology of the Archean granite suites of the Rio Maria granite-greenstone terrane, Carajás Province, Brazil. Journal of South American Earth Sciences. **42**:103–126

Armstron, J.T. 1991. Quantitative Elemental Analysis of Individual Microparticles with Electron Beam Instruments. In: Heinrich K.F.J., Newbury D.E. (eds) Electron Probe Quantitation. Springer, Boston, MA. DOI: 10.1007/978-1-4899-2617-3_15

Althoff, F.J., Barbey P., Boullier A.M. 2000. 2.8-3.0 Ga plutonism and deformation in the SE Amazonian craton: the Archean granitoids of Marajoara (Carajás Mineral province, Brazil). Precambrian Research, 104:187-206.

Avelar, V.G., Lafon J.M., Correia F.C.Jr., Macambira B.E.M. 1999. O magmatismo arqueano da região de Tucumã, Província Mineral de Carajás, Amazônia Oriental, Brasil: novos dados geocronológicos. Rev. Bras. Geoci., 29:453–460.

Avelar, V.O. 1996. Geocronologia Pb-Pb por evaporação em monocristal de zircão do magmatiwsmo da região de Tucumã, SE do Estado do Pará, Amazônia oriental. Dissertação de Mestrado, Universidade Federal do Pará, 149p. Avelar V.G, Lafon J.M., Correia F.C.Jr., Macambira B.E.M. 1999. O magmatismo arqueano da região de Tucumã, Província Mineral de Carajás, Amazônia Oriental, Brasil: novos dados geocronológicos. Rev Bras Geoc. 29:453–460

Angélica, R.S. 1996. Mineralogia e geoquímica de gossans e lateritos auríferos da região de Carajás, Estado do Pará: os depósitos do Igarapé Bahia e Águas Claras. Tese de Doutorado, UFPA, 115 p.

Araújo, O.J.B., Maia R.G.N., Jorge-João, X.S. Costa, J.B.S., 1988. A megaestruturação da folha Serra dos Carajás. In: Congr. Latino Am. Geol., 7, pp. 324–333.Araújo O.J.B., Maia, R.G.N., 1991. Serra dos Carajás: folha SB.22-Z-A. Estado do Pará. Escala 1:250.000. Texto explicativo. DNPM/CPRM. 164 p. il.

Barbosa, J.P.O. 2004. Geologia Estrutural, Geoquímica, Petrografia e Geocronologia de granitóides da região do Igarapé Gelado, norte da Província Mineral de Carajás. Dissertação de Mestrado, UFPA, 96p.

Barros, C.E.M., Barbey, P., and Boullier, A.M., 2001, Role of magma pressure, tectonic stress and crystallization progress in the emplacement of syn-tectonic granites. The A-type Estrela Granite Complex (Carajás mineral province, Brazil): Tectonophysics, v. 343, p. 93–109.

Barros, C.E.M., Macambira, M.J.B., Barbey P., and Scheller, T., 2004, Dados isotópicos Pb–Pb em zircão (evaporação) e Sm–Nd do Complexo Granítico Estrela, Província Mineral de Carajás, Brasil: implicações petrológicas e tectônicas. Rev. Brasil. Geoci. 34, 531–538.

Barros, C.E.M., Sardinha A.S., Barbosa J.P.O., Macambira M.J.B. 2009. Structure, Petrology, Geochemistry and zircon U/Pb and Pb/Pb geochronology of the synkinematic Archean (2.7 Ga) A-type granites from the Carajás Metallogenic Province, northern Brazil, The Canadian Mineralogist. 47: 1423-1440

Bigeleisen, J., Mayer, M.G., 1947. Calculation of equilibrium constants for isotopic exchange reactions. J. Chem. Phys. 15, 261–267. Berger G.W., York D. 1981. Geothermometry from 40Ar39Ar dating experiments. Geochim Cosmochim Acta 45:795-811

Brito Neves, B.B. & Cordani, U.G. 1991. Tectonic evolution of South América during Late Proterozoic. Precambrian Research, 53: 23-40. Brito Neves, B. B. 1999. América do Sul: quatro fusões, quatro fissões e o processo acrescionário Andino. Revista Brasileira Geociências, 29(3):379-392

Cabral, A.R., Lehmann B., Kwitko-Ribeiro R. Costa, C.H.C. 2002a. Palladium and platinum minerals from the Serra Pelada Au-Pd-Pt Deposit, Carajás Mineral Province, Northern Brazil. Can. Mineral., 40:1451-1463.

Cabral, A.R., Lehmann B., Kwitko-Ribeiro R., Costa C.H.C. 2002b. The Serra Pelada Au-Pd-Pt Deposit, Carajás Mineral Province, Northern Brazil: reconnaissance mineralogy and chemistry of very high grade palladian gold mineralization. Econ. Geol., 97:1127–1138.

Clayton, R. N., & Mayeda, T. K. (1963). The use of bromine pentafluoride in the extraction of oxygen from oxides and silicates for isotopic analysis. *Geochimica et* cosmochimica acta, 27(1), 43-52.

Condie, K. C. (1998). Episodic continental growth and supercontinents: a mantle avalanche connection?. Earth and Planetary Science Letters, 163(1), 97-108.

Cordeiro, A.A.C., Alves C.A., Fonseca L.R., de Nascimento J.A.S., Azevedo L.L., Santos F.F. 1984. Pesquisa geológica da jazida de wolframita de Pedra Preta, Rio Maria. In: SBG, Simp. Geol. Amaz., 2, Manaus, Anais, p. 374-390.

Costa, J.B.S., Araújo, O.J.B., Santos, A., Jorge João X.S., Macambira, M.J.B., Lafon, J.M. 1995. A Província Mineral de Carajás: aspectos tectono-estruturais, estratigráficos e geocronológicos. Boletim do Museu Paraense Emílio Goeldi, série Ciências da Terra, 7:199-235

Dall'Agnol, R., Lafon J.M., Macambira M.J.B., 1994. Proterozoic anorogenic magmatism in the Central Amazonian Province, Amazonian Craton: geochronological, petrological and geochemical aspects, Miner. Petrol., 50: 113-138.

Dall'Agnol R.; Rämö, O.T.; Magalhães, M.S.; Macambira, M.J.B. 1999. Petrology of the anorogenic, oxidised Jamon and Musa granites, Amazonian craton: implications for the genesis of Proterozoic A-type granites. Lithos 46:431-462.

Dall'Agnol, R., Teixeira N.P., Rämö O.T., Moura C.A.V., Macambira M.J.B. and Oliveira D.C., 2005. Petrogenesis of the Paleoproterozoic, rapakivi, A-type granites of the Archean Carajás Metallogenic Province, Brazil. Lithos, 80: 101-129.

Dall'Agnol, R, Oliveira MA, Almeida JAC, Althoff FJ, Leite AAS, Oliveira DC, Barros CEM. 2006. Archean and paleoproterozoic granitoids of the Carajás Metallogenic Province, eastern Amazonian craton. In: Symposium on magmatism, crustal evolution and metallogenesis of the Amazoniam Craton, Belém, Excursion Guide, pp 99–150

Dall'Agnol, R. & Oliveira D. C. 2007. Oxidized, magnetite-series, rapakivi-type granites of Carajás, Brazil: Implications for classification and petrogenesis of A-type granites. Lithos 93: 215–233.

Dardenne, M.A., Ferreira Filho, C.F. and Meirelles, M.R., 1988, The role of shoshonitic and calc-alkaline suites in the tectonic evolution of the Carajás district, Brazil. Journal of South American Earth Sciences, 1: 363–372. Davis DW, Williams IS, Krogh TE. 2003. Historical development of zircon geochronology. Rev Mineral Geochem 53:145-181.

Dardenne, M.A. & Schobbenhaus C.S. 2001. Metalogênese do Brasil. Ed.UnB/CNPq, Brasília, 392 p.

Dias, G.S., Macambira M.B., Dall'Ágno, R., Soare, A.D.V. Barro, C.E.M., 1996. Datações de zircões de sill de metagabro: comprovação de idade arqueana da Formação Águas Claras, Carajás, Pará. In: Simp. Geol. Amaz., 5, SBG, Belém, pp. 376-378.

DOCEGEO, 1988. Revisão litoestratigráfica da Província Mineral de Carajás – Litoestratigrafia e principais depósitos minerais. In: Cong. Bras. Geol., 35, SBG, p. 11-54.

Domingos, F.H.G., 2009, The structural setting of the Canaã dos Carajás region and Sossego-Sequeirinho deposits, Carajás, Brazil: Unpublished Ph.D. dissertation, Durhan, United Kingdom, Durham University, 483 p.

Fabre, S., Nédélec, A., Poitrasson, F., Strauss, H., Thomazo, C., Nogueira, A. 2011. Iron and Sulphur isotopes from the Carajás mining province (Pará, Brazil): implications for the oxidation of the ocean and the atmosphere across the Archaean-Proterozoic transition. Chem. Geol. 289: 124-139.

Ferreira Filho, C.F., Cançado, F., Correa, C., Macambira, E.M.B., Junqueira-Brod, T.C., Siepierski, L. 2007. Mineralizações estratiformes de PGE-Ni associadas a complexos acamadados em Carajás: os exemplos de Luanga e Serra da Onça. In: Rosa-Costa, L. T., Klein, E.L., Viglio, E.P. (Ed.). Contribuições à geologia da Amazônia. Belém: SBG-Núcleo Norte, v. 5, p. 1-14.

Gabriel, E.O.; Oliveira D.C.; Galarza M.A. 2010. Petrografia e Geocronologia de granitoides do Complexo Xingu da região nordeste de Água Azul do Norte, Província Mineral de Carajás, In: SBG, Congresso Brasileiro de Geologia, 45, Anais, Belém, CDrom.

Gibbs, A.K., Wirth K.R., Hirata W.K., Olszewski Jr., W.J., 1986. Age and composition of the Grão Pará Group volcanics, Serra dos Carajás. Rev. Bras. Geoc. 16: 201–211. Gomes C.B. & Girardi V.A.V. 1973. Princípios e aplicações da microssonda eletrônica. Ciência e Cultura (SBPC), 25(8): 711-722.

Godfrey, J. D. (1962). The deuterium content of hydrous minerals from the east-central Sierra Nevada and Yosemite National Park. *Geochimica et Cosmochimica Acta*, *26*(12), 1215-1245.

Gomes, C.B., Cordani, U.G. e Basel, M.A.S., 1975. Radiometric ages from the Serra dos Carajás Area, Northern Brazil. Bull. Geol. Soc. Am., 86: 939-945.

Groves, D.I., Bierlein F.P., Meinert L.D., Hitzman M.W. 2010. Iron Oxide Copper-Gold (IOCG) deposits through Earth history: implications for origin, lithospheric setting, and distinction from other epigenetic iron oxide deposits. Econ Geol. 105:641-654.

Hawthorne, F.C., Oberti, R., Harlow, G.E., Maresch, W.V., Martin, R.F., Schumacher, J.C., Welch, M.D. 2012. IMA report nomenclature of the amphibole supergroup. American Mineralogist, 97: 2031–2048.

Hirata, W.K., Rigon J.C., Kadekaru K., Cordeiro A.A.C., Meireles E.A. 1982. Geologia Regional da Província Mineral de Carajás. In: Simp. Geol. Amaz., 1, Belém, SBG/NO, p. 100–110.

Hitzman, M.W., Oreskes, N., Einaudi, M.T., 1992, Geological characteristics and tectonic setting of Proterozoic iron oxide (Cu-U-Au-REE) deposits. Precamb. Res. 58:241–287.

Huhn, S.R.B. 1992. Geologia, controle estrutural e gênese do depósito aurífero Babaçu, região de Rio Maria, sul do Pará. Dissertação de Mestrado, IG/ UnB, 168p.

Huhn, S.R.B., Santos A.B.S., Amaral A.F., Ledsham E.J. Gouveia J.L., Martins L.B.P., Montalvão R.M.G., Costa V.G. 1988. O terreno granito greenstone da região de Rio Maria-sul do Pará. In: Cong. Bras. Geol., 35, Belém. Anais... SBG. v.3, p. 1438-1453.

Huhn, SRB, Souza CIJ, Albuquerque MC, Leal ED, Brustolin V. 1999a. Descoberta do depósito Cu(Au) Cristalino: Geologia e mineralização associada região da Serra do Rabo - Carajás – PA. SBG/NO, Simpósio de Geologia da Amazônia, 6, pp 140□143

Huhn, S.R.B., Macambira M.J.B., Dall'Agnol R. 1999b. Geologia e geocronologia Pb-Pb do Granito Alcalino Planalto, Região da Serra do Rabo, Carajás-PA. In: SBG, Simp. Geol. Amaz., 6, Boletim de Resumos, p. 463-466.

Isley, A. E., & Abbott, D. H. (2002). Implications of the temporal distribution of high-Mg magmas for mantle plume volcanism through time. The Journal of Geology, 110(2), 141-158.

Jackson, S. E., Pearson, N. J., Griffin, W. L., & Belousova, E. A. (2004). The application of laser ablation-inductively coupled plasma-mass spectrometry to in situ U–Pb zircon geochronology. *chemical Geology*, *211*(1), 47-69.

Janoušek, V., Farrow, C. M., & Erban, V. 2006. Interpretation of whole-rock geochemical data in igneous geochemistry: introducing Geochemical Data Toolkit (GCDkit). Journal of Petrology, 47(6), 1255-1259.

Jorge João, X.S.; Neves, A.P.; Leal, J.W.L. 1982. Ouro da Serra Pelada: aspectos da geologia e garimpagem. In: Simpósio De Geologia Da Amazônia, 1., Belém. Anais... Belém: SBG–Núcleo Norte, v. 2, p. 52-62.

Justo, A.P., Freitas-Silva, F.H., Schorscher J.H.D., Nascimento, J.A.S., Dantas, E.L. 2015. Derrames komatiíticos do greenstone belt a sul da serra sul, Província Mineral de Carajás, Pará, Brasil. 14° Simp. Geol. Amaz, [CD-ROM].

Klein, E.L. & Carvalho J.M. de A. 2008. Recursos Minerais. In: M.L Vasquez & L.T. Rosa-Costa. (Orgs) Geologia e Recursos Minerais do Estado do Pará: SIG: Texto explicativo dos Mapas Geológico e Tectônico e de Recursos Minerais do Estado do Pará. Escala 1:1.000.000. Belém: CPRM.

Kotschoubey B. & Lemos V.P. 1985. Considerações sobre a origem e a gênese das bauxitas da Serra dos Carajás. In: SBG, Simp. Geol. Amaz., 3, Belém, Anais, v. 3, p. 48-61.

Lafon, J.M., Macambira M.J.B., Pidgeon R.T. 2000. Zircon U-Pb SHRIMP dating of Neoarchean magmatism in the southwestern part of the Carajás Province (eastern Amazonian Craton, Brazil). In: Inter. Geol. Congr., 31., Abstracts, Rio de Janeiro, [CD-ROM].

Leite, A.A.S. 2001. Geoquímica, petrogênese e evolução estrutural dos granitóides arqueanos da região de Xinguara, SE do Cráton Amazônico. Belém, Universidade Federal do Pará, Centro de Geociências. (Tese de Doutorado).

Leite, A.A.S., Dall'Agnol, R., Macambira, M.J.B., Althoff, F.J., 2004. Geologia e Geocronologia dos granitóides Arqueanos da região de Xinguara (PA) e suas implicações na evolução do Terreno GranitoGreenstone de Rio Maria. Revista Brasileira de Geociências 34: 447-458 (in Portuguese).

Lindenmayer, Z. G., Fleck, A., Gomes, C.H., Santos, A.B.S., Caron, R., Paula, F.C., Laux, J.H., Pimentel, M.M., and Sardinha, A.S. 2005. Caracterização geológica do alvo estrela (Cu-Au), Serra dos Carajás, Pará In: Caracterização de Depósitos Minerais em Distritos Mineiros da Amazônia. DNPM, CT-Mineral / FINEP, ADIMB, CD-ROM, 2005, cap. IV, 1, 137-205.

Locock, A. J. 2014. An Excel spreadsheet to classify chemical analyses of amphiboles following the IMA 2012 recommendations. Computers and Geosciences, 62: 1-11.

Lobato, L.M., Rosière C.A., Silva R.C.F., Zucchetti M., Baars F.J., Sedane J.C.S., Javier Rios F., Pimentel M., Mendes G.E., Monteiro A.M. 2005. A mineralização hidrotermal de ferro da Província Mineral de Carajás – controle estrutural e contexto na evolução metalogenética da província. In: Marini, O.J., Queiroz, E.T., Ramos, B.W. (Eds.). Caracterização de Depósitos Minerais em Distritos Mineiros da Amazônia, DNPM-CT-Mineral-FINEP-ADIMB, pp. 25-92.

Lafon, J.M., Rodrigues E., Duarte K.D. 1994. Le granite Mata Surrão: un magmatisme monzogranitique contemporain des associations tonalitiques-trondhjemitiquesgranodioritiques archéennes de la région de Rio Maria (Amazonie Orientale, Brésil). p. 642- 649.

Leonardos, O.H., Santos M.D., Giuliani G., Araújo L.R. 1991. The Cumaru mesothermal granodiorite-hosted gold mineralization, Amazon Craton, Brazil. In: E.A. Ladeira (ed.) Brazil gold'91, the economics geology geochemistry and genesis of gold deposits. Belo Horizonte, Proceedings, Rotterdam, Balkema, p. 557-562.

Loios, V.A.P. 2009. Método de preparação e separação de minerais no CPGeo-IGc-USP. In: Boletim de resumos expandidos. Simpósio 45 anos de Geocronologia no Brasil. 330p. Lopez G. P. & Hitzman M. W. & Nelson E. P. 2014. Alteration patterns and structural controls of the El Espino IOCG mining district, Chile. Miner Deposita (2014) 49:235–259

Ludwig, K. R. (2009). Isoplot v. 4 for Excel 2007. *Berkeley Geochronological Centre, Berkeley, California.*

Macambira, E.M.B. & Vale A.G. 1997. Programa Levantamentos Geológicos Básicos do Brasil. São Felix do Xingu. Folha SB.22-Y-B. Estado do Pará. DNPM/ CPRM. Brasília, 384p.

Macambira, M.J.B., Lancelot J. 1996. Time constraints for the formation of the Archean Rio Maria crust, southeastern Amazonian Craton, Brazil. International Geology Review 38, 1134-1142.

Macambira, M.J.B., Vasquez M.L., Silva D.C.C., Galarza M.A., Barros C.E.M., Camelo J.F. 2009. Crustal growth of the central-eastern Paleoproterozoic domain, SW Amazonian craton: Juvenile accretion vs. reworking. Journal of South American Earth Sciences 27 (2009) 235–246.

Magdaleno, G.B., Ruiz, I.R. 2009. Metodologia Isotópica Pb-Pb no CPGeo-USP. Boletim de Resumos Expandidos. In: simpósio 45 anos de geocronologia no Brasil. São Paulo: Instituto de Ciências Exatas. Centro de Pesquisas Geocronológicas – CPGeo.

McNaughton, N. J., & Groves, D. I. (1996). A review of Pb-isotope constraints on the genesis of lode-gold deposits in the Yilgarn Craton, Western Australia. *Journal of the Royal Society of Western Australia*, *79*(1), 123-129.

Meirelles, M.R. 1986. Geoquímica e petrologia dos jaspilitos e rochas vulcânicas associadas, Grupo Grão-Pará, Serra dos Carajás. Dissertação de Mestrado, UnB, pp.

Meireles, E. M., Teixeira, J. T., Lourenço, R. S., Medeiros Filho, C. A. 1982. Geologia estrutura e mineralização aurífera de Serra Pelada. Anais, 31l Congresso Brasileiro de Geologia, Salvador. v3, 900-910.

Meireles, E.M. & Silva A.R.B. 1988. Depósito de ouro de Serra Pelada, Marabá, Pará. In: C. Schobbenhaus, C.E.S. Coelho (eds) Principais Depósitos Minerais do Brasil, Brasília, DNPM/CVRD, v. 3, pp. 547-557. McCulloch M.T. & Chappell B.W. 1982. Nd isotopic characteristics of S- and I-type granites. Earth and Planetary Science Letters 58, 51–64.

Meirelles, M.R., Dardenne, M.A., 1991 - Vulcanismo basáltico de afinidade shoshonítica em ambiente de arco arqueano, Grupo Grão Pará, Serra dos Carajás, Pa. Rev. Bras. Geoc., 21: 41-50.

Moreto, C.P.N., Monteiro L.V.S., Xavier R.P., Amaral W.S., Santos T.J.S., Juliani C., Souza Filho C.R. 2011. Mesoarchean (3.0 and 2.86 Ga) host rocks of the iron oxide-Cu-Au Bacaba deposit, Carajas Mineral Province: U-Pb geochronology and metallogenetic implications. Miner. Dep., 46: 789-811.

Moreto, C.P.N., Monteiro L.V.S., Xavier R.P., Delinardo M.A. S., Melo G.H.C., Tassinari C.G.C., Creaser R., Sato K, Dufrane A., Kemp T. 2015a. A protracted evolution of the iron oxide-copper-gold deposits in the Carajás province. : 47 Cong. Bras. Geol, Salvador, SBG. [CD-ROM].

Moreto, C.P.N., Monteiro L.V.S., Xavier R.P., Creaser, R., Dufrane, A., Tassinari, C.G., Sato, K., Kemp T.I.S., Amaral, W.S. 2015b. Overprinting of Paleoproterozoic on Archean Iron Oxide -Copper-Gold System at the Sossego Deposit, Carajas Province: Re-Os And U-Pb Geochronological Evidences. Economic Geology.

Moroni, M., Girardi V.A.V., Ferrario A. 2001. The Serra Pelada Au–PGE deposit, Serra dos Carajás (Pará State, Brazil): geological and geochemical indications for a composite mineralising process. Min. Depos., 36:768-785.

Mougeot, R., Respaut J.P., Briqueu L., Ledru P., Milesi J.P., Macambira M.J.B., Huhn S.B. 1996. Geochronological constrains for the age of the Águas Claras Formation (Carajás Province, Pará, Brazil). In: Cong. Bras. Geol, 39, Anais., Salvador, SBG. 6:579-581.

Nogueira, A.C.R., Truckenbrodt, W., Pinheiro, R.V.L. 1995. Formação Águas Claras, Pré-Cambriano da Serra dos Carajás: redescrição e redefinição litoestratigráfica. Bol. Mus. Par. Em. Goeldi, Ciênc. da Terra, (7), pg. 177-277.

Oliveira, C.G. & Leonardos O.H. 1990. Gold mineralization in the Diadema shear belt, northern Brazil. Econ. Geol., 85:1034-1043.

Oliveira, M.A., Dall'Agnol, R., Althoff, F.J., Leite, A.A.S. 2009. Mesoarchean sanukitoid rocks of the Rio Maria Granite-Greenstone Terrane, Amazonian craton, Brazil. Journal of South American Earth Sciences 27, 146-160.

Oliveira, C.G. & Santos R.V. 2003. Isotopic domains controlled by transtentional and transpressional sectors in the auriferous Diadema shear belt, northern Brazil. J. South Am. Earth Sci., 16:513-522.

Olszewski, W.J., Wirth, K.R., Gibbs, A.K, and Gaudette, H.E., 1989, The age, origin, and tectonics of the Grão Pará Group and associated rocks, Serra dos Carajás, Brazil: Archean continental volcanism and rifting: Precambrian Research, v. 42, p. 229–254.

Paixão, M.A.P., Nilson A.A., Dantas E.L. 2008. The Neoproterozoic Quatipuru ophiolite and the Araguaia fold belt, central-northern Brazil, compared with correlatives in NW Africa. Geological Society, London, Special Publications, 294:297-318.

Pimentel, M.M., Machado, N. 1994. Geocronologia U-Pb dos Terrenos granito-greenstone de Rio Maria, Pará. In: Congresso Brasileiro de Geologia, 38, Camboriú, 1988. Boletim de Resumos Expandidos. Camboriú, SBG. p. 390-391.

Pinheiro, R.V.L., Holdsworth R.E., 1997. Reactivation of Archaean strike-slip fault systems, Amazon region, Brazil. Journal of the Geological Society of London 154, 99–103.

Pinheiro R.V.L., Kiyoshi, K., Viana, S.A., Cantidiano, F., Nunes, F.S., Viera, F.M. 2013. Carajás, Brazil – A short tectonic review. In: Simp. Geol. Amaz., 13, Belém, Anais, [CDROM]

Porto, C.G., Imbernon R.A.L., Toledo M.C.M., Menezes R.O.G., Souza J.J., Borges C.E.P. 2010. Depósitos de Cu-Au lateríticos do Brasil: casos de Chapada (GO), Igarapé Bahia e Salobo (Carajás, PA). In: R.S.C. Brito, M.G. Silva, R.M. Kuyumjian. (Org.). Modelos de depósitos de cobre do Brasil e sua resposta ao intemperismo. Brasilia: CPRM, 2010, p. 191213.

Réquia, K., Stein, H., Fontboté, L. Chiaradia, M. 2003. Re-Os and Pb-Pb geochronology of the Archean Salobo iron oxide copper–gold deposit, Carajás Mineral Province, northern Brazil. Miner. Dep., 38: 727-738.

Ricci, P.S.F., Carvalho M.A. 2006. Rocks of the Pium-Area, Carajás Block, Brazil – A Deep seated High-T Gabbroic Pluton (Charnockitoid-Like) with Xenoliths of Enderbitic Gneisses Dated at 3002 Ma – The Basement Problem Revisited. In: Simp. Geol. Amaz., 8, [CD-ROM]

Richards, J. R. 1971. Major lead orebodies, mantle origin?. *Economic geology*, *66*(3), 425-434.

Rios, F..J., Villas R.N., Fuzikawa K., Sial A.N., Mariano G. 1998. Isótopos de oxigênio e temperatura de formação dos veios mineralizados com wolframita da jazida Pedra Preta, sul do Pará. Rev. Bras. Geoc., 28:253-256.

Rolando, A.P., Macambira M.J.B. 2003. Archean crust formation in Inajá range area, SSE of Amazonian Craton, Brazil, based on zircon ages and Nd isotopes. In: South American Symposium on Isotope Geology, 4, Expanded Abstract.Salvador, [CDROM]

Santos, J.O.S., Hartmann, L.A., Gaudette, H.E., Groves, D.I., Mcnaughton, N.J., Fletcher, I.R., 2000. A new understanding of the provinces of the Amazonian Craton based on integration of field mapping and U-Pb and Sm-Nd geochronology. Gondwana Research, 3, 453-488.

Santos, J.O.S. 2003. Geotectônica do Escudo das Guianas e Brasil-Central. In: Bizzi, L.A. (Ed.). Geologia, tectônica e recursos minerais do Brasil: texto, mapas e SIG. Brasília: CPRM, p. 169-226.

Santos, J.O.S., Hartmann, L.A., Faria M.S., Riker S.R. Souza M.M., Almeida M.E., Mcnaughton, N.J. 2006. A Compartimentação do Cráton Amazonas em províncias: avanços ocorridos no pe´riodo de 2000-2006. In: SBG Simp. Geol. Amaz. 9 Belém, Anais.

Santos, M.D., Leonardos O.H., Foster R.P., Fallick A.E. 1998. The lode-porphyry model as deduce from the Cumaru, mesothermal granitoid-hosted gold deposit, southern Pará, Brazil. Rev. Bras. Geoc., 28:327338.

Santos, P.A. 2013. Geologia, petrografia e geoquímica da Associação Tonalito-Trondhjemito Granodiorito (TTG) do extremo leste do Subdomínio de

Transição, Província Carajás. Dissertação de Mestrado. Universidade Federal do Pará. Instituto de Geociencias. 113p.

Santos, P.A., Feio G.R.L., Dall'Agnol R., Costi H.T., Lamarão C.N., Galarza M.A. 2013. Petrography, magnetic susceptibility and geochemistry of the Rio Branco Granite, Carajás Province, southeast of Pará, Brazil. Brazilian Journal of Geology, 43(1): 2-15

Sardinha, A.S; Barros, C.E.M.; Krymsky, R. S.; Macambira, M.J.B. 2001. Petrografia e geocronologia U-Pb em zircão do Granito Serra do Rabo, Província Mineral de Carajás, Pará. In: Simpósio de Geologia da Amazônia, 7, Belém. Resumos expandidos...Belém: SBG-Núcleo Norte, 2001. 1 CD-ROM.

Sato, K., Basei, M. A. S., Júnior, O. S., Sproesser, W. M., & Passarelli, C. R. (2008). Novas técnicas aplicadas ao método U-Pb no CPGeo-IGc/USP: avanços na digestão química, espectrometria de massa (TIMS) e exemplos de aplicação integrada com SHRIMP. *Geologia USP. Série Científica*, *8*(2), 76-99.

Siepierski, L. (2016). Geologia, petrologia e potencial para mineralizações magmáticas dos corpos máfico-ultramáficos da região de Canaã dos Carajás, Província Mineral de Carajás.

Silva, M.G., Teixeira J.B.G., Pimentel M.M., Vasconcelos P.M., Arielo A. e Rocha W.J.S.F., 2005. Geologia e mineralizações de Fe-Cu-Au do Alvo GT46 (Igarapé Cinzento, Carajás). In: Marini, O.J., Queiroz, E.T., Ramos, B.W. (eds.), Caracterização de Depósitos Minerais em Distritos Mineiros da Amazônia, DNPM-CT-Mineral-FINEP-ADIMB, p. 94-151.

Silva, K. S. 2016. Geologia, petrologia, geocronologia e mineralizações sulfetadas do Complexo Ézio, província mineral de carajás, Brasil.

Sharp, Z. D. (1990). A laser-based microanalytical method for the in situ determination of oxygen isotope ratios of silicates and oxides. *Geochimica et Cosmochimica Acta*, *54*(5), 1353-1357.

Sharp, Z. D. Principles of Stable Isotope Geochemistry. New Jersey: Pearson Prentice Hall, 2007. 344 p.

Souza, S.R.B., Macambira M.J.B., Sheller T. 1996. Novos dados geocronológicos para os granitos deformados do Rio Itacaiúnas (Serra dos Carajás, PA), implicações estratigráficas. In: Simp. Geol. Amaz., 5, Belém, Anais, 380–383.

Souza, Z.S., Potrel A., Lafon J.M., Althoff F.J., Pimentel M.M., Dall'Agnol R., Oliveira C.G., 2001. Nd, Pb and Sr isotopes in the Identidade Belt, an Archean greenstone belt of Rio Maria region (Carajás Province, Brazil): implications for the geodynamic evolution of the Amazonian Craton. Precambrian Research 109: 293–315.

Sousa, S.D.; Oliveira, D.C.; Gabriel, E.O.; Macambira, M.J.B. 2010. Geologia, Petrografia e Geocronologia das rochas granitoides do Complexo Xingu da porção a leste da cidade de Água Azul do Norte (PA) - PMC. In: SBG, Congresso Brasileiro de Geologia, 45, Anais, Belém, CDrom.

Tallarico, F.H.B., Coimbra C.R., Costa C.H.C. 2000. The Serra Leste Sediment-Hosted Au-(Pd-Pt) Mineralization, Carajás Province. Rev. Bras. Geoc., 30:226229.

Tallarico, F.H.B. 2003. O cinturão cupro-aurífero de Carajás, Brasil. Tese de Doutorado, UNICAMP, 229p

Tallarico, F.H.B., Figueiredo B.R., Groves D.I., Kositcin N., McNaughton N.J., Fletcher I.R., Rego J.L. 2005. Geology and SHRIMP U–Pb geochronology of the Igarapé Bahia deposit, Carajás copper–gold belt, Brazil: an Archean (2.57 Ga) example of iron–oxide Cu–Au–(U– REE) mineralization. Econ Geol 100:7–28.

Tassinari, C.C.G. 1996. O mapa geocronológico do Cráton Amazônico no Brasil: revisão dos dados isotópicos. Tese de Livre Docência, IG-USP, 139p. Tassinari C.C.G., Macambira M.J.B. 1999. Geochronological Provinces of the Amazonian Craton. Episodes, 22:174-182.

Tassinari, C.C.G. & Macambira M.J.B. 1999. Geochronological Provinces of the Amazonian Craton. Episodes, 22:174-182.

Tassinari, C.C.G. and Macambira, M.J.B., 2004. A evolução tectônica do Cráton Amazônico. In: MantessoNeto, V., Bartorelli, A., Carneiro, C.D.R. and Brito Neves, B.B. (Eds.) Geologia do Continente SulAmericano: Evolução da Obra de Fernando Flávio Marques de Almeida. pp. 471-485.

Tassinari, T., Tachibana J., Tulio M., Lívio R., Gaia C. 2005. Geologia isotópica aplicada nas mineralizações de Cu-Au do greenstone belt da Serra dos Gradaús, Província Mineral de Carajás, 190 Cráton Amazônico: exemplo de mineralizações policíclicas. In: SIMPÓSIO BRASILEIRO DE METALOGENIA, 1., Gramado, RS. Resumos... Porto Alegre: SBG/SEG/SGMTM-MME, 2005. 1 CD-ROM.

Tavares, F. M., Silva, C. M. G., Justo, A. P., Lopes, E. C. S., Oliveira, J. K. M. 2013. Evolução geotectônica arqueana-paleoproterozoica do segmento oriental do domínio carajás: uma nova abordagem. Anais. 13º Simpósio de Geologia da Amazônia. CD-ROOM.

Tavares, F. M. 2015. Evolução geotectônica do nordeste da Província Carajás. Tese de Doutorado. Universidade Federal do Rio de Janeiro.

Teixeira, W., Tassinari, C.C.G., Cordani, U.G., Kawashita, K. 1989. A review of the geochronological of the Amazonian Craton: tectonic implications. Precamb. Res., 42: 213-227.

Teixeira, J.B.G., Eggler, D.H., 1994. Petrology, geochemistry, and tectonic setting of Archean basaltic and dioritic rocks from the N4 iron deposit, Serra dos Carajás, Pará, Brazil. Acta Geology Leopoldensia 17, 71-114.

Teixeira, J.B.G. 1994. Geochemistry, petrology, and tectonic setting of archean basaltic and dioritic rocks from the N4 Iron deposit, Serra dos Carajás, Pará, Brazil. 1994. 161 f. Tese de Doutorado, Penn State University.

Teixeira, J.B.G., Lindenmayer, Z.G., Silva, M.G. 2010. Depósitos de Óxido de Fe, Cu-Au de Carajás. In: R.S.C. Brito, M.G. Silva, R.M. Kuyumjian. (Org.). Modelos de depósitos de cobre do Brasil e sua resposta ao intemperismo. CPRM, p. 15-48.

The Open University Electron Microprobe Laboratory. 2010. Free Structural Formula Calculators. Available in http://www.open.ac.uk/earth-research/tindle/AGT/AGT_Home_2010/Microprobe-2.html

Trendall, A.F., Basei M.A.S., De Laeter J.R., Nelson D.R. 1998. SHRIMP U-Pb constraints on the age of the Carajás formation, Grão Pará Group, Amazon Craton. J. South Am. Earth Sci. 11, 265-277.

Vasquez, L.V., Rosa-Costa L.R., Silva C.G., Ricci P.F., Barbosa J.O., Klein E.L., Lopes E.S., Macambira E.B., Chaves C.L., Carvalho J.M., Oliveira J.G., Anjos G.C., Silva H.R.. 2008 Geologia e Recursos Minerais do Estado do Pará: Sistema de Informações Geográficas —SIG: texto explicativo dos mapas Geológico e Tectônico e de Recursos Minerais do Estado do Pará 1:1.000.000. CPRM, Belém, p328.

Veloso, A.S.R. Evolução metalogenética do depósito de Cu-(Ni-Zn) Jatobá, Província Mineral de Carajás. 2017. 213p. Tese (Doutorado), Instituto de Geociências, Universidade of São Paulo, São Paulo, 2017.

Villas, R.N. & Santos M.D. 2001. Gold deposits of the Carajás Mineral Province: deposit types and metallogenesis. Miner. Dep., 36:300-331.

Xavier, R.P. Monteiro, L.V.S., Moreto, C.P.N., Pestilho, A.L.S., Melo, G.H.C., Silva, M.A.D. da; Aires, B., Ribeiro, C., Freitas e Silva, F.H. 2012. The Iron Oxide Copper-Gold systems of the Carajas Mineral Province. In: J. Hedenquist, M. Harris, F. Camus. (Org.). SEG Special Publication 16, Geology and Genesis of Major Copper Deposits and Districts of the World: A Tribute to Richard H. Sillitoe. 1ed. Littleton: Society of Economic Geologists, 1: 433-454.

Yavuz, F., Kumral, M., Karakaya, N., Karakaya, M. Ç., Yıldırıma, D.K. 2015. A Windows program for chlorite calculation and classification. Computers & Geosciences, 81: 101-113.

Wirth, K.R. Gibbs A.K. Olszewski,W.J.Jr. 1986. U–Pb ages of zircons from the Grão Pará Group and Serra dos Carajás granite, Pará, Brasil. Rev. Bras. Geoci. 16: 195–200.

Zang, W. & Fyfe W.S. 1995. Chloritization of the hydrothermally altered bedrock at the Igarapé Bahia gold deposit, Carajás, Brazil. Miner. Dep., 30:30-38.

Zartman, R. E., & Doe, B. R. (1981). Plumbotectonics—the model. *Tectonophysics*, *75*(1-2), 135-162.

Zucchetti, M. 2007. Rochas máficas do Grupo Grão Pará e sua relação com a mineralização de ferro dos depósitos N4 E N5, Carajás, PA. Tese de Doutorado, UFMG, 165p.

Apêndice 1

Análises de química mineral por microssonda eletrônica

Apêndice A. Análises de química mineral por microssonda eletrônica em escapolita.

	JAT-28 (166,40)	JAT-28 (166,40)	JAT-28 (166,40)	JAT-28 (166,40)	JAT-28 (166,40)	JAT-28 (166,40)	JAT-28 (166,40)	JAT-28 (166,40)	JAT-28 (166,40)	JAT-28 (166,40)	JAT-28 (166,40)	JAT-28 (166,40)
	Diabásio	Diabásio	Diabásio	Diabásio	Diabásio	Diabásio	Diabásio	Diabásio	Diabásio	Diabásio	Diabásio	Diabásio
	Scp 1	Scp 1	Scp 1	Scp 1	Scp 1	Scp 1	Scp 1	Scp 1	Scp 1	Scp 1	Scp 1	Scp 1
ído (%)												
$O)_2$	54.68	55.59	55.12	55.21	56.03	55.08	56.03	54.95	55.87	55.30	55.00	56.16
$_2O_3$	24.10	23.97	23.82	23.90	24.13	23.67	23.52	24.04	24.13	23.81	23.56	23.96
$_3(O_4$	0.28	0.28	0.20	0.11	0.24	0.15	0.14	0.10	0.25	0.12	0.11	0.20
nO		0.01	0.01		0.01	0.00	0.00					
O)	0.27	0.29	0.32	0.27	0.30	0.32	0.31	0.34	0.31	0.35	0.32	0.32
aO	7.86	7.41	7.43	7.41	7.24	7.27	6.87	7.60	7.35	7.39	7.26	7.18
O_{f2}		0.04		0.03	0.03				0.02	0.03	0.03	
$_2$aO	9.45	9.52	9.70	9.93	9.65	9.82	10.25	9.85	9.45	9.92	9.85	9.58
O_{33}					0.04			0.04	0.03		0.01	0.01
	3.03	3.21	3.07	3.20	3.32	3.27	3.26	3.16	3.16	3.18	3.28	3.10
			0.00	0.02	0.01		0.01				0.01	
rma	99.68	100.32	99.68	100.07	101.00	99.59	100.39	100.08	100.57	100.09	99.42	100.50
=F	0	0	0.001	0.006	0.003	0.000	0.005	0.000	0.000	0.000	0.003	0.000
=Cl	0.684	0.724	0.693	0.722	0.749	0.738	0.736	0.713	0.713	0.718	0.740	0.700
TAL	98.995	99.595	98.983	99.342	100.247	98.850	99.653	99.367	99.857	99.375	98.682	99.804
rmula (apfu)												
Si	7.491	7.549	7.544	7.527	7.551	7.544	7.604	7.499	7.560	7.541	7.545	7.600
Al^{IV}	4.509	4.451	4.456	4.473	4.449	4.456	4.396	4.501	4.440	4.459	4.455	4.400
TAL	12.000	12.000	12.000	12.000	12.000	12.000	12.000	12.000	12.000	12.000	12.000	12.000
Al^{VI}	-0.6173	-0.6146	-0.6145	-0.6331	-0.6166	-0.6357	-0.6347	-0.6345	-0.5916	-0.6331	-0.6458	-0.5795
Fe	0.029	0.028	0.021	0.011	0.025	0.016	0.014	0.010	0.026	0.012	0.012	0.020
Mn	0.000	0.001	0.001	0.000	0.001	0.000	0.000	0.000	0.000	0.000	0.000	0.000
K	0.048	0.050	0.056	0.047	0.051	0.056	0.054	0.060	0.054	0.061	0.055	0.054
Ca	1.154	1.078	1.089	1.082	1.045	1.067	0.999	1.111	1.066	1.080	1.067	1.041
Ti	0.000	0.004	0.000	0.003	0.003	0.000	0.000	0.000	0.002	0.003	0.003	0.000
Na	2.510	2.506	2.574	2.625	2.521	2.607	2.697	2.606	2.479	2.622	2.620	2.513
Mg	0.000	0.000	0.000	0.000	0.000	0.000	0.000	0.000	0.000	0.000	0.000	0.000
TAL	3.124	3.054	3.126	3.135	3.030	3.111	3.129	3.153	3.035	3.144	3.111	3.049
S	0.000	0.000	0.000	0.000	0.004	0.000	0.000	0.004	0.003	0.000	0.001	0.001
Cl	0.704	0.739	0.712	0.739	0.758	0.759	0.750	0.731	0.725	0.735	0.763	0.711
F	0.000	0.020	0.025	0.031	0.000	0.000	0.000	0.000	0.000	0.000	0.000	0.000
An	50.284	48.361	48.546	49.102	48.299	48.541	46.542	50.029	47.990	48.645	48.494	46.683
9%	68.5	69.9	70.3	70.8	70.7	71.0	73.0	70.1	69.9	70.8	71.1	70.7
9%	31.5	30.1	29.7	29.2	29.3	29.0	27.0	29.9	30.1	29.2	28.9	29.3

Apêndice B. Análises de química mineral por microssonda eletrônica em escapolita.

	JAT-21 (64,80)	JAT-21 (64,80)	JAT-21 (64,80)	JAT-21 (64,80)	JAT-21 (64,80)	JAT-21 (64,80)	JAT-21 (64,80)	JAT-21 (64,80)
	Diabásio	Diabásio	Diabásio	Diabásio	Diabásio	Diabásio	Diabásio	Diabásio
	Scp 1	Scp 1	Scp 1	Scp 1	Scp 1	Scp 1	Scp 1	Scp 1
Óxido (%)								
SiO_2	52.63	52.39	50.59	52.85	52.99	60.38	54.04	53.39
Al_2O_3	24.71	24.63	25.86	24.59	24.59	20.29	23.78	24.42
Fe_3O_4	0.06	0.03	0.05	0.07	0.04	0.10	0.07	0.06
MnO	0.01		0.02	0.01	0.02	0.02		0.01
K_2O	0.30	0.30	0.24	0.28	0.32	0.24	0.33	0.37
CaO	9.46	9.18	11.05	9.01	9.77	7.79	7.93	8.84
TiO_2	0.04			0.03	0.07	0.00	0.01	0.01
Na_2O	7.85	7.92	6.80	8.27	8.10	7.21	9.04	8.47
MgO								
SO_3		0.05		0.03				0.02
Cl	2.30	2.35	1.95	2.52	2.49	2.11	2.98	2.58
F		0.01		0.02				0.01
Soma	97.36	96.86	96.56	97.69	98.39	98.15	98.17	98.17
O=F	0	0.00	0	0.010	0	0	0	0.004
O=Cl	0.519	0.530	0.440	0.569	0.562	0.476	0.672	0.582
TOTAL	96.846	96.323	96.121	97.115	97.827	97.670	97.502	97.584
Fórmula (apfu)								
T_Si	7.390	7.388	7.190	7.393	7.379	8.242	7.509	7.433
T_AlIV	4.610	4.612	4.810	4.607	4.621	3.758	4.491	4.567
TOTAL	12.000	12.000	12.000	12.000	12.000	12.000	12.000	12.000
M_AlVI	-0.5205	-0.5180	-0.4779	-0.5537	-0.5860	-0.4945	-0.5969	-0.5609
M_Fe	0.007	0.003	0.005	0.007	0.004	0.010	0.007	0.006
M_Mn	0.001	0.000	0.003	0.001	0.003	0.002	0.000	0.001
M_K	0.055	0.054	0.043	0.051	0.057	0.042	0.059	0.065
M_Ca	1.423	1.387	1.683	1.350	1.457	1.139	1.180	1.318
M_Ti	0.004	0.000	0.000	0.004	0.007	0.000	0.001	0.001
M_Na	2.137	2.165	1.874	2.243	2.187	1.908	2.435	2.286
M_Mg	0.000	0.000	0.000	0.000	0.000	0.000	0.000	0.000
TOTAL	3.106	3.091	3.130	3.102	3.129	2.608	3.085	3.117
A_S	0.000	0.006	0.000	0.003	0.000	0.000	0.000	0.002
A_Cl	0.547	0.562	0.470	0.597	0.588	0.488	0.702	0.609
A_F	0.008	0.024	0.024	0.002	0.000	0.000	0.024	0.000
Eq An	53.655	53.718	60.318	53.579	54.044	25.278	49.701	52.246
Ma %	60.0	61.0	52.7	62.4	60.0	62.6	67.4	63.4
Me%	40.0	39.0	47.3	37.6	40.0	37.4	32.6	36.6

Apêndice C. Análises de química mineral por microssonda eletrônica em escapolita.

	JAT-28 (54,22)	JAT-28 (54,22)	JAT-28 (54,22)	JAT-28 (54,22)	JAT-28 (54,22)	JAT-28 (54,22)	JAT-28 (54,22)	JAT-28 (54,22)	JAT-28 (54,22)	JAT-28 (54,22)
	Scp-Hs-Bt milonito	Scp-Hs-Bt milonito	Scp-Hs-Bt milonito	Scp-Hs-Bt milonito	Scp-Hs-Bt milonito	Scp-Hs-Bt milonito	Scp-Hs-Bt milonito	Scp-Hs-Bt milonito	Scp-Hs-Bt milonito	Scp-Hs-Bt milonito
Óxido (%)	Scp 2	Scp 2	Scp 2	Scp 2	Scp 2	Scp 2	Scp 2	Scp 2	Scp 2	Scp 2
SiO_2	53.73	58.35	60.74	53.92	53.62	54.64	53.53	54.02	55.03	54.96
Al_2O_3	24.51	22.51	21.10	24.24	24.44	23.82	24.11	24.31	23.91	24.05
Fe_3O_4	0.05	0.23	0.10	0.19	0.10	0.10	0.71	0.08	0.25	0.19
MnO			0.00						0.02	0.00
K_2O	0.26	0.51	0.27	0.26	0.21	0.33	0.75	0.26	0.32	0.28
CaO	8.75	5.49	6.89	8.65	9.33	7.40	8.34	8.84	7.58	7.70
TiO_2	0.02	0.02	0.00			0.02			0.01	0.01
Na_2O	8.57	9.69	8.26	8.88	8.50	9.67	8.33	8.86	9.57	9.39
MgO							0.34			
SO_3	0.01		0.02			0.07	0.01	0.02		
Cl	2.52	2.34	2.64	2.67	2.45	3.38	2.49	2.75	3.13	2.92
F		0.02			0.02		0.01	0.01	0.01	
Soma	98.42	99.17	100.02	98.81	98.67	99.43	98.62	99.14	99.83	99.51
O=F	0	0.008	0	0	0.008	0	0.004	0.002	0.002	0
O=Cl	0.569	0.528	0.596	0.603	0.553	0.763	0.562	0.621	0.706	0.659
TOTAL	97.854	98.630	99.427	98.208	98.109	98.668	98.056	98.521	99.118	98.854
Fórmula (apfu)										
T_Si	7.453	7.938	8.145	7.460	7.433	7.497	7.437	7.449	7.523	7.531
T_Al^{IV}	4.547	4.062	3.855	4.540	4.567	4.503	4.563	4.551	4.477	4.469
TOTAL	12.000	12.000	12.000	12.000	12.000	12.000	12.000	12.000	12.000	12.000
M_Al^{VI}	-0.5400	-0.4529	-0.5204	-0.5879	-0.5748	-0.6518	-0.6159	-0.6004	-0.6255	-0.5858
M_Fe	0.006	0.024	0.010	0.020	0.011	0.010	0.074	0.008	0.025	0.020
M_Mn	0.000	0.000	0.001	0.000	0.000	0.000	0.000	0.000	0.002	0.000
M_K	0.046	0.089	0.046	0.046	0.037	0.058	0.133	0.046	0.056	0.049
M_Ca	1.300	0.800	0.990	1.282	1.386	1.088	1.241	1.306	1.110	1.130
M_Ti	0.002	0.002	0.000	0.000	0.000	0.002	0.000	0.000	0.001	0.001
M_Na	2.305	2.556	2.147	2.382	2.284	2.572	2.244	2.369	2.536	2.494
M_Mg	0.000	0.000	0.000	0.000	0.000	0.000	0.070	0.000	0.000	0.000
TOTAL	3.119	3.018	2.674	3.142	3.143	3.079	3.146	3.128	3.106	3.110
A_S	0.001	0.000	0.002	0.000	0.000	0.007	0.001	0.002	0.000	0.000
A_Cl	0.592	0.540	0.600	0.626	0.576	0.786	0.586	0.643	0.725	0.678
A_F	0.000	0.014	0.014	0.013	0.000	0.000	0.020	0.018	0.006	0.010
Eq An	51.560	35.395	28.497	51.337	52.244	50.111	52.109	51.700	49.247	48.979
Ma %	63.9	76.2	68.4	65.0	62.2	70.3	64.4	64.5	69.6	68.8
Me%	36.1	23.8	31.6	35.0	37.8	29.7	35.6	35.5	30.4	31.2

Apêndice D. Análises de química mineral por microssonda eletrônica em escapolita.

	JAT-28 (54,22)	JAT-28 (54,22)	JAT-28 (54,22)	JAT-28 (54,22)	JAT-28 (54,22)	JAT-28 (54,22)	JAT-28 (54,22)	JAT-28 (54,22)	JAT-28 (54,22)	JAT-28 (54,22)
	Scp-Hs-Bt milonito	Scp-Hs-Bt milonito	Scp-Hs-Bt milonito	Scp-Hs-Bt milonito	Scp-Hs-Bt milonito	Scp-Hs-Bt milonito	Scp-Hs-Bt milonito	Scp-Hs-Bt milonito	Scp-Hs-Bt milonito	Scp-Hs-Bt milonito
Óxido (%)	Scp 2	Scp 2	Scp 2	Scp 2	Scp 2	Scp 2	Scp 2	Scp 2	Scp 2	Scp 2
SiO_2	54.03	54.33	53.60	54.14	53.58	54.38	54.47	54.06	54.03	54.99
Al_2O_3	24.14	23.85	24.18	23.96	24.19	23.97	24.22	24.17	24.00	23.91
Fe_3O_4	0.12	0.30	0.15	0.11	0.47	0.22	0.14	0.11	0.13	0.18
MnO	0.01	0.01	0.02		0.01				0.01	0.02
K_2O	0.24	0.25	0.25	0.23	0.27	0.97	0.30	0.24	0.29	0.26
CaO	8.49	7.75	9.07	8.30	8.58	7.57	8.58	8.46	8.13	7.41
TiO_2	0.01			0.02	0.02	0.01	0.01			0.02
Na_2O	8.91	9.36	8.68	9.14	8.73	8.69	8.91	9.22	9.36	9.47
MgO			0.01		0.13					
SO_3	0.05		0.04		0.02	0.01	0.01	0.02	0.03	
Cl	2.64	3.01	2.62	2.98	2.70	2.63	2.78	2.72	2.91	3.06
F						0.01				
Soma	98.65	98.86	98.62	98.88	98.70	98.45	99.42	98.99	98.89	99.32
O=F	0	0	0	0	0	0.003	0	0	0	0
O=Cl	0.596	0.679	0.591	0.672	0.609	0.594	0.627	0.614	0.657	0.691
TOTAL	98.054	98.177	98.025	98.209	98.086	97.849	98.797	98.377	98.231	98.625
Fórmula (apfu)										
T_Si	7.479	7.502	7.437	7.479	7.428	7.543	7.483	7.466	7.469	7.543
T_Al^{IV}	4.521	4.498	4.563	4.521	4.572	4.457	4.517	4.534	4.531	4.457
TOTAL	12.000	12.000	12.000	12.000	12.000	12.000	12.000	12.000	12.000	12.000
M_Al^{VI}	-0.5828	-0.6164	-0.6085	-0.6206	-0.6203	-0.5393	-0.5951	-0.5996	-0.6209	-0.5917
M_Fe	0.013	0.031	0.015	0.011	0.049	0.023	0.015	0.011	0.013	0.019
M_Mn	0.001	0.001	0.002	0.000	0.002	0.000	0.000	0.000	0.002	0.002
M_K	0.043	0.044	0.044	0.041	0.047	0.171	0.053	0.041	0.050	0.045
M_Ca	1.259	1.147	1.348	1.228	1.274	1.125	1.263	1.252	1.204	1.089
M_Ti	0.001	0.000	0.000	0.002	0.002	0.001	0.001	0.000	0.000	0.002
M_Na	2.391	2.506	2.335	2.448	2.346	2.337	2.373	2.469	2.509	2.518
M_Mg	0.000	0.000	0.003	0.000	0.026	0.000	0.000	0.000	0.000	0.000
TOTAL	3.125	3.112	3.139	3.110	3.126	3.117	3.109	3.173	3.157	3.083
A_S	0.005	0.000	0.004	0.000	0.002	0.001	0.001	0.002	0.003	0.000
A_Cl	0.619	0.704	0.616	0.698	0.634	0.618	0.647	0.637	0.682	0.711
A_F	0.000	0.000	0.017	0.000	0.000	0.051	0.010	0.006	0.000	0.011
Eq An	50.695	49.923	52.086	50.706	52.410	48.581	50.553	51.121	51.029	48.564
Ma %	65.5	68.6	63.4	66.6	64.8	67.5	65.3	66.4	67.6	69.8
Me%	34.5	31.4	36.6	33.4	35.2	32.5	34.7	33.6	32.4	30.2

Apêndice E. Análises de química mineral por microssonda eletrônica em escapolita.

	JAT-15 (87,63)	JAT-15 (87,63)	JAT-15 (87,63)	JAT-15 (87,63)	JAT-15 (87,63)	JAT-15 (87,63)	JAT-15 (87,63)	JAT-15 (87,63)	JAT-15 (87,63)	JAT-15 (87,63)
	Scp_FBS	Scp_FBS	Scp_FBS	Scp_FBS	Scp_FBS	Scp_FBS	Scp_FBS	Scp_FBS	Scp_FBS	Scp_FBS
	Scp 3	Scp 3	Scp 3	Scp 3	Scp 3	Scp 3	Scp 3	Scp 3	Scp 3	Scp 3
Óxido (%)										
SiO_2	53.83	56.58	56.35	55.77	55.96	56.45	56.36	56.34	55.95	56.53
Al_2O_3	22.59	22.57	23.05	22.83	22.94	22.81	22.95	22.94	23.25	22.91
Fe_3O_4	2.50	0.06	0.09	0.40	0.03	0.07	0.05	0.02	0.12	0.15
MnO	0.01		0.01			0.01		0.01	0.01	0.01
K_2O	0.31	0.35	0.31	0.31	0.29	0.31	0.29	0.26	0.30	0.43
CaO	5.79	5.67	5.86	5.70	6.27	6.08	5.92	6.35	6.31	5.63
TiO_2			0.05	0.01	0.01		0.01	0.04		
Na_2O	9.55	10.61	10.40	9.78	10.54	10.47	10.52	10.35	10.28	10.67
MgO	0.74			0.08		0.00				
SO_3			0.03		0.01					0.01
Cl	3.12	3.60	3.32	3.18	3.40	3.37	3.31	3.50	3.29	3.45
F		0.02							0.00	
Soma	98.45	99.46	99.47	98.06	99.45	99.57	99.41	99.81	99.51	99.78
O=F	0	0.007	0	0	0	0	0	0	0	0
O=Cl	0.704	0.812	0.749	0.718	0.767	0.761	0.747	0.790	0.742	0.779
TOTAL	97.741	98.637	98.720	97.343	98.683	98.812	98.663	99.021	98.766	99.003
Fórmula (apfu)										
T_Si	7.490	7.722	7.689	7.708	7.656	7.703	7.699	7.672	7.645	7.698
T_Al^{IV}	4.510	4.278	4.311	4.292	4.344	4.297	4.301	4.328	4.355	4.302
TOTAL	12.000	12.000	12.000	12.000	12.000	12.000	12.000	12.000	12.000	12.000
M_Al^{VI}	-0.8053	-0.6484	-0.6044	-0.5741	-0.6454	-0.6292	-0.6067	-0.6473	-0.6104	-0.6254
M_Fe	0.262	0.006	0.009	0.041	0.003	0.007	0.005	0.002	0.012	0.015
M_Mn	0.002	0.000	0.001	0.000	0.000	0.001	0.000	0.001	0.001	0.001
M_K	0.055	0.061	0.053	0.055	0.051	0.054	0.051	0.046	0.052	0.074
M_Ca	0.863	0.829	0.857	0.844	0.919	0.889	0.866	0.926	0.924	0.821
M_Ti	0.000	0.000	0.005	0.001	0.001	0.000	0.001	0.004	0.000	0.000
M_Na	2.576	2.807	2.751	2.620	2.796	2.770	2.786	2.732	2.723	2.817
M_Mg	0.154	0.000	0.000	0.017	0.000	0.000	0.000	0.000	0.000	0.000
TOTAL	3.106	3.055	3.072	3.005	3.124	3.092	3.102	3.064	3.102	3.103
A_S	0.000	0.000	0.003	0.000	0.001	0.000	0.000	0.000	0.000	0.001
A_Cl	0.736	0.833	0.768	0.745	0.788	0.779	0.766	0.808	0.762	0.796
A_F	0.042	0.000	0.000	0.000	0.000	0.007	0.007	0.000	0.000	0.013
Eq An	50.323	42.614	43.701	43.082	44.803	43.241	43.374	44.283	45.153	43.401
Ma %	74.9	77.2	76.3	75.6	75.3	75.7	76.3	74.7	74.7	77.4
Me%	25.1	22.8	23.7	24.4	24.7	24.3	23.7	25.3	25.3	22.6

Apêndice F. Análises de química mineral por microssonda eletrônica em escapolita.

	JAT-15 (87,63)	JAT-15 (87,63)	JAT-15 (87,63)	JAT-15 (87,63)	JAT-15 (87,63)	JAT-15 (44,35)	JAT-15 (44,35)	JAT-15 (44,35)	JAT-15 (44,35)
	Scp_FBS	Scp_FBS	Scp_FBS	Scp_FBS	Scp_FBS	Scp_FBS	Scp_FBS	Scp_FBS	Scp_FBS
	Scp 3	Scp 3	Scp 3	Scp 3	Scp 3	Scp 4	Scp 4	Scp 4	Scp 4
Óxido (%)									
SiO_2	56.43	55.45	55.85	55.91	51.06	55.35	55.27	55.24	55.03
Al_2O_3	22.94	23.20	22.90	22.85	22.20	23.78	24.04	23.60	23.77
Fe_3O_4	0.01	0.07	0.33	0.34	6.29		0.08	0.01	
MnO		0.02	0.03				0.01	0.01	0.02
K_2O	0.34	0.31	0.34	0.33	0.30	0.46	0.31	0.32	0.32
CaO	5.93	6.60	6.43	5.88	5.13	7.36	7.63	7.26	7.59
TiO_2			0.01	0.01			0.01	0.02	
Na_2O	10.52	10.21	10.15	10.40	8.62	9.66	9.74	9.63	9.62
MgO			0.04	0.08	1.84				
SO_3	0.03	0.05		0.01	0.06	0.04			
Cl	3.34	3.41	3.27	3.54	2.83	2.91	3.09	2.97	2.99
F		0.01			0.01				0.01
Soma	99.54	99.33	99.34	99.34	98.34	99.56	100.19	99.06	99.34
O=F	0	0.003	0	0	0.004	0	0	0	0.004
O=Cl	0.754	0.770	0.738	0.799	0.639	0.657	0.697	0.670	0.675
TOTAL	98.791	98.554	98.606	98.540	97.693	98.901	99.492	98.387	98.663
Fórmula (apfu)									
T_Si	7.698	7.601	7.654	7.653	7.200	7.578	7.528	7.593	7.553
T_Al^{IV}	4.302	4.399	4.346	4.347	4.800	4.422	4.472	4.407	4.447
TOTAL	12.000	12.000	12.000	12.000	12.000	12.000	12.000	12.000	12.000
M_Al^{VI}	-0.6138	-0.6515	-0.6480	-0.6605	-1.1111	-0.5852	-0.6135	-0.5835	-0.6014
M_Fe	0.001	0.007	0.034	0.035	0.667	0.000	0.009	0.001	0.000
M_Mn	0.000	0.002	0.003	0.000	0.000	0.000	0.001	0.001	0.002
M_K	0.059	0.055	0.060	0.057	0.053	0.080	0.055	0.056	0.055
M_Ca	0.867	0.969	0.944	0.862	0.775	1.080	1.113	1.069	1.116
M_Ti	0.000	0.000	0.001	0.001	0.000	0.000	0.001	0.002	0.000
M_Na	2.782	2.713	2.697	2.760	2.356	2.564	2.572	2.566	2.560
M_Mg	0.000	0.000	0.008	0.016	0.387	0.000	0.000	0.000	0.000
TOTAL	3.095	3.095	3.098	3.071	3.128	3.138	3.137	3.112	3.132
A_S	0.003	0.005	0.000	0.001	0.006	0.004	0.000	0.000	0.000
A_Cl	0.772	0.792	0.759	0.821	0.676	0.675	0.713	0.692	0.696
A_F	0.018	0.000	0.009	0.000	0.000	0.017	0.000	0.000	0.000
Eq An	43.395	46.643	44.878	44.888	60.008	47.402	49.073	46.889	48.217
Ma %	76.2	73.7	74.1	76.2	75.3	70.4	69.8	70.6	69.6
Me%	23.8	26.3	25.9	23.8	24.7	29.6	30.2	29.4	30.4

Apêndice G. Análises de química mineral por microssonda eletrônica em escapolita.

	JAT-15 (44,35) Veio Scp 4	JAT-15 (44,35) Veio Scp 4	JAT-15 (44,35) Veio Scp 4	JAT-15 (44,35) Veio Scp 4	JAT-15 (44,35) Veio Scp 4	JAT-15 (44,35) Veio Scp 4	JAT-15 (44,35) Veio Scp 4	JAT-15 (44,35) Veio Scp 4	JAT-15 (44,35) Veio Scp 4	JAT-15 (44,35) Veio Scp 4
Óxido (%)										
SiO2	55.35	55.27	55.24	55.03	55.95	55.40	56.17	54.56	55.48	56.00
Al2O3	23.78	24.04	23.60	23.77	23.44	23.51	23.47	24.28	23.66	23.25
Fe3O4		0.08	0.01		0.11	0.07	0.08	0.05	0.04	0.05
MnO		0.01	0.01	0.02	0.01		0.03			0.01
K2O	0.46	0.31	0.32	0.32	0.38	0.54	0.33	0.34	0.38	0.36
CaO	7.36	7.63	7.26	7.59	7.19	7.07	6.92	8.21	7.34	6.88
TiO2		0.01	0.02		0.01			0.02		
Na2O	9.66	9.74	9.63	9.62	9.78	9.35	9.69	9.39	9.51	9.86
MgO										
SO3	0.04				0.05	0.14				
Cl	2.91	3.09	2.97	2.99	3.09	3.06	3.09	2.85	2.93	3.14
F				0.01			0.00	0.00		
Soma	99.56	100.19	99.06	99.34	100.02	99.14	99.78	99.69	99.34	99.55
O=F	0	0	0	0.004	0	0	0	0	0	0
O=Cl	0.657	0.697	0.670	0.675	0.697	0.691	0.697	0.643	0.661	0.709
TOTAL	98.901	99.492	98.387	98.663	99.323	98.453	99.082	99.048	98.681	98.837
Fórmula (apfu)										
T_Si	7.578	7.528	7.593	7.553	7.618	7.601	7.651	7.480	7.603	7.652
T_Al^{IV}	4.422	4.472	4.407	4.447	4.382	4.399	4.349	4.520	4.397	4.348
TTOTAL	12.000	12.000	12.000	12.000	12.000	12.000	12.000	12.000	12.000	12.000
M_Al^{VI}	-0.5852	-0.6135	-0.5835	-0.6014	-0.6210	-0.5974	-0.5816	-0.5973	-0.5753	-0.6040
M_Fe	0.000	0.009	0.001	0.000	0.011	0.007	0.008	0.005	0.004	0.005
M_Mn	0.000	0.001	0.001	0.002	0.002	0.000	0.003	0.000	0.000	0.001
M_K	0.080	0.055	0.056	0.055	0.067	0.095	0.058	0.059	0.067	0.063
M_Ca	1.080	1.113	1.069	1.116	1.049	1.039	1.010	1.206	1.078	1.007
M_Ti	0.000	0.001	0.002	0.000	0.001	0.000	0.000	0.002	0.000	0.000
M_Na	2.564	2.572	2.566	2.560	2.582	2.487	2.559	2.496	2.527	2.612
M_Mg	0.000	0.000	0.000	0.000	0.000	0.000	0.000	0.000	0.000	0.000
TTOTAL	3.138	3.137	3.112	3.132	3.090	3.032	3.056	3.170	3.100	3.084
A_S	0.004	0.000	0.000	0.000	0.005	0.014	0.000	0.000	0.000	0.000
A_Cl	0.675	0.713	0.692	0.696	0.713	0.712	0.713	0.662	0.681	0.727
A_F	0.017	0.000	0.000	0.000	0.019	0.000	0.000	0.035	0.009	0.015
Eq An	47.402	49.073	46.889	48.217	46.071	46.630	44.969	50.670	46.554	44.933
Ma %	70.4	69.8	70.6	69.6	71.1	70.5	71.7	67.4	70.1	72.2
Me%	29.6	30.2	29.4	30.4	28.9	29.5	28.3	32.6	29.9	27.8

Apêndice H. Análises de química mineral por microssonda eletrônica em escapolita.

	JAT-15 (44,35)	JAT-15 (44,35)	JAT-15 (44,35)	JAT-15 (44,35)	JAT-15 (44,35)	JAT-15 (44,35)	JAT-15 (44,35)	JAT-15 (44,35)	JAT-15 (44,35)
	Veio	Veio	Veio	Veio	Veio	Veio	Veio	Veio	Veio
	Scp 4	Scp 4	Scp 4	Scp 4	Scp 4	Scp 4	Scp 4	Scp 4	Scp 4
Óxido (%)									
SiO_2	56.24	56.22	55.76	54.94	55.62	55.82	55.37	55.60	55.28
Al_2O_3	23.33	23.26	23.21	23.65	23.57	23.23	24.03	23.36	23.99
Fe_3O_4	0.06	0.07	0.01	0.05	0.04	0.21	0.14	0.08	0.10
MnO	0.00	0.02	0.02	0.02	0.03	0.02		0.02	
K_2O	0.38	0.48	0.52	0.38	0.43	0.50	0.32	0.43	0.39
CaO	6.92	6.60	7.16	7.57	7.39	6.46	7.69	7.40	7.76
TiO_2		0.02			0.04	0.01	0.01		
Na_2O	9.95	9.77	9.70	9.46	9.64	8.82	9.37	9.43	9.34
MgO						0.06			
SO_3	0.04	0.01		0.01	0.05				0.02
Cl	3.18	3.05	3.05	3.02	2.94	2.76	2.71	2.85	2.89
F	0.01		0.00		0.01			0.01	
Soma	100.10	99.49	99.43	99.10	99.75	97.89	99.64	99.17	99.76
O=F	0.002	0	0	0	0.005	0	0	0.002	0
O=Cl	0.718	0.688	0.688	0.682	0.663	0.623	0.612	0.643	0.652
TOTAL	99.384	98.803	98.742	98.416	99.082	97.272	99.029	98.526	99.109
Fórmula (apfu)									
T_Si	7.644	7.679	7.640	7.559	7.598	7.720	7.571	7.634	7.554
T_Al^{IV}	4.356	4.321	4.360	4.441	4.402	4.280	4.429	4.366	4.446
TOTAL	12.000	12.000	12.000	12.000	12.000	12.000	12.000	12.000	12.000
M_Al^{VI}	-0.6195	-0.5768	-0.6115	-0.6055	-0.6076	-0.4940	-0.5562	-0.5856	-0.5826
M_Fe	0.006	0.007	0.001	0.005	0.004	0.022	0.014	0.008	0.010
M_Mn	0.000	0.002	0.002	0.002	0.003	0.002	0.000	0.002	0.000
M_K	0.065	0.084	0.092	0.067	0.075	0.089	0.056	0.075	0.067
M_Ca	1.008	0.966	1.051	1.116	1.082	0.957	1.127	1.089	1.136
M_Ti	0.000	0.002	0.000	0.000	0.004	0.001	0.002	0.000	0.000
M_Na	2.622	2.587	2.577	2.523	2.553	2.365	2.484	2.510	2.474
M_Mg	0.000	0.000	0.000	0.000	0.000	0.013	0.000	0.000	0.000
TOTAL	3.082	3.071	3.111	3.107	3.113	2.955	3.126	3.099	3.105
A_S	0.004	0.001	0.000	0.001	0.005	0.000	0.000	0.000	0.002
A_Cl	0.732	0.706	0.708	0.704	0.681	0.647	0.628	0.663	0.669
A_F	0.000	0.000	0.000	0.041	0.000	0.027	0.034	0.000	0.000
Eq An	45.210	44.031	45.318	48.018	46.735	42.671	47.620	45.522	48.200
Ma %	72.2	72.8	71.0	69.3	70.2	71.2	68.8	69.8	68.5
Me%	27.8	27.2	29.0	30.7	29.8	28.8	31.2	30.2	31.5

Apêndice I. Análises de química mineral por microssonda eletrônica em anfibólio.

	JAT-21 (64,80)	JAT-21 (64,80)	JAT-21 (64,80)	JAT-21 (64,80)	JAT-21 (64,80)	JAT-21 (64,80)	JAT-21 (64,80)	JAT-21 (64,80)	JAT-21 (64,80)	JAT-21 (64,80)
	DIABÁSIO	DIABÁSIO	DIABÁSIO	DIABÁSIO	DIABÁSIO	DIABÁSIO	DIABÁSIO	DIABÁSIO	DIABÁSIO	DIABÁSIO
	Anf 2/	Anf 2/	Anf 2/	Anf 2/	Anf 2/	Anf 2/	Anf 2/	Anf 2/	Anf 2/	Anf 2/
	Fe-Pg	Fe-Pg	Fe-Pg	Fe-Pg	Fe-Pg	Fe-Pg	Fe-Pg	Fe-Pg	Fe-Pg	Fe-Pg
Óxido (wt%)										
SiO_2	36.45	37.33	36.73	36.89	38.63	37.33	37.16	37.95	38.01	38.52
TiO_2	0.03	0.24	0.26	0.20	0.22	0.11	0.14	0.09	0.12	0.25
Al_2O_3	17.04	15.22	15.76	16.21	14.11	13.80	14.61	10.03	14.82	15.00
MnO	0.10	0.11	0.09	0.10	0.12	0.05	0.09	0.06	0.08	0.09
FeO	22.86	23.60	24.04	23.42	22.56	24.50	23.39	20.87	23.33	22.36
ZnO	0.02	0.01		0.02					0.03	
MgO	4.15	4.85	4.43	4.43	5.66	4.67	5.12	7.33	5.32	5.56
CaO	11.38	11.12	11.22	11.12	11.36	11.20	11.05	13.74	11.36	11.22
Na_2O	1.47	1.51	1.66	1.68	1.44	1.43	1.61	0.74		1.63
K_2O	1.95	1.89	1.70	1.66	1.63	2.19	1.73	1.73	1.66	1.40
F	0.00	0.01		0.00	0.01	0.00		0.17	0.01	
Cl	2.96	2.95	2.97	2.93	2.60	3.32	2.84	2.39	2.59	2.55
O=F,Cl	-0.67	-0.67	-0.67	-0.66	-0.59	-0.75	-0.64	-0.61	-0.59	-0.58
TOTAL	97.74	98.17	98.18	97.99	97.75	97.85	97.10	94.48	96.74	98.00
Fórmula (apfu)										
Si	5.794	5.905	5.823	5.842	6.081	5.994	5.932	6.121	5.985	6.026
Al	2.206	2.095	2.177	2.158	1.919	2.006	2.068	1.879	2.015	1.974
T subtotal	8.000	8.000	8.000	8.000	8.000	8.000	8.000	8.000	8.000	8.000
Ti	0.004	0.029	0.031	0.023	0.026	0.014	0.017	0.011	0.014	0.030
Al	0.987	0.743	0.767	0.867	0.698	0.606	0.681	0.028	0.735	0.792
Fe3+	0.428	0.572	0.595	0.515	0.492	0.557	0.619	1.242	0.918	0.476
Zn	0.002	0.001		0.002					0.003	
Fe2+	2.595	2.512	2.560	2.547	2.456	2.706	2.464	1.574	2.081	2.406
Mg	0.983	1.144	1.047	1.046	1.328	1.118	1.219	1.763	1.249	1.297
C subtotal	4.999	5.001	5.000	5.000	5.000	5.001	5.000	4.626	5.000	5.001
Mn2+	0.013	0.015	0.012	0.014	0.017	0.007	0.012		0.011	0.012
Fe2+	0.016	0.039	0.032	0.039	0.023	0.027	0.040		0.073	0.044
Ca	1.938	1.885	1.906	1.887	1.916	1.927	1.890	2.000	1.916	1.881
Na	0.033	0.061	0.050	0.060	0.045	0.039	0.059			0.064
B subtotal	2.000	2.000	2.000	2.000	2.001	2.000	2.001	2.000	2.000	2.001
Ca	0.000	0.000	0.000	0.000	0.000	0.000	0.000	0.375	0.000	0.000
Na	0.420	0.402	0.460	0.455	0.395	0.406	0.440	0.231		0.431
K	0.395	0.381	0.344	0.335	0.327	0.449	0.352	0.356	0.333	0.279
A subtotal	0.815	0.783	0.804	0.790	0.722	0.855	0.792	0.962	0.333	0.710
O (non-W)	22.000	22.000	22.000	22.000	22.000	22.000	22.000	22.000	22.000	22.000
OH	1.202	1.203	1.202	1.214	1.303	1.096	1.232	1.262	1.304	1.324
F	0.001	0.006			0.003	0.001		0.084	0.004	
Cl	0.797	0.791	0.798	0.786	0.694	0.903	0.768	0.653	0.691	0.676
W subtotal	2.000	2.000	2.000	2.000	2.000	2.000	2.000	1.999	1.999	2.000
Sum T,C,B,A	15.814	15.784	15.804	15.790	15.723	15.856	15.793	15.588	15.333	15.712

Apêndice J. Análises de química mineral por microssonda eletrônica em anfibólio.

	JAT-32 (383,00)	JAT-32 (383,00)	JAT-32 (383,00)	JAT-32 (383,00)	JAT-32 (383,00)	JAT-32 (383,00)	JAT-32 (383,00)	JAT-32 (383,00)
	Anf 3-ZC/	Anf 3-ZC/	Anf 3-ZC/	Anf 3-ZC/	Anf 3-ZC/	Anf 3-ZC/	Anf 3-ZC/	Anf 3-ZC/
	Act II	Act II	Act II	Act II	Act II	Act II	Act II	Act II
Óxido (wt%)								
SiO_2	56.10	54.22	55.61	56.24	55.96	55.74	55.83	55.84
TiO_2	0.13	0.03	0.00	0.03	0.06	0.08		0.02
Al_2O_3	0.27	0.78	0.18	0.24	0.25	0.18	0.39	0.24
MnO	0.08	0.08	0.09	0.10	0.10	0.09	0.07	0.10
FeO	11.07	13.81	10.79	10.84	10.49	10.23	10.76	10.25
NiO	0.01	0.01	0.00	0.03	0.00	0.01	0.00	0.04
ZnO			0.03	0.02	0.01			0.01
MgO	18.45	16.35	18.51	18.36	18.38	18.42	17.85	18.51
CaO	12.29	12.27	12.48	12.37	12.52	12.37	12.28	12.42
Na_2O	0.11	0.12	0.09	0.11	0.07	0.07	0.13	0.07
K_2O	0.03	0.25	0.02	0.00	0.03	0.00	0.03	
F	0.05	0.05	0.08	0.05	0.08	0.06	0.06	0.08
Cl	0.03	0.16	0.00	0.03	0.00	0.05	0.00	0.02
O=F,Cl	-0.03	-0.06	-0.03	-0.03	-0.03	-0.04	-0.03	-0.04
TOTAL	98.60	98.07	97.84	98.40	97.93	97.27	97.39	97.56
Formula (apfu)								
Si	7.891	7.788	7.870	7.923	7.915	7.930	7.953	7.917
Al	0.046	0.131	0.029	0.041	0.042	0.031	0.047	0.040
Ti	0.014	0.003		0.003	0.006	0.009		0.002
Fe3+	0.049	0.077	0.100	0.033	0.037	0.031		0.041
T subtotal	8.000	7.999	7.999	8.000	8.000	8.001	8.000	8.000
Ti	0.000	0.000	0.000	0.000	0.000	0.000	0.000	0.000
Al	0.000	0.000	0.000	0.000	0.000	0.000	0.019	0.000
Fe3+	0.089	0.162	0.127	0.073	0.073	0.061	0.035	0.081
Ni	0.002	0.002		0.003		0.001		0.004
Fe2+	1.040	1.335	0.965	1.066	1.051	1.031	1.155	1.001
Mg	3.869	3.501	3.905	3.856	3.875	3.906	3.791	3.912
C subtotal	5.000	5.000	5.000	5.000	5.000	4.999	5.000	4.999
Mn2+	0.010	0.010	0.010	0.012	0.012	0.011	0.008	0.013
Fe2+	0.124	0.085	0.085	0.105	0.080	0.094	0.092	0.092
Ca	1.852	1.888	1.892	1.867	1.897	1.886	1.874	1.887
Na	0.014	0.017	0.012	0.016	0.010	0.010	0.025	0.009
B subtotal	2.000	2.000	1.999	2.000	1.999	2.001	1.999	2.001
Ca	0.000	0.000	0.000	0.000	0.000	0.000	0.000	0.000
Na	0.014	0.017	0.012	0.016	0.010	0.010	0.011	0.009
K	0.006	0.046	0.003	0.001	0.006	0.001	0.006	
A subtotal	0.020	0.063	0.015	0.017	0.016	0.011	0.017	0.009
O (non-W)	22.000	22.000	22.000	22.000	22.000	22.000	22.000	22.000
OH	1.969	1.941	1.965	1.970	1.965	1.961	1.971	1.958
F	0.023	0.021	0.035	0.022	0.035	0.027	0.029	0.037
Cl	0.007	0.038	0.000	0.008	0.000	0.012	0.000	0.005
W subtotal	1.999	2.000	2.000	2.000	2.000	2.000	2.000	2.000
Sum T,C,B,A	15.020	15.062	15.013	15.017	15.015	15.012	15.016	15.009

Apêndice K. Análises de química mineral por microssonda eletrônica em anfibólio.

	JAT-28 (54,22)	JAT-28 (54,22)	JAT-28 (54,22)	JAT-28 (54,22)	JAT-28 (54,22)	JAT-28 (54,22)	JAT-28 (54,22)	JAT-28 (54,22)
	Anf-4/ZC	Anf-4/ZC	Anf-4/ZC	Anf-4/ZC	Anf-4/ZC	Anf-4/ZC	Anf-4/ZC	Anf-4/ZC
	Hast I	Hast I	Hast I	Hast I	Hast I	Hast I	Hast I	Hast I
Óxido (wt%)								
SiO_2	42.18	39.44	40.86	48.91	38.07	46.09	38.35	48.52
TiO_2	0.15	0.10	0.18	0.08	0.30	0.16	0.10	0.06
Al_2O_3	10.64	13.00	12.33	4.19	12.69	7.19	13.20	4.63
MnO	0.10	0.10	0.07	0.26	0.10	0.14	0.09	0.27
FeO	22.65	24.83	24.29	24.38	25.37	22.69	25.38	24.87
ZnO	0.01	0.03	0.01	0.02				
MgO	7.81	5.67	5.53	12.90	5.37	10.45	5.08	12.38
CaO	10.96	10.91	10.40	4.94	10.62	8.36	10.75	4.61
Na_2O	1.57	2.08	1.98	0.64	2.00	1.18	2.03	0.79
K_2O	0.87	1.03	1.17	0.31	1.12	0.49	1.18	0.34
F	0.02		0.01	0.00	0.01			
Cl	1.81	2.09	2.17	0.66	2.38	1.07	2.34	0.77
O=F,Cl (calc)	-0.42	-0.47	-0.49	-0.15	-0.54	-0.24	-0.53	-0.17
TOTAL	98.35	98.82	98.51	97.13	97.49	97.58	97.97	97.07
Fórmula (apfu)								
Si	6.459	6.132	6.389	7.361	6.037	6.952	6.056	7.336
Al	1.541	1.868	1.611	0.639	1.963	1.048	1.944	0.664
T subtotal	8.000	8.000	8.000	8.000	8.000	8.000	8.000	8.000
Ti	0.017	0.012	0.022	0.009	0.036	0.019	0.012	0.007
Al	0.380	0.514	0.661	0.104	0.408	0.230	0.513	0.161
Fe3+	0.704	0.694	0.274	0.457	0.850	0.683	0.740	0.423
Zn	0.001	0.004	0.001	0.002				
Fe2+	2.115	2.462	2.754	1.533	2.436	1.719	2.539	1.619
Mg	1.783	1.314	1.289	2.894	1.269	2.350	1.196	2.790
C subtotal	5.000	5.000	5.001	4.999	4.999	5.001	5.000	5.000
Mn2+	0.013	0.013	0.010	0.033	0.014	0.017	0.012	0.035
Fe2+	0.081	0.072	0.148	1.078	0.078	0.461	0.073	1.103
Ca	1.798	1.817	1.742	0.797	1.804	1.351	1.819	0.747
Na	0.107	0.097	0.100	0.092	0.104	0.171	0.096	0.115
B subtotal	1.999	1.999	2.000	2.000	2.000	2.000	2.000	2.000
Ca	0.000	0.000	0.000	0.000	0.000	0.000	0.000	0.000
Na	0.359	0.530	0.500	0.094	0.511	0.175	0.525	0.117
K	0.171	0.204	0.233	0.059	0.227	0.094	0.238	0.065
A subtotal	0.530	0.734	0.733	0.153	0.738	0.269	0.763	0.182
O (non-W)	22.000	22.000	22.000	22.000	22.000	22.000	22.000	22.000
OH	1.522	1.449	1.421	1.831	1.355	1.726	1.374	1.803
F	0.008		0.004	0.001	0.005			
Cl	0.470	0.551	0.575	0.168	0.640	0.274	0.626	0.197
W subtotal	2.000	2.000	2.000	2.000	2.000	2.000	2.000	2.000
Sum T,C,B,A	15.529	15.733	15.734	15.152	15.737	15.270	15.763	15.182

Apêndice I. Análises de química mineral por microssonda eletrônica em anfibólio.

	JAT-15 (44,35)	JAT-15 (44,35)	JAT-15 (44,35)	JAT-15 (44,35)	JAT-15 (44,35)	JAT-15 (44,35)
	Anf-5/Vênulas	Anf-5/Vênulas	Anf-5/Vênulas	Anf-5/Vênulas	Anf-5/Vênulas	Anf-5/Vênulas
	Hst II	Hst II	Hst II	Hst II	Hst II	Hst II
Óxido (wt%)						
SiO_2	37.66	36.69	37.76	37.76	37.49	37.47
TiO_2	0.06	0.20	0.24	0.26	0.17	0.20
Al_2O_3	12.80	13.52	13.09	12.64	12.97	13.02
MnO	0.12	0.12	0.11	0.12	0.10	0.10
FeO	27.00	27.33	26.89	27.18	27.26	26.85
ZnO	0.01					
MgO	4.23	3.69	4.17	4.01	3.88	3.95
CaO	10.90	10.87	10.88	11.03	11.01	10.90
Na_2O	2.00	2.04	1.93	1.86	1.89	1.84
K_{2O}	1.38	1.51	1.39	1.39	1.51	1.60
F		0.01				0.01
Cl	3.19	3.39	3.02	3.19	3.23	3.35
O=F,Cl (calc)	-0.72	-0.77	-0.68	-0.72	-0.73	-0.76
TOTAL	98.63	98.60	98.81	98.72	98.78	98.53
Formula (apfu)						
Si	6.015	5.898	6.005	6.035	5.999	6.012
Al	1.985	2.102	1.995	1.965	2.001	1.988
T subtotal	8.000	8.000	8.000	8.000	8.000	8.000
Ti	0.007	0.025	0.029	0.031	0.020	0.024
Al	0.425	0.460	0.459	0.416	0.445	0.474
Fe3+	0.789	0.783	0.757	0.746	0.741	0.702
Zn	0.002					
Fe2+	2.770	2.848	2.767	2.851	2.868	2.856
Mg	1.007	0.884	0.989	0.955	0.926	0.945
C subtotal	5.000	5.000	5.001	4.999	5.000	5.001
Mn2+	0.016	0.016	0.015	0.017	0.014	0.014
Fe2+	0.047	0.043	0.053	0.035	0.039	0.045
Ca	1.865	1.872	1.854	1.889	1.888	1.874
Na	0.072	0.068	0.078	0.059	0.060	0.067
B subtotal	2.000	1.999	2.000	2.000	2.001	2.000
Ca	0.000	0.000	0.000	0.000	0.000	0.000
Na	0.548	0.568	0.517	0.517	0.526	0.505
K	0.281	0.310	0.282	0.283	0.308	0.327
A subtotal	0.829	0.878	0.799	0.800	0.834	0.832
O (non-W)	22.000	22.000	22.000	22.000	22.000	22.000
OH	1.137	1.071	1.186	1.136	1.124	1.086
F		0.005				0.003
Cl	0.863	0.924	0.814	0.864	0.876	0.911
W subtotal	2.000	2.000	2.000	2.000	2.000	2.000
Sum T,C,B,A	15.829	15.877	15.800	15.799	15.835	15.833

Apêndice L. Análises de química mineral por microssonda eletrônica em biotita.

	JAT-21 (64,80) Diabásio Bt 1	JAT-21 (64,80) Diabásio Bt 1	JAT-21 (64,80) Diabásio Bt 1	JAT-21 (64,80) Diabásio Bt 1	JAT-21 (64,80) Diabásio Bt 1	JAT-21 (64,80) Diabásio Bt 1	JAT-21 (64,80) Diabásio Bt 1	JAT-21 (64,80) Diabásio Bt 1	JAT-21 (64,80) Diabásio Bt 1	JAT-21 (64,80) Diabásio Bt 1	JAT-21 (64,80) Diabásio Bt 1
Óxido (%)											
FeOT	22.90	24.880	24.88	17.91	13.96	21.69	21.68	24	23.61	23.97	23.78
SiO_2	35.34	33.63	33.21	32.21	43.51	34.88	35.29	34.75	34.84	35.06	33.00
TiO_2	1.61	1.04	1.57	10.75	0.86	1.57	1.80	1.45	1.63	1.47	1.45
Al_2O_3	15.24	14.95	14.76	11.57	19.21	14.78	15.07	14.71	14.90	14.88	14.21
FeO	19.54	20.32	20.64	16.40	6.81	18.12	18.52	20.30	20.18	20.41	19.73
Fe_2O_3	3.74	5.06	4.71	1.68	7.95	3.96	3.51	4.11	3.81	3.96	4.50
MnO	0.05	0.07	0.07	0.05	0.02	0.04	0.05		0.04	0.07	0.02
MgO	9.88	9.47	9.78	7.52	4.86	11.19	11.01	9.55	9.74	9.80	9.58
CaO	0.07	0.46	0.09	7.71	3.40	0.13	0.05	0.17	0.08	0.11	0.53
Na_2O	0.16	0.17	0.12	0.08	4.63	0.25	0.19	0.08	0.13	0.10	0.16
K_2O	9.11	8.13	8.38	5.67	5.23	9.08	9.28	9.18	9.44	9.33	9.19
ZnO	0.01		0.02	0.0005		0.0334		0.0214	0.0131	0.0207	0.0077
F	0.01			0.01						0.01	
Cl	1.38	1.19	1.23	0.81	1.89	1.44	1.49	1.35	1.35	1.53	1.40
Li_2O	0.59	0.10			2.94	0.46	0.58	0.42	0.45	0.51	
H_2O	3.46	3.36	3.34	3.57	3.76	3.42	3.45	3.40	3.43	3.40	3.25
Subtotal	100.18	97.95	97.93	98.02	105.05	99.36	100.29	99.50	100.03	100.66	97.03
O=F,Cl	0.31	0.27	0.28	0.19	0.43	0.32	0.34	0.30	0.30	0.35	0.32
TOTAL	99.86	97.69	97.65	97.83	104.63	99.03	99.95	99.19	99.73	100.31	96.72
Fórmula (apfu)											
Si	5.562	5.506	5.447	5.113	6.152	5.531	5.525	5.563	5.535	5.546	5.484
Al iv	2.438	2.494	2.553	2.165	1.848	2.469	2.475	2.437	2.465	2.454	2.516
Al vi	0.389	0.391	0.301	0.000	1.354	0.293	0.306	0.339	0.325	0.320	0.267
Ti	0.191	0.128	0.194	1.283	0.091	0.187	0.212	0.175	0.195	0.175	0.181
Fe2	2.571	2.783	2.832	2.177	0.805	2.404	2.425	2.718	2.682	2.700	2.742
Fe3	0.148	0.208	0.194	0.067	0.282	0.158	0.138	0.165	0.152	0.157	0.188
Mn	0.006	0.010	0.010	0.006	0.002	0.005	0.007	0.000	0.005	0.009	0.003
Mg	2.318	2.311	2.391	1.779	1.024	2.645	2.570	2.279	2.307	2.311	2.373
Zn	0.001	0.000	0.003	0.000	0.000	0.004	0.000	0.003	0.002	0.002	0.001
Li*	0.374	0.066	0.000	0.000	1.669	0.292	0.363	0.271	0.286	0.325	0.000
Ca	0.011	0.081	0.016	1.311	0.515	0.022	0.009	0.029	0.014	0.019	0.094
Na	0.050	0.053	0.038	0.023	1.269	0.078	0.056	0.026	0.040	0.032	0.053
K	1.829	1.698	1.753	1.148	0.943	1.837	1.853	1.874	1.913	1.883	1.948
OH*	3.629	3.670	3.658	3.777	3.547	3.613	3.605	3.634	3.636	3.585	3.606
F	0.003	0.000	0.000	0.005	0.000	0.000	0.000	0.000	0.000	0.004	0.000
Cl	0.368	0.330	0.342	0.219	0.453	0.387	0.395	0.366	0.364	0.410	0.394
TOTAL	19.887	19.728	19.731	19.074	19.956	19.925	19.940	19.878	19.919	19.933	19.850

Apêndice M. Análises de química mineral por microssonda eletrônica em biotita.

	JAT-21 (64,80) Diabásio Bt 1	JAT-21 (64,80) Diabásio Bt 1	JAT-21 (64,80) Diabásio Bt 1	JAT-21 (64,80) Diabásio Bt 1	JAT-21 (64,80) Diabásio Bt 1	JAT-21 (64,80) Diabásio Bt 1	JAT-21 (64,80) Diabásio Bt 1	JAT-21 (64,80) Diabásio Bt 1	JAT-21 (64,80) Diabásio Bt 1	JAT-21 (64,80) Diabásio Bt 1	JAT-21 (64,80) Diabásio Bt 1	JAT-21 (64,80) Diabásio Bt 1	JAT-21 (64,80) Diabásio Bt 1
Óxido (%)													
FeOT	23.71	22.91	22.01	24.16	24.2	22.89	23.38	23.97	23.81	22.57	23.29	23.15	24.64
SiO2	34.51	33.47	34.85	33.44	33.87	33.54	34.62	34.44	32.02	34.98	35.00	34.72	34.66
TiO2	1.71	1.07	0.99	1.15	1.24	0.83	1.14	1.38	0.99	1.74	1.40	1.46	1.65
Al2O3	14.76	14.54	15.48	15.13	15.19	16.26	15.51	14.37	15.42	15.34	15.30	15.08	15.13
FeO	20.24	18.96	18.44	20.44	20.53	18.27	19.83	20.26	18.95	19.63	19.84	19.66	21.06
Fe2O3	3.86	4.39	3.97	4.13	4.08	5.14	3.95	4.13	5.40	3.26	3.83	3.88	3.98
MnO	0.03	0.03	0.02	0.06	0.08	0.05	0.02	0.05	0.02	0.06	0.06	0.03	0.06
MgO	9.87	10.37	10.41	9.42	9.41	11.09	10.08	9.31	11.35	10.32	10.35	10.20	8.69
CaO	0.05	0.16	0.76	0.09	0.06	0.22	0.11	0.13	0.13	0.08	0.07	0.12	0.09
Na2O	0.12	0.18	0.13	0.07	0.06	0.15	0.11	0.09	0.04	0.06	0.09	0.10	0.09
K2O	9.44	9.26	9.00	9.32	9.18	6.65	9.18	9.45	6.88	9.62	9.17	9.17	9.04
ZnO			0.0409	0.02	0.02		0.02				0.04	0.01	
F												0.02	
Cl	1.47	1.60	1.44	1.30	1.29	1.00	1.47	1.47	1.05	1.44	1.40	1.29	1.35
Li2O	0.35	0.05	0.45	0.05	0.17	0.07	0.38	0.33		0.49	0.49	0.41	0.40
H2O	3.38	3.24	3.41	3.33	3.37	3.44	3.40	3.33	3.34	3.45	3.45	3.43	3.40
Subtotal	99.79	97.32	99.40	97.94	98.54	96.71	99.82	98.73	95.58	100.47	100.50	99.58	99.60
O=F,Cl	0.33	0.36	0.32	0.29	0.29	0.23	0.33	0.33	0.24	0.32	0.32	0.30	0.30
TOTAL	99.46	96.96	99.07	97.64	98.25	96.49	99.49	98.40	95.34	100.15	100.18	99.28	99.29
Fórmula (apfu)													
Si	5.513	5.511	5.530	5.478	5.496	5.440	5.505	5.584	5.330	5.495	5.512	5.522	5.549
Al iv	2.487	2.489	2.470	2.522	2.504	2.560	2.495	2.416	2.670	2.505	2.488	2.478	2.451
Al vi	0.293	0.333	0.426	0.399	0.401	0.549	0.412	0.330	0.355	0.336	0.352	0.348	0.405
Ti	0.205	0.133	0.119	0.142	0.151	0.102	0.136	0.168	0.123	0.206	0.166	0.175	0.199
Fe2	2.704	2.611	2.447	2.801	2.786	2.478	2.637	2.746	2.639	2.579	2.613	2.615	2.820
Fe3	0.155	0.181	0.158	0.170	0.166	0.209	0.157	0.168	0.225	0.129	0.151	0.155	0.160
Mn	0.004	0.005	0.003	0.008	0.011	0.007	0.003	0.007	0.003	0.008	0.008	0.005	0.008
Mg	2.351	2.545	2.463	2.300	2.276	2.681	2.389	2.250	2.816	2.417	2.430	2.418	2.074
Zn	0.000	0.000	0.005	0.002	0.003	0.000	0.002	0.000	0.000	0.000	0.005	0.001	0.000
Li*	0.226	0.036	0.287	0.030	0.110	0.048	0.246	0.217	0.000	0.308	0.312	0.264	0.255
Ca	0.008	0.028	0.130	0.015	0.010	0.039	0.019	0.023	0.022	0.013	0.011	0.020	0.015
Na	0.038	0.056	0.040	0.021	0.017	0.046	0.033	0.028	0.012	0.018	0.029	0.030	0.029
K	1.924	1.945	1.822	1.947	1.900	1.376	1.862	1.954	1.461	1.928	1.842	1.860	1.846
OH*	3.602	3.553	3.613	3.639	3.645	3.725	3.604	3.596	3.704	3.617	3.626	3.644	3.634
F	0.000	0.000	0.000	0.000	0.000	0.000	0.000	0.000	0.000	0.000	0.000	0.008	0.000
Cl	0.398	0.447	0.387	0.361	0.355	0.275	0.396	0.404	0.296	0.383	0.374	0.348	0.366
TOTAL	19.908	19.873	19.899	19.834	19.831	19.535	19.897	19.891	19.657	19.941	19.918	19.890	19.810

Apêndice N. Análises de química mineral por microssonda eletrônica em biotita.

	JAT-3 (130,05) MVM Bt 1	JAT-3 (130,05) MVM Bt 1	JAT-3 (130,05) MVM Bt 1	JAT-3 (130,05) MVM Bt 1	JAT-3 (130,05) MVM Bt 1	JAT-3 (130,05) MVM Bt 1	JAT-3 (130,05) MVM Bt 1	JAT-3 (130,05) MVM Bt 1	JAT-3 (130,05) MVM Bt 1	JAT-3 (130,05) MVM Bt 1
Óxido (%)										
FeOT	29.3	28.38	26.33	25.98	27.32	26.72	25.88	25.22	29.99	30.5
SiO2	31.38	32.22	33.64	34.22	33.77	33.57	33.49	33.83	31.24	31.13
TiO2	1.01	0.96	1.01	1.06	0.97	1.00	0.86	0.88	0.99	0.93
Al2O3	15.17	15.01	15.23	15.83	15.00	14.97	15.56	15.93	14.96	15.11
FeO	23.20	22.87	21.76	22.09	22.87	22.19	21.61	21.22	23.67	23.95
Fe2O3	6.78	6.12	5.08	4.33	4.94	5.03	4.75	4.44	7.02	7.28
MnO	0.02	0.03		0.02	0.02	0.02	0.07	0.02	0.03	0.04
MgO	9.61	9.45	9.96	9.39	8.62	9.49	9.45	9.87	9.10	9.21
CaO	0.02	0.07		0.04	0.01	0.02		0.04	0.02	0.03
Na2O	0.01	0.02	0.05	0.03	0.03	0.01	0.07	0.09	0.03	0.04
K2O	5.91	7.01	8.19	8.95	8.78	8.48	8.62	8.84	5.81	5.47
ZnO	0.07	0.03	0.03	0.04					0.06	0.01
F	0.01									
Cl	1.05	1.34	1.68	1.60	1.61	1.48	1.67	1.63	1.15	1.11
Li2O			0.10	0.27	0.14	0.08	0.06	0.16		
H2O	3.31	3.27	3.28	3.37	3.28	3.31	3.27	3.33	3.26	3.27
Subtotal	97.55	98.40	100.01	101.23	100.04	99.67	99.48	100.29	97.35	97.59
O=F,Cl	0.24	0.30	0.38	0.36	0.36	0.33	0.38	0.37	0.26	0.25
TOTAL	97.31	98.10	99.63	100.87	99.68	99.34	99.10	99.92	97.09	97.34
Fórmula (apfu)										
Si	5.260	5.348	5.435	5.436	5.491	5.457	5.438	5.417	5.276	5.249
Al iv	2.740	2.652	2.565	2.564	2.509	2.543	2.562	2.583	2.724	2.751
Al vi	0.257	0.284	0.335	0.400	0.366	0.325	0.417	0.424	0.254	0.251
Ti	0.127	0.119	0.123	0.127	0.119	0.122	0.105	0.106	0.126	0.118
Fe2	3.252	3.175	2.940	2.934	3.110	3.017	2.935	2.842	3.344	3.378
Fe3	0.285	0.255	0.206	0.172	0.202	0.205	0.193	0.178	0.297	0.308
Mn	0.003	0.004	0.000	0.002	0.002	0.003	0.010	0.003	0.005	0.006
Mg	2.401	2.338	2.399	2.224	2.089	2.300	2.288	2.356	2.291	2.315
Zn	0.009	0.003	0.003	0.005	0.000	0.000	0.000	0.000	0.008	0.002
Li*	0.000	0.000	0.067	0.172	0.092	0.054	0.039	0.101	0.000	0.000
Ca	0.003	0.013	0.000	0.007	0.002	0.004	0.000	0.007	0.003	0.005
Na	0.004	0.007	0.016	0.010	0.009	0.004	0.022	0.029	0.010	0.014
K	1.264	1.484	1.688	1.814	1.821	1.758	1.785	1.806	1.252	1.176
OH*	3.699	3.623	3.540	3.569	3.556	3.592	3.540	3.558	3.671	3.683
F	0.003	0.000	0.000	0.000	0.000	0.000	0.000	0.000	0.000	0.000
Cl	0.298	0.377	0.460	0.431	0.444	0.408	0.460	0.442	0.329	0.317
TOTAL	19.606	19.683	19.775	19.866	19.812	19.793	19.794	19.852	19.591	19.573

Apêndice O. Análises de química mineral por microssonda eletrônica em biotita.

	JAT-28 (160,40) MIN-I Bt 1	JAT-28 (160,40) MIN-I Bt 1	JAT-28 (160,40) MIN-I Bt 1	JAT-28 (160,40) MIN-I Bt 1	JAT-28 (160,40) MIN-I Bt 1	JAT-28 (160,40) MIN-I Bt 1	JAT-28 (160,40) MIN-I Bt 1	JAT-28 (160,40) MIN-I Bt 1
Óxido (%)								
FeOT	24.99	26.47	25.78	28.17	28.46	25.63	26.12	26.67
SiO2	34.49	33.64	34.47	32.93	31.60	34.06	35.12	33.94
TiO2	1.30	1.17	1.24	1.07	1.10	1.21	1.10	1.22
Al2O3	13.79	13.82	14.04	14.43	13.76	13.72	14.72	13.83
FeO	20.78	21.60	21.43	22.48	22.54	21.09	21.77	21.93
Fe2O3	4.68	5.41	4.84	6.32	6.58	5.04	4.84	5.27
MnO	0.04	0.01	0.01	0.04		0.01	0.03	0.01
MgO	10.20	9.89	9.52	9.61	9.08	9.82	9.14	9.45
CaO	0.01	0.04			0.08	0.02	0.06	
Na2O	0.08	0.14	0.10	0.12	0.13	0.13	0.14	0.09
K2O	9.23	8.60	9.04	6.95	7.17	9.02	8.78	8.68
ZnO		0.04		0.02	0.03		0.02	
F		0.01	0.01					0.01
Cl	1.69	1.79	1.96	1.47	1.38	1.88	2.00	1.76
Li2O	0.35	0.10	0.34			0.22	0.53	0.19
H2O	3.29	3.20	3.21	3.25	3.16	3.19	3.27	3.21
Subtotal	99.92	99.46	100.19	98.70	96.61	99.42	101.51	99.59
O=F,Cl	0.38	0.41	0.44	0.33	0.31	0.42	0.45	0.40
TOTAL	99.54	99.05	99.75	98.37	96.30	99.00	101.06	99.19
Fórmula (apfu)								
Si	5.564	5.514	5.572	5.443	5.396	5.562	5.580	5.548
Al iv	2.436	2.486	2.428	2.557	2.604	2.438	2.420	2.452
Al vi	0.187	0.184	0.247	0.255	0.165	0.202	0.336	0.213
Ti	0.158	0.144	0.151	0.133	0.141	0.149	0.131	0.150
Fe2	2.803	2.961	2.896	3.108	3.218	2.881	2.893	2.998
Fe3	0.190	0.223	0.196	0.262	0.282	0.207	0.193	0.216
Mn	0.005	0.002	0.001	0.006	0.000	0.001	0.004	0.001
Mg	2.453	2.417	2.294	2.368	2.311	2.390	2.165	2.303
Zn	0.000	0.004	0.000	0.003	0.004	0.000	0.002	0.000
Li*	0.225	0.068	0.222	0.000	0.000	0.147	0.337	0.124
Ca	0.001	0.007	0.000	0.000	0.014	0.004	0.011	0.000
Na	0.026	0.043	0.030	0.038	0.042	0.041	0.043	0.028
K	1.899	1.798	1.864	1.465	1.562	1.879	1.779	1.810
OH*	3.538	3.498	3.459	3.588	3.601	3.480	3.461	3.505
F	0.000	0.005	0.004	0.000	0.000	0.000	0.000	0.008
Cl	0.462	0.497	0.537	0.412	0.399	0.520	0.539	0.488
TOTAL	19.947	19.850	19.900	19.638	19.739	19.899	19.894	19.843

Apêndice P. Análises de química mineral por microssonda eletrônica em biotita.

	JAT-28 (160,40) MIN-I Bt 1	JAT-28 (160,40) MIN-I Bt 1	JAT-28 (160,40) MIN-I Bt 1	JAT-28 (160,40) MIN-I Bt 1	JAT-28 (160,40) MIN-I Bt 1	JAT-28 (160,40) MIN-I Bt 1	JAT-28 (160,40) MIN-I Bt 1
Óxido (%)							
FeOT	27.5	28.11	27.93	25.49	28.07	28.93	29.11
SiO2	32.94	32.40	32.22	33.74	32.24	31.44	32.01
TiO2	1.11	1.24	1.20	1.29	1.22	1.79	1.06
Al2O3	14.00	13.88	13.82	13.63	14.18	13.91	13.69
FeO	22.13	22.46	22.25	20.81	22.47	22.83	23.22
Fe2O3	5.97	6.28	6.31	5.20	6.22	6.77	6.55
MnO	0.03		0.03	0.02	0.02	0.01	0.03
MgO	9.11	10.31	10.26	9.67	9.67	10.47	9.14
CaO	0.06			0.06	0.05		0.06
Na2O	0.12	0.07	0.10	0.14	0.05	0.07	0.07
K2O	7.68	7.31	7.36	8.67	7.11	6.11	7.36
ZnO	0.04	0.03		0.04	0.02		0.02
F							0.01
Cl	1.54	1.38	1.44	1.87	1.44	1.14	1.53
Li2O			0.00	0.13			
H2O	3.20	3.26	3.23	3.16	3.22	3.29	3.16
Subtotal	97.92	97.38	98.22	98.43	97.91	97.84	97.89
O=F,Cl	0.35	0.31	0.32	0.42	0.32	0.26	0.35
TOTAL	97.57	97.07	97.90	98.01	97.59	97.58	97.54
Si	5.500	5.381	5.379	5.567	5.390	5.264	5.409
Al iv	2.500	2.619	2.621	2.433	2.610	2.736	2.591
Al vi	0.255	0.098	0.098	0.218	0.184	0.010	0.136
Ti	0.139	0.155	0.151	0.160	0.153	0.225	0.135
Fe2	3.090	3.119	3.107	2.871	3.141	3.198	3.282
Fe3	0.250	0.262	0.264	0.215	0.261	0.285	0.277
Mn	0.004	0.000	0.005	0.002	0.002	0.001	0.004
Mg	2.267	2.552	2.553	2.378	2.410	2.613	2.303
Zn	0.004	0.003	0.000	0.005	0.003	0.000	0.002
Li*	0.000	0.000	0.000	0.087	0.000	0.000	0.000
Ca	0.011	0.000	0.000	0.011	0.008	0.000	0.010
Na	0.038	0.022	0.033	0.046	0.017	0.023	0.023
K	1.636	1.548	1.567	1.825	1.516	1.305	1.586
OH*	3.564	3.612	3.593	3.477	3.592	3.676	3.557
F	0.000	0.000	0.000	0.000	0.000	0.000	0.005
Cl	0.436	0.388	0.407	0.523	0.408	0.324	0.438
TOTAL	19.695	19.760	19.779	19.819	19.696	19.659	19.759

Apêndice Q. Análises de química mineral por microssonda eletrônica em biotita.

	JAT-28 (54,22) ZC Bt 2	JAT-28 (54,22) ZC Bt 2	JAT-28 (54,22) ZC Bt 2	JAT-28 (54,22) ZC Bt 2	JAT-28 (54,22) ZC Bt 2	JAT-28 (54,22) ZC Bt 2	JAT-28 (54,22) ZC Bt 2	JAT-28 (54,22) ZC Bt 2	JAT-28 (54,22) ZC Bt 2	JAT-28 (54,22) ZC Bt 2	JAT-28 (54,22) ZC Bt 2	JAT-28 (54,22) ZC Bt 2	JAT-28 (54,22) ZC Bt 2	JAT-28 (54,22) ZC Bt 2
dio (%)														
22	34.11	35.66	35.59	35.27	35.40	34.82	35.31	34.09	35.29	32.66	34.35	38.19	35.46	35.41
22	1.41	1.50	1.62	1.39	1.58	1.44	1.49	1.41	1.49	1.50	1.32	1.36	1.51	1.24
03	13.92	14.62	14.40	14.12	14.32	14.16	14.18	13.72	14.58	13.21	13.74	13.53	14.41	14.82
T	22.58	22.89	22.12	22.98	22.8	23.22	22.96	23.03	23.1	23.62	23.58	21.22	22.91	23.72
)	18.67	19.08	18.64	19.16	19.14	19.22	19.14	18.96	19.48	19.21	19.73	17.42	19.29	19.76
O3	4.34	4.24	3.86	4.25	4.07	4.44	4.25	4.52	4.03	4.90	4.28	4.22	4.02	4.40
)	0.05	0.02	0.03	0.07	0.02	0.07	0.02	0.03	0.02	0.05	0.08		0.06	0.06
)	10.92	10.62	10.84	10.89	10.55	10.59	10.91	11.27	10.48	10.70	10.33	10.21	10.67	10.52
)	0.04	0.05	0.04	0.08	0.03	0.13	0.03			0.04	0.15	0.06	0.03	0.10
O	0.14	0.14	0.19	0.10	0.19	0.07	0.17	0.15	0.14	0.06	0.04	0.14	0.17	0.09
)	9.16	8.62	9.33	9.08	9.22	8.62	9.12	9.19	9.22	8.76	9.52	8.50	9.31	8.60
)		0.01	0.01					0.02	0.04	0.04				
		0.01				0.01		0.01		0.01			0.01	0.01
	1.28	1.14	1.18	1.20	1.37	1.18	1.26	1.35	1.31	1.26	1.28	1.22	1.30	1.23
)*	0.24	0.68	0.66	0.57	0.61	0.44	0.58	0.23	0.58	0.00	0.31	1.41	0.63	0.61
)*	3.35	3.52	3.51	3.47	3.44	3.43	3.47	3.34	3.46	3.24	3.37	3.57	3.47	3.49
total	97.64	99.91	99.91	99.66	99.94	98.63	99.92	98.31	100.12	95.62	98.49	99.83	100.32	100.35
,,Cl	0.29	0.26	0.27	0.27	0.31	0.27	0.28	0.31	0.30	0.29	0.29	0.27	0.30	0.28
all	97.35	99.65	99.64	99.39	99.63	98.36	99.64	98.00	99.82	95.33	98.21	99.55	100.03	100.07
mula (apfu)														
	5.558	5.608	5.600	5.597	5.599	5.590	5.589	5.537	5.575	5.504	5.579	5.909	5.586	5.576
v	2.442	2.392	2.400	2.403	2.401	2.410	2.411	2.463	2.425	2.496	2.421	2.091	2.414	2.424
i	0.231	0.318	0.270	0.238	0.269	0.270	0.234	0.164	0.290	0.128	0.210	0.377	0.262	0.326
	0.173	0.177	0.192	0.166	0.188	0.174	0.177	0.172	0.177	0.190	0.161	0.158	0.179	0.147
	0.000	0.000	0.000	0.000	0.000	0.000	0.000	0.000	0.000	0.000	0.000	0.000	0.000	0.000
2	2.545	2.509	2.453	2.542	2.532	2.581	2.534	2.576	2.574	2.708	2.680	2.255	2.542	2.602
3	0.177	0.167	0.152	0.169	0.161	0.179	0.169	0.184	0.160	0.207	0.175	0.164	0.159	0.174
	0.007	0.003	0.003	0.010	0.003	0.010	0.002	0.004	0.003	0.007	0.010	0.000	0.007	0.008
	2.652	2.490	2.543	2.576	2.488	2.534	2.574	2.729	2.468	2.688	2.501	2.355	2.506	2.469
	0.000	0.001	0.001	0.000	0.000	0.000	0.000	0.003	0.005	0.004	0.000	0.000	0.000	0.000
	0.000	0.000	0.000	0.000	0.000	0.000	0.000	0.000	0.000	0.000	0.000	0.000	0.000	0.000
	0.000	0.000	0.000	0.000	0.000	0.000	0.000	0.000	0.000	0.000	0.000	0.000	0.000	0.000
	0.000	0.000	0.000	0.000	0.000	0.000	0.000	0.000	0.000	0.000	0.000	0.000	0.000	0.000
	0.000	0.000	0.000	0.000	0.000	0.000	0.000	0.000	0.000	0.000	0.000	0.000	0.000	0.000
	0.156	0.432	0.419	0.364	0.387	0.285	0.370	0.151	0.366	0.000	0.200	0.877	0.396	0.387
	0.007	0.008	0.007	0.014	0.005	0.023	0.006	0.000	0.000	0.007	0.027	0.010	0.004	0.017
	0.044	0.044	0.058	0.031	0.057	0.021	0.051	0.048	0.043	0.018	0.014	0.041	0.050	0.029
	1.904	1.729	1.872	1.838	1.860	1.765	1.841	1.904	1.858	1.883	1.972	1.678	1.871	1.727
	0.000	0.000	0.000	0.000	0.000	0.000	0.000	0.000	0.000	0.000	0.000	0.000	0.000	0.000
	0.000	0.000	0.000	0.000	0.000	0.000	0.000	0.000	0.000	0.000	0.000	0.000	0.000	0.000
	0.000	0.000	0.000	0.000	0.000	0.000	0.000	0.000	0.000	0.000	0.000	0.000	0.000	0.000
	0.000	0.000	0.000	0.000	0.000	0.000	0.000	0.000	0.000	0.000	0.000	0.000	0.000	0.000
*	3.646	3.692	3.685	3.677	3.633	3.673	3.662	3.621	3.649	3.637	3.648	3.680	3.650	3.667
	0.000	0.004	0.000	0.000	0.000	0.006	0.000	0.007	0.000	0.003	0.000	0.000	0.003	0.005
	0.354	0.304	0.315	0.323	0.367	0.321	0.338	0.372	0.351	0.360	0.352	0.320	0.347	0.328
TAL	19.896	19.878	19.972	19.949	19.949	19.842	19.958	19.937	19.944	19.841	19.950	19.914	19.976	19.887

Apêndice R. Análises de química mineral por microssonda eletrônica em biotita.

	JAT-21 (40,00)	JAT-21 (40,00)	JAT-21 (40,00)	JAT-21 (40,00)	JAT-21 (40,00)	JAT-21 (40,00)	JAT-21 (40,00)	JAT-21 (40,00)	JAT-21 (40,00)	JAT-21 (40,00)	JAT-21 (40,00)	JAT-21 (40,00)	JAT-21 (40,00)	JAT-21 (40,00)
	Veios-Min-III	Veios-Min-III	Veios-Min-III	Veios-Min-III	Veios-Min-III	Veios-Min-III	Veios-Min-III	Veios-Min-III	Veios-Min-III	Veios-Min-III	Veios-Min-III	Veios-Min-III	Veios-Min-III	Veios-Min-III
	Bt 3	Bt 3	Bt 3	Bt 3	Bt 3	Bt 3	Bt 3	Bt 3	Bt 3	Bt 3	Bt 3	Bt 3	Bt 3	Bt 3
;idio (%)														
:00T	27.81	27.1	27.32	28.8	27.55	27.96	27.28	27.7	27.38	27.55	28.73	27.59	28.03	28.07
022	33.92	33.56	33.61	33.38	34.02	33.59	33.40	31.90	33.62	34.05	33.44	34.30	33.60	33.18
022	1.00	1.09	1.06	0.89	1.12	0.89	0.99	0.92	1.13	1.13	0.92	1.04	1.14	0.96
2C03	15.29	15.26	15.10	15.09	15.26	15.20	14.95	14.49	15.30	15.05	14.95	14.41	15.16	14.86
:00	23.52	22.69	22.82	24.07	23.26	23.44	22.73	22.62	23.08	23.14	24.01	22.99	23.61	23.47
2203	4.77	4.91	5.00	5.26	4.76	5.03	5.05	5.64	4.77	4.90	5.24	5.12	4.92	5.11
nO	0.06	0.06	0.04	0.02	0.07	0.02		0.03	0.03	0.06	0.02	0.02	0.02	0.01
gO	7.74	8.07	7.71	7.41	7.84	7.28	8.02	8.09	7.89	7.95	7.43	8.23	7.61	7.71
aO	0.03	0.06	0.06	0.02	0.00		0.04	0.04		0.06	0.04	0.00	0.00	0.02
a20	0.20	0.24	0.26	0.25	0.17	0.19	0.22	0.26	0.20	0.20	0.20	0.18	0.17	0.17
200	9.40	8.97	9.00	9.17	9.10	9.06	9.06	8.72	9.14	9.04	9.12	9.14	9.08	9.20
n00	0.02	0.02	0.02	0.02		0.00			0.01	0.03	0.02	0.03	0.01	
		0.01		0.01		0.01		0.01			0.01			
	2.43	2.20	2.58	2.83	2.47	3.02	2.44	2.50	2.38	2.34	2.82	2.44	2.53	2.49
200*	0.18	0.08	0.09	0.03	0.21	0.09	0.03	0.00	0.10	0.22	0.05	0.29	0.09	0.00
20)*	3.09	3.11	3.00	2.93	3.08	2.88	3.02	2.90	3.08	3.11	2.93	3.08	3.03	3.00
;bttotal	101.66	100.32	100.35	101.37	101.37	100.70	99.97	98.12	100.73	101.28	101.21	101.27	100.98	100.18
=F,Cl	0.55	0.50	0.58	0.64	0.56	0.69	0.55	0.57	0.54	0.53	0.64	0.55	0.57	0.56
talil	101.12	99.82	99.77	100.73	100.81	100.01	99.42	97.56	100.20	100.76	100.57	100.72	100.41	99.62
;rmula (apfu)														
	5.485	5.476	5.507	5.475	5.499	5.519	5.496	5.407	5.475	5.508	5.490	5.561	5.483	5.481
iv	2.515	2.524	2.493	2.525	2.501	2.481	2.504	2.593	2.525	2.492	2.510	2.439	2.517	2.519
vi	0.400	0.411	0.424	0.392	0.407	0.463	0.396	0.302	0.411	0.378	0.382	0.314	0.398	0.374
	0.122	0.134	0.131	0.110	0.136	0.110	0.123	0.117	0.138	0.137	0.114	0.127	0.140	0.120
r	0.000	0.000	0.000	0.000	0.000	0.000	0.000	0.000	0.000	0.000	0.000	0.000	0.000	0.000
e2	3.181	3.096	3.127	3.302	3.145	3.220	3.128	3.207	3.144	3.130	3.297	3.117	3.221	3.243
e3	0.194	0.201	0.206	0.216	0.193	0.207	0.209	0.240	0.195	0.199	0.216	0.208	0.201	0.212
In	0.009	0.008	0.005	0.003	0.009	0.003	0.000	0.004	0.005	0.009	0.003	0.003	0.003	0.001
lg	1.866	1.963	1.883	1.812	1.889	1.783	1.967	2.044	1.915	1.917	1.818	1.989	1.851	1.898
n	0.003	0.002	0.003	0.002	0.000	0.001	0.000	0.000	0.001	0.004	0.003	0.004	0.001	0.000
n	0.000	0.000	0.000	0.000	0.000	0.000	0.000	0.000	0.000	0.000	0.000	0.000	0.000	0.000
a	0.000	0.000	0.000	0.000	0.000	0.000	0.000	0.000	0.000	0.000	0.000	0.000	0.000	0.000
	0.000	0.000	0.000	0.000	0.000	0.000	0.000	0.000	0.000	0.000	0.000	0.000	0.000	0.000
u	0.000	0.000	0.000	0.000	0.000	0.000	0.000	0.000	0.000	0.000	0.000	0.000	0.000	0.000
*	0.119	0.052	0.062	0.019	0.138	0.058	0.022	0.000	0.063	0.143	0.030	0.190	0.060	0.000
a	0.006	0.011	0.010	0.003	0.000	0.000	0.007	0.008	0.000	0.010	0.006	0.000	0.000	0.003
a	0.064	0.075	0.081	0.078	0.053	0.060	0.070	0.085	0.062	0.062	0.065	0.057	0.054	0.056
	1.939	1.867	1.881	1.918	1.876	1.899	1.902	1.885	1.898	1.865	1.910	1.890	1.890	1.938
r	0.000	0.000	0.000	0.000	0.000	0.000	0.000	0.000	0.000	0.000	0.000	0.000	0.000	0.000
a	0.000	0.000	0.000	0.000	0.000	0.000	0.000	0.000	0.000	0.000	0.000	0.000	0.000	0.000
o	0.000	0.000	0.000	0.000	0.000	0.000	0.000	0.000	0.000	0.000	0.000	0.000	0.000	0.000
s	0.000	0.000	0.000	0.000	0.000	0.000	0.000	0.000	0.000	0.000	0.000	0.000	0.000	0.000
H*	3.334	3.386	3.283	3.208	3.323	3.153	3.319	3.275	3.343	3.358	3.212	3.329	3.300	3.303
	0.000	0.005	0.000	0.005	0.000	0.006	0.000	0.007	0.000	0.000	0.003	0.000	0.000	0.000
	0.666	0.608	0.717	0.787	0.677	0.841	0.681	0.718	0.657	0.642	0.785	0.671	0.700	0.697
OTAL	19.900	19.819	19.813	19.856	19.847	19.804	19.824	19.893	19.833	19.855	19.844	19.900	19.821	19.845

Apêndice S. Análises de química mineral por microssonda eletrônica em biotita.

	JAT-21 (40,00)	JAT-21 (40,00)	JAT-15 (44,35)	JAT-15 (44,35)	JAT-15 (44,35)	JAT-15 (44,35)	JAT-15 (44,35)	JAT-15 (44,35)	JAT-15 (44,35)	JAT-15 (44,35)	JAT-15 (44,35)	JAT-15 (44,35)
	Veios-Min-III	Veios-Min-III	Veios-Min-III	Veios-Min-III	Veios-Min-III	Veios-Min-III	Veios-Min-III	Veios-Min-III	Veios-Min-III	Veios-Min-III	Veios-Min-III	Veios-Min-III
	Bt 3	Bt 3	Bt 3	Bt 3	Bt 3	Bt 3	Bt 3	Bt 3	Bt 3	Bt 3	Bt 3	Bt 3
ddo (%)												
0)T	28.27	27.2	27.47	27.7	27.13	26.75	27.5	27.61	27.4	26.73	27.04	27.25
022	33.45	33.32	34.84	34.26	34.92	34.58	34.43	34.32	34.12	34.65	34.49	34.72
022	0.93	0.99	0.92	1.01	1.05	1.02	0.88	0.98	0.89	1.02	0.98	1.09
2C3	15.08	15.06	14.38	14.79	14.37	14.36	14.23	14.19	14.58	14.39	14.29	14.33
0)	23.67	22.73	22.84	23.21	22.62	22.17	22.75	22.89	22.74	22.32	22.54	22.84
2?O3	5.11	4.97	5.14	4.99	5.01	5.09	5.28	5.25	5.18	4.91	5.00	4.91
nC	0.03	0.03	0.09	0.06	0.09	0.09	0.07	0.11	0.08	0.11	0.08	0.08
gC	7.58	8.03	8.63	8.07	8.48	8.70	8.52	8.63	8.46	8.76	8.33	8.31
aC	0.04	0.02	0.13	0.01	0.00	0.07	0.05	0.07	0.04	0.01	0.03	
a2?O	0.22	0.20	0.17	0.19	0.21	0.23	0.22	0.17	0.15	0.16	0.21	0.18
2O	9.19	9.07	9.10	9.20	9.16	9.04	9.16	9.06	8.93	9.21	9.37	9.37
nO		0.02		0.00	0.01	0.01	0.06	0.00	0.01	0.04	0.04	0.04
										0.01	0.01	
	2.82	2.49	2.35	2.32	2.51	2.38	2.15	2.23	2.26	2.23	2.55	2.51
2O*	0.05	0.01	0.45	0.28	0.47	0.37	0.33	0.30	0.24	0.39	0.35	0.41
2O*	2.94	3.01	3.15	3.12	3.11	3.11	3.16	3.14	3.12	3.16	3.05	3.09
bMotal	101.11	99.96	102.18	101.52	102.00	101.22	101.28	101.34	100.79	101.36	101.32	101.88
F,Cl	0.64	0.56	0.53	0.52	0.57	0.54	0.48	0.50	0.51	0.51	0.58	0.57
taal	100.48	99.40	101.65	100.99	101.43	100.69	100.80	100.83	100.28	100.85	100.74	101.31
rmula (apfu)												
	5.483	5.484	5.576	5.534	5.594	5.577	5.573	5.556	5.545	5.573	5.584	5.583
iw	2.517	2.516	2.424	2.466	2.406	2.423	2.427	2.444	2.455	2.427	2.416	2.417
vi	0.396	0.405	0.288	0.351	0.307	0.307	0.287	0.264	0.338	0.300	0.311	0.298
	0.114	0.123	0.111	0.123	0.126	0.124	0.107	0.120	0.108	0.123	0.120	0.132
	0.000	0.000	0.000	0.000	0.000	0.000	0.000	0.000	0.000	0.000	0.000	0.000
e2?	3.245	3.128	3.058	3.136	3.030	2.990	3.080	3.099	3.091	3.002	3.053	3.071
e3	0.210	0.205	0.206	0.202	0.201	0.206	0.214	0.213	0.211	0.198	0.203	0.198
n	0.005	0.005	0.012	0.008	0.012	0.013	0.009	0.015	0.010	0.015	0.010	0.011
g	1.852	1.970	2.059	1.943	2.025	2.092	2.056	2.083	2.050	2.100	2.010	1.992
	0.000	0.002	0.000	0.000	0.001	0.001	0.007	0.001	0.001	0.005	0.005	0.005
	0.000	0.000	0.000	0.000	0.000	0.000	0.000	0.000	0.000	0.000	0.000	0.000
	0.000	0.000	0.000	0.000	0.000	0.000	0.000	0.000	0.000	0.000	0.000	0.000
	0.000	0.000	0.000	0.000	0.000	0.000	0.000	0.000	0.000	0.000	0.000	0.000
	0.000	0.000	0.000	0.000	0.000	0.000	0.000	0.000	0.000	0.000	0.000	0.000
	0.032	0.007	0.288	0.182	0.303	0.242	0.214	0.194	0.157	0.254	0.226	0.267
	0.007	0.004	0.023	0.002	0.001	0.012	0.009	0.012	0.007	0.002	0.006	0.000
	0.069	0.064	0.051	0.060	0.064	0.072	0.068	0.053	0.048	0.050	0.066	0.056
	1.921	1.904	1.858	1.896	1.872	1.860	1.891	1.871	1.851	1.889	1.935	1.922
	0.000	0.000	0.000	0.000	0.000	0.000	0.000	0.000	0.000	0.000	0.000	0.000
	0.000	0.000	0.000	0.000	0.000	0.000	0.000	0.000	0.000	0.000	0.000	0.000
	0.000	0.000	0.000	0.000	0.000	0.000	0.000	0.000	0.000	0.000	0.000	0.000
	0.000	0.000	0.000	0.000	0.000	0.000	0.000	0.000	0.000	0.000	0.000	0.000
	3.216	3.305	3.363	3.365	3.318	3.349	3.410	3.388	3.377	3.388	3.295	3.316
	0.000	0.000	0.000	0.000	0.000	0.000	0.000	0.000	0.000	0.004	0.005	0.000
	0.784	0.695	0.637	0.635	0.682	0.651	0.590	0.612	0.623	0.608	0.700	0.684
TAL	19.852	19.818	19.953	19.903	19.942	19.917	19.943	19.923	19.872	19.938	19.944	19.951

Apêndice T. Análises de química mineral por microssonda eletrônica em biotita.

	JAT-15 (44,35)	JAT-15 (44,35)	JAT-15 (44,35)	JAT-15 (44,35)	JAT-15 (44,35)	JAT-15 (44,35)	JAT-15 (44,35)	JAT-15 (87,63)	JAT-15 (87,63)	JAT-15 (87,63)	JAT-15 (87,63)	JAT-15 (87,63)
	Veios-Min-III	Veios-Min-III	Veios-Min-III	Veios-Min-III	Veios-Min-III	Veios-Min-III	Veios-Min-III	Veios	Veios	Veios	Veios	Veios
	Bt 3	Bt 3	Bt 3	Bt 3	Bt 3	Bt 3	Bt 3	Bt 3	Bt 3	Bt 3	Bt 3	Bt 3
Óxido (%)												
FeOT	26.63	26.97	26.74	26.7	26.97	27.1	28.17	27.19	27.18	27.36	26.42	25.85
SiO2	34.80	34.97	34.67	34.79	34.30	34.06	34.07	34.36	34.52	34.79	34.80	34.41
TiO2	0.98	1.00	0.95	1.05	1.08	0.93	0.99	0.28	0.27	0.30	0.44	0.42
Al2O3	14.34	14.44	14.33	14.43	14.34	14.41	13.92	14.48	14.40	14.65	14.04	14.25
FeO	22.40	22.56	22.22	22.47	22.62	22.53	23.30	22.33	22.31	22.51	21.62	21.03
Fe2O3	4.70	4.90	5.02	4.70	4.84	5.08	5.41	5.40	5.41	5.39	5.34	5.36
MnO	0.09	0.10	0.06	0.12	0.09	0.09	0.12		0.04	0.03	0.03	0.06
MgO	8.69	8.77	8.37	8.43	8.50	8.49	8.00	8.85	8.58	8.79	9.02	9.16
CaO		0.05	0.08		0.01	0.07		0.04	0.01	0.03	0.01	
Na2O	0.06	0.19	0.23	0.12	0.13	0.18	0.24	0.18	0.18	0.21	0.21	0.25
K2O	9.40	9.33	9.27	9.37	9.36	9.19	9.24	9.25	9.19	9.18	9.24	9.04
ZnO	0.01	0.02	0.02		0.07				0.03	0.05		0.01
F	0.01									0.01		
Cl	2.30	2.28	2.55	2.31	2.35	2.25	2.98	3.04	3.04	2.90	2.96	2.70
Li2O*	0.44	0.48	0.40	0.43	0.29	0.22	0.23	0.31	0.36	0.43	0.44	0.32
H2O*	3.14	3.18	3.06	3.14	3.10	3.11	2.91	2.92	2.91	2.99	2.94	2.98
Subtotal	101.37	102.27	101.24	101.36	101.08	100.62	101.40	101.44	101.25	102.26	101.08	99.99
O=F,Cl	0.52	0.51	0.57	0.52	0.53	0.51	0.67	0.69	0.69	0.66	0.67	0.61
Total	100.84	101.76	100.66	100.84	100.55	100.11	100.73	100.75	100.57	101.60	100.42	99.38
Fórmula (apfu)												
Si	5.592	5.574	5.602	5.592	5.556	5.549	5.578	5.584	5.617	5.590	5.645	5.624
Al iv	2.408	2.426	2.398	2.408	2.444	2.451	2.422	2.416	2.383	2.410	2.355	2.376
Al vi	0.308	0.287	0.332	0.327	0.295	0.315	0.264	0.357	0.378	0.365	0.329	0.369
Ti	0.119	0.120	0.115	0.127	0.132	0.114	0.122	0.034	0.033	0.037	0.054	0.051
Cr	0.000	0.000	0.000	0.000	0.000	0.000	0.000	0.000	0.000	0.000	0.000	0.000
Fe2	3.011	3.007	3.003	3.021	3.064	3.069	3.191	3.035	3.036	3.025	2.932	2.875
Fe3	0.189	0.196	0.204	0.190	0.197	0.208	0.222	0.220	0.221	0.217	0.217	0.220
Mn	0.013	0.013	0.009	0.016	0.013	0.013	0.016	0.000	0.006	0.004	0.005	0.008
Mg	2.082	2.084	2.016	2.020	2.053	2.062	1.953	2.144	2.081	2.105	2.181	2.232
Zn	0.002	0.002	0.003	0.000	0.009	0.000	0.000	0.000	0.004	0.006	0.000	0.001
Sn	0.000	0.000	0.000	0.000	0.000	0.000	0.000	0.000	0.000	0.000	0.000	0.000
Ga	0.000	0.000	0.000	0.000	0.000	0.000	0.000	0.000	0.000	0.000	0.000	0.000
Ni	0.000	0.000	0.000	0.000	0.000	0.000	0.000	0.000	0.000	0.000	0.000	0.000
Cu	0.000	0.000	0.000	0.000	0.000	0.000	0.000	0.000	0.000	0.000	0.000	0.000
Li*	0.282	0.311	0.259	0.280	0.190	0.146	0.149	0.202	0.232	0.280	0.284	0.213
Ca	0.000	0.008	0.013	0.000	0.001	0.012	0.000	0.008	0.002	0.004	0.002	0.000
Na	0.018	0.059	0.073	0.036	0.040	0.057	0.077	0.056	0.056	0.066	0.065	0.079
K	1.927	1.897	1.911	1.921	1.934	1.910	1.930	1.917	1.907	1.882	1.912	1.884
Sr	0.000	0.000	0.000	0.000	0.000	0.000	0.000	0.000	0.000	0.000	0.000	0.000
Ba	0.000	0.000	0.000	0.000	0.000	0.000	0.000	0.000	0.000	0.000	0.000	0.000
Rb	0.000	0.000	0.000	0.000	0.000	0.000	0.000	0.000	0.000	0.000	0.000	0.000
Cs	0.000	0.000	0.000	0.000	0.000	0.000	0.000	0.000	0.000	0.000	0.000	0.000
OH*	3.368	3.384	3.302	3.371	3.355	3.379	3.173	3.163	3.162	3.204	3.186	3.252
F	0.006	0.000	0.000	0.000	0.000	0.000	0.000	0.000	0.000	0.007	0.000	0.000
Cl	0.626	0.616	0.698	0.629	0.645	0.621	0.827	0.837	0.838	0.790	0.814	0.748
TOTAL	19.950	19.985	19.937	19.937	19.927	19.906	19.923	19.973	19.956	19.991	19.981	19.931

Apêndice U. Análises de química mineral por microssonda eletrônica em biotita.

	JAT-15 (87,63) Veios Bt 3	JAT-15 (87,63) Veios Bt 3	JAT-15 (87,63) Veios Bt 3	JAT-15 (87,63) Veios Bt 3	JAT-15 (87,63) Veios Bt 3	JAT-15 (87,63) Veios Bt 3	JAT-15 (87,63) Veios Bt 3	JAT-15 (87,63) Veios Bt 3	JAT-15 (87,63) Veios Bt 3	JAT-15 (87,63) Veios Bt 3	JAT-15 (87,63) Veios Bt 3	JAT-15 (87,63) Veios Bt 3
Óxido (%)												
FeOT	27.05	26.86	27.41	27.2	27.21	26.65	26.75	27.21	26.88	26.98	27.08	28.36
SiO2	34.31	35.25	33.22	34.59	34.44	34.66	34.07	34.29	34.17	34.21	34.76	32.60
TiO2	0.09	0.36	0.43	0.30	0.31	0.94	1.23	0.40	1.01	1.21	0.32	0.48
Al2O3	14.37	14.32	15.08	14.38	14.32	14.31	14.68	14.34	14.34	14.27	14.42	15.06
FeO	22.00	21.95	22.19	22.34	22.32	22.15	22.48	22.21	22.38	22.53	22.16	22.50
Fe2O3	5.61	5.46	5.80	5.40	5.43	5.00	4.75	5.55	5.00	4.95	5.47	6.52
MnO	0.05	0.01	0.05	0.04	0.01	0.02	0.05	0.03	0.05	0.04	0.04	0.04
MgO	8.77	9.03	9.21	8.83	8.74	8.41	8.15	8.74	8.25	8.37	8.60	9.54
CaO	0.04	0.01	0.01	0.02		0.03		0.03		0.01	0.02	0.10
Na2O	0.22	0.24	0.12	0.12	0.19	0.15	0.19	0.18	0.15	0.17	0.20	0.07
K2O	9.11	9.06	7.90	9.09	9.26	9.12	9.26	8.88	9.14	9.18	8.99	6.73
ZnO	0.02			0.04	0.01	0.01	0.02		0.01			
F					0.00				0.01			
Cl	3.19	2.70	2.18	2.79	3.11	2.63	2.63	2.86	2.80	2.71	2.86	1.99
Li2O*	0.29	0.56	0.00	0.38	0.33	0.40	0.23	0.29	0.25	0.27	0.42	0.00
H2O*	2.85	3.06	3.08	2.99	2.89	3.03	3.02	2.94	2.96	3.00	2.97	3.11
Subtotal	100.93	102.01	99.26	101.31	101.36	100.86	100.75	100.75	100.51	100.91	101.25	98.73
O=F,Cl	0.72	0.61	0.49	0.63	0.70	0.59	0.59	0.64	0.63	0.61	0.64	0.45
Total	100.21	101.40	98.77	100.68	100.66	100.27	100.16	100.10	99.88	100.30	100.61	98.28
Fórmula (apfu)												
Si	5.614	5.645	5.478	5.608	5.605	5.615	5.541	5.600	5.583	5.565	5.633	5.411
Al iv	2.386	2.355	2.522	2.392	2.395	2.385	2.459	2.400	2.417	2.435	2.367	2.589
Al vi	0.385	0.347	0.409	0.356	0.352	0.348	0.354	0.361	0.345	0.301	0.387	0.358
Ti	0.011	0.043	0.053	0.037	0.038	0.115	0.150	0.049	0.124	0.148	0.040	0.060
Cr	0.000	0.000	0.000	0.000	0.000	0.000	0.000	0.000	0.000	0.000	0.000	0.000
Fe2	3.011	2.939	3.060	3.030	3.039	3.002	3.057	3.034	3.059	3.064	3.003	3.123
Fe3	0.230	0.219	0.240	0.219	0.222	0.203	0.194	0.227	0.205	0.202	0.222	0.271
Mn	0.007	0.002	0.007	0.005	0.001	0.002	0.007	0.004	0.006	0.006	0.006	0.006
Mg	2.139	2.155	2.264	2.134	2.121	2.031	1.976	2.128	2.009	2.030	2.078	2.361
Zn	0.002	0.000	0.000	0.005	0.001	0.001	0.002	0.000	0.001	0.000	0.000	0.000
Sn	0.000	0.000	0.000	0.000	0.000	0.000	0.000	0.000	0.000	0.000	0.000	0.000
Ga	0.000	0.000	0.000	0.000	0.000	0.000	0.000	0.000	0.000	0.000	0.000	0.000
Ni	0.000	0.000	0.000	0.000	0.000	0.000	0.000	0.000	0.000	0.000	0.000	0.000
Cu	0.000	0.000	0.000	0.000	0.000	0.000	0.000	0.000	0.000	0.000	0.000	0.000
Li*	0.194	0.364	0.000	0.245	0.218	0.258	0.148	0.190	0.167	0.174	0.276	0.000
Ca	0.007	0.001	0.002	0.003	0.000	0.006	0.000	0.006	0.000	0.001	0.004	0.017
Na	0.069	0.074	0.037	0.038	0.059	0.048	0.061	0.056	0.048	0.054	0.064	0.024
K	1.901	1.850	1.662	1.880	1.922	1.885	1.921	1.850	1.905	1.905	1.858	1.425
Sr	0.000	0.000	0.000	0.000	0.000	0.000	0.000	0.000	0.000	0.000	0.000	0.000
Ba	0.000	0.000	0.000	0.000	0.000	0.000	0.000	0.000	0.000	0.000	0.000	0.000
Rb	0.000	0.000	0.000	0.000	0.000	0.000	0.000	0.000	0.000	0.000	0.000	0.000
Cs	0.000	0.000	0.000	0.000	0.000	0.000	0.000	0.000	0.000	0.000	0.000	0.000
OH*	3.115	3.267	3.391	3.233	3.141	3.278	3.275	3.208	3.222	3.253	3.214	3.440
F	0.000	0.000	0.000	0.000	0.001	0.000	0.000	0.000	0.003	0.000	0.000	0.000
Cl	0.885	0.733	0.609	0.767	0.858	0.722	0.725	0.792	0.776	0.747	0.786	0.560
TOTAL	19.957	19.996	19.733	19.953	19.972	19.897	19.870	19.905	19.869	19.885	19.939	19.644

Apêndice V. Análises de química mineral por microssonda eletrônica em biotita.

	JAT-15 (87,63) Veios Bt 3	JAT-15 (87,63) Veios Bt 3	JAT-15 (87,63) Veios Bt 3	JAT-15 (87,63) Veios Bt 3	JAT-15 (87,63) Veios Bt 3	JAT-15 (87,63) Veios Bt 3	JAT-15 (87,63) Veios Bt 3	JAT-15 (87,63) Veios Bt 3	JAT-15 (87,63) Veios Bt 3	JAT-15 (87,63) Veios Bt 3	JAT-15 (87,63) Veios Bt 3	JAT-15 (87,63) Veios Bt 3	JAT-15 (87,63) Veios Bt 3
Óxido (%)													
FeOT	27.56	26.84	26.72	26.5	26.98	26.27	27.55	27.06	26.5	26.8	27.77	27.11	26.94
SiO2	33.68	34.64	34.39	34.65	34.40	33.79	34.27	34.41	34.78	34.70	34.27	34.37	34.41
TiO2	0.46	0.49	0.36	0.36	1.05	0.51	0.40	0.70	0.95	0.60	0.36	1.14	1.00
Al2O3	14.88	14.50	14.34	14.47	14.27	14.34	14.47	14.36	14.31	14.55	14.33	14.40	14.41
FeO	22.21	22.14	21.85	21.78	22.41	21.40	22.62	22.31	21.23	22.18	22.73	22.68	22.41
Fe2O3	5.94	5.22	5.41	5.25	5.08	5.42	5.48	5.28	5.85	5.14	5.60	4.92	5.03
MnO		0.06	0.02	0.05	0.02	0.02	0.04	0.04	0.02	0.05	0.04	0.03	0.06
MgO	9.19	8.68	8.55	8.82	8.76	9.00	8.44	8.69	8.86	8.61	8.47	8.11	8.24
CaO	0.06	0.03	0.02	0.07	0.01		0.02	0.01	9.13		0.04	0.01	
Na2O	0.16	0.20	0.20	0.15	0.17	0.17	0.19	0.17	0.23	0.20	0.20	0.17	0.20
K2O	7.85	9.20	9.04	9.10	9.11	8.80	9.05	9.02	9.13	9.21	9.05	9.22	9.13
ZnO	0.01	0.05	0.06	0.02		0.03		0.03		0.00	0.01	0.01	0.04
F			0.01										0.01
Cl	2.25	2.61	3.01	2.68	2.60	2.61	2.96	2.75	2.65	2.71	2.98	2.79	2.88
Li2O*	0.11	0.39	0.32	0.39	0.32	0.15	0.28	0.32	0.43	0.41	0.28	0.31	0.32
H2O*	3.09	3.04	2.90	3.02	3.05	2.97	2.92	2.99	3.31	3.03	2.92	2.99	2.95
Subtotal	99.90	101.26	100.46	100.81	101.24	99.18	101.15	101.08	110.88	101.38	101.28	101.16	101.10
O=F,Cl	0.51	0.59	0.68	0.60	0.59	0.59	0.67	0.62	0.60	0.61	0.67	0.63	0.65
Total	99.39	100.67	99.78	100.21	100.66	98.59	100.48	100.46	110.28	100.77	100.60	100.53	100.44
Fórmula (apfu)													
Si	5.516	5.602	5.629	5.620	5.566	5.583	5.590	5.587	5.235	5.602	5.594	5.578	5.588
Al iv	2.484	2.398	2.371	2.380	2.434	2.417	2.410	2.413	2.539	2.398	2.406	2.422	2.412
Al vi	0.388	0.366	0.396	0.386	0.288	0.376	0.372	0.335	0.000	0.370	0.351	0.333	0.347
Ti	0.057	0.060	0.044	0.044	0.128	0.063	0.049	0.085	0.107	0.073	0.044	0.139	0.122
Cr	0.000	0.000	0.000	0.000	0.000	0.000	0.000	0.000	0.000	0.000	0.000	0.000	0.000
Fe2	3.042	2.994	2.991	2.954	3.033	2.957	3.086	3.030	2.673	2.994	3.103	3.079	3.044
Fe3	0.244	0.212	0.222	0.213	0.206	0.225	0.224	0.215	0.221	0.208	0.229	0.200	0.205
Mn	0.000	0.008	0.003	0.007	0.003	0.002	0.005	0.006	0.002	0.007	0.005	0.004	0.008
Mg	2.244	2.092	2.086	2.133	2.113	2.217	2.052	2.103	1.988	2.072	2.061	1.962	1.995
Zn	0.001	0.006	0.007	0.003	0.000	0.003	0.000	0.003	0.000	0.000	0.001	0.001	0.004
Sn	0.000	0.000	0.000	0.000	0.000	0.000	0.000	0.000	0.000	0.000	0.000	0.000	0.000
Ga	0.000	0.000	0.000	0.000	0.000	0.000	0.000	0.000	0.000	0.000	0.000	0.000	0.000
Ni	0.000	0.000	0.000	0.000	0.000	0.000	0.000	0.000	0.000	0.000	0.000	0.000	0.000
Cu	0.000	0.000	0.000	0.000	0.000	0.000	0.000	0.000	0.000	0.000	0.000	0.000	0.000
Li*	0.075	0.253	0.209	0.256	0.209	0.097	0.186	0.211	0.260	0.264	0.186	0.204	0.211
Ca	0.010	0.005	0.003	0.013	0.001	0.000	0.003	0.001	1.473	0.000	0.007	0.002	0.000
Na	0.052	0.063	0.062	0.049	0.053	0.054	0.060	0.055	0.067	0.064	0.063	0.054	0.063
K	1.640	1.898	1.887	1.883	1.880	1.855	1.883	1.868	1.753	1.896	1.884	1.909	1.891
Sr	0.000	0.000	0.000	0.000	0.000	0.000	0.000	0.000	0.000	0.000	0.000	0.000	0.000
Ba	0.000	0.000	0.000	0.000	0.000	0.000	0.000	0.000	0.000	0.000	0.000	0.000	0.000
Rb	0.000	0.000	0.000	0.000	0.000	0.000	0.000	0.000	0.000	0.000	0.000	0.000	0.000
Cs	0.000	0.000	0.000	0.000	0.000	0.000	0.000	0.000	0.000	0.000	0.000	0.000	0.000
OH*	3.375	3.285	3.162	3.263	3.287	3.269	3.182	3.243	3.324	3.258	3.175	3.232	3.201
F	0.000	0.000	0.003	0.000	0.000	0.000	0.000	0.000	0.000	0.000	0.000	0.000	0.006
Cl	0.625	0.715	0.835	0.737	0.713	0.731	0.818	0.757	0.676	0.742	0.825	0.768	0.793
TOTAL	19.753	19.957	19.911	19.940	19.913	19.848	19.922	19.913	20.318	19.949	19.935	19.888	19.891

Apêndice X. Análises de química mineral por microssonda eletrônica em clorita.

	JAT-28 (166,40)	JAT-28 (166,40)	JAT-28 (166,40)	JAT-03 (130,05)	JAT-03 (130,05)	JAT-03 (130,05)	JAT-03 (130,05)	JAT-03 (130,05)	JAT-03 (130,05)
	Diabásio	Diabásio	Diabásio	Diabásio	Diabásio	Diabásio	Diabásio	Diabásio	Diabásio
	Chl 1	Chl 1	Chl 1	Chl 2	Chl 2	Chl 2	Chl 2	Chl 2	Chl 2
Óxido (%)									
SiO2	25.17	25.56	25.65	26.280	25.830	25.990	25.340	25.460	25.810
TiO2	0.00	0.04	0.01	0.104	0.073	0.048	0.087	0.180	0.006
Al2O3	17.06	17.52	17.10	20.360	19.980	20.620	21.190	21.350	20.810
FeO	36.15	32.93	33.47	22.130	22.910	23.120	24.210	24.490	22.410
MnO	0.04	0.03	0.03	0.048	0.027	0.045	0.048	0.045	0.024
ZnO	0.04	0.02	0.04	0.061	0.083	0.059	0.003	0.067	0.063
CuO	0.00	0.00	0.00	0.000	0.000	0.000	0.000	0.000	0.000
MgO	9.22	11.30	11.05	18.120	17.860	17.420	16.310	16.420	18.450
CaO	0.04	0.05	0.20	0.018	0.041	0.019	0.000	0.013	0.000
BaO	0.00	0.00	0.00	0.000	0.000	0.000	0.000	0.000	0.000
Na2O	0.03	0.01	0.08	0.010	0.033	0.025	0.014	0.001	0.009
K2O	0.10	0.17	0.14	0.037	0.020	0.007	0.044	0.022	0.000
F	0.00	0.00	0.00	0.003	0.000	0.000	0.000	0.000	0.000
Cl	0.09	0.08	0.09	0.130	0.118	0.118	0.162	0.208	0.131
O=F	0.00	0.00	0.00	0.001	0.000	0.000	0.000	0.000	0.000
O=Cl	0.02	0.02	0.02	0.029	0.027	0.027	0.037	0.047	0.030
TOTAL	87.93	87.70	87.84	87.270	86.949	87.445	87.371	88.209	87.684
Fórmula (apfu)									
Si	2.8180	2.8192	2.8395	2.7382	2.7103	2.7154	2.6679	2.6575	2.6704
Ti	0.0000	0.0036	0.0006	0.0081	0.0058	0.0038	0.0069	0.0141	0.0005
Al	2.2511	2.2775	2.2311	2.5002	2.4709	2.5390	2.6293	2.6264	2.5375
Fe(3+)	0.0813	0.0375	0.0055	0.0000	0.0783	0.0125	0.0124	0.0242	0.1190
Fe(2+)	3.3034	3.0000	3.0931	1.9283	1.9321	2.0076	2.1193	2.1136	1.8201
Mn	0.0036	0.0026	0.0032	0.0042	0.0024	0.0040	0.0042	0.0040	0.0021
Zn	0.0037	0.0018	0.0034	0.0047	0.0064	0.0045	0.0002	0.0052	0.0048
Mg	1.5389	1.8580	1.8236	2.8145	2.7938	2.7132	2.5599	2.5550	2.8457
Ca	0.0048	0.0061	0.0234	0.0021	0.0046	0.0021	0.0000	0.0015	0.0000
Na	0.0069	0.0029	0.0169	0.0019	0.0066	0.0051	0.0029	0.0002	0.0018
K	0.0150	0.0244	0.0196	0.0050	0.0027	0.0009	0.0058	0.0029	0.0000
F	0.0000	0.0000	0.0000	0.0011	0.0000	0.0000	0.0000	0.0000	0.0000
Cl	0.0165	0.0142	0.0166	0.0229	0.0210	0.0209	0.0289	0.0368	0.0230
OH	7.9835	7.9858	7.9834	7.9761	7.9790	7.9791	7.9711	7.9632	7.9770
[Si	2.8180	2.8192	2.8395	2.7382	2.7103	2.7154	2.6679	2.6575	2.6704
Al(IV)	1.1820	1.1808	1.1605	1.2618	1.2897	1.2846	1.3321	1.3425	1.3296
Σ-Tetrahedral	4.0000	4.0000	4.0000	4.0000	4.0000	4.0000	4.0000	4.0000	4.0000
Al(VI)	1.0691	1.0966	1.0706	1.2383	1.1812	1.2544	1.2972	1.2839	1.2079
Ti	0.0000	0.0036	0.0006	0.0081	0.0058	0.0038	0.0069	0.0141	0.0005
Fe3+	0.0813	0.0375	0.0055	0.0000	0.0783	0.0125	0.0124	0.0242	0.1190
Fe2+	3.3034	3.0000	3.0931	1.9283	1.9321	2.0076	2.1193	2.1136	1.8201
Mn	0.0036	0.0026	0.0032	0.0042	0.0024	0.0040	0.0042	0.0040	0.0021
Zn	0.0037	0.0018	0.0034	0.0047	0.0064	0.0045	0.0002	0.0052	0.0048
Cu	0.0000	0.0000	0.0000	0.0000	0.0000	0.0000	0.0000	0.0000	0.0000
Mg	1.5389	1.8580	1.8236	2.8145	2.7938	2.7132	2.5599	2.5550	2.8457
Σ-Octahedral	6.0000	6.0000	6.0000	5.9981	6.0000	6.0000	6.0000	6.0000	6.0000
Vacant	0.0000	0.0000	0.0000	0.0019	0.0000	0.0000	0.0000	0.0000	0.0000
Ca	0.0048	0.0061	0.0234	0.0021	0.0046	0.0021	0.0000	0.0015	0.0000
Na	0.0069	0.0029	0.0169	0.0019	0.0066	0.0051	0.0029	0.0002	0.0018
K	0.0150	0.0244	0.0196	0.0050	0.0027	0.0009	0.0058	0.0029	0.0000
Rb	0.0000	0.0000	0.0000	0.0000	0.0000	0.0000	0.0000	0.0000	0.0000
Total	0.0267	0.0334	0.0599	0.0089	0.0139	0.0081	0.0088	0.0046	0.0018
OH	7.9835	7.9858	7.9834	7.9761	7.9790	7.9791	7.9711	7.9632	7.9770
F	0.0000	0.0000	0.0000	0.0011	0.0000	0.0000	0.0000	0.0000	0.0000
Cl	0.0165	0.0142	0.0166	0.0229	0.0210	0.0209	0.0289	0.0368	0.0230
TOTAL	8.0000	8.0000	8.0000	8.0000	8.0000	8.0000	8.0000	8.0000	8.0000

Apêndice Y. Análises de química mineral por microssonda eletrônica em clorita.

	JAT-03 (130,05)	JAT-03 (130,05)	JAT-03 (130,05)	JAT-03 (130,05)	JAT-03 (130,05)	JAT-03 (130,05)	JAT-03 (130,05)
	Diabásio	Diabásio	Diabásio	Diabásio	Diabásio	Diabásio	Diabásio
	Chl 2	Chl 2	Chl 2	Chl 2	Chl 2	Chl 2	Chl 2
Óxido (%)							
SiO2	25.810	24.910	25.27	25.95	25.67	25.88	25.62
TiO2	0.006	0.031	0.02	0.06	0.10	0.09	0.08
Al2O3	20.810	21.010	21.05	21.01	21.02	20.54	21.01
FeO	22.410	23.520	23.32	23.07	23.18	23.07	23.06
MnO	0.024	0.053	0.04	0.03	0.02	0.05	0.04
ZnO	0.063	0.061	0.07	0.10	0.04	0.04	0.09
MgO	18.450	17.290	17.33	17.47	17.42	17.77	17.71
CaO	0.000	0.036	0.04	0.01	0.01	0.02	0.02
Na2O	0.009	0.030	0.02	0.02	0.03	0.02	0.01
K2O	0.000	0.000	0.03	0.01	0.00	0.05	0.03
F	0.000	0.004	0.01	0.00	0.00	0.00	0.00
Cl	0.131	0.158	0.19	0.10	0.14	0.18	0.14
O=F	0.000	0.002	0.01	0.00	0.00	0.00	0.00
O=Cl	0.030	0.036	0.04	0.02	0.03	0.04	0.03
Total](%)	87.684	87.066	87.33	87.80	87.59	87.66	87.76
[H2O(c)	11.5585	11.3794	11.40	11.51	11.47	11.47	11.51
Fe2O3(c)	1.5280	1.8873	1.18	0.17	0.53	0.74	1.03
FeO(c)](%)	21.0351	21.8218	22.26	22.92	22.70	22.40	22.13
Fórmula (apfu)							
Si	2.6704	2.6158	2.6456	2.6978	2.6762	2.6957	2.6626
Ti	0.0005	0.0025	0.0015	0.0045	0.0078	0.0069	0.0059
Al	2.5375	2.6002	2.5974	2.5743	2.5828	2.5215	2.5734
Fe(3+)	0.1190	0.1491	0.0928	0.0134	0.0414	0.0579	0.0805
Fe(2+)	1.8201	1.9163	1.9490	1.9923	1.9796	1.9516	1.9237
Mn	0.0021	0.0047	0.0038	0.0026	0.0019	0.0040	0.0035
Zn	0.0048	0.0047	0.0051	0.0075	0.0029	0.0030	0.0067
Mg	2.8457	2.7066	2.7048	2.7076	2.7074	2.7593	2.7438
Ca	0.0000	0.0040	0.0042	0.0007	0.0013	0.0020	0.0020
Na	0.0018	0.0061	0.0038	0.0047	0.0051	0.0046	0.0013
K	0.0000	0.0000	0.0034	0.0015	0.0000	0.0068	0.0040
F	0.0000	0.0013	0.0045	0.0000	0.0000	0.0000	0.0000
Cl	0.0230	0.0280	0.0329	0.0176	0.0247	0.0316	0.0240
OH](apfu)	7.9770	7.9707	7.9626	7.9824	7.9753	7.9684	7.9760
Si	2.6704	2.6158	2.6456	2.6978	2.6762	2.6957	2.6626
B	0.0000	0.0000	0.0000	0.0000	0.0000	0.0000	0.0000
Al(IV)	1.3296	1.3842	1.3544	1.3022	1.3238	1.3043	1.3374
Total]Tetrahedral	4.0000	4.0000	4.0000	4.0000	4.0000	4.0000	4.0000
[Al(VI)	1.2079	1.2160	1.2430	1.2721	1.2590	1.2172	1.2360
Ti	0.0005	0.0025	0.0015	0.0045	0.0078	0.0069	0.0059
Fe3+	0.1190	0.1491	0.0928	0.0134	0.0414	0.0579	0.0805
Fe2+	1.8201	1.9163	1.9490	1.9923	1.9796	1.9516	1.9237
Mn	0.0021	0.0047	0.0038	0.0026	0.0019	0.0040	0.0035
Zn	0.0048	0.0047	0.0051	0.0075	0.0029	0.0030	0.0067
Cu	0.0000	0.0000	0.0000	0.0000	0.0000	0.0000	0.0000
Mg	2.8457	2.7066	2.7048	2.7076	2.7074	2.7593	2.7438
Σ-Octahedral	6.0000	6.0000	6.0000	6.0000	6.0000	6.0000	6.0000
Vacant	0.0000	0.0000	0.0000	0.0000	0.0000	0.0000	0.0000
Ca	0.0000	0.0040	0.0042	0.0007	0.0013	0.0020	0.0020
Na	0.0018	0.0061	0.0038	0.0047	0.0051	0.0046	0.0013
K	0.0000	0.0000	0.0034	0.0015	0.0000	0.0068	0.0040
Total	0.0018	0.0101	0.0113	0.0069	0.0064	0.0134	0.0072
[OH	7.9770	7.9707	7.9626	7.9824	7.9753	7.9684	7.9760
F	0.0000	0.0013	0.0045	0.0000	0.0000	0.0000	0.0000
Cl	0.0230	0.0280	0.0329	0.0176	0.0247	0.0316	0.0240
Total	8.0000	8.0000	8.0000	8.0000	8.0000	8.0000	8.0000

Apêndice W. Análises de química mineral por microssonda eletrônica em magnetita.

	JAT-28 (91,60)	JAT-28 (91,60)	JAT-28 (91,60)	JAT-28 (91,60)	JAT-28 (91,60)	JAT-28 (91,60)	JAT-28 (91,60)	JAT-28 (91,60)	JAT-28 (91,60)	JAT-28 (91,60)	JAT-28 (91,60)	JAT-28 (91,60)	JAT-28 (91,60)
	MVM MT 2	MVM MT 2	MVM MT 2	MVM MT 2	MVM MT 2	MVM MT 2	MVM MT 2	MVM MT 2	MVM MT 2	MVM MT 2	MVM MT 2	MVM MT 2	MVM MT 2
xido (%)													
	0.07660	0.09380	0.10740	0.08350	0.06700	0.13630	0.13340	0.07910	0.12680	0.10830	0.06820	0.43860	0.13150
CO2	0.0000	0.0000	0.2530	0.0204	0.2325	0.3104	0.0000	0.1507	0.0000	0.0000	0.0000	0.3435	0.1998
2O3	0.0764	0.0450	0.0647	0.0442	0.0369	0.0145	0.0482	0.0656	0.0963	0.0403	0.1457	0.1794	0.0646
r2O3	0.0079	0.0356	0.0000	0.0106	0.0000	0.0000	0.0000	0.0408	0.0000	0.0066	0.0026	0.0199	0.0040
e2O3	103.8000	103.4800	103.1300	103.28	102.87	103.04	102.74	103.03	102.77	103.69	103.58	101.59	102.94
eO	93.3992	93.1113	92.7964	92.9313	92.5624	92.7154	92.4455	92.7064	92.4724	93.3003	93.2013	91.4107	92.6254
2O3	0.2040	0.0382	0.2361	0.0106	0.2433	0.1937	0.1821	0.1962	0.1863	0.1874	0.1951	0.1817	0.1736
uO	0.0000	0.1236	0.0000	0.0000	0.0000	0.0186	0.0000	0.0000	0.0000	0.0000	0.0000	0.0000	0.0198
mO	0.0075	0.0000	0.0000	0.0037	0.0168	0.0379	0.0001	0.0080	0.0000	0.0000	0.0245	0.0000	0.0198
2O	0.0000	0.0248	0.0064	0.0000	0.0184	0.0326	0.0455	0.0077	0.0145	0.0000	0.0000	0.0713	0.0325
aa	0.0000	0.0091	0.0226	0.0139	0.0000	0.0042	0.0000	0.0028	0.0000	0.0010	0.0000	0.0000	0.0000
iO	0.0086	0.0000	0.0143	0.0029	0.0000	0.0150	0.0000	0.0000	0.0324	0.0000	0.0154	0.0084	0.0000
gO	0.0224	0.0003	0.0407	0.0093	0.0343	0.0013	0.0318	0.0000	0.0010	0.0007	0.0000	0.1728	0.0433
nO	0.0000	0.0382	0.0000	0.0000	0.0000	0.0164	0.0360	0.0257	0.0000	0.0000	0.0000	0.0170	0.0433
OTAL	93.7260	93.4261	93.4342	93.0469	93.1446	93.3600	92.7892	93.2039	92.8029	93.5363	93.5846	92.4047	93.2261
órmula (apfu)						(4 O)							
	0.003	0.004	0.004	0.003	0.003	0.006	0.005	0.003	0.005	0.004	0.003	0.018	0.005
	0.000	0.000	0.008	0.001	0.007	0.010	0.000	0.005	0.000	0.000	0.000	0.011	0.006
	0.004	0.002	0.003	0.002	0.002	0.001	0.002	0.003	0.005	0.002	0.007	0.009	0.003
r	0.000	0.001	0.000	0.000	0.000	0.000	0.000	0.001	0.000	0.000	0.000	0.001	0.000
e3+	1.991	1.988	1.987	1.990	1.992	1.983	1.983	1.990	1.984	1.987	1.992	1.946	1.984
e2+	0.405	0.408	0.395	0.410	0.391	0.399	0.407	0.396	0.406	0.411	0.400	0.415	0.399	
	0.007	0.001	0.008	0.000	0.008	0.006	0.006	0.006	0.006	0.006	0.006	0.006	0.006
Cuu	0.000	0.005	0.000	0.000	0.000	0.001	0.000	0.000	0.000	0.000	0.000	0.000	0.001
Mm	0.000	0.000	0.000	0.000	0.001	0.001	0.000	0.000	0.000	0.000	0.001	0.000	0.001
Ni	0.000	0.000	0.000	0.000	0.000	0.000	0.000	0.000	0.001	0.000	0.001	0.000	0.000
(	0.000	0.001	0.000	0.000	0.001	0.002	0.002	0.000	0.001	0.000	0.000	0.004	0.002
Ca	0.787	0.790	0.787	0.793	0.790	0.788	0.793	0.790	0.793	0.788	0.788	0.787	0.789
Mgg	0.001	0.000	0.002	0.001	0.002	0.000	0.002	0.000	0.000	0.000	0.000	0.011	0.003
Zn	0.000	0.001	0.000	0.000	0.000	0.000	0.001	0.001	0.000	0.000	0.000	0.001	0.001
Tottal	3.198	3.202	3.196	3.200	3.196	3.197	3.203	3.197	3.201	3.199	3.198	3.207	3.199
Enod-members													
Spiinel	0.001	0.000	0.002	0.001	0.002	0.000	0.002	0.000	0.000	0.000	0.000	0.011	0.003
Hercynite	-0.591	-0.587	-0.614	-0.586	-0.620	-0.612	-0.584	-0.609	-0.586	-0.582	-0.596	-0.579	-0.605
Galaxite	0.000	0.000	0.000	0.000	0.001	0.001	0.000	0.000	0.000	0.000	0.001	0.000	0.001
Galahnite	0.000	0.001	0.000	0.000	0.000	0.000	0.001	0.001	0.000	0.000	0.000	0.001	0.001
Tevorite	0.000	0.000	0.000	0.000	0.000	0.000	0.000	0.000	0.001	0.000	0.001	0.000	0.000
Maagnetite	0.995	0.994	0.993	0.995	0.996	0.992	0.992	0.995	0.992	0.993	0.996	0.973	0.992
Chromite	0.000	0.001	0.000	0.000	0.000	0.000	0.000	0.001	0.000	0.000	0.000	0.000	0.000
Ulvöspinel	0.000	0.000	0.008	0.001	0.007	0.010	0.000	0.005	0.000	0.000	0.000	0.011	0.006

Apêndice Z. Análises de química mineral por microssonda eletrônica em magnetita.

	JAT-28 (91,60)	JAT-28 (91,60)	JAT-28 (91,60)	JAT-28 (91,60)	JAT-28 (91,60)	JAT-28 (91,60)	JAT-28 (91,60)	JAT-28 (91,60)	JAT-28 (91,60)
	Veios-Precoces	Veios-Precoces	Veios-Precoces	Veios-Precoces	Veios-Precoces	Veios-Precoces	Veios-Precoces	Veios-Precoces	Veios-Precoces
	MT 3	MT 3	MT 3	MT 3	MT 3	MT 3	MT 3	MT 3	MT 3
Óxido (%)									
Si	0.042	0.0613	0.078	0.071	0.3049	0.0848	0.0901	12312	0.0571
TiO2	4.95	0.2728	2.03	0.212	0.2653	0	0.1508	1.5	0
Al2O3	0.0342	0.0505	0.0698	0.0446	0.1429	0.0874	0.067	0.0868	0.07
Cr2O3	0.0055	0.0211	0.0522	0	0.0079	0.0118	0.0145	0.26	0
Fe2O3	97.96	102.66	101.65	103.29	103.03	103.04	102.66	99.75	103.36
FeO	88.144	92.373	91.464	92.9403	92.7063	92.7153	92.3734	89.755	93.0033
V2O3	0.2186	0.2062	0.2117	0.2196	0.2853	0.2736	0.2848	0.26	0.2727
CuO	0	0.0246	0	0	0.0359	0	0	0	0
MnO	0.1258	0.0174	0.0303	0	0	0.0068	0	0	0.0153
K2O	0	0.0234	0.0113	0.0064	0.0202	0.019	0	0.0168	0.0109
Ca	0	0	0.0018	0.0317	0.0723	0.0143	0.0001	0.8627	0.0138
NiO	0	0.0059		0.0218	0.0141	0.0128	0.0073	0.0053	0.0055
MgO	0.0428	0.0075	0.0031	0	0.0205	0	0.0084	0.0038	0.0027
ZnO	0.0269	0	0.0225	0	0	0.0352	0	0	0
Total	93.5482	93.0028	93.897	93.4764	93.5707	93.1762	92.9063	92.750	93.3942
				4(O)					
Fórmula (apfu)									
Si	0.002	0.003	0.003	0.003	0.012	0.003	0.004	1.992	0.002
Ti	0.147	0.008	0.061	0.007	0.008	0.000	0.005	0.000	0.000
Al	0.002	0.002	0.003	0.002	0.007	0.004	0.003	0.000	0.003
Cr	0.000	0.001	0.002	0.000	0.000	0.000	0.000	0.000	0.000
Fe3+	1.995	1.992	1.991	1.991	1.963	1.990	1.989	1515.018	1.993
Fe2+	0.195	0.387	0.320	0.396	0.413	0.399	0.394	1517.330	0.399
V	0.007	0.007	0.007	0.007	0.009	0.009	0.009	0.000	0.009
Cu	0.000	0.001	0.000	0.000	0.001	0.000	0.000	0.000	0.000
Mn	0.004	0.001	0.001	0.000	0.000	0.000	0.000	0.000	0.001
Ni	0.000	0.000	0.000	0.001	0.000	0.000	0.000	0.000	0.000
K	0.000	0.001	0.001	0.000	0.001	0.001	0.000	0.000	0.001
Ca	0.763	0.791	0.775	0.788	0.783	0.791	0.792	0.003	0.790
Mg	0.003	0.000	0.000	0.000	0.001	0.000	0.001	0.000	0.000
Zn	0.001	0.000	0.001	0.000	0.000	0.001	0.000	0.000	0.000
Total	3.119	3.195	3.165	3.195	3.200	3.199	3.197	4.308	3.198
End-members									
Spinel	0.003	0.000	0.000	0.000	0.001	0.000	0.001	0.000	0.000
Hercynite	-1.097	-0.626	-0.799	-0.613	-0.585	-0.596	-0.610	2274.838	-0.597
Galaxite	0.004	0.001	0.001	0.000	0.000	0.000	0.000	0.000	0.001
Gahnite	0.001	0.000	0.001	0.000	0.000	0.001	0.000	0.000	0.000
Trevorite	0.000	0.000	0.000	0.001	0.000	0.000	0.000	0.000	0.000
Magnetite	0.998	0.996	0.995	0.996	0.981	0.995	0.994	-757.509	0.996
Chromite	0.000	0.000	0.001	0.000	0.000	0.000	0.000	0.000	0.000
Ulvöspinel	0.147	0.008	0.061	0.007	0.008	0.000	0.005	0.000	0.000

Apêndice AA. Análises de química mineral por microssonda eletrônica em magnetita.

	JAT-32 (383,00)	JAT-32 (383,00)	JAT-32 (383,00)	JAT-32 (383,00)
	Magnetitito	Magnetitito	Magnetitito	Magnetitito
	MT 4	MT 4	MT 4	MT 4
Óxido (%)				
Si	16390	0.2727	0	0.0773
TiO2	0.336	0.0082	0.1715	0.4572
Al2O3	0.1073	0.0097	0.1054	0.0268
Cr2O3	0.0186	0	0.0475	0.0119
Fe2O3	100.41	99.7	104.2	104.36
FeO	90.3489	89.710	93.759	93.9031
V2O3	0.3389	0.329	0.3447	0.3422
CuO	0	0.0297	0.0607	0
MnO	0.0546	0	0.0346	0
K2O	0	0	0.0034	0.0055
Ca	0.0466	0	0	0
NiO	0.0148	0.0404	0.0093	0.0101
MgO	0.5569	0.1702	0.0325	0.002
ZnO	0.0258		0	0.0049
Total	91.8484	90.297	94.568	94.7637
Fórmula (apfu)				
		4(O)		
Si	1.994	0.011	0.000	0.003
Ti	0.000	0.000	0.005	0.014
Al	0.000	0.000	0.005	0.001
Cr	0.000	0.000	0.002	0.000
Fe3+	-2028.386	1.966	2.000	1.991
Fe2+	2030.726	0.402	0.382	0.389
V	0.000	0.011	0.011	0.011
Cu	0.000	0.001	0.002	0.000
Mn	0.000	0.000	0.001	0.000
Ni	0.000	0.001	0.000	0.000
K	0.000	0.000	0.000	0.000
Ca	0.002	0.807	0.781	0.778
Mg	0.000	0.011	0.002	0.000
Zn	0.000	0.000	0.000	0.000
Total	4.336	3.211	3.192	3.188
End-members				
Spinel	0.000	0.011	0.002	0.000
Hercynite	3044.919	-0.581	-0.629	-0.634
Galaxite	0.000	0.000	0.001	0.000
Gahnite	0.000	0.000	0.000	0.000
Trevorite	0.000	0.001	0.000	0.000
Magnetite	-1014.193	0.983	1.000	0.995
Chromite	0.000	0.000	0.001	0.000
Ulvöspinel	0.000	0.000	0.005	0.014

Apêndice AB. Análises de química mineral por microssonda eletrônica em magnetita.

	JAT-28 (91,60)	JAT-28 (91,60)	JAT-28 (91,60)	JAT-28 (91,60)	JAT-28 (91,60)	JAT-28 (91,60)	JAT-28 (91,60)	JAT-28 (91,60)	JAT-28 (91,60)	JAT-28 (91,60)	JAT-28 (160,40)
	ZC/Min-II	ZC/Min-II	ZC/Min-II	ZC/Min-II	ZC/Min-II	ZC/Min-II	ZC/Min-II	ZC/Min-II	ZC/Min-II	ZC/Min-II	ZC/Min-II
	MT 5	MT 5	MT 5	MT 5	MT 5	MT 5	MT 5	MT 5	MT 5	MT 5	MT 5
Óxido (%)											
Si	0.15070	0.10670	0.09600	0.17790	0.18610	0.17820	0.12110	0.10130	0.12660	0.11620	0.07320
TiO2	0.0000	0.1957	0.1182	0.0000	0.1835	0.0000	0.1428	0.0163	0.1796	0.0489	0.2727
Al2O3	0.0675	0.0289	0.0427	0.0241	0.0507	0.0709	0.0408	0.0435	0.0324	0.0576	0.0970
Cr2O3	0.0000	0.0013	0.0369	0.0224	0.0000	0.0000	0.0105	0.0369	0.0581	0.0013	0.0514
Fe2O3	103.30	103.71	103.28	102.35	102.37	102.94	102.72	102.78	102.59	103.03	102.38
FeO	92.9493	93.3183	92.9313	92.0945	92.1125	92.6254	92.4275	92.4814	92.3105	92.7064	92.1215
V2O3	0.2130	0.2187	0.2116	0.1601	0.1693	0.1878	0.1576	0.1624	0.1760	0.1688	0.3405
CuO	0.0000	0.0247	0.0000	0.0581	0.0000	0.0000	0.0247	0.0185	0.0297	0.0408	0.0480
MnO	0.0094	0.0023	0.0000	0.0000	0.0155	0.0017	0.0017	0.0196	0.0017	0.0133	0.0000
K2O	0.0394	0.0428	0.0000	0.0101	0.0291	0.0612	0.0373	0.0728	0.0476	0.0693	0.0032
Ca	0.0147	0.0000	0.0000	0.0143	0.0207	0.0599	0.0176	0.0605	0.0602	0.0272	0.0108
NiO	0.0066	0.0238	0.0086	0.0000	0.0276	0.0097	0.0097	0.0097	0.0313	0.0141	0.0174
MgO	0.0000	0.0000	0.0000	0.0087	0.0201	0.0379	0.0379	0.0233	0.0293	0.0427	0.0129
ZnO	0.0051	0.0000	0.0221	0.0163	0.0166	0.0455	0.0307	0.0061	0.0455	0.0265	0.0000
Total	93.3050	93.8565	93.3714	92.4086	92.6456	93.1000	92.9388	92.9510	93.0019	93.2169	92.9754
Formula (apfu)						4(O)					
Si	0.006	0.004	0.004	0.007	0.008	0.007	0.005	0.004	0.005	0.005	0.003
Ti	0.000	0.006	0.004	0.000	0.006	0.000	0.004	0.001	0.006	0.002	0.008
Al	0.003	0.001	0.002	0.001	0.002	0.003	0.002	0.002	0.002	0.003	0.005
Cr	0.000	0.000	0.001	0.001	0.000	0.000	0.000	0.001	0.002	0.000	0.002
Fe3+	1.981	1.987	1.988	1.978	1.977	1.978	1.985	1.987	1.984	1.986	1.991
Fe2+	0.412	0.402	0.401	0.413	0.406	0.412	0.400	0.402	0.397	0.403	0.380
V	0.007	0.007	0.007	0.005	0.006	0.006	0.005	0.005	0.006	0.006	0.011
Cu	0.000	0.001	0.000	0.002	0.000	0.000	0.001	0.001	0.001	0.002	0.002
Mn	0.000	0.000	0.000	0.000	0.001	0.000	0.000	0.001	0.000	0.000	0.000
Ni	0.000	0.001	0.000	0.000	0.001	0.000	0.000	0.000	0.001	0.000	0.001
K	0.002	0.002	0.000	0.001	0.002	0.003	0.002	0.004	0.002	0.004	0.000
Ca	0.789	0.785	0.789	0.795	0.792	0.790	0.792	0.793	0.791	0.790	0.790
Mg	0.000	0.000	0.000	0.001	0.001	0.002	0.002	0.001	0.002	0.003	0.001
Zn	0.000	0.000	0.001	0.000	0.001	0.001	0.001	0.000	0.001	0.001	0.000
Total	3.202	3.197	3.197	3.204	3.201	3.205	3.201	3.203	3.200	3.203	3.194
End-members											
Spinel	0.000	0.000	0.000	0.001	0.001	0.002	0.002	0.001	0.002	0.003	0.001
Hercynite	-0.579	-0.604	-0.601	-0.577	-0.594	-0.577	-0.601	-0.593	-0.607	-0.593	-0.633
Galaxite	0.000	0.000	0.000	0.000	0.001	0.000	0.000	0.001	0.000	0.000	0.000
Gahnite	0.000	0.000	0.001	0.000	0.001	0.001	0.001	0.000	0.001	0.001	0.000
Trevorite	0.000	0.001	0.000	0.000	0.001	0.000	0.000	0.000	0.001	0.000	0.001
Magnetite	0.991	0.993	0.994	0.989	0.988	0.989	0.993	0.994	0.992	0.993	0.995
Chromite	0.000	0.000	0.001	0.000	0.000	0.000	0.000	0.001	0.001	0.000	0.001
Ulvöspinel	0.000	0.006	0.004	0.000	0.006	0.000	0.004	0.001	0.006	0.002	0.008

Apêndice AC. Análises de química mineral por microssonda eletrônica em magnetita.

	JAT-28 (160,40)	JAT-28 (160,40)	JAT-28 (160,40)	JAT-28 (160,40)	JAT-28 (160,40)	JAT-28 (160,40)	JAT-28 (160,40)	JAT-28 (160,40)	JAT-28 (160,40)	JAT-28 (160,40)	JAT-28 (160,40)
	ZC/Min-II	ZC/Min-II	ZC/Min-II	ZC/Min-II	ZC/Min-II	ZC/Min-II	ZC/Min-II	ZC/Min-II	ZC/Min-II	ZC/Min-II	ZC/Min-II
	MT 5	MT 5	MT 5	MT 5	MT 5	MT 5	MT 5	MT 5	MT 5	MT 5	MT 5
ÓXIDO (%)											
Si	0.07320	0.08270	0.12440	0.06820	0.10070	0.07910	0.09670	0.06020	0.76050	0.09750	0.10320
TiO2	0.2727	0.0000	0.0000	0.3141	0.2285	0.0937	0.0000	0.3709	0.1308	0.0775	0.0204
Al2O3	0.0970	0.1018	0.0848	0.0741	0.0852	0.0776	0.0504	0.0966	0.1618	0.1064	0.0682
Cr2O3	0.0514	0.0922	0.0447	0.0581	0.0449	0.0764	0.0685	0.1202	0.0344	0.0422	0.1332
Fe2O3	102.38	103.00	102.94	102.32	103.29	103.11	102.43	102.74	101.72	103.25	102.54
FeO	92.1215	92.6794	92.6254	92.0675	92.9403	92.7784	92.1665	92.4455	91.5277	92.9044	92.2655
V2O3	0.3405	0.3508	0.3392	0.3513	0.3522	0.3476	0.3826	0.3279	0.3413	0.3736	0.4707
CuO	0.0480	0.0000	0.0666	0.0037	0.0853	0.0642	0.1024	0.0000	0.1051	0.0815	0.0964
MnO	0.0000	0.0016	0.0084	0.0057	0.0000	0.0049	0.0032	0.0136	0.0000	0.0000	0.0112
K2O	0.0032	0.0067	0.0000	0.0000	0.0148	0.0000	0.0013	0.0052	0.0221	0.0184	0.0052
Ca	0.0108	0.0000	0.0096	0.0184	0.0140	0.0126	0.0000	0.0003	0.0156	0.0141	0.0028
NiO	0.0174	0.0297	0.0233	0.0000	0.0075	0.0194	0.0101	0.0167	0.0066	0.0000	0.0090
MgO	0.0129	0.0000	0.0000	0.0251	0.0044	0.0000	0.0126	0.0000	0.2764	0.0109	0.0155
ZnO	0.0000	0.0029	0.0000	0.0080	0.0000	0.0000	0.0135	0.0000	0.0291	0.0000	0.0000
Total	92.9754	93.2651	93.2020	92.9260	93.7771	93.4748	92.8111	93.3969	92.6509	93.6290	93.0981
Formula (apfu)						4(O)					
Si	0.003	0.003	0.005	0.003	0.004	0.003	0.004	0.002	0.031	0.004	0.004
Ti	0.008	0.000	0.000	0.010	0.007	0.003	0.000	0.011	0.004	0.002	0.001
Al	0.005	0.005	0.004	0.004	0.004	0.004	0.002	0.005	0.008	0.005	0.003
Cr	0.002	0.003	0.001	0.002	0.001	0.002	0.002	0.004	0.001	0.001	0.004
Fe3+	1.991	1.990	1.985	1.992	1.988	1.990	1.988	1.993	1.906	1.988	1.987
Fe2+	0.380	0.394	0.400	0.379	0.390	0.391	0.393	0.377	0.453	0.393	0.388
V	0.011	0.012	0.011	0.012	0.011	0.011	0.013	0.011	0.011	0.012	0.015
Cu	0.002	0.000	0.003	0.000	0.003	0.002	0.004	0.000	0.004	0.003	0.004
Mn	0.000	0.000	0.000	0.000	0.000	0.000	0.000	0.000	0.000	0.000	0.000
Ni	0.001	0.001	0.001	0.000	0.000	0.001	0.000	0.001	0.000	0.000	0.000
K	0.000	0.000	0.000	0.000	0.001	0.000	0.000	0.000	0.001	0.001	0.000
Ca	0.790	0.790	0.790	0.791	0.785	0.788	0.793	0.787	0.780	0.786	0.790
Mg	0.001	0.000	0.000	0.002	0.000	0.000	0.001	0.000	0.017	0.001	0.001
Zn	0.000	0.000	0.000	0.000	0.000	0.000	0.000	0.000	0.001	0.000	0.000
Total	3.194	3.198	3.200	3.193	3.195	3.196	3.200	3.191	3.218	3.197	3.199
End-members											
Spinel	0.001	0.000	0.000	0.002	0.000	0.000	0.001	0.000	0.017	0.001	0.001
Hercynite	-0.633	-0.602	-0.593	-0.637	-0.619	-0.611	-0.603	-0.644	-0.508	-0.606	-0.609
Galaxite	0.000	0.000	0.000	0.000	0.000	0.000	0.000	0.000	0.000	0.000	0.000
Gahnite	0.000	0.000	0.000	0.000	0.000	0.000	0.000	0.000	0.001	0.000	0.000
Trevorite	0.001	0.001	0.001	0.000	0.000	0.001	0.000	0.001	0.000	0.000	0.000
Magnetite	0.995	0.995	0.992	0.996	0.994	0.995	0.994	0.996	0.953	0.994	0.994
Chromite	0.001	0.001	0.001	0.001	0.001	0.001	0.001	0.002	0.001	0.001	0.002
Ulvöspinel	0.008	0.000	0.000	0.010	0.007	0.003	0.000	0.011	0.004	0.002	0.001

Apêndice AD. Análises de química mineral por microssonda eletrônica em magnetita.

	JAT-28 (160,40) ZC/Min-II MT 5	JAT-28 (160,40) ZC/Min-II MT 5	JAT-28 (160,40) ZC/Min-II MT 5	JAT-28 (160,40) ZC/Min-II MT 5	JAT-28 (160,40) ZC/Min-II MT 5	JAT-28 (160,40) ZC/Min-II MT 5	JAT-28 (160,40) ZC/Min-II MT 5	JAT-28 (160,40) ZC/Min-II MT 5	JAT-28 (160,40) ZC/Min-II MT 5	JAT-28 (160,40) ZC/Min-II MT 5
ÓXIDO (%)										
Si	0.13120	0.06110	0.07120	0.05890	0.09320	0.11130	0.08010	0.10100	0.08980	0.05870
TiO2	0.1549	0.1386	0.2283	0.1018	0.0449	0.0000	0.0000	48.6700	48.6400	48.8600
Al2O3	0.0911	0.0763	0.0756	0.0754	0.0662	0.0656	0.0771	0.0191	0.0079	0.0302
Cr2O3	0.0409	0.1174	0.1240	0.0105	0.1504	0.1528	0.0158	0.0594	0.0000	0.0099
Fe2O3	102.34	102.60	102.08	102.99	102.45	102.59	102.20	53.30	52.83	53.35
FeO	92.0855	92.3195	91.8516	92.6704	92.1845	92.3105	91.9596	47.9593	47.5364	48.0043
V2O3	0.3367	0.3334	0.3440	0.3711	0.3667	0.3621	0.3963	0.2978	0.3040	0.2851
CuO	0.0592	0.0482	0.0000	0.0913	0.0000	0.0050	0.1051	0.0560	0.0871	0.0125
MnO	0.0000	0.0000	0.0000	0.0131	0.0000	0.0187	0.0000	0.1637	0.1847	0.1749
K2O	0.0163	0.0125	0.0050	0.0228	0.0138	0.0000	0.0187	0.0345	0.0871	0.0157
Ca	0.0012	0.0110	0.0170	0.0000	0.0120	0.0135	0.0101	0.0059	0.0176	0.0000
NiO	0.0106	0.0165	0.0051	0.0000	0.0117	0.0277	0.0112	0.0224	0.0088	0.0000
MgO	0.0329	0.0101	0.0076	0.0000	0.0096	0.0000	0.0328	0.0238	0.0382	0.0161
ZnO	0.0000	0.0000	0.0000	0.0000	0.0000	0.0229	0.0000	0.0000	0.0000	0.0171
Total	92.8293	93.0835	92.6582	93.3564	92.8598	92.9788	92.6267	97.3119	96.9118	97.4258
Fórmula (apfu)					4(O)					
Si	0.005	0.003	0.003	0.002	0.004	0.005	0.003	0.003	0.003	0.002
Ti	0.005	0.004	0.007	0.003	0.001	0.000	0.000	1.097	1.099	1.100
Al	0.004	0.004	0.004	0.004	0.003	0.003	0.004	0.001	0.000	0.001
Cr	0.001	0.004	0.004	0.000	0.005	0.005	0.001	0.001	0.000	0.000
Fe3+	1.984	1.992	1.991	1.993	1.988	1.986	1.990	1.991	1.992	1.995
Fe2+	0.391	0.384	0.381	0.388	0.391	0.395	0.389	-1.089	-1.095	-1.093
V	0.011	0.011	0.011	0.012	0.012	0.012	0.013	0.007	0.007	0.007
Cu	0.002	0.002	0.000	0.004	0.000	0.000	0.004	0.002	0.002	0.000
Mn	0.000	0.000	0.000	0.000	0.000	0.001	0.000	0.004	0.005	0.004
Ni	0.000	0.001	0.000	0.000	0.000	0.001	0.000	0.001	0.000	0.000
K	0.001	0.001	0.000	0.001	0.001	0.000	0.001	0.001	0.003	0.001
Ca	0.791	0.791	0.793	0.789	0.792	0.791	0.794	0.578	0.579	0.577
Mg	0.002	0.001	0.000	0.000	0.001	0.000	0.002	0.001	0.002	0.001
Zn	0.000	0.000	0.000	0.000	0.000	0.001	0.000	0.000	0.000	0.000
Total	3.199	3.196	3.195	3.197	3.198	3.199	3.201	2.597	2.598	2.595
End-members										
Spinel	0.002	0.001	0.000	0.000	0.001	0.000	0.002	0.001	0.002	0.001
Hercynite	-0.611	-0.623	-0.631	-0.614	-0.609	-0.601	-0.607	-4.278	-4.289	-4.290
Galaxite	0.000	0.000	0.000	0.000	0.000	0.001	0.000	0.004	0.005	0.004
Gahnite	0.000	0.000	0.000	0.000	0.000	0.001	0.000	0.000	0.000	0.000
Trevorite	0.000	0.001	0.000	0.000	0.000	0.001	0.000	0.001	0.000	0.000
Magnetite	0.992	0.996	0.996	0.996	0.994	0.993	0.995	0.995	0.996	0.997
Chromite	0.001	0.002	0.002	0.000	0.002	0.002	0.000	0.001	0.000	0.000
Ulvöspinel	0.005	0.004	0.007	0.003	0.001	0.000	0.000	1.097	1.099	1.100

Apêndice 2

Análises químicas de rocha total

SAMPLE	Locality	Petrology	SiO2	Al2O3	Fe2O3	MgO	CaO	Na2O	K2O
JAT-32/357,10	JAT-Min (I)	Minério	0.00	0.32	63.91	1.14	7.16	0.08	0.00
JAT-32/358,90	JAT-Min (I)	Minério	0.00	0.26	63.91	0.99	6.65	0.00	0.00
JAT-32/362,80	JAT-Min (I)	Minério	0.00	0.30	71.49	0.60	3.34	0.07	0.00
JAT-15/194,20	JAT-Min (II)	Brecha	20.31	4.60	32.90	2.51	5.42	0.02	2.12
JAT-28/160,40A	JAT-Min (II)	Foliacao	19.02	2.23	50.45	1.33	8.99	0.00	0.69
JAT-28/160,40B	JAT-Min (II)	Brecha	20.18	2.56	46.80	1.66	9.25	0.01	1.18
JAT-3/81,65	JAR-Min (IV)	Minerio	27.84	3.71	25.30	1.39	6.59	0.02	1.06
JAT-15/186,74	JAR-Min (IV)	Minerio	24.49	4.89	26.41	2.46	11.47	0.00	1.91
JAT-28/119,00	JAR-Min (IV)	Minerio	41.22	8.51	21.00	1.99	1.08	0.44	4.77
JAT-15/185,22	JAR-Min (IV)	Minerio	19.37	1.96	34.19	0.92	0.40	0.03	0.95

SAMPLE	Locality	Petrology	TiO2	P2O5	MnO	Cr2O3	LOI	C/TOT	S/TOT
JAT-32/357,10	JAT-Min (I)	Minério	0.22	4.45	0.04	0.04	0.00	0.00	0.00
JAT-32/358,90	JAT-Min (I)	Minério	0.17	4.32	0.03	0.03	0.00	0.00	0.00
JAT-32/362,80	JAT-Min (I)	Minério	0.00	0.21	0.01	0.01	0.00	0.00	0.00
JAT-15/194,20	JAT-Min (II)	Brecha	0.48	3.85	0.02	0.01	11.30	0.00	16.70
JAT-28/160,40A	JAT-Min (II)	Foliacao	1.06	6.32	0.01	0.03	5.10	0.00	8.94
JAT-28/160,40B	JAT-Min (II)	Brecha	0.89	6.39	0.02	0.01	5.20	0.00	10.41
JAT-3/81,65	JAR-Min (IV)	Minerio	0.32	4.69	0.02	0.01	10.50	0.00	14.07
JAT-15/186,74	JAR-Min (IV)	Minerio	0.88	7.97	0.03	0.01	8.40	0.00	12.86
JAT-28/119,00	JAR-Min (IV)	Minerio	0.23	0.07	0.02	0.00	8.00	0.03	11.04
JAT-15/185,22	JAR-Min (IV)	Minerio	0.17	0.25	0.00	0.00	13.60	0.00	23.51

SAMPLE	Locality	Petrology	Ba	Rb	Sr	Cs	Ga	Tl	Ta
JAT-32/357,10	JAT-Min (I)	Minério	0.00	0.00	40.00	0.00	0.00	0.00	0.60
JAT-32/358,90	JAT-Min (I)	Minério	0.00	0.00	40.00	0.00	0.00	0.00	0.40
JAT-32/362,80	JAT-Min (I)	Minério	0.00	0.00	20.00	0.00	0.00	0.00	0.60
JAT-15/194,20	JAT-Min (II)	Brecha	380.00	97.00	30.40	1.20	9.80	0.20	0.70
JAT-28/160,40A	JAT-Min (II)	Foliacao	81.00	21.10	35.30	0.40	11.70	0.50	0.70
JAT-28/160,40B	JAT-Min (II)	Brecha	139.00	29.80	31.90	0.60	9.40	0.50	0.50
JAT-3/81,65	JAR-Min (IV)	Minerio	230.00	36.90	35.10	0.50	8.40	0.10	0.50
JAT-15/186,74	JAR-Min (IV)	Minerio	311.00	54.00	55.30	0.90	10.20	0.10	0.90
JAT-28/119,00	JAR-Min (IV)	Minerio	778.00	108.70	149.30	0.40	7.10	0.20	1.00
JAT-15/185,22	JAR-Min (IV)	Minerio	205.00	25.80	5.70	0.30	3.10	0.10	0.80

SAMPLE	Locality	Petrology	Nb	Hf	Zr	Y	Th	U	Ni
JAT-32/357,10	JAT-Min (I)	Minério	3.60	0.00	0.00	133.00	0.00	0.00	1790.00
JAT-32/358,90	JAT-Min (I)	Minério	3.50	0.00	0.00	143.50	0.00	0.00	1270.00
JAT-32/362,80	JAT-Min (I)	Minério	6.40	0.00	0.00	120.50	0.00	0.00	3930.00
JAT-15/194,20	JAT-Min (II)	Brecha	5.70	1.00	40.50	163.80	14.80	6.20	287.40
JAT-28/160,40A	JAT-Min (II)	Foliacao	2.90	0.30	13.30	223.60	16.20	8.80	727.40
JAT-28/160,40B	JAT-Min (II)	Brecha	2.80	0.80	31.00	241.90	16.10	8.10	1715.50
JAT-3/81,65	JAR-Min (IV)	Minerio	7.50	0.80	31.20	274.90	17.20	48.50	218.00
JAT-15/186,74	JAR-Min (IV)	Minerio	4.40	1.00	35.00	330.50	23.30	8.70	360.60
JAT-28/119,00	JAR-Min (IV)	Minerio	2.00	0.80	28.60	39.10	1.10	0.20	43.40
JAT-15/185,22	JAR-Min (IV)	Minerio	1.60	0.50	17.10	39.80	1.50	0.70	273.80

SAMPLE	Locality	Petrology	Co	Sc	V	Pb	Zn	Bi	Cd
JAT-32/357,10	JAT-Min (I)	Minério	1170.00	0.00	740.00	20.00	40.00	0.00	0.00
JAT-32/358,90	JAT-Min (I)	Minério	2320.00	0.00	590.00	20.00	30.00	0.00	0.00
JAT-32/362,80	JAT-Min (I)	Minério	670.00	0.00	630.00	0.00	20.00	0.00	0.00
JAT-15/194,20	JAT-Min (II)	Brecha	361.10	20.00	214.00	13.70	90.00	0.20	1.10
JAT-28/160,40A	JAT-Min (II)	Foliacao	220.90	18.00	715.00	21.00	176.00	0.30	2.10
JAT-28/160,40B	JAT-Min (II)	Brecha	403.00	19.00	548.00	11.00	204.00	0.20	2.50
JAT-3/81,65	JAR-Min (IV)	Minerio	273.90	14.00	113.00	19.00	482.00	0.40	3.50
JAT-15/186,74	JAR-Min (IV)	Minerio	418.10	24.00	194.00	16.00	111.00	0.60	1.40
JAT-28/119,00	JAR-Min (IV)	Minerio	66.80	15.00	85.00	12.00	52.00	0.40	4.20
JAT-15/185,22	JAR-Min (IV)	Minerio	152.30	14.00	50.00	7.20	269.00	0.30	4.00

SAMPLE	Locality	Petrology	Sn	W	Mo	Be	Ag	Au	Hg
JAT-32/357,10	JAT-Min (I)	Minério	0.00	60.00	0.00	0.00	0.00	7.00	0.00
JAT-32/358,90	JAT-Min (I)	Minério	0.00	50.00	0.00	0.00	0.00	14.00	0.00
JAT-32/362,80	JAT-Min (I)	Minério	0.00	0.00	0.00	0.00	0.00	12.00	0.00
JAT-15/194,20	JAT-Min (II)	Brecha	19.00	204.40	2.70	0.00	0.05	1263.90	3.80
JAT-28/160,40A	JAT-Min (II)	Foliacao	4.00	256.40	2.30	0.00	0.00	463.20	3.50
JAT-28/160,40B	JAT-Min (II)	Brecha	4.00	114.10	1.70	4.00	0.02	282.20	3.80
JAT-3/81,65	JAR-Min (IV)	Minerio	22.00	223.30	112.40	0.00	0.04	116.50	5.20
JAT-15/186,74	JAR-Min (IV)	Minerio	14.00	171.80	1.60	1.00	0.07	1310.80	2.70
JAT-28/119,00	JAR-Min (IV)	Minerio	8.00	332.50	0.00	3.00	0.00	546.40	10.40
JAT-15/185,22	JAR-Min (IV)	Minerio	24.00	322.30	1.30	1.00	0.00	146.80	5.20

SAMPLE	Locality	Petrology	Sm	Eu	Gd	Tb	Dy	Ho	Er
JAT-32/357,10	JAT-Min (I)	Minério	0.00	0.00	0.00	0.00	0.00	0.00	0.00
JAT-32/358,90	JAT-Min (I)	Minério	0.00	0.00	0.00	0.00	0.00	0.00	0.00
JAT-32/362,80	JAT-Min (I)	Minério	0.00	0.00	0.00	0.00	0.00	0.00	0.00
JAT-15/194,20	JAT-Min (II)	Brecha	67.14	10.01	55.63	7.06	35.38	6.11	14.97
JAT-28/160,40A	JAT-Min (II)	Foliacao	97.31	11.18	79.91	9.69	48.48	7.94	19.66
JAT-28/160,40B	JAT-Min (II)	Brecha	96.60	10.34	81.36	10.22	52.51	8.88	23.03
JAT-3/81,65	JAR-Min (IV)	Minerio	180.20	31.68	142.94	17.18	74.77	10.94	23.50
JAT-15/186,74	JAR-Min (IV)	Minerio	146.59	25.73	118.71	15.11	71.86	11.40	29.06
JAT-28/119,00	JAR-Min (IV)	Minerio	1.83	0.62	3.11	0.75	5.55	1.51	3.76
JAT-15/185,22	JAR-Min (IV)	Minerio	9.76	2.10	8.55	1.17	6.91	1.40	4.18

SAMPLE	Locality	Petrology	Tm	Yb	Lu	Ni+Co	Sn+W+Be	Sn+W	Ag+Zn+Pb
JAT-32/357,10	JAT-Min (I)	Minério	0.00	0.00	0.00	2960.00	60.00	60.00	60.00
JAT-32/358,90	JAT-Min (I)	Minério	0.00	0.00	0.00	3590.00	50.00	50.00	50.00
JAT-32/362,80	JAT-Min (I)	Minério	0.00	0.00	0.00	4600.00	0.00	0.00	20.00
JAT-15/194,20	JAT-Min (II)	Brecha	1.81	10.31	1.26	648.50	223.40	223.40	103.75
JAT-28/160,40A	JAT-Min (II)	Foliacao	2.35	12.89	1.61	948.30	260.40	260.40	197.00
JAT-28/160,40B	JAT-Min (II)	Brecha	2.93	16.08	1.97	2118.50	122.10	118.10	215.02
JAT-3/81,65	JAR-Min (IV)	Minerio	2.76	14.79	1.69	491.90	245.30	245.30	501.04
JAT-15/186,74	JAR-Min (IV)	Minerio	3.76	20.64	2.60	778.70	186.80	185.80	127.07
JAT-28/119,00	JAR-Min (IV)	Minerio	0.60	3.92	0.55	110.20	343.50	340.50	64.00
JAT-15/185,22	JAR-Min (IV)	Minerio	0.62	3.59	0.49	426.10	347.30	346.30	276.20

SAMPLE	Locality	Petrology	Sn+W+Be+Bi	Sn+W+Nb	Y+La+Ce	La + Ce	LaN	CeN	PrN
JAT-32/357,10	JAT-Min (I)	Minério	60.00	63.60	1756.00	1623.00	1606.45	1392.33	NA
JAT-32/358,90	JAT-Min (I)	Minério	50.00	53.50	1523.50	1380.00	1348.39	1190.59	NA
JAT-32/362,80	JAT-Min (I)	Minério	0.00	6.40	1077.50	957.00	938.71	824.26	NA
JAT-15/194,20	JAT-Min (II)	Brecha	223.60	229.10	1774.60	1610.80	1689.03	1345.54	1022.38
JAT-28/160,40A	JAT-Min (II)	Foliacao	260.70	263.30	2403.50	2179.90	2207.42	1850.99	1368.44
JAT-28/160,40B	JAT-Min (II)	Brecha	122.30	120.90	2498.90	2257.00	2300	1910.89	1431.31
JAT-3/81,65	JAR-Min (IV)	Minerio	245.70	252.80	5040.80	4765.90	5302.26	3864.11	2767.79
JAT-15/186,74	JAR-Min (IV)	Minerio	187.40	190.20	3866.30	3535.80	3629.35	2983.54	2114.02
JAT-28/119,00	JAR-Min (IV)	Minerio	343.90	342.50	69.30	30.20	31.61	25.25	18.93
JAT-15/185,22	JAR-Min (IV)	Minerio	347.60	347.90	246.80	207.00	221.61	171.16	129.67

SAMPLE	Locality	Petrology	NdN	PmN	SmN	EuN	GdN	TbN	DyN
JAT-32/357,10	JAT-Min (I)	Minério	NA	NA	NA	NA	NA	NA	NA
JAT-32/358,90	JAT-Min (I)	Minério	NA	NA	NA	NA	NA	NA	NA
JAT-32/362,80	JAT-Min (I)	Minério	NA	NA	NA	NA	NA	NA	NA
JAT-15/194,20	JAT-Min (II)	Brecha	732.83	NA	344.31	136.19	214.79	148.95	109.88
JAT-28/160,40A	JAT-Min (II)	Foliacao	1044.33	NA	499.03	152.11	308.53	204.43	150.56
JAT-28/160,40B	JAT-Min (II)	Brecha	1061.17	NA	495.38	140.68	314.13	215.61	163.07
JAT-3/81,65	JAR-Min (IV)	Minerio	1949.83	NA	924.1	431.02	551.89	362.45	232.2
JAT-15/186,74	JAR-Min (IV)	Minerio	1564.33	NA	751.74	350.07	458.34	318.78	223.17
JAT-28/119,00	JAR-Min (IV)	Minerio	15.67	NA	9.38	8.44	12.01	15.82	17.24
JAT-15/185,22	JAR-Min (IV)	Minerio	95.5	NA	50.05	28.57	33.01	24.68	21.46

SAMPLE	Locality	Petrology	HoN	ErN	TmN	YbN	LuN	Eu/Eu*
JAT-32/357,10	JAT-Min (I)	Minério	NA	NA	NA	NA	NA	NA
JAT-32/358,90	JAT-Min (I)	Minério	NA	NA	NA	NA	NA	NA
JAT-32/362,80	JAT-Min (I)	Minério	NA	NA	NA	NA	NA	NA
JAT-15/194,20	JAT-Min (II)	Brecha	85.1	71.29	55.86	49.33	39.13	0.5
JAT-28/160,40A	JAT-Min (II)	Foliacao	110.58	93.62	72.53	61.67	50	0.39
JAT-28/160,40B	JAT-Min (II)	Brecha	123.68	109.67	90.43	76.94	61.18	0.36
JAT-3/81,65	JAR-Min (IV)	Minerio	152.37	111.9	85.19	70.77	52.48	0.6
JAT-15/186,74	JAR-Min (IV)	Minerio	158.77	138.38	116.05	98.76	80.75	0.6
JAT-28/119,00	JAR-Min (IV)	Minerio	21.03	17.9	18.52	18.76	17.08	0.79
JAT-15/185,22	JAR-Min (IV)	Minerio	19.5	19.9	19.14	17.18	15.22	0.7

SAMPLE	Locality	Petrology	LaN/YbN	LaN/SmN	CeN/YbN	CeN/SmN	EuN/YbN	Sum_REE
JAT-32/357,10	JAT-Min (I)	Minério	NA	NA	NA	NA	NA	1623
JAT-32/358,90	JAT-Min (I)	Minério	NA	NA	NA	NA	NA	1380
JAT-32/362,80	JAT-Min (I)	Minério	NA	NA	NA	NA	NA	957
JAT-15/194,20	JAT-Min (II)	Brecha	34.24	4.91	27.28	3.91	2.76	2384.91
JAT-28/160,40A	JAT-Min (II)	Foliacao	35.79	4.42	30.01	3.71	2.47	3264.47
JAT-28/160,40B	JAT-Min (II)	Brecha	29.89	4.64	24.84	3.86	1.83	3372.24
JAT-3/81,65	JAR-Min (IV)	Minerio	74.93	5.74	54.6	4.18	6.09	6773.92
JAT-15/186,74	JAR-Min (IV)	Minerio	36.75	4.83	30.21	3.97	3.54	5177.77
JAT-28/119,00	JAR-Min (IV)	Minerio	1.69	3.37	1.35	2.69	0.45	64.11
JAT-15/185,22	JAR-Min (IV)	Minerio	12.9	4.43	9.96	3.42	1.66	318.89

Universidade de São Paulo

Pós Graduação em Geociências
Programa de Recursos Minerais e Hidrogeologia